

Measurement of the Helicity Asymmetry E for the $\gamma p \rightarrow \pi^0 p$ reaction in the
Resonance Region

by Chan Wook Kim

B.S. in Physics, Dec. 2012, University of California, San Diego
B.S. in Mathematics, Dec. 2012, University of California, San Diego
M.Phil. in Physics, May 2018, The George Washington University

A Dissertation submitted to

The Faculty of
The Columbian College of Arts and Sciences
of The George Washington University
in partial fulfillment of the requirements
for the degree of Doctor of Philosophy

January 7, 2022

Dissertation directed by

Igor Strakovsky
Research Professor of Physics

William Briscoe
Professor Emeritus of Physics

The Columbian College of Arts and Sciences of The George Washington University certifies that Chan Wook Kim has passed the Final Examination for the degree of Doctor of Philosophy as of November 23, 2021. This is the final and approved form of the dissertation.

Measurement of the Helicity Asymmetry E for the $\gamma p \rightarrow \pi^0 p$ reaction in the Resonance Region

Chan Wook Kim

Dissertation Research Committee:

Igor Strakovsky, Research Professor of Physics, Dissertation Co-Director

William Briscoe, Professor Emeritus of Physics, Dissertation Co-Director

Evangeline Downie, Associate Professor of Physics, Committee Member

Axel Schmidt, Assistant Professor of Physics, Committee Member

© Copyright 2022 by Chan Wook Kim
All rights reserved

Dedication

For my beloved wife, Victoria Lee, the most precious gift from God.

Acknowledgments

First and foremost, I would like to thank God for His love and guidance every day. I would like to express my sincere gratitude to my supervisors Igor Strakovsky and William Briscoe for their consistent support and patience in ensuring the finishing of this dissertation. All students in our research group would not have made it to this point if it weren't for their sacrifices. Countless times, they have supported the students above and beyond so that we could only think about physics. This project could not have been completed without the help of Nick Zachariou for his amazing work on his analysis that paved the way for the next generations to follow. I sincerely thank Franz Klein for providing his encyclopedic knowledge in the field of nuclear physics. His passion for physics and willingness to help the students were a true example to follow. No matter how nonsensical my questions were, his responses have always solved the problem. I would like to thank Dan Carman for all the meetings he held with me to educate me on the basics of experimental nuclear physics. As a beginning calibrator, I could not have asked for a better mentor. The weekly meetings we had laid the groundwork for my understanding of the CLAS detector.

My sincere gratitude goes to Axel Schmidt whose passion for physics has renewed my passion for physics as well. His questions and suggestions have led me to see the big picture of my research and inspired me to continue studying physics. I am grateful to have spent my last semester at GWU in his research group - All the best wishes to every member of his research group. I would like to thank Evie Downie for being an invaluable reader of my dissertation. Her detailed reading and expertise from the Mainz experiments have fixed countless errors and significantly improved the quality of the analysis. Especially, most of the figures in this dissertation would have been indecipherable if it weren't for her. I thank Stuart Fegan for his help in making the skim files and a kind introduction into the JLab life. I would like to thank the FROST

experiment run group for producing such an incredible project for students and for all the guidance along the way.

I am also grateful to Oleg Kargaltsev for being the best mentor and making my defense possible in Fall 2021. His suggestions on the application of machine learning have opened many possible solutions. My sincere gratitude goes to all members of the GWU physics department. All the coursework, exams, and discussions have prepared me well to conduct my own research and survive the outside world. I am incredibly thankful to Leah Kochenderfer for her continuous support for the students and the physics department. It was her detailed care and management that made my involvement at JLab as smooth as possible.

I would like to thank Donghyun Kim, Homin Kang, Haniel Kim, Jayoo Song, Kyuin Park, and all other members of the House of Angels in San Diego. They have taken me into their house to provide everything I needed to survive in San Diego and pursue my studies in physics - I will never forget our friendship. I also thank my friend Hossein Niyazi for the friendship as we shared the office space for the past five years. All the “outdoor” breaks we held a little too often have helped me to concentrate on finishing this dissertation work.

My most sincere gratitude goes to my wife, Victoria Lee, for all of her sacrifices and for taking the courage to embark on this challenging journey together. Without her help, I would have never been able to recover from the injury. Lastly, I thank my beloved dog, Chuddie, for being such a trooper and walking me every day.

Abstract of Dissertation

Measurement of the Polarization Observables E for $\gamma p \rightarrow \pi^0 p$ Reaction in the Resonance Region

In pursuit of resolving the missing baryon resonances problem, measurement of the double polarization observable E for $\gamma p \rightarrow \pi^0 p$ was performed using circularly polarized photons on longitudinally polarized proton targets (FROzen Spin Target experiment) at photon energies between 350 MeV and 2400 MeV. The final state particles were detected with the CEBAF Large Acceptance Spectrometer (CLAS) in Hall B at the Thomas Jefferson National Accelerator Facility (JLab). A new and unique application of deep learning algorithms was attempted in this analysis to better determine and minimize the hydrogen contamination in the collected data that occurred during the experiment. While it did not lead to a significant improvement for this particular experiment, it does show promise for future experiments under conditions optimized to take advantage of machine learning techniques. The extracted data of helicity asymmetry E is compared to the SAID, MAID, and BnGa partial-wave analyses (PWA) predictions and the experimental results from the CBELSA/TAPS experiment. In search of the baryon resonances via PWA, the newly analyzed data of polarization observable E will be included in the GW SAID database. The inclusion of this thesis's result demonstrated promising improvements in the higher energy ranges ($E_\gamma = [1.73, 2.37]$ GeV) where the experimental data was previously scarce. The current study provides more refined values of the helicity asymmetry E than previous analyses of the FROST data and is useful for testing theoretical predictions of the QCD-inspired models and Lattice QCD calculations.

Table of Contents

Dedication	iv
Acknowledgments	v
Abstract of Dissertation	vii
List of Figures	xi
List of Tables	xix
1 Introduction	1
1.1 Historical Background	1
1.2 Quantum Chromodynamics (QCD)	8
1.2.1 Constituent quark model predictions	13
1.2.2 Lattice QCD Predictions	16
1.2.3 Baryon Resonances	18
1.3 Pion photoproduction	21
1.3.1 Chew-Goldberger-Low-Nambu (CGLN) amplitudes	24
1.3.2 Multipole amplitudes	25
1.3.3 Helicity Amplitudes	28
1.3.4 Polarization Observables	31
1.3.5 Helicity asymmetry E	37
1.4 Partial Wave Analysis	39
1.5 Current challenges in Baryon spectroscopy	44
2 The FROST Experiment at Jefferson Lab	49
2.1 Continuous Electron Beam Accelerator Facility (CEBAF)	49
2.2 Photon Tagging Spectrometer	54

2.3	CLAS Spectrometer	57
2.3.1	Start Counter	58
2.3.2	Torus magnets	60
2.3.3	Drift Chambers	63
2.3.4	Time-of-Flight System	65
2.3.5	Electromagnetic Calorimeters	67
2.3.6	Trigger System	70
2.4	CLAS Frozen Spin Target (FROST) Experiment	72
2.4.1	Frozen Spin Target (FROST) - Longitudinal Polarization	73
2.4.2	Circularly Polarized Photon Beam	80
3	Data Analysis I - Event Selection	83
3.1	Overview of Event Selection	83
3.2	Raw Data Reconstruction	86
3.3	Initial Reaction Channel Filter	88
3.4	Energy Loss and Momentum Correction	89
3.5	Fiducial Selections	98
3.6	Particle ID: Proton Selection	103
3.7	Photon identification	105
3.8	Event vertex selection	108
3.8.1	Transverse vertex selection	108
3.8.2	Z-vertex selection	110
3.9	Binning	117
3.10	M_X^2 Selection	119
4	Data Analysis II - Application of Deep Learning	123
4.1	Feature Selection	124
4.2	Setup of Applied Neural Network	130

4.3	Initial Target Classification	135
4.4	Ice versus Carbon Classification	136
4.5	Possible Solutions	140
5	Data Analysis III - Helicity Asymmetry E	143
5.1	Scale Factor	144
5.1.1	Initial Scale Factor	144
5.1.2	First free proton peak extraction	151
5.1.3	Final Scale Factor	153
5.1.4	Second free proton peak extraction	159
5.2	Scale Factor: Alternative Method	162
5.3	Dilution Factor	165
5.4	Extraction of Helicity Asymmetry E	169
6	Results and Discussion	171
6.1	Results Interpretation	172
6.2	Comparison to CBELSA/TAPS Data	174
6.3	Comparison to PWA Predictions	175
6.4	Future Works	179
6.5	Summary	180
	Appendices	182
A	Additional plots	182

List of Figures

1	<i>The Eightfold Way</i> representation of baryons and mesons.	4
2	<i>The Eightfold Way</i> representation of lightest quarks.	5
3	An illustration of proton inner structure.	9
4	Feynman diagrams of possible strong interaction vertices of quarks and gluons	10
5	Experimental determination of electromagnetic and strong interactions' coupling constants in the function of momentum transfer Q^2	12
6	N^* resonances spectrum predicted by the instanton model	14
7	Drawing of three effective degrees of freedom configurations in constituent quark models	15
8	Space-time lattice defined in lattice QCD	16
9	N^* and Δ^* resonance spectrum obtained by LQCD with $m_{\pi^0} = 396$ MeV	18
10	The total cross section of meson photon production	20
11	Description of electric dipole moments in πN system at rest	28
12	Angle ϕ between the photon polarization vector and the reaction plane	37
13	Feynman diagrams showing contributions to π photoproduction	40
14	Schematic overview of baryon spectroscopy	45
15	Schematic layout and an aerial view of the CEBAF accelerator	50

16	Diagram of a cryomodule with radio-frequency cavities.	51
17	A picture of recirculation arcs with dipole magnets	53
18	The overall geometry of tagging system	56
19	Side view of the tagging system	56
20	A schematic of the CLAS spectrometer	57
21	A picture of the CLAS start counter	60
22	Magnetic field map of CLAS torus magnet	62
23	Top and cross sectional views of CLAS detector	63
24	A diagram of R3 superlayers of the drift chambers	64
25	Photograph of drift chambers R1 and R2	65
26	A photograph and an illustration of one sector of TOF counters	67
27	An illustration of the layer structure of one of the Forward electromagnetic calorimeter's module	69
28	An illustration of the internal structure of the electromagnetic calorimeter at large angles	70
29	Schematic diagrams of the triggering system	71
30	Kinematics for $\gamma p \rightarrow \pi^0 p$	72
31	Schematic diagram of frozen spin target for longitudinal and transverse polarization	74

32	Schematic diagram of the target polarization process with the 5 T superconducting magnet	75
33	A schematic overview of FROST experiment target system	77
34	Photograph of the polarizing magnet and the holding magnet	78
35	Target polarization versus the run number in each of run periods	79
36	Circular polarization as a function of the photon energy k and electron energy E_0	81
37	Electron beam polarization measured by the Møller polarimeter	81
38	Cross sections for all channels of γp reactions	84
39	Energy loss correction overall effect on kinematics	91
40	Energy loss correction on low momentum particles	92
41	Effect of energy loss corrections	93
42	Momentum correction: ϕ vs M_X^2	95
43	Momentum correction: θ vs M_X^2	96
44	Effects of energy loss corrections on momentum	97
45	Before and after momentum corrections on protons of $\gamma p \rightarrow Xp$	97
46	The angular distribution after the removal of inactive CLAS regions	98
47	Momentum versus laboratory angle in partitions of energy bins.	100
48	Missing mass squared distribution in partitions of momentum bins.	101

49	Inefficient Time-of-flight paddles removal	102
50	Particle identification β vs p	105
51	Photon identification	107
52	Transverse vertex selection	109
53	Schematic of FROST target side view	109
54	Event vertex positions 2D histogram	111
55	Butanol z -vertex selection range	113
56	Carbon z -vertex selection range	114
57	The reconstructed z -vertex positions in selected bins of E_γ and recoiling proton's θ_{lab}	116
58	The reconstructed z -vertex positions versus $\cos \theta_{cm}$ in partitions of E_γ	117
59	M_X^2 distribution used for determination of bins	119
60	Binning used for the analysis: E_γ vs $\cos \theta_{cm}$	119
61	Selection range of butanol M_X^2 distributions in four kinematic bins	121
62	Momentum versus $\cos \theta_{cm}$ in partitions of E_γ	122
63	Hydrogen contamination evidence	124
64	A heatmap showing correlation values between all the variables associ- ated with each $\gamma p \rightarrow \pi^0 p$ event	127

65	A schematic flowchart of a three-layered feed-forward neural network used in hydrogen contamination classification	130
66	Result of classification between butanol and carbon events in region $z = (3, 5)$ cm	136
67	Selection of ice training data	138
68	Selection of carbon training data	139
69	Results of classification between ice and carbon events in $z = [4, 8]$ cm.	140
70	π^0 missing mass squared distributions in selected bins of photon energies E_γ and $\cos \theta_{cm}$ for $E_\gamma \leq 0.71$ GeV	147
71	π^0 missing mass squared distributions in selected bins of photon energies E_γ and $\cos \theta_{cm}$ for $E_\gamma = (0.66, 1.6)$ GeV	148
72	π^0 missing mass squared distributions in selected bins of photon energies E_γ and $\cos \theta_{cm}$ for $E_\gamma = (1.6, 2.4)$ GeV	149
73	Example of scaled carbon events using initial scale factors overlaid with butanol distributions	150
74	Difference between butanol and initially scaled carbon M_X^2 distributions in selected bins of photon energies E_γ and $\cos \theta_{cm}$ with first free nucleon region extractions.	152
75	Example of scaled carbon events using final scale factors overlaid with butanol distributions	155
76	Scaled carbon M_X^2 distribution overlaid over butanol and carbon distribution for $E_\gamma \leq 0.94$ GeV	156

77	Scaled carbon M_X^2 distribution overlaid over butanol and carbon distribution for $1.6 \leq E_\gamma \leq 2.4$ GeV	157
78	Scaled carbon M_X^2 distribution overlaid over butanol and carbon distribution for $E_\gamma \in (1.6, 2.4)$ GeV and $\cos \theta_{cm} \in (-1, 0.2)$	158
79	Final scale factor obtained by χ^2 minimization for each kinematic bin.	159
80	Final extraction of butanol free nucleon ranges in M_X^2 distributions	161
81	Overview of final butanol free nucleon peak ranges	162
82	Selected examples of successfully obtained scale factors by fitting carbon M_X^2 distribution by cubic splines interpolation	165
83	Dilution factors for each kinematic bin	168
84	Helicity asymmetry E for $E_\gamma \in (0.35, 1.6)$ GeV	171
85	Helicity asymmetry E for $E_\gamma \in (1.60, 2.4)$ GeV	172
86	The comparison of the helicity asymmetry E predictions from the new SAID solution KI21 and the previous SAID solution MA19 for $E_\gamma \in (0.35, 1.6)$ GeV	175
87	The comparison of the helicity asymmetry E predictions from the new SAID solution KI21 and the previous SAID solution MA19 for $E_\gamma \in (1.60, 2.4)$ GeV	176
88	The comparison of χ^2 per data point for the new SAID solution KI21 and the previous SAID solution MA19	176

89	The comparison of the helicity asymmetry E predictions from the new SAID solution KI21 and the BnGa prediction for $E_\gamma \in (1.60, 2.4)$ GeV	177
90	The reconstructed z -vertex positions in partitions of θ_{lab} and E_γ	183
91	π^0 missing mass squared distribution partitioned in photon energies E_γ and $\cos \theta_{cm}$ for $E_\gamma \leq 0.71$ GeV	184
92	π^0 missing mass squared distribution partitioned in photon energies E_γ and $\cos \theta_{cm}$ for $E_\gamma = (0.71, 1.6)$ GeV	185
93	π^0 missing mass squared distribution partitioned in photon energies E_γ and $\cos \theta_{cm}$ for $E_\gamma = 2.4$ GeV	186
94	Difference between butanol and initially scaled carbon missing mass distributions partitioned in photon energies E_γ and $\cos \theta_{cm}$ for $E_\gamma \leq 0.66$ GeV	187
95	Difference between butanol and initially scaled carbon missing mass distributions partitioned in photon energies E_γ and $\cos \theta_{cm}$ for $E_\gamma = (0.66, 1.6)$ GeV	188
96	Difference between butanol and initially scaled carbon missing mass distributions partitioned in photon energies E_γ and $\cos \theta_{cm}$ for $E_\gamma = (1.6, 2.4)$ GeV	189
97	Scaled carbon M_X^2 distribution overlaid over butanol and carbon distribution for $E_\gamma \leq 0.66$ GeV	190
98	Scaled carbon M_X^2 distribution overlaid over butanol and carbon distribution for $E_\gamma = (0.66, 1.6)$ GeV	191

99	Scaled carbon M_X^2 distribution overlaid over butanol and carbon distribution for $E_\gamma \in (1.6, 2.4)$ GeV and $\cos \theta_{cm} \in (-1, 0.2)$	192
100	Final butanol free nucleon ranges for $E_\gamma \leq 0.66$ GeV and $\cos \theta_{cm} \in (-1, 1)$	193
101	Final butanol free nucleon ranges for $E_\gamma = (0.66, 1.6)$ GeV and $\cos \theta_{cm} \in (-1, 1)$	194
102	Final butanol free nucleon ranges for $E_\gamma \in (1.6, 2.4)$ GeV and $\cos \theta_{cm} \in (-1, 0.2)$	195

List of Tables

1	Elementary particles as described in the Standard Model	7
2	The roadmap of QCD	13
3	The status of N^* and Δ^* resonances by the Particle Data Group 2020	19
4	Basic properties of π	23
5	Quantum numbers of $\gamma N \rightarrow \pi N$ multipole amplitudes	27
6	Basic rules and definitions for multipole amplitudes	27
7	Helicity amplitudes $H_i(\theta)$ for $\gamma p \rightarrow \pi^0 p$	30
8	Polarization observables of meson photoproduction	32
9	Polarization observables in terms of helicity and transversity representation	35
11	Summary of the CLAS detector specifications	58
12	Hall B g9a/FROST run from 12/2007 - 2/2008	73
13	Degree of circularly polarized photon beam polarization measured by Møller polarimeter for 7 run periods	82
14	The average of the beam charge asymmetry (BCA) for each experiment period	82
15	The physical quantities derived from raw signals and associated data bank names	88

16	Malfunctioning TOF paddles with low statistics which are removed in the analysis	103
17	Z -vertex selection range for butanol and carbon targets	111
18	The polarization states of each run period	170

1 Introduction

Starting from J. J. Thompson’s discovery of electrons in 1897 and Ernest Rutherford’s discovery of protons in 1918, the search for the fundamental constituents of matter and the governing dynamics within has been pursued to this day. Following James Chadwick’s discovery of the neutron in 1932, protons and neutrons were believed to be point-like particles, that is until Hofstadter and his team at SLAC successfully showed in 1950s that protons and neutrons were rather “soft” entities with an internal structure [1]. Various scattering experiments have followed worldwide and shown that protons and neutrons are mere representations of a large ensemble of particles, called *hadrons*. More than 100 hadrons have been discovered experimentally and the quark model was introduced in an attempt to establish an order among discovered the hadrons by Murray Gell-Mann [2]. The excited states of hadrons are called *resonances* which are the main scope of this thesis. This chapter covers a brief overview of the theoretical framework which motivated the design of the FROST/g9a experiment from the Jefferson Lab.

1.1 Historical Background

As famously speculated by Hideki Yukawa, a type of middle-weight (*mesons*) particles, which are lighter than nucleons but heavier than electrons, were predicted to be responsible for the short range force (*strong force*). Yukawa’s predicted force would hold the nucleus together and counter the repulsive electromagnetic force of positively charged protons inside the nucleus [4]. The first unusual particles in the middle-weight range as Yukawa predicted were discovered by Cecil Powell [3] via observing cosmic rays at high altitudes using simple photographic emulsions; these were called pions (π). Followed by discoveries of the K^0 and K^+ kaons from cosmic rays, by observing

their decay products of charged pions (π^- and π^+):

$$\begin{aligned} K^0 &\rightarrow \pi^- + \pi^+ \\ K^+ &\rightarrow \pi^+ + \pi^0 + \pi^-, \end{aligned} \tag{1}$$

many mesons were starting to be discovered: η , ϕ , ω , ρ , *etc.* Meanwhile in 1950, a particle (Λ^0) with substantially heavier mass (1115 MeV) than protons and neutrons was found from cosmic rays whose decay products were a proton and a meson π^- :

$$\Lambda^0 \rightarrow p + \pi^-. \tag{2}$$

Such heavy particles are called the *baryons* family, together with the proton and the neutron. Discoveries of many new baryons followed over the years: Δ , Σ , Ξ , Ω , *etc.* Since proton decay was never observed (i.e., $p \nrightarrow e^+ + \gamma$) and the fact that all these heavy baryons decay to nucleons in the end, the law of *conservation of baryon number* was established, which assigns +1 to baryons and -1 to antibaryons.

Another surprising phenomenon was noticed when the time scale at which some baryons were produced was about 10^{-23} sec whereas they decayed at a relatively slower rate of about 10^{-10} sec. Such differences in time scales suggested that the force responsible for the production of baryons must be different from the force responsible for the disintegration of the baryons; the former is what is now considered the strong nuclear force and the latter is the weak nuclear force. As a remedy for this inconsistency, Gell-Mann and Nishijima postulated another conserved quantity called, *strangeness* such that any reactions via strong nuclear interactions conserve *strangeness*, but are not conserved in weak nuclear interactions. For example, the K-mesons (K) would have strangeness of $S = 1$ and Λ and Σ baryons would have $S = -1$. On the other hand, the non-strange hadrons ($S = 0$) would be π , n , and p . Hence, the following reactions in π^-p scattering would produce two strange particles

via strong interactions and conserve strangeness:

$$\begin{aligned}
\pi^- p &\rightarrow K^+ + \Sigma^-, \\
&\rightarrow K^0 + \Sigma^0, \\
&\rightarrow K^0 + \Lambda^0.
\end{aligned} \tag{3}$$

For decays of hadrons with $S \neq 0$ via weak nuclear force, strangeness would not be conserved:

$$\begin{aligned}
\Lambda &\rightarrow p + \pi^-, \\
K^0 &\rightarrow \pi^+ + \pi^-, \\
\Sigma^+ &\rightarrow p + \pi^0, \\
&\rightarrow n + \pi^+.
\end{aligned} \tag{4}$$

Because neutrons and protons would be indistinguishable in the absence of electromagnetic force, another quantum number, isospin I analogous to spin, was introduced by Werner Heisenberg to differentiate neutrons and protons under the strong force. Heisenberg proposed that neutrons and protons are two distinctive states of a particle *nucleon* which carries the isospin of $I = \frac{1}{2}$; the third component of isospin I_3 would be $\frac{1}{2}$ for protons and $-\frac{1}{2}$ for neutrons.

To establish a periodic order among the discovered hadrons, Gell-Mann introduced *The Eightfold Way* [2] to arrange the baryons and mesons according to their strangeness and isospin (the charge relates to isospin by $I_3 = Q - \frac{1}{2}(S + B)$) as shown in Fig. 1. In *The Eightfold Way*, the hadrons with the same spin (J) and parity (P) are grouped into SU(3) representation multiplets to form an array where the charge and the strangeness are two axes. For baryons with $J^P = \frac{1}{2}^+$, the particles form a *baryon octet* (Fig. 1 (a)) with two particles occupying the center with $Q = 0$ and $S = -1$. For baryons with $J^P = \frac{3}{2}^+$ and relatively heavier mass than the baryon octet family, they form a triangular array called the *baryon decuplet* as shown in Fig. 1 (b).

With the final discovery of the Ω^- baryon [5] in 1964, all the predicted particles in the decuplet were experimentally discovered in the laboratory. Since then, every newly detected hadron was beautifully placed in its *The Eightfold Way* multiplets and the *antibaryon* multiplets with opposite charge and strangeness. For the case of the pseudoscalar mesons ($J^P = 0^-$) and the vector mesons ($J^P = 1^-$), they each form a nonet, a combination of an octet and a singlet as shown in Fig. 1 (c, d).

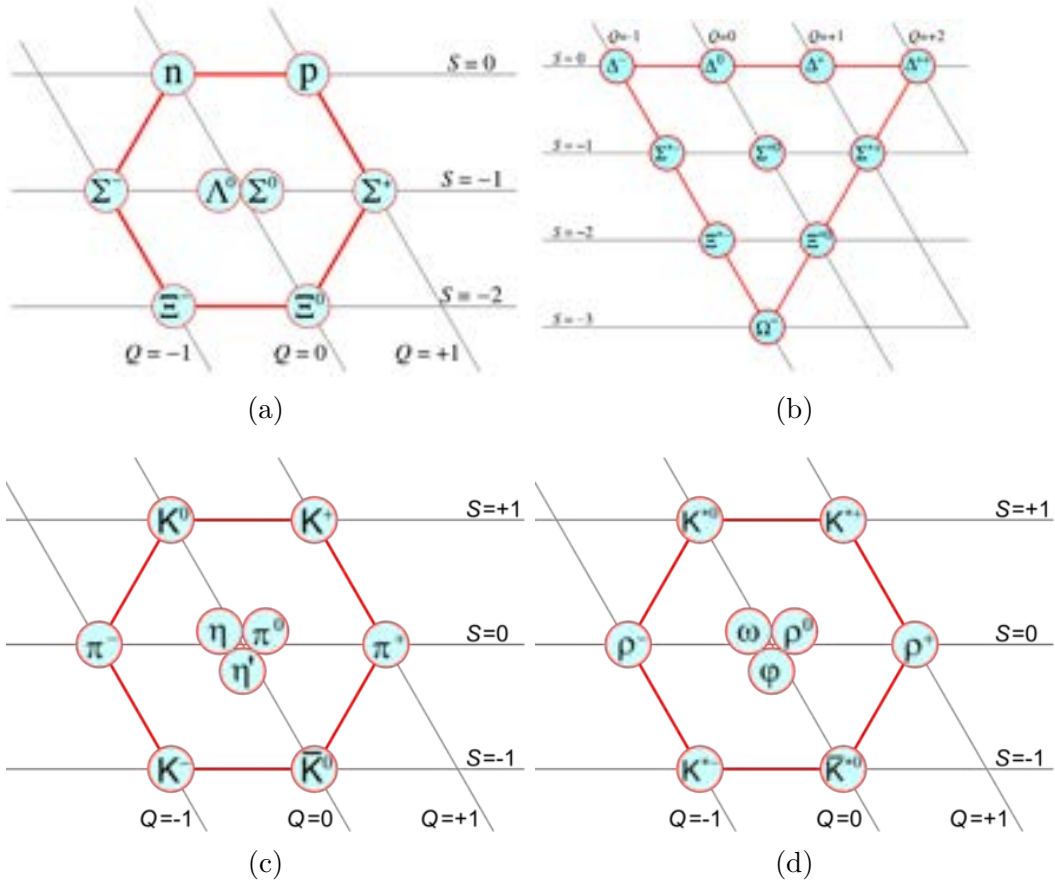


Figure 1: *The Eightfold Way* representation of baryons and mesons according to their charge and strangeness: (a) $J^P = \frac{1}{2}^+$ baryon octet, (b) $J^P = \frac{3}{2}^+$ baryon decuplet, (c) $J^P = 0^-$ pseudoscalar meson nonet, and (d) $J^P = 1^-$ vector meson nonet. Image source: *Wikimedia Commons*.

One might raise the question of why hadrons follow such patterns and representations of the $SU(3)$ group. A possible solution was proposed by Murray Gell-Mann and George Zweig independently that the hadrons are composed of even smaller

constituents called *quarks*, which are classified by three flavors: “up”, “down”, and “strange”. Gell-Mann’s proposed quark model states that the composition of baryons are three quarks (qqq) and mesons are composed of a quark and an *antiquark* ($q\bar{q}$). Three quark composition of baryons gives rise to 27 possible qqq flavor combinations and the decomposition according to SU(3) explain baryon octets and decuplets: $3 \otimes 3 \otimes 3 = 10 \oplus 8 \oplus 8 \oplus 1$. For mesons, $q\bar{q}$ structure allows for nine possible flavor combinations and its decomposition gives meson nonets: $3 \otimes 3 = 1 \oplus 8$. The postulated internal entities, *quarks*, would carry fractions of quantum numbers (S , Q , *etc*) of hadrons in a way that the sum of all quarks’ fractional quantum numbers inside a hadron would yield the observed hadrons’ quantum numbers in *The Eightfold Way* representation. Fig. 2 shows the triangular *Eightfold Way* of quarks and *antiquarks* with the charge and strangeness as the axes, which forms the three dimensional representation of SU(3).

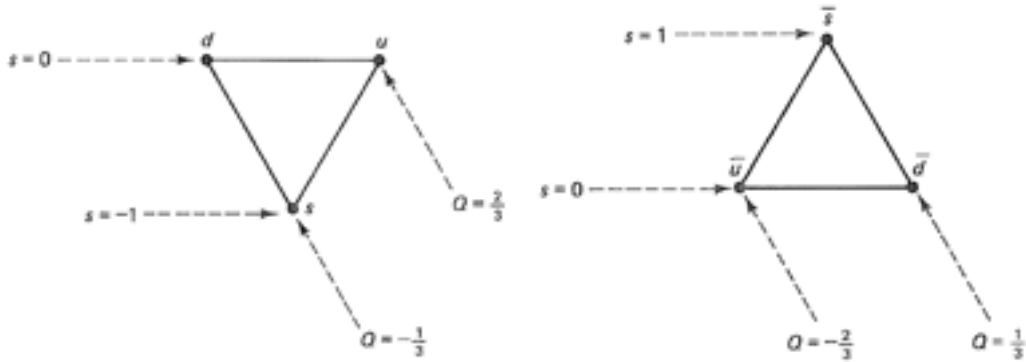


Figure 2: *The Eightfold Way* representation of “up”, “down”, and “strange” quarks (left) and their *antiquarks* (right). Image source: [4]

Even though the quark model successfully described SU(3) multiplet structures of hadrons, the model faced two significant obstacles, each from the experimental and theoretical sides. No experiments have isolated and observed free quarks for reasons not yet apprehended, which led to the notion of *quark confinement*. On the theory side, the three baryons which are positioned at the vertices of the baryon decuplet

are composed of identical flavor quarks, violating the Pauli exclusion principle: Δ^{++} (uuu), Δ^{-} (ddd), and Ω^{-} (sss). According to the Pauli exclusion principle, two or more identical fermions cannot occupy the same quantum state. Thus, the total wave function should be antisymmetric when two quarks are exchanged. Since each quark carries a spin of $\frac{1}{2}$, these baryons all have a total spin of $\frac{3}{2}$ and all quarks inside should have parallel spins, resulting in a symmetric baryon wave function. The remedy for the violation of the Pauli exclusion principle was the assignment of a new quantum number, the *color* charge, to each quark which could take one of three colors: “*red*”, “*green*”, or “*blue*”. For an example of Δ^{++} , the three u quarks would each take one of the color charges, differentiating against each other and resulting in an antisymmetric total wave function of the baryon. The color charge introduced here is used as a property of quarks and gluons that causes the particles to experience strong force described by the theory of Quantum Chromodynamics (QCD).

		generation			mass [GeV]			electric	color	weak	spin
		1	2	3	1	2	3	charge	charge	isospin	
fermions	quarks	u	c	t	2.2×10^{-3}	1.28	173.1	2/3	r,g,b	1/2	1/2
		d	s	b	4.7×10^{-3}	0.096	4.18	-1/3	r,g,b	-1/2	1/2
	leptons	e	μ	τ	5.11×10^{-4}	0.11	1.78	-1	0	1/2	1/2
		v_e	v_μ	v_τ	$< 0.1 \times 10^{-8}$	$< 1.7 \times 10^{-4}$	< 0.018	0	0	-1/2	1/2
		particles			mass [GeV]			couples to			spin
								electric	color	weak	
bosons	gauge bosons	g			0			no	yes	no	1
		W^\pm			80			no	no	yes	1
		Z^0			91			yes	no	yes	1
		γ			0			yes	no	no	1
	scalar boson	H			125						0

Table 1: The discovered quarks and leptons are grouped into three generations in the order of increasing mass. The properties of their charge to electromagnetic, strong nuclear, and weak nuclear interactions, and spin are listed. The gauge bosons (*force carriers*) mediate the interactions of electromagnetic, strong and weak forces between the listed quarks and leptons. The Higgs boson, H , is a *spin* -0 scalar boson without electric and color charge which are hypothesized to allow some fundamental particles to acquire mass [38].

In 1974, a very peculiar particle (J/ψ) was found both at BNL and SLAC whose mass was about three times the mass of a proton, but also electrically neutral [6]. J/ψ decayed electromagnetically to e^+e^- with a total baryon number of 0, but its mass totally defied the meaning of meson, which is supposed to be a *middle-weight* particle, lighter than baryons. Such finding leads to a hypothesis that a new flavor of quark, the *charm quark*, exists whose mass is heavier than a nucleon. If the charm quark's existence was true, the SU(3) symmetry is now extended to SU(4) and many other baryons and mesons must have been found whose quark contents include combinations of “u”, “d”, “s” and “c” quarks. Subsequently from 1974 to 1977, the following baryons and mesons were discovered which contain a single charm quark

and validated the charm quark's existence: Λ_c^+ (udc), Ω_c^{++} (uuc), Ξ_c (usc), Ω_c (ssc), D^0 ($c\bar{u}$), D^+ ($c\bar{d}$), and D_s^+ ($c\bar{s}$). Furthermore, two more quark flavors were discovered and confirmed their existences in a similar way: bottom quark (b) in 1977 [7] and top quark (t) in 1995 [8]. The quark model SU(3) symmetry was then extended to SU(6), but with a serious problem of large differences in masses of the quarks; the top quark mass ($m_t = 175.6$ GeV) is about 40 times the mass of the bottom quark ($m_b = 4.2$ GeV) whereas the bottom quark is about 1000 times heavier than up quarks. Table 1 lists the properties of all discovered quarks and leptons (fermions) which makes up all matter and gauge bosons that mediate the interactions among fermions, as described in the theory of the Standard Model.

1.2 Quantum Chromodynamics (QCD)

When scattering the proton targets with electrons at the invariant mass then $W < 2$ GeV, the proton would be excited into resonances such as the Δ state and produce a π meson: $ep \rightarrow e\Delta^+ \rightarrow \pi^0 p$. However, if W exceeds 2 GeV and the momentum transferred (Q^2) to the proton is very large, the proton would break up into many debris, resulting in more particles in final states than the initial electron and proton. The extra energy, used to scatter the target nucleon to the point of separating the quarks, will create new quark pairs in the process which form new hadrons. Such experiments are called the deep inelastic scattering (DIS) experiments; where a short wavelength virtual photon will probe into a more detailed inner structure of the proton with better spatial resolution. In 1968, a DIS experiment with 17 GeV on a proton target covering a range of $Q^2 < 7.2 \text{ GeV}^2$ was performed at SLAC [9]. The results showed that in $W < 2$ GeV region, the cross section fell significantly with increasing Q^2 . On the other hand, in $W > 2$ GeV region, the cross section (and structure functions) showed an unexpectedly weak Q^2 dependence. As more DIS experiments followed, the idea of proton consisting of only three valence quarks started to falter as

the fraction (Bjorken- x) carried by each of three valence quarks at lower values of Q^2 did not sum up to be $1/3$ of the total. An interpretation of such phenomena was given that there exist many virtual quark-*anti*quark pairs, called *sea quarks*, inside hadrons that are bound by gluons. The depiction of nucleons composed of valence quarks, sea quarks and gluons is shown in Fig. 3. In this description of hadrons, the hadrons' quantum numbers such as Q , I , color, and spin solely come from valence quark's quantum numbers and the sea quark pairs exist only briefly until they annihilate each other inside the hadron. In addition, the existence of sea quarks would support resolving the problem of significant difference in mass between the measured hadron mass and the sum of valence quarks' mass; the valence quarks of protons (uud) only make up about 1% of the total proton mass.

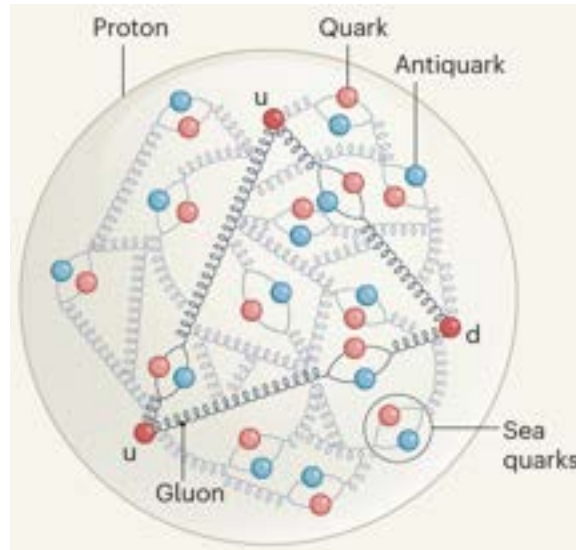


Figure 3: An illustration of proton inner structure as described in the theory of QCD. Three valence quarks are surrounded by sea quarks (quark-*anti*quark pair) and gluons. Image Source: [10]

The color charges of the quarks are carried off by gluons and the color charge is always expected to be conserved at the vertices of interactions in the Feynman diagrams. For example, a *quark* \rightarrow *quark* + *gluon* vertex is shown in Fig. 4 where u quark with blue color charge changes its color to red as the gluon carries off a unit of

blue color charge and a negative red color charge. Since gluons themselves carry color and *anticolor* charges, gluons couple to other gluons directly, unlike in QED where photons are electrically neutral. The gluon-gluon vertices have: three gluon vertices and four gluon vertices, as shown in the two right Feynman diagrams of Fig. 4.

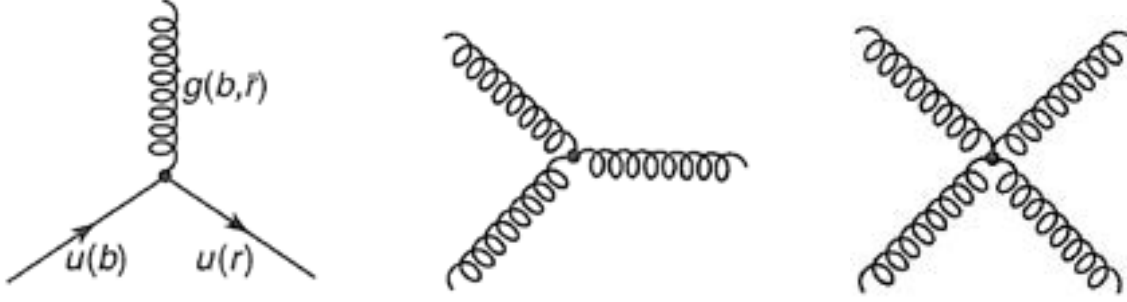


Figure 4: Feynman diagrams of possible strong interaction vertices of quarks and gluons. The left diagram depicts $q(b) \rightarrow q(r) + g(b, \bar{r})$ where the color charge of an *up* quark is changed from *blue* to *red* by a gluon carrying off one unit of blue charge and one unit of negative red charge. The right two diagrams show 3-gluon and 4-gluon vertices. Image source: [4]

Each vertex of the strong interactions in the Feynman diagram has the magnitude of strong force proportional to the strong coupling constant α_s . Experiments have shown that the strong coupling constant α_s is inversely proportional to the momentum transferred (Q^2) [11] as opposed to the electromagnetic coupling constant α_{em} being proportional to Q^2 [12]. In DIS, higher Q^2 indicates shorter wavelength photon which enables probing of the quarks inside the nucleon: $\lambda \approx 1/\sqrt{Q^2}$. Therefore, an increase of Q^2 could be considered as a shorter distance at which the incident particle interacts with the quarks inside the target nucleon. From Fig. 5(b), strong coupling constant α_s in the function of Q^2 are plotted and one can safely deduce that the α_s increases (decreases) as the separation distance of color charges increases (decreases) within 1 Fermi, which is an effect also known as the running coupling constant. At very short distances, the strong force (attractive) is decreased to the point that quarks

inside the hadron are free and non-interacting, a phenomenon which is called the *asymptotic freedom*. One possible explanation for why asymptotic freedom occurs is that the countless spontaneous creation and annihilation of gluons and sea quarks cause the *anti-screening* effect. As more gluons and sea quarks are present inside the nucleon, more vertices of strong interactions are present where each vertex contributes a factor of α_s . If the separation distance between the color charges (of valence quarks) increases, the probability of those color charges interacting with additional gluons and sea quarks would increase, increasing the strong force experienced at large distances within the nucleon. Inside a nucleon, there is also electromagnetic force present but it has a dependence on the distance which is the opposite of the strong force. The *screening* of the core electric charge ($+q$) occurs as virtual positron-electron pairs are created in a vacuum, causing virtual electrons to be attracted towards $+q$ and virtual positron to be repelled away. The overall *vacuum polarization* causes a reduction of the core charge's field strength. Hence, as the distance between the electric charges increases inside a nucleon, more virtual e^-e^+ pairs become available, and *screening* of the test charge increases, causing the decrease of the α_{em} . The experimental result on α_{em} is shown in Fig. 5(a).

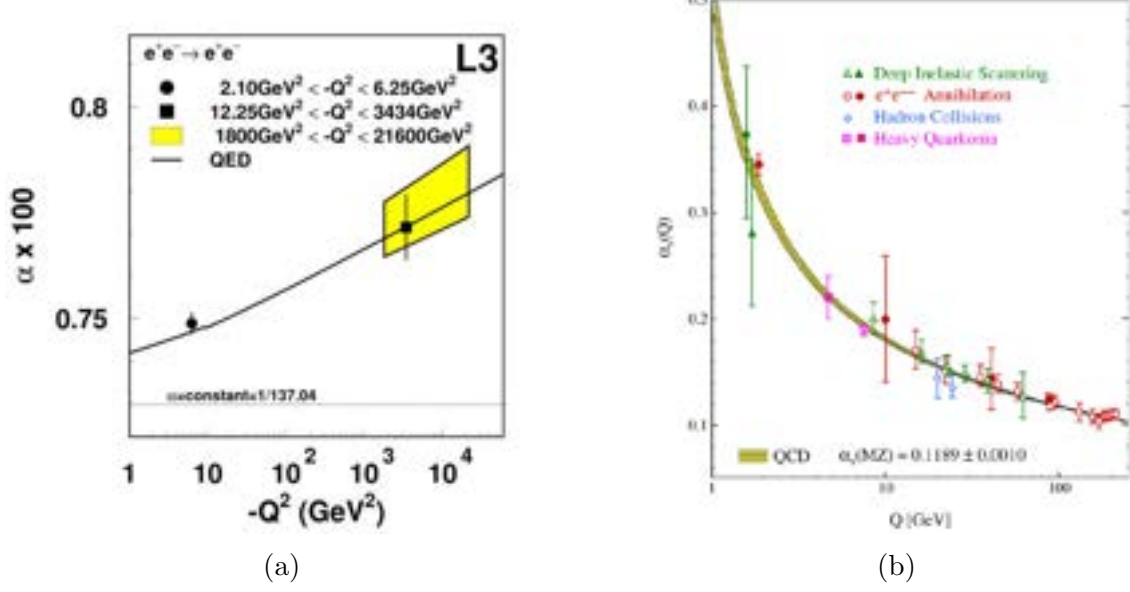


Figure 5: Experimental determination of (a) electromagnetic [12] and (b) strong interactions' [11] coupling constants in the function of momentum transfer Q^2 . Figure sources: Ref. [12] for (a) and Ref. [11] for (b)

Because of the running coupling constant of strong nuclear interaction, different approaches are required to tackle QCD at high and low energy regimes. At high Q^2 , small α_s allow QCD to be tackled with perturbation theory techniques: the expansion of observable in powers of $\alpha_s \ll 1$. In this energy range of perturbative QCD (pQCD), the quarks inside hadrons are considered free and non-interacting. For lower energy regions where low Q^2 could excite the target nucleons into resonances, instead of breaking them into debris, the larger α_s prohibit the perturbation technique in powers of α_s and any other analytical solutions to QCD. Currently, various Constituent quark models (CQMs) and lattice QCD calculations yield the best theoretical predictions to the properties of hadrons and their excited states in this energy range.

Range	Features	Theory	Experiment
high energy / short distance (quarks and gluons)	small α_s , asymptotic freedom, weak QCD	perturbative QCD	deep inelastic scattering
low energy / long distance (hadrons and baryons)	large α_s , quark confinement, strong QCD	lattice QCD, constituent QM	resonance experiments

Table 2: The roadmap of QCD in which varying α_s leads to different theoretical and experimental approaches for low and high energy ranges.

1.2.1 Constituent quark model predictions

In the non-perturbative region of QCD where the strong coupling constant $\alpha_s \gg 1$, the interactions between sea quarks and gluons must be accounted for along with the valence quarks' interactions. The Constituent Quark Models (CQM) hypothesize that the baryons are composed of entities called constituent quarks, include valence quarks and interactions between sea quarks and gluons. Hence, the masses of u and d constituent quarks range from 220 MeV for relativistic models and 330 MeV for non-relativistic models, which are much heavier than bare quarks masses [57]. Also, constituent quarks are not considered as point-like entities, but rather have electric and strong form factors to account for interactions contributing to the mass. The most important task is to determine the correct effective degrees of freedom that reflect the nature of interactions since the number of effective degrees of freedom is directly correlated to the number of predicted resonances. Therefore, experimentally determined resonance states should help to constrain the determination of the effective degrees of freedom in CQMs.

Many different CQMs have postulated various forms of this confining short-range

interactions and potentials to describe what is going on inside the baryon. Three of the most successful models are One-Gluon-Exchange (OGE) model [13, 14, 15], the Goldstone boson exchange model [16, 17], and the instanton exchange model [28]. The OGE model uses gluons as the mediator for the short-range interactions whereas the Goldstone model used pseudoscalar octet mesons (Goldstone bosons) to be the mediator. Fig. 6 shows the N^* resonances predicted by the instanton model which is a relativistic quark model where potentials are of the 't Hooft's instanton-induced quark interaction [18, 19]; instantons refer to strong fluctuations of gluon fields. One can see that the predicted resonances are fairly comparable to experimental findings in the lower energy region of $W \leq 1.7$ GeV, but at higher energies ($W \geq 1.7$ GeV), significantly more resonances are predicted than discovered.

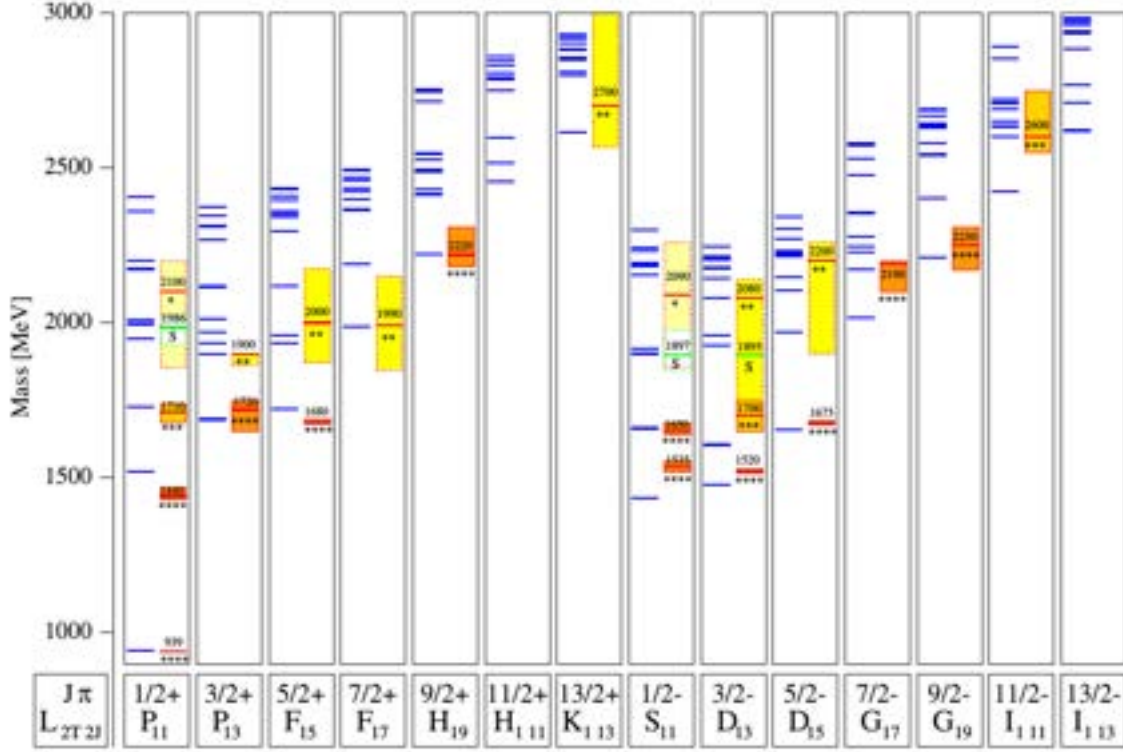


Figure 6: N^* resonances spectrum predicted by a relativistic quark model with instanton quark forces. Left sidebars are CQM predictions and right sidebars are experimentally confirmed states with *'s denoting the ranking of existence by PDG2016. The height of the boxes around experimental results indicates uncertainties in the measurement [28].

As mentioned before, a decreased number of effective degrees of freedom in CQM will result in fewer predicted resonances. One example of CQM with fewer effective degrees of freedom is the diquark-quark model where two of the three quarks in baryons are strongly bound as described in the second figure of Fig. 7. A strongly bound diquark results in fewer effective degrees of freedom and excitation of a diquark does not contribute to lower energy resonances. Although lesser excited states are produced, there are still more resonances predicted than experimentally confirmed.

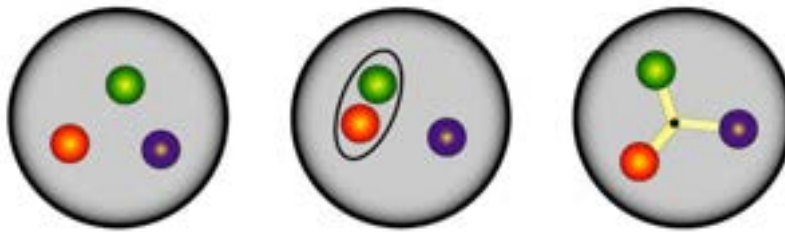


Figure 7: Drawing of three effective degrees of freedom configurations in constituent quark models: three equivalent constituent quarks, diquark-quark mode, and flux tube model. Image source: [57]

Great theoretical efforts are underway to reformulate the CQMs and the following list contains the ongoing models being developed. Most of the models fairly agree on their predictions of resonance spectrum in the lower energy region ($W \leq 1.7$ GeV) and also agree with the partial wave analysis results of πN scattering experiments [42]. Further experimental efforts are necessary to help configure the right effective degrees of freedom and distinguish between these models:

- Algebraic models [20]
- Colour-dielectric models [21]
- Bag models [22]
- Chiral bag models [23]
- Soliton models [24]

- Skyrme models [25]
- Covariant models based on Dyson-Schwinger equations [26]
- Vibron models [27]

1.2.2 Lattice QCD Predictions

Lattice QCD (LQCD) calculations showed promising results in simulating the non-perturbative region QCD on a quantized space-time lattice as the technology of supercomputers advanced. In LQCD, the space-time continuum is replaced by space-time lattice with a finite lattice size and spacing between grids where gluons, valence quarks, and sea quarks can propagate along with the grids. The quark fields q_n are positioned at every lattice site whereas the gluon fields $U_{n\mu}$ is on every lattice link as shown in Fig. 8. The size of the lattice is taken to be larger than the size of the hadron to allow a proper depiction of the hadron and the spacing between grids is set to be significantly smaller than the size of the hadron down to the limit of allowed computational power.

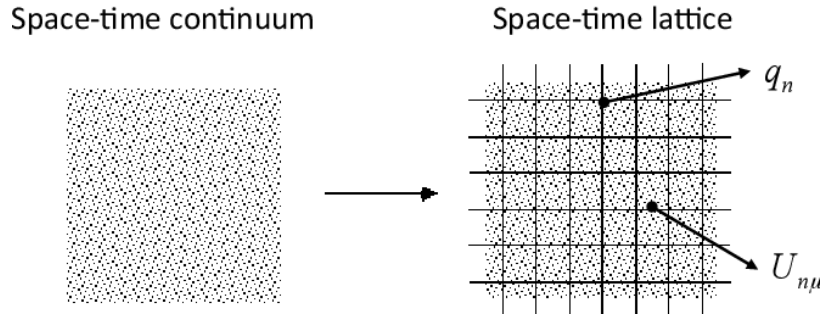


Figure 8: Space-time continuum is replaced by space-time lattice in lattice QCD where quark fields q_n is at every lattice site and gluon fields $U_{n\mu}$ is on every lattice link. Image source: [30]

The calculation of any interesting physical quantities, such as the proton mass, can be numerically computed by path integrals using Monte Carlo simulation in the lattice space; integrals are replaced with sums in lattice space-time. Calculated

quantities in lattice space then require extrapolation to approximate closer to the physical and real quantities. At first, the quark masses used in LQCD are set to be much bigger than actual quark masses because the computational cost increases significantly as quark masses are decreased. Therefore, when solving systems with heavier generations of quarks (c , b , and t) [31], LQCD produced much better results than a system with lighter quarks (u and d). However, the recent advancements of supercomputers and LQCD led to the successful calculation of the masses of light hadron spectrum of QCD [32]: ρ , K^* , N , Λ , Σ , Ξ , Δ , Σ^* , Ξ^* and Ω in the order of increasing mass. In Fig. 9, LQCD calculations on N^* and Δ^* resonance spectrum by using the unphysical neutral pion mass of $\pi^0 = 396$ MeV are shown [29]; resonances are partitioned by their total angular momentum and parity J^P . Even though the obtained resonance spectrum is quantitatively incomparable to experimental results nor constituent quark model (CQM) predictions because of the unphysical π^0 mass used, one can see that LQCD predictions roughly align with the CQM predictions (Fig. 6). With the prospect of advancements in technology and the promising LQCD results, LQCD remains one of the leading tools to provide a theoretical standpoint for baryon resonance studies.

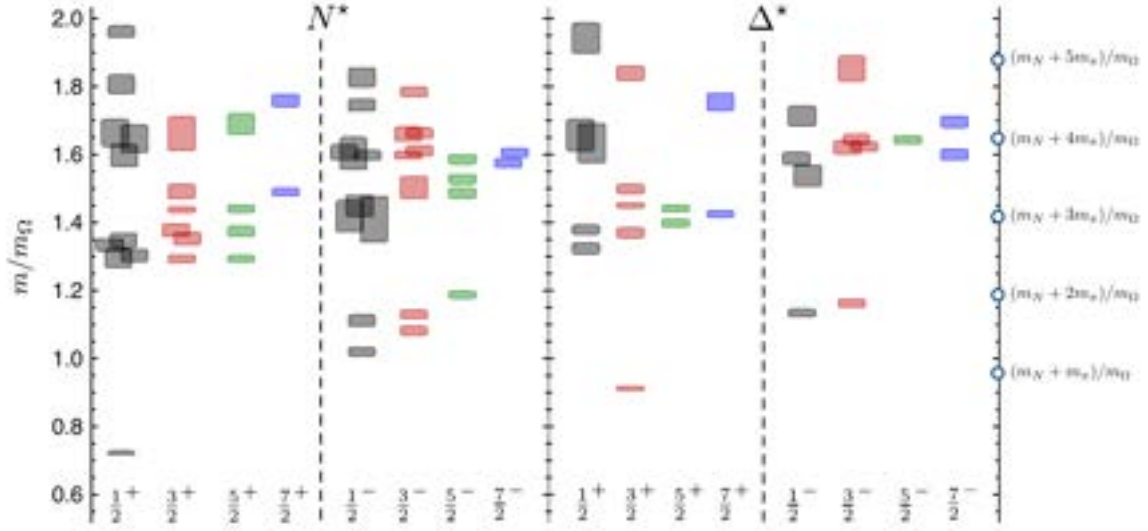


Figure 9: N^* and Δ^* resonance spectrum obtained by LQCD with $m_{\pi^0} = 391$ MeV. Each column and subcolumn are categorized according to the total angular momentum and parity states J^P . The resonance masses are divided by the Ω baryon mass to give mass ratios [29].

1.2.3 Baryon Resonances

The successful prediction of excited states of the hydrogen atom by the Bohr model confirmed the quantum mechanical description of an isolated physical system at the atomic scale. Similarly, information about excited states of hadrons can lead us to discover key information on the dynamics of the hadron's constituents formulated by various theoretical models. The baryon resonances which are excited states of baryons can be classified by their total angular momentum ($J = L + S$), parity (P), Breit-Wigner mass, and decay widths (Γ). Since parity is a multiplicative quantum number, the product of parities of quark (+1) and antiquark (−1) contents of a hadron gives the parity of a hadron; baryons will have parity of $(+1)^3$ and mesons with $(-1)(+1)$. For excited states (resonances), corresponding orbital angular momentum (l) will introduce an extra factor of $(-1)^l$ to parity, which arises from the angular part of the spatial wave function ($Y_l^m(\theta, \phi)$). The resonances have particularly short lifetimes (10^{-24}) and decay energy widths of $\Gamma = 0.1 \sim 0.3$ GeV, which indicate that the decay

process is via strong interactions. Their lifetimes (τ) can be directly measured from the uncertainty relation:

$$\tau = \Delta t = \frac{\hbar}{\Delta E} \simeq \frac{\hbar}{0.2 \text{ GeV}} \simeq 10^{-24} \text{ s.} \quad (5)$$

Status as seen in											
Particle J^P	overall	$N\gamma$	$N\pi$	$\Delta\pi$	$N\sigma$	$N\eta$	ΔK	ΣK	$N\rho$	$N\omega$	$N\eta'$
$N(1440)1/2^+$	****	****	*****								
$N(1520)3/2^+$	****	****	*****								
$N(1535)1/2^+$	****	****	*****	+	****						
$N(1650)1/2^+$	****	****	*****	+	****						
$N(1675)3/2^+$	****	****	*****		+	+					
$N(1680)5/2^+$	****	****	*****		+	+					
$N(1700)3/2^+$	***	***	****	+	+	+			+		
$N(1710)1/2^+$	****	****	*****		****	***	***	***	+	+	***
$N(1720)3/2^+$	****	****	*****	+	+	****	***	***	+	+	
$N(1860)5/2^+$	***	***	****	+	+						
$N(1875)3/2^+$	***	***	****	+	***	+	+	+	+	+	+
$N(1890)1/2^+$	***	***	****	+	+	***	***	***	***	***	***
$N(1890)1/2^+$	****	****	*****	+	+	****	***	***	***	***	****
$N(1900)3/2^+$	****	****	*****	***	***	***	***	***	***	***	***
$N(1990)7/2^+$	***	***	****		***	***	***	***			
$N(2000)5/2^+$	***	***	****	+	***	+	+	+			+
$N(2040)3/2^+$	+	+									
$N(2060)5/2^+$	***	***	****	+	+	+	+	+	+	+	+
$N(2100)1/2^+$	***	***	****	***	***	***	***	***	***	***	***
$N(2120)3/2^+$	***	***	****	***	***	***	***	***	***	***	***
$N(2190)7/2^+$	****	****	*****	***	***	***	***	***	***	***	***
$N(2220)9/2^+$	****	****	*****	***	***	***	***	***	***	***	***
$N(2250)9/2^+$	****	****	*****	***	***	***	***	***	***	***	***
$N(2300)1/2^+$	***	***	****								
$N(2570)5/2^+$	***	***	****								
$N(2600)11/2^+$	****	****	*****								
$N(2700)13/2^+$	***	***	****								
**** Existence is certain. *** Existence is very likely. ** Evidence of existence is fair. + Evidence of existence is poor.											

(a)

(b)

Table 3: The status of (a) N^* and (b) Δ^* resonances with *'s denoting the ranking of existence provided by Ref. [38]. Table is taken from [38].

Most resonances' energy widths are larger than the spacing distances between each resonance. Therefore, there exist many overlaps of resonances in the γp reaction as shown in Fig. 10. Heavily overlapped resonances and their identifications are the main challenges in developing dynamical reaction models in $W < 2$ GeV region [41]. In Fig. 10(a) where the total cross section of π photoproduction is plotted, 1 π and 2 π reaction channels are compared. At $W > 1.5$ GeV, it is apparent that the 2 π

reactions' cross section dominates over the 1π reactions, complicating the extraction of photoproduction amplitudes associated with N^* and Δ^* resonances in that region. In Fig. 10(b), cross sections of $K^+\Lambda$, $K^+\Sigma^0$, $K^+\Sigma^+$, ηp , and ωp are compared against $\pi^0 p$, $\pi^0\pi^0 p$, and $\pi^+\pi^- p$ reaction channels. Aside from the most dominant reaction channel $\pi^+\pi^- p$, many reactions are closely positioned in a similar range of the cross section and about ten orders of magnitude smaller than the dominant $\pi^+\pi^- p$.

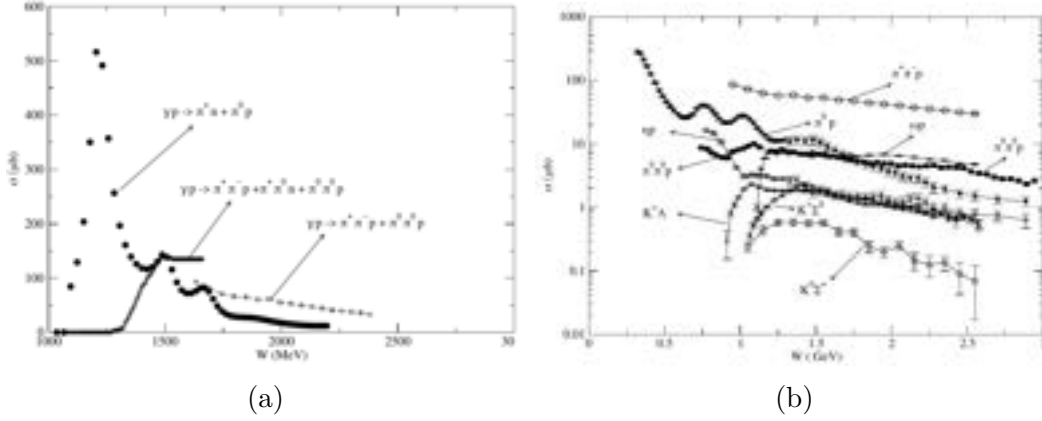


Figure 10: The total cross section of meson photoproduction. (a) The comparison of one-pion and two-pion reactions. (b) The comparison of $K^+\Lambda$, $K^+\Sigma^0$, $K^+\Sigma^+$, ηp , ωp , one- π and two- π reactions [41].

Table. 3 shows the listing of N and Δ resonances with the evaluations on its experimentally confirmed status given by the Particle Data Group [38]; stars (*) indicate the ranking of each resonance's existence. Most of the resonances are found in the $N\pi$ and $N\gamma$ scattering and using meson and photon beams have their specific advantages over one another. First, two reasons for not using baryon beams (protons, deuterons, and alpha particles) for exciting a nucleon to a resonance state is that (1) baryons need significantly higher energies to cause resonances due to their heavy mass and (2) the final states have three or more hadrons which complicate the interaction kinematics by the final state interactions (FSI) [45]. In contrast, the meson and photon beams have significantly less FSI and it is easier to tailor the experiment to probe

specific resonances of interest. Mostly used meson beams to study resonances are π^+ , π^- , K^+ , and K^- due to their relatively long lifetimes. In the case of pion beam (πN) whose isospin is $I = 1$, more isospin degrees of freedom for resonances are available than for the electron beam ($I = 0$). At the same time, the large branching ratio into other meson reaction channels such as $\pi N \rightarrow \eta N$ limits the quantity of resonance data, hence requiring a larger accumulation of data to obtain sensitivity in the extraction of resonances. From the theory side, constituent quark models (Sec 1.2.1) predict that some of the missing resonances only couple weakly to the πN channel, but couple strongly to the γN channel. Additionally, the fact that pions carry zero spins (non-polarizable) limits the extraction of polarization observables which could be used in extraction of resonances' parameters. On the other hand, photon beams for resonance studies allow good advantages over meson beams, suited especially for obtaining asymmetries of observables arising from pre-determined polarized states of the beam and the target. Photon beams are used to study resonances by extracting the CGLN amplitudes (Sec. 1.3.1), the electric ($E_{l\pm}$) and magnetic($M_{l\pm}$) transition amplitudes (Sec. 1.3.2), and helicity amplitudes (Sec. 1.3.3) of $\gamma N \rightarrow \pi N$ reaction channels. The source of photon beams delivered to the nucleon target could be either high energy real photons (*meson photoproduction* $Q^2 = 0$) or virtual photons as high energy electrons (meson electroproduction $Q^2 > 0$) electromagnetically interacts with the nucleon.

1.3 Pion photoproduction

The pion production experiments have been conducted since the 1960s in pursuit of understanding the dynamics within the nucleon. This thesis focuses on the polarization observable E (Sec. 1.3.5) measured in the reaction channel of $\gamma p \rightarrow \pi^0 p$. The pions being the lightest meson of the meson family, consisting of the first generation of quarks and *anti*quarks, the number of pion events observed is generally larger

than other meson photoproduction reaction channels. According to the Standard Model, the pions carry isospin of $I = 1$ which forms an isospin triplet: $\pi^+(I_3 = +1)$, $\pi^-(I_3 = -1)$, and $\pi^0(I_3 = 0)$; basic properties of charged and neutral pions are listed in Table. 4. The relatively long lifetime of charged pions (2.6×10^{-8} s) indicates that they decay through weak interactions ($10^{-8} \sim 10^{-15}$ s) and it allows charged pions to be detected more easily in experiments than for the particles decaying via strong ($< 10^{-22}$ s) or electromagnetic interactions ($10^{-14} \sim 10^{-20}$ s). The neutral pions (π^0), on the other hand, have a very short lifetime of 8.4×10^{-17} s which suggests the electromagnetic decay; hence, direct detections of neutral pions are not carried out in pion photoproduction experiments. Alternatively, there are two often used indirect methods to extract information about the neutral pions involved in the reactions. First, one can measure the two photons (dominant decay mode) decaying from a neutral pion, which is the approach that CBELSA/TAPS experiments [112] used for the measurement of the helicity asymmetry E for the same reaction channel as ours ($\gamma p \rightarrow \pi^0 p$). In our experiment, we have reconstructed π^0 by using measured kinematics of incident particles (incoming photon and proton target) and recoiling protons via simple energy-momentum conservation laws.

Composition	I^G	I_3	J^{PC}	Mass (MeV)	Lifetime (s)	$c\tau$ (m)	Decay Modes	BR(%)	
π^+	$u\bar{d}$	1^-	1	0^-	139.57	2.6×10^{-8}	7.80	$\mu^+ + \nu_\mu$	99.9
								$e^+ + \nu_e$	1.24×10^{-4}
								$\pi^0 + e^+ + \nu_e$	1.00×10^{-8}
π^-	$d\bar{u}$	1^-	-1	0^-	139.57	2.6×10^{-8}	7.80	$\mu^- + \bar{\nu}_\mu$	99.9
								$e^- + \bar{\nu}_e$	1.24×10^{-4}
								$\pi^0 + e^- + \bar{\nu}_e$	1.00×10^{-8}
π^0	$u\bar{u}$ or $d\bar{d}$	1^-	0	0^{-+}	134.97	8.4×10^{-17}	25.1×10^{-9}	2γ	98.8
								$\gamma + e^- + e^+$	1.17×10^{-2}
								$2e^- + 2e^+$	3.34×10^{-5}
								$e^- + e^+$	6.46×10^{-8}

Table 4: Basic properties of π . I , G , J , P , C , $c\tau$, and BR refer to isospin, G parity, total angular momentum, parity, charge parity, maximum path length, and branching ratio, respectively [38].

With the advancement of polarization techniques, unpolarized scattering experiments have evolved into single and double polarization photoproduction experiments which provides crucial information on the electromagnetic transition amplitudes of the lower mass resonances: $\Delta(1232)$, $N(1440)$, $N(1520)$, $N(1535)$, and $N(1680)$ [43]. In the polarization experiments, there exist fifteen measurable polarization observables (Sec. 1.3.4) and a non-polarization observables ($\frac{d\sigma}{dt}$). Each of these observables could be expressed in terms of CGLN amplitude, multipole amplitudes, or helicity amplitudes; their relations will be discussed in upcoming sections. According to the work of Ref. [47], a set of eight carefully chosen polarization observables can determine four helicity amplitudes without any ambiguities for pseudoscalar meson photoproduction. With the obtained four helicity amplitudes of pion photoproduction, CGLN amplitudes can be calculated which also are expressible in terms of electric ($E_{l\pm}$) and magnetic ($M_{l\pm}$) transition amplitudes. After the extraction of multipoles and partial waves, parameters of resonances can be constructed using various Partial-Wave

Analysis (PWA) tools (Sec. 1.4).

1.3.1 Chew-Goldberger-Low-Nambu (CGLN) amplitudes

Following the convention used for π^0 photoproduction ($\gamma p \rightarrow \pi^0 p$) in Ref. [48], four-momenta of the incident photon and outgoing neutral pion will be denoted as k and q , respectively. The initial stationary proton target and the recoiling proton will take four momenta as p_1 and p_2 . The momentum-energy conservation gives:

$$p_1 + k = p_2 + q. \quad (6)$$

The photoproduction amplitude will be denoted by $\mathcal{F}_{\lambda_\gamma}$ for a specific photon's helicity labeled by λ_γ . Then, the differential cross section of meson photoproduction can be expressed as [48]:

$$\frac{d\sigma}{d\Omega} = \frac{q}{k} |\langle f | \mathcal{F}_\lambda | i \rangle|^2, \quad (7)$$

where $|i\rangle$ and $|f\rangle$ refer to the initial and final states of our system.

The photoproduction amplitude \mathcal{F}_λ could be decomposed into the current operator \mathbf{J} and the photon polarization vector $\boldsymbol{\epsilon}_\lambda$:

$$\mathcal{F}_\lambda \equiv \mathbf{J} \cdot \boldsymbol{\epsilon}_\lambda(\mathbf{k}). \quad (8)$$

We can relate the T matrix (interaction part of scattering S matrix) in terms of a current operator \mathbf{J} and the photon polarization vector $\boldsymbol{\epsilon}_{\lambda_\gamma}$ [46]:

$$\begin{aligned} \langle \mathbf{q} \ m_{s'} | T | \mathbf{k} \ m_s \ \lambda \rangle &= \langle m_{s'} | \mathcal{F}_\lambda | m_s \rangle \\ &= \langle m_{s'} | \mathbf{J} | m_s \rangle \cdot \boldsymbol{\epsilon}_\lambda(\mathbf{k}), \end{aligned} \quad (9)$$

where λ , m_s , and $m_{s'}$ refer to photon helicity, initial and final spin configuration of the proton, respectively.

The amplitude \mathcal{F}_λ and current \mathbf{J} could be expressed in terms of Pauli-spin matrices $\boldsymbol{\sigma}$ and the famous four CGLN amplitudes ($\mathcal{F}_1, \dots, \mathcal{F}_4$) which are functions of energy and scattering angle [48, 49]:

$$\begin{aligned}\mathbf{J} &= i\mathcal{F}_1\boldsymbol{\sigma} + \mathcal{F}_2\frac{(\boldsymbol{\sigma} \cdot \mathbf{q})(\boldsymbol{\sigma} \times \mathbf{k})}{qk} + i\mathcal{F}_3\frac{\boldsymbol{\sigma} \cdot \mathbf{k}}{qk}\mathbf{q} + \mathcal{F}_4\frac{\boldsymbol{\sigma} \cdot \mathbf{q}}{q^2}\mathbf{q}, \\ \mathcal{F}_\lambda &= \mathbf{J} \cdot \boldsymbol{\epsilon}_\lambda \\ &= i\mathcal{F}_1\boldsymbol{\sigma} \cdot \hat{\boldsymbol{\epsilon}}_\lambda + \mathcal{F}_2(\boldsymbol{\sigma} \cdot \hat{\mathbf{q}})\boldsymbol{\sigma} \cdot (\hat{\mathbf{k}} \times \hat{\boldsymbol{\epsilon}}_\lambda) + i\mathcal{F}_3(\boldsymbol{\sigma} \cdot \hat{\mathbf{k}})(\hat{\mathbf{q}} \cdot \hat{\boldsymbol{\epsilon}}_\lambda) + i\mathcal{F}_4(\boldsymbol{\sigma} \cdot \hat{\mathbf{q}})(\hat{\mathbf{q}} \cdot \hat{\boldsymbol{\epsilon}}_\lambda).\end{aligned}\tag{10}$$

When considering all possible number of states, photo polarization has two states $\lambda = \pm 1$, initial proton spin has two states $m_s = \pm \frac{1}{2}$, and the final recoil proton has two states $m_{s'} = \pm \frac{1}{2}$ which results in a total of eight T matrix elements. Each of these complex amplitudes can be decomposed into a real part and a phase which allows a total of sixteen real and experimentally observable parameters (Sec. 1.3.4).

1.3.2 Multipole amplitudes

The CGLN amplitudes are expressible in terms of two multipole amplitudes, the magnetic ($M_{l\pm}$) and electric ($E_{l\pm}$) amplitudes where l is the orbital angular momentum of the final state. The following introduction on multipole amplitudes is based on Refs. [46, 48, 43, 51, 52].

Because the target proton is stationary, the initial state has fixed and measurable quantum states. The extracted multipoles will directly show the quantum numbers of the resonances that decay into πN . The multipole amplitudes provide a more convenient way of studying resonances especially when only a few resonances are at play because the baryon resonances (N^* , Δ^* , etc.) are also eigenstates of parity, total angular momentum and isospin. The CGLN amplitudes $\mathcal{F}_1, \dots, \mathcal{F}_4$ are expressed in terms of multipole decomposition which are eigenstates of the total angular momen-

tum and parity are as follows:

$$\begin{aligned}
\mathcal{F}_1 &= \sum_{l=0}^{\infty} [lM_l^+ + E_l^+] P'_{l+1}(x) + [(l+1)M_l^- + E_l^-] P'_{l-1}(x), \\
\mathcal{F}_2 &= \sum_{l=1}^{\infty} [(l+1)M_l^+ + lM_L^-] P'_l(x), \\
\mathcal{F}_3 &= \sum_{l=1}^{\infty} (E_l^+ - M_l^+) P''_{l+1}(x) + (E_L^- + M_L^-) P''_{L-1}(x), \\
\mathcal{F}_4 &= \sum_{l=2}^{\infty} [M_L^+ - E_L^+ - M_L^- - E_L^-] P''_l(x),
\end{aligned} \tag{11}$$

where l , E , M , P'_l and P''_l denote angular momentum of the final πN system, electric and magnetic nature of the absorbed photon, and derivatives of the Legendre polynomial, respectively. The \pm superscripts denote not the parity, but the addition and subtraction in $J = l \pm 1/2$.

The CGLN amplitudes equations can be inverted to have $M_{l\pm}$ and $E_{l\pm}$ in terms of $\mathcal{F}_1, \dots, \mathcal{F}_4$ and Legendre polynomials [106]:

$$\begin{aligned}
M_{l\pm} &= \frac{1}{2} \begin{pmatrix} \frac{1}{l+1} \\ -\frac{1}{l} \end{pmatrix} \int_{-1}^{+1} dx \left[\mathcal{F}_1 P_l(x) - \mathcal{F}_2 P_{l\pm}(x) - \mathcal{F}_3 \frac{P_{l-1}(x) - P_{l+1}(x)}{2l+1} \right] \\
E_{l\pm} &= \frac{1}{2} \begin{pmatrix} \frac{1}{l+1} \\ \frac{1}{l} \end{pmatrix} \int_{-1}^{+1} dx \left[\mathcal{F}_1 P_l(x) - \mathcal{F}_2 P_{l\pm 1}(x) + \begin{pmatrix} l \\ -(l+1) \end{pmatrix} \mathcal{F}_3 \frac{P_{l-1}(x) - P_{l+1}(x)}{2l+1} \right. \\
&\quad \left. + \begin{pmatrix} \frac{l+1}{2l+3} \\ \frac{l}{2l+1} \end{pmatrix} \mathcal{F}_4 (P_l(x) - P_{l\pm 2}(x)) \right]
\end{aligned} \tag{12}$$

These multipole amplitudes are classified according to total angular momentum $J = l \pm 1/2$ of the final πN system and the character of the photon whether it is transverse or longitudinal. For transverse photons, states with parity $(-1)^{L_\gamma}$ are electric multipole states and states with parity $(-1)^{L_\gamma+1}$ are magnetic where L_γ is the total angular momentum of a photon; since photon has spin 1, the minimum is $L_\gamma = 1$. Table 5 lists electric and magnetic multipoles under $J \leq 3/2$ and $L_\gamma \leq 2$ and

their quantum numbers and Table 6 shows the basic rules between angular momentum and parity selection [46].

Multipole	l	J	L_γ	Parity
E_{0+}	0	1/2	1	-
M_{1-}	1	1/2	1	+
M_{1+}	1	3/2	1	+
E_{1+}	1	3/2	2	+
E_{2-}	2	3/2	2	+

Table 5: Quantum numbers of $\gamma N \rightarrow \pi N$ multipole amplitudes under $J \leq 3/2$.

Final state	Initial state	Amplitude
πN	γN	$J_\gamma = L_\gamma$ (Magnetic) $J_\gamma = L_\gamma \pm 1$ (Electric)
$J = L + \frac{1}{2}$	$J_\gamma = J - \frac{1}{2} = L$	Magnetic M_{L+}
$J = L + \frac{1}{2}$	$J_\gamma = J + \frac{1}{2} = L + 1$	Electric E_{L+}
$J = L - \frac{1}{2}$	$J_\gamma = J - \frac{1}{2} = L - 1$	Electric M_{L-}
$J = L - \frac{1}{2}$	$J_\gamma = J + \frac{1}{2} = L$	Magnetic E_{L-}
$\Delta^*(J, L, \frac{1}{2})$	$\Delta^*(J, J_\gamma, \frac{1}{2})$	Parity = $-(-1)^L$
	$\Delta^*(J_\gamma, L_\gamma, 1)$	Parity = $-(-1)^{L_\gamma}$

Table 6: Basic rules and definitions for multipole amplitudes on angular momentum, parity selection, and properties of magnetic ($M_{L\pm}$) and electric multipoles ($E_{L\pm}$). Since $J_\gamma \geq L_\gamma \geq 1$ (i.e. minimum of $L_\gamma = 1$ because photon spin is 1), M_{0-} , M_{0+} , E_{0-} , and E_{1-} does not exist. $L_\gamma = L$ except for E_{L-} where $L_\gamma = L - 2$ [46]

One can refer to $M_{l\pm}$ and $E_{l\pm}$ as transition amplitudes caused by magnetic and

electric multipole radiation. For example, E_{0+} is the transition amplitude initiated by electric dipole radiation which involves the final πN state to be in s-wave ($l = 0$). The magnetic dipole amplitude M_{l-} and M_{l+} refers to transitions to the final πN state to be in p-wave ($l = 1$) with the total angular momentum of $J = 1/2$ or $J = 3/2$. A simple illustration of the electric and magnetic dipole amplitudes in the πN systems is shown in Fig. 11.





Reaction	Configuration	Dipole moment	Relative ratio
	$ \leftarrow z \rightarrow $		
$\gamma p \rightarrow \pi^+ n$		ez	1
$\gamma p \rightarrow \pi^0 p$		$-\frac{m_\pi}{M} ez$	$-\frac{m_\pi}{M}$
$\gamma n \rightarrow \pi^- p$		$-\left(1 + \frac{m_\pi}{M}\right) ez$	$-\left(1 + \frac{m_\pi}{M}\right)$
$\gamma n \rightarrow \pi^0 n$		0	0

Figure 11: Description of electric dipole moments in πN system at rest. Image source: [52]

1.3.3 Helicity Amplitudes

Helicity is the projection of the particle's spin onto its direction of momentum: $\lambda = \frac{\mathbf{p} \cdot \mathbf{s}}{|\mathbf{p}| |\mathbf{s}|}$. With the polarization setup of our experiment, we can measure the helicity asymmetry of $\gamma p \rightarrow \pi^0 p$ events, i.e., given the prior knowledge of initial helicity states (γp), we can determine the difference in numbers of $\gamma p \rightarrow \pi^0 p$ events that have opposite final helicity states ($\pi^0 p$).

Let λ_k , λ_q , λ_1 , and λ_2 denote helicities of the incoming photon, π^0 in the final state, initial proton, and final recoiling proton, respectively:

$$\begin{aligned}
 \lambda_k &\in \left\{ \pm 1 \right\}, & \lambda_1 &\in \left\{ \pm \frac{1}{2} \right\}, \\
 \lambda_q &\in \left\{ 0 \right\}, & \lambda_2 &\in \left\{ \pm \frac{1}{2} \right\}.
 \end{aligned} \tag{13}$$

The total initial and final helicity states of our reaction channel are then given by $\lambda_i = \lambda_k - \lambda_1$ and $\lambda_f = \lambda_q - \lambda_2$. The possible states are then:

$$\begin{aligned}\lambda_i &\in \left\{ \pm \frac{1}{2}, \pm \frac{3}{2} \right\}, \\ \lambda_f &\in \left\{ \pm \frac{1}{2} \right\}.\end{aligned}\tag{14}$$

If we align the initial and final spins along with the directions of the incoming photon \mathbf{k} and outgoing pion \mathbf{q} , the helicity amplitudes ($H_i(\theta)$) are the T matrix elements and we can define them according to the current operator $J_{1\lambda_k} = \mp(J_x \pm iJ_y)/\sqrt{2}$ [46]:

$$H_i(\theta) = \langle \lambda_2 | J_{1\lambda_k} | \lambda_1 \rangle .\tag{15}$$

We have total of eight possible combinations of initial and final helicity states because the photon, initial proton and recoiling proton each has two possible states. However, these eight amplitudes are not independent as four amplitudes with $\lambda_k = -1$ are related to four amplitudes with $\lambda_k = +1$ by the parity symmetry [53, 54]:

$$H_{-\lambda_i, -\lambda_f}(\theta, \phi) = -e^{i(\lambda_i - \lambda_f)(\pi - 2\phi)} H_{\lambda_i, \lambda_f}(\theta, \phi)\tag{16}$$

Then, four possible helicity amplitudes corresponding to each configuration in our reaction are shown in Table. 7 and in Eq. 17 with respect to the current operator \mathbf{J} .

$$\begin{aligned}H_1(\theta) &= \left\langle +\frac{1}{2} \left| J_{11} \right| -\frac{1}{2} \right\rangle = + \left\langle -\frac{1}{2} \left| J_{1-1} \right| +\frac{1}{2} \right\rangle, \\ H_2(\theta) &= \left\langle +\frac{1}{2} \left| J_{11} \right| +\frac{1}{2} \right\rangle = - \left\langle -\frac{1}{2} \left| J_{1-1} \right| -\frac{1}{2} \right\rangle, \\ H_3(\theta) &= \left\langle -\frac{1}{2} \left| J_{11} \right| -\frac{1}{2} \right\rangle = - \left\langle +\frac{1}{2} \left| J_{1-1} \right| +\frac{1}{2} \right\rangle, \\ H_4(\theta) &= \left\langle -\frac{1}{2} \left| J_{11} \right| +\frac{1}{2} \right\rangle = + \left\langle -\frac{1}{2} \left| J_{1-1} \right| -\frac{1}{2} \right\rangle.\end{aligned}\tag{17}$$

		$\lambda_k = +1$		$\lambda_k = -1$	
λ_f	λ_i	$\frac{3}{2}$	$\frac{1}{2}$	$-\frac{1}{2}$	$-\frac{3}{2}$
		H_1	H_2	H_4	$-H_3$
$\frac{1}{2}$		H_1	H_2	H_4	$-H_3$
$-\frac{1}{2}$		H_3	H_4	$-H_2$	H_1

Table 7: Helicity amplitudes $H_i(\theta)$ for $\gamma p \rightarrow \pi^0 p$ where λ_k , λ_i and λ_f refer to helicity states of the incoming polarized photon, total initial state (γp), and total final state ($\pi^0 p$) [53].

For a circularly polarized photon, the helicity states of photon have the polarization vectors [53]:

$$\epsilon_{\pm} = \mp \left(\frac{1}{2} \right) (\hat{e}_x \pm i\hat{e}_y), \quad \text{for } \lambda_k = \pm 1, \quad (18)$$

where \hat{e}_x and \hat{e}_y are unit vectors in the x and y directions of the coordinate system in which its z -axis aligns with photon direction \mathbf{k} and y -axis in the direction of $\mathbf{k} \times \mathbf{q}$. Setting $\hat{e}_{\lambda} = \epsilon_{+}$ in Eq. 10 for photon helicity of $+1$, the helicity amplitudes are related to the CGLN amplitudes (Eq. 10) by [53]:

$$\begin{aligned} H_1(\theta, \phi) &= - \left(\frac{1}{\sqrt{2}} \right) e^{i\phi} \sin(\theta) \cos\left(\frac{\theta}{2}\right) (\mathcal{F}_3 + \mathcal{F}_4), \\ H_2(\theta, \phi) &= \sqrt{2} \cos\left(\frac{\theta}{2}\right) \left[(\mathcal{F}_2 - \mathcal{F}_1) + \frac{1}{2}(1 - \cos(\theta))(\mathcal{F}_3 - \mathcal{F}_4) \right], \\ H_3(\theta, \phi) &= \left(\frac{1}{\sqrt{2}} \right) e^{2i\phi} \sin(\theta) \sin\left(\frac{\theta}{2}\right) (\mathcal{F}_3 - \mathcal{F}_4), \\ H_4(\theta, \phi) &= \sqrt{2} e^{i\phi} \sin\left(\frac{\theta}{2}\right) \left[(\mathcal{F}_1 + \mathcal{F}_2) + \frac{1}{2}(1 + \cos(\theta))(\mathcal{F}_3 + \mathcal{F}_4) \right]. \end{aligned} \quad (19)$$

The cross section is the same for both photon helicities $\lambda_k = \pm 1$ due to parity symmetry and in terms of helicity amplitudes, it is [53]:

$$\sigma(\theta) = \frac{1}{2} \frac{q}{k} \sum_{i=1}^4 |H_i|^2, \quad (20)$$

where q and k are the magnitudes of neutral pion and photon momentum in the center-of-mass frame.

An alternative representation of helicity amplitude, called transversity helicity amplitude, is introduced to simplify the calculation of magnitudes of amplitudes with only single polarization observables and the differential cross section as shown in Table. 9. The helicity transversity amplitudes b_i are constructed via unitary transformation $U_{ij}^{(4)}$ [47]:

$$H_i \longrightarrow b_i = U_{ij}^{(4)} H_j, \quad (21)$$

where

$$U_{ij}^{(4)} = \frac{1}{2} \begin{bmatrix} 1 & -i & i & 1 \\ 1 & i & -i & 1 \\ 1 & i & i & -1 \\ 1 & -i & -i & -1 \end{bmatrix} \quad (22)$$

1.3.4 Polarization Observables

When considering all possible number of helicity states in $\gamma N \rightarrow \pi N$ reaction where the outgoing meson is indirectly reconstructed from measured kinematics of the rest of the system, there is a total of eight possible helicity states ($2 \times 2 \times 2$): two helicity states from each photon, initial proton, and recoiling proton. Each of eight helicity states constitutes to eight complex helicity amplitudes which can be decomposed into a real part and a phase, yielding a total of sixteen experimentally measurable observables. From the work of Ref. [47], we know that a set of eight (out of sixteen) carefully chosen variables suffice to construct four complex helicity amplitudes, which in turn can construct CGLN amplitudes and multipole amplitudes. There exist four

categories of polarization experimental setups: unpolarized (\mathcal{UP}), single polarization (\mathcal{S}) where either the beam or the target is polarized, double polarization of the beam and target (\mathcal{BT}), double polarization of the beam and recoiling nucleon (\mathcal{BR}), and double polarization of the target and recoiling nucleon (\mathcal{TR}). The unpolarized setting gives the differential cross section σ_0 , single polarization experiments yield three observables (Σ , T , and P), \mathcal{BT} double polarization experiments give four observables (G , H , E , and F), \mathcal{BR} double polarization gives four observables (O_x , O_z , C_x , and C_z), and \mathcal{TR} double polarization gives four observables (T_x , T_z , L_x , and L_z).

The σ_0 from an unpolarized experiment and three single polarization observables determine the magnitudes of the four helicity transversity amplitudes without any ambiguities as shown in Table. 9. Relative phases between four helicity amplitudes are then obtainable from four double polarization observables without any ambiguities [47].

Photon	Target				Recoil			Target + Recoil			
	-	-	-	-	x'	y'	z'	x'	x'	z'	z'
	-	x	y	z	-	-	-	x	z	x	z
unpolarized	σ_0	T			P			$T_{x'}$	$-L_{x'}$	$T_{z'}$	$L_{z'}$
linearly pol.	$-\Sigma$	H	$(-P)$	$-G$	$O_{x'}$	$(-T)$	$O_{z'}$	$(-L_{z'})$	$(T_{z'})$	$(-L_{x'})$	$(-T)$
circular pol.		F			$-C_{x'}$		$-C_{z'}$				

Table 8: Polarization observables of meson photoproduction. The observables in brackets are measurable in two different setups [55].

The experimental definition of polarization observables are given in Eq. (24) - (27) [46]. The notation for differential cross sections for various polarization setups is given by:

$$\sigma(B, T, R) \equiv \frac{d\sigma^{(B,T,R)}}{d\Omega} , \quad (23)$$

where (B, T, R) stand for the polarization state of the photon beam, target proton, and the recoiling baryon, respectively. Below experimental definitions are provided under the assumption of 100% polarization whereas in real experiments, factors accounting for partial polarization must be employed (Eq. (29) - (31)). Zeroes in the polarization state refer to unpolarized states. The perpendicular(\perp) and parallel (\parallel) notations denote the direction with respect to the scattering plane. The possible values for (B, T, R) are:

$$\begin{aligned}
B &\in (\perp, \parallel, \pi/4) && \text{for linearly polarized photon beam,} \\
B &\in (\pm 1) && \text{for circularly polarized photon beam,} \\
T &\in (x, y, z) && \text{for target spin orientation in the c.m. frame,} \\
R &\in (x', y', z') && \text{for recoil baryon spin orientation in the rest frame of recoil baryon.}
\end{aligned}$$

$$\begin{aligned}
\text{Recoil polarization :} & \quad P = \frac{\sigma(0, 0, +y') - \sigma(0, 0, -y')}{\sigma(0, 0, +y') + \sigma(0, 0, -y')}, \\
\text{Beam polarization :} & \quad \Sigma = \frac{\sigma(\perp, 0, 0) - \sigma(\parallel, 0, 0)}{\sigma(\perp, 0, 0) + \sigma(\parallel, 0, 0)}, \\
\text{Target polarization :} & \quad T = \frac{\sigma(0, +y, 0) - \sigma(0, -y, 0)}{\sigma(0, +y, 0) + \sigma(0, -y, 0)},
\end{aligned} \tag{24}$$

$$\begin{aligned}
\text{circ. beam - long. target :} & \quad E = \frac{\sigma(+1, +z, 0) - \sigma(-1, +z, 0)}{\sigma(+1, +z, 0) + \sigma(-1, +z, 0)}, \\
\text{circ. beam - transv. target :} & \quad F = \frac{\sigma(+1, +x, 0) - \sigma(-1, +x, 0)}{\sigma(+1, +x, 0) + \sigma(-1, +x, 0)}, \\
\text{lin. beam - long. target :} & \quad G = \frac{\sigma(\pi/4, +z, 0) - \sigma(\pi/4, -z, 0)}{\sigma(\pi/4, +z, 0) + \sigma(\pi/4, -z, 0)}, \\
\text{lin. beam - transv. target :} & \quad H = \frac{\sigma(\pi/4, +x, 0) - \sigma(\pi/4, -x, 0)}{\sigma(\pi/4, +x, 0) + \sigma(\pi/4, -x, 0)},
\end{aligned} \tag{25}$$

$$\begin{aligned}
\text{circ. beam - recoil } x' : \quad C_{x'} &= \frac{\sigma(+1, 0, +x') - \sigma(-1, 0, +x')}{\sigma(+1, 0, +x') + \sigma(-1, 0, +x')}, \\
\text{circ. beam - recoil } z' : \quad C_{z'} &= \frac{\sigma(+1, 0, +z') - \sigma(-1, 0, +z')}{\sigma(+1, 0, +z') + \sigma(-1, 0, +z')}, \\
\text{lin. beam - recoil } x' : \quad O_{x'} &= \frac{\sigma(\pi/4, 0, +x') - \sigma(\pi/4, 0, -x')}{\sigma(\pi/4, 0, +x') + \sigma(\pi/4, 0, -x')}, \\
\text{lin. beam - recoil } z' : \quad O_{z'} &= \frac{\sigma(\pi/4, 0, +z') - \sigma(\pi/4, 0, -z')}{\sigma(\pi/4, 0, +z') + \sigma(\pi/4, 0, -z')},
\end{aligned} \tag{26}$$

$$\begin{aligned}
\text{transv. beam - recoil } x' : \quad T_{x'} &= \frac{\sigma(0, +x, +x') - \sigma(0, +x, -x')}{\sigma(0, +x, +x') + \sigma(0, +x, -x')}, \\
\text{transv. beam - recoil } z' : \quad T_{z'} &= \frac{\sigma(0, +x, +z') - \sigma(0, +x, -z')}{\sigma(0, +x, +z') + \sigma(0, +x, -z')}, \\
\text{long. beam - recoil } x' : \quad L_{x'} &= \frac{\sigma(0, +z, +x') - \sigma(0, +z, -x')}{\sigma(0, +z, +x') + \sigma(0, +z, -x')}, \\
\text{long. beam - recoil } z' : \quad L_{z'} &= \frac{\sigma(0, +z, +z') - \sigma(0, +z, -z')}{\sigma(0, +z, +z') + \sigma(0, +z, -z')},
\end{aligned} \tag{27}$$

The sixteen polarization observables are not independent to each other and their algebraic correlations are expressed in the following nonlinear relations [47, 77]:

$$\begin{aligned}
E^2 + F^2 + G^2 + H^2 &= 1 + P^2 - \Sigma^2 - T^2, \\
FG - EH &= P - \Sigma T, \\
T_{x'}^2 + T_{z'}^2 + L_{x'}^2 + L_{z'}^2 &= 1 + \Sigma^2 - P - T^2, \\
T_{x'}L_{z'} - T_{z'}L_{x'} &= \Sigma - PT, \\
C_{x'}^2 + C_{z'}^2 + O_{x'}^2 + O_{z'}^2 &= 1 + T^2 - P - \Sigma^2, \\
C_{x'}O_{z'} - C_{z'}O_{x'} &= T - P\Sigma.
\end{aligned} \tag{28}$$

In Table. 9, all polarization observables in terms of helicity amplitudes and helicity transversity amplitudes are listed [47]. The differential cross section with unpolarized beam and target is denoted by $\mathcal{I} = \frac{d\sigma}{d\Omega}$

Observable	Helicity Representation	Transversity Representation	Experiment
$\mathcal{I}(\theta)$	$\frac{1}{2} (H_1 ^2 + H_2 ^2 + H_3 ^2 + H_4 ^2)$	$\frac{1}{2} (b_1 ^2 + b_2 ^2 + b_3 ^2 + b_4 ^2)$	\mathcal{UP}
$\Sigma \mathcal{I}$	$\text{Re}(-H_1 H_4^* + H_2 H_3^*)$	$\frac{1}{2} (b_1 ^2 + b_2 ^2 - b_3 ^2 - b_4 ^2)$	\mathcal{S}
$-T \mathcal{I}$	$\text{Im}(H_1 H_2^* + H_3 H_4^*)$	$\frac{1}{2} (- b_1 ^2 + b_2 ^2 + b_3 ^2 - b_4 ^2)$	
$P \mathcal{I}$	$\text{Im}(-H_1 H_3^* - H_2 H_4^*)$	$\frac{1}{2} (- b_1 ^2 + b_2 ^2 - b_3 ^2 + b_4 ^2)$	
$G \mathcal{I}$	$\text{Im}(H_1 H_4^* - H_3 H_2^*)$	$\text{Im}(-b_1 b_3^* - b_2 b_4^*)$	\mathcal{BT}
$H \mathcal{I}$	$\text{Im}(-H_2 H_4^* + H_1 H_3^*)$	$\text{Re}(b_1 b_3^* - b_2 b_4^*)$	
$E \mathcal{I}$	$\frac{1}{2} (H_1 ^2 - H_2 ^2 + H_3 ^2 - H_4 ^2)$	$\text{Re}(b_1 b_3^* + b_2 b_4^*)$	
$F \mathcal{I}$	$\text{Re}(-H_2 H_1^* - H_4 H_3^*)$	$\text{Im}(b_1 b_3^* - b_2 b_4^*)$	
$O_x \mathcal{I}$	$\text{Im}(-H_2 H_1^* + H_4 H_3^*)$	$\text{Re}(-b_1 b_4^* + b_2 b_3^*)$	\mathcal{BR}
$-O_z \mathcal{I}$	$\text{Im}(H_1 H_4^* - H_2 H_3^*)$	$\text{Im}(-b_1 b_4^* - b_2 b_3^*)$	
$-C_x \mathcal{I}$	$\text{Re}(H_2 H_4^* + H_1 H_3^*)$	$\text{Im}(b_1 b_4^* - b_2 b_3^*)$	
$-C_z \mathcal{I}$	$\frac{1}{2} (H_1 ^2 + H_2 ^2 - H_3 ^2 - H_4 ^2)$	$(b_1 b_4^* + b_2 b_3^*)$	
$-T_x \mathcal{I}$	$\text{Re}(-H_1 H_4^* - H_2 H_3^*)$	$\text{Re}(-b_1 b_2^* + b_3 b_4^*)$	\mathcal{TR}
$-T_z \mathcal{I}$	$\text{Re}(-H_1 H_2^* + H_4 H_3^*)$	$\text{Im}(b_1 b_2^* - b_3 b_4^*)$	
$L_x \mathcal{I}$	$\text{Re}(H_2 H_4^* - H_1 H_3^*)$	$\text{Im}(-b_1 b_2^* - b_3 b_4^*)$	
$L_z \mathcal{I}$	$\frac{1}{2} (- H_1 ^2 + H_2 ^2 + H_3 ^2 + H_4 ^2)$	$\text{Re}(-b_1 b_2^* - b_3 b_4^*)$	

Table 9: Polarization observables in terms of helicity and transversity representation. The polarization setup abbreviations \mathcal{UP} , \mathcal{S} , \mathcal{BT} , \mathcal{BR} , and \mathcal{TR} denote unpolarized, single polarization, polarized beam-target, polarized beam-recoil, and polarized target-recoil. The differential cross section with unpolarized beam and target is denoted by $\mathcal{I} = \frac{d\sigma}{d\Omega}$ [47].

The differential cross sections in each of the double polarization setups (\mathcal{BT} , \mathcal{BR} , and \mathcal{TR}) are listed in Eq. (29) - (31), where degrees of polarization for the beam and target are considered.

- Polarized Beam - Target (\mathcal{BT})

$$\begin{aligned} \frac{d\sigma}{d\Omega} = \sigma_0 \bigg\{ & 1 - P_T \Sigma \cos(2\phi) + P_x [-P_T H \sin(2\phi) + P_\lambda F] \\ & - P_y [-T + P_T P \cos(2\phi)] - P_z [-P_T G \sin(2\phi) + P_\lambda E] \bigg\}, \end{aligned} \quad (29)$$

- Polarized Beam - Recoil (\mathcal{BR})

$$\begin{aligned} \rho_f \frac{d\sigma}{d\Omega} = \sigma_0 \bigg\{ & 1 + \sigma_y P - P_T \cos(2\phi) (\Sigma + \sigma_y T) \\ & - P_T \sin(2\phi) (O_x \sigma_x + O_z \sigma_z) - P_\lambda (C_x \sigma_x + C_z \sigma_z) \bigg\}, \end{aligned} \quad (30)$$

- Polarized Beam - Target (\mathcal{TR})

$$\begin{aligned} \rho_f \frac{d\sigma}{d\Omega} = \sigma_0 \bigg\{ & 1 + \sigma_y P + P_x (T_x \sigma_x + T_z \sigma_z) \\ & + P_y (T + \Sigma \sigma_y) - P_z (L_x \sigma_x - L_z \sigma_z) \bigg\} \end{aligned} \quad (31)$$

where σ_0 , (P_x, P_y, P_z) , P_T , P_λ , $\rho_f = \frac{1}{2}(\mathbb{1} + \sigma \cdot P_f)$, P_f and $\mathbb{1}$ refer to the differential cross section without any polarization, the target polarization in (x, y, z) , the transverse beam polarization at angle ϕ to the reaction plane, the degree of right circular beam polarization, the density matrix of the recoiling proton, the polarization of recoiling proton, and the identity matrix, respectively.

Polarization observables are also expressible in CGLN and multipole amplitudes [47]. For the scope of this thesis' focus, only helicity asymmetry E will be shown here [47]. The result for multipole expansion of E includes only up to $L \leq 1$ terms.

$$\begin{aligned}
E &= -\frac{1}{\sigma_0} \text{Re} \left\{ |\mathcal{F}_1|^2 + |\mathcal{F}_2|^2 - 2x\mathcal{F}_2\mathcal{F}_1^* + \sin^2(\theta)(\mathcal{F}_1\mathcal{F}_4^* + \mathcal{F}_2\mathcal{F}_3^*) \right\} \\
E &= -\frac{1}{\sigma_0} \text{Re} \left\{ -|E_{0+}|^2 - |M_{1-}|^2 + 2|M_{1+}|^2 - M_{1-}^*(3E_{1+} + M_{1+}) - 6E_{1+}M_{1+} - \right. \\
&\quad \left. \cos(\theta)[2E_{0+}^*(3E_{1+} + M_{1-})] + \cos^2(\theta)[-9|E_{1+}|^2 - 3|M_{1+}|^2 + \right. \\
&\quad \left. 3M_{1-}^*(3E_{1+} + M_{1+})] \right\}.
\end{aligned} \tag{32}$$

1.3.5 Helicity asymmetry E

The circularly polarized photon beam with a longitudinally polarized proton yields two kinds of total helicity states: $\lambda = \pm\frac{1}{2}$ and $\pm\frac{3}{2}$; The former represents the *anti*-parallel helicity states and the latter is the parallel helicity states between the photon and the recoiling proton. From Eq. 25, the experimental definition of E is simply written as:

$$E = \frac{\sigma_{\frac{1}{2}} - \sigma_{\frac{3}{2}}}{\sigma_{\frac{1}{2}} + \sigma_{\frac{3}{2}}}, \tag{33}$$

which measures the difference of parallel ($\sigma_{3/2}$) and *anti*-parallel ($\sigma_{1/2}$) helicity states of $\gamma p \rightarrow \pi^0 p$, hence the name *helicity asymmetry* E .

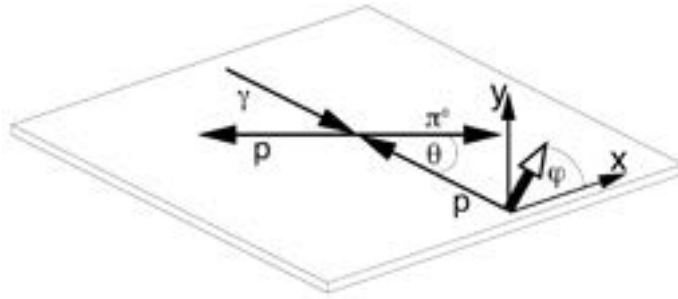


Figure 12: Illustration of the azimuthal angle ϕ and scattering angle θ of the $\gamma p \rightarrow \pi^0 p$ in the center-of-mass frame. Image source: [98]

The theoretical expression for $\sigma_{1/2}$ and $\sigma_{3/2}$ can be derived from Eq. (29) where

the transverse beam polarization (P_T) and xy component (P_x, P_y) of the target polarization vanishes to zero in our experimental setup. The theoretical equation for $\frac{d\sigma}{d\Omega}$ reduces to:

$$\left(\frac{d\sigma}{d\Omega}\right)_{\frac{1}{2}, \frac{3}{2}} = \sigma_0 (1 - P_z P_\lambda E), \quad (34)$$

where $\sigma_0 = \frac{d\sigma_0}{d\Omega}$, P_z and P_λ are the cross section without any polarization, target polarization in the z-direction, and circular photon beam polarization, respectively.

The differential cross section that is measured in the experiments with our polarization setting is given by:

$$\left(\frac{d\sigma}{d\Omega}\right)_{\frac{1}{2}, \frac{3}{2}} = \frac{N_{\frac{1}{2}, \frac{3}{2}}}{A \cdot F \cdot \rho \cdot \Delta x_i}, \quad (35)$$

where $N_{\frac{1}{2}, \frac{3}{2}}$, A , F , ρ , and Δx_i are the number of events in helicity 1/2 or 3/2 states, detector acceptance, photon flux, target area density parameter, and the width of the kinematic bin, respectively.

While calculating for the final expression for E , the denominators of Eq. (34) get canceled out under the conditions that the integrated luminosity of the two beam helicity states are equal and the target polarization remains constant during the experiments. These conditions are fairly met when the beam charge asymmetry is negligibly small and the beam helicity is flipped at a high frequency such that the target polarization remains constant during the flip. The beam charge asymmetry refers to the difference in the integral of the electron beam current with one helicity state to the opposite helicity state; the average of beam charge asymmetry for each experiment period is given in Table. 14. Because helicity is flipped at the frequency of 30 Hz during the g9a/FROST experiment, the flux F can safely be estimated to be the same on average and gets canceled during the final calculation of E :

$$E = \left[\frac{1}{D_f} \right] \left[\frac{1}{P_z P_\lambda} \right] \left[\frac{N_{\frac{1}{2}} - N_{\frac{3}{2}}}{N_{\frac{1}{2}} + N_{\frac{3}{2}}} \right]. \quad (36)$$

D_f refers to the dilution factor to account for the impact of having events of photons scattering from unpolarized proton targets to our measured E . The procedure for computing the dilution factor will be discussed extensively in Ch. 5.

For the circularly polarized photon beam, the polarization of the photon P_λ is approximated by [95]:

$$P_\lambda = P_e \frac{4x - x^2}{4 - 4x + 3x^2}, \quad \text{where } x = \frac{\text{photon energy } E_k}{\text{electron energy } E_0}, \quad (37)$$

where P_e is the polarization of the electron beam before producing photons through bremsstrahlung radiation. Details on the production of photon beams and the range of beam polarization in our experiment will be discussed in Sec. 2.2 and Sec. 2.4.2.

1.4 Partial Wave Analysis

With the measured polarization observables, the parameters of resonances are calculated using various partial wave analysis (PWA) methods. When sufficient data is accumulated, PWA can also produce predictions on the polarization observables which are not yet measured. Therefore, the inclusion of more photo- and electro-production data helps to reduce the uncertainties in the construction of resonance parameters. The photoproduction amplitudes (Sec. 1.3) have many contributions arising from various interactions as shown in Fig. 13; only the first diagram (s -channel) is the interested resonant term where the intermediate state is the N^* or Δ^* resonance. The objective of PWA is to correctly parameterize and separate the resonant and non-resonant contributions. The following section will briefly discuss the basic formalism on resonances and different PWA models (SAID, MAID, and BnGa) used to produce the helicity asymmetry E values to be compared to this thesis' final results.

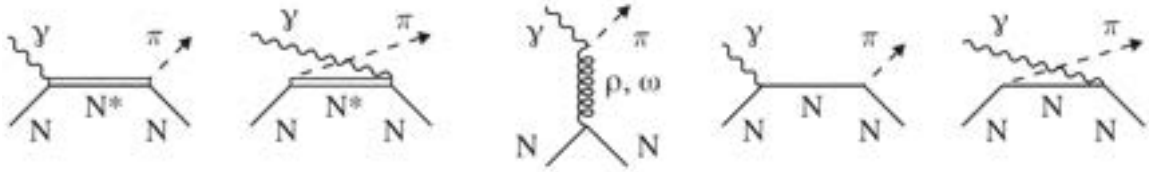


Figure 13: Feynman diagrams showing contributions to π photoproduction. First diagram corresponds to the resonant s-channel with the intermediate resonance state (N^* or Δ^*). The second diagram is a u -channel with a resonance. The third diagram corresponds to t -channel where a vector meson is exchanged. The fourth and fifth diagrams refer to Born terms where the exchanged particle is a nucleon. Image source: [57]

Resonances

The wave function involved in scattering a potential is composed of an incident plane wave $\phi(z) \sim e^{ikz}$ and an outgoing spherical wave at large distances r [58]:

$$\phi(r, \theta) \xrightarrow{r \rightarrow \infty} e^{ikz} + f(\theta, k) \frac{e^{ikr}}{r} \quad (38)$$

where $k = \frac{\sqrt{2mE}}{\hbar}$ and $f(\theta, k)$ is the wave number related to the incident particle's energy and the scattering amplitude.

The incident wave and scattering amplitude can both be expanded in terms of Legendre polynomials:

$$\begin{aligned} e^{ikz} &= e^{ikr \cos(\theta)} = \sum_{l=0}^{\infty} i^l (2l+1) j_l(kr) P_l(\cos(\theta)) \\ f(\theta, k) &= \sum_{l=0}^{\infty} (2l+1) a_l(k) P_l(\cos(\theta)), \end{aligned} \quad (39)$$

where j_l , P_l , and a_l are the spherical Bessel function, the Legendre polynomials, and l^{th} partial wave amplitude, respectively.

In the region of interaction, the amplitude of incident and outgoing waves must be the same due to conservation of probability, but differ by a phase shift δ_l . The magnitude of the interaction between the incident particle and any potential is reflected

by attaching the phase shift factor $e^{2i\delta_l}$ to the outgoing wave.

The partial wave amplitude $a_l(k)$ and the scattering amplitude $f(\theta)$ can be described with a phase shift:

$$\begin{aligned} a_l(k) &= \frac{e^{2i\delta_l} - 1}{2ik} = \frac{1}{k} e^{i\delta_l} \sin(\delta_l) \\ f(\theta) &= \frac{1}{k} \sum_{l=0}^{\infty} (2l+1) e^{i\delta_l} \sin(\delta_l) P_l(\cos(\theta)) \end{aligned} \quad (40)$$

Then, the cross section (σ) and partial cross sections (σ_l) at each l can be expressed in terms of phase shift:

$$\begin{aligned} \sigma &= \int |f(\theta)|^2 d\Omega \\ &= \frac{4\pi}{k^2} \sum_{l=0}^{\infty} (2l+1) \sin^2(\delta_l) \\ \sigma_l &= \frac{4\pi}{k^2} (2l+1) \sin^2(\delta_l). \end{aligned} \quad (41)$$

At certain ranges of energies the cross section suddenly becomes large while little to no changes are visible in the background. Such phenomena are referred to as resonances (excited states of hadrons) and one can relate it to the phase shift δ_l , varying rapidly from 0 to π near $E = E_0$:

$$\delta_l = \tan^{-1} \left(\frac{\Gamma/2}{E_0 - E} \right) + \delta_b, \quad (42)$$

where δ_b , $\Gamma = \hbar/\tau$, and τ denote some background phase shift that does not vary significantly, the decay rate at which the resonance decays into particles, and the lifetime of the resonance, respectively. The corresponding expression of cross section that accounts for resonances are called the *Breit-Wigner* formula:

$$\sigma_l = \frac{4\pi(2l+1)}{k^2} \frac{(\Gamma/2)^2}{(E_0 - E)^2 + (\Gamma/2)^2}, \quad (43)$$

where the background phase δ_b is neglected. By the *S*-matrix approach, we can relate

the S -matrix element $s_l(k)$ to the phase shift δ_l by:

$$\begin{aligned} s_l(k) &= e^{2i\delta_l} \\ &= \frac{1 + i \tan(\delta_l)}{1 - i \tan(\delta_l)} \\ &= \frac{E - E_0 - i\Gamma/2}{E - E_0 + i\Gamma/2}. \end{aligned} \tag{44}$$

This description allows us to conclude that the resonance corresponds to a pole position in a complex plane:

$$E = E_0 - \frac{i\Gamma}{2}. \tag{45}$$

The task of extracting resonance parameters becomes significantly challenging when multiple resonances contribute to a single scattering cross section σ_l . As discussed in Sec. 1.2.3, At $W > 1.5$ GeV, multiple channels are overlapping and parametrization of resonant and non-resonant terms requires more robust techniques. First introduced by Wigner [60, 61], the K -matrix approach is widely used to describe multi-channelled resonances and background contributions. The K -matrix is a symmetric, Hermitian and real matrix which relates to the scattering S -matrix and T -matrix by [59]:

$$\begin{aligned} S &= \mathbb{1} + iT \\ &= \frac{\mathbb{1} + iK}{\mathbb{1} - iK}. \end{aligned} \tag{46}$$

The resonances correspond to a sum of pole positions in the K -matrix which causes K -matrix elements to vary abruptly at these poles, leading to significant phase shifts [62].

The resonant and non-resonant terms are included in the K -matrix by:

$$K_{ij} = \sum_{\alpha}^n \frac{g_{\alpha i}(m)g_{\alpha j}(m)}{m_{\alpha}^2 - m^2} + f_{ij}, \tag{47}$$

where n , m_{α} , $g_{\alpha i}$, $g_{\alpha j}$, and f_{ji} are the number of resonances, the mass of a resonance

α , couplings to the initial and final states i and j , and the non-resonant background contribution, respectively. The coupling $g_{\alpha i}$ (or residue function) to the reaction channel i is given by [59]:

$$g_{\alpha i}^2(m) = m_\alpha \Gamma_{\alpha i}(m). \quad (48)$$

The total decay width Γ_α for a resonance α is a sum of contributions from all channels:

$$\Gamma_\alpha(m) = \sum_i \Gamma_{\alpha i}(m) \quad (49)$$

Each of the PWA models described below differs in the process of parametrizing the resonant and non-resonant contributions and the way experimental data are fitted all together. Hence, one can see significant deviations between models when the database is scarce. Such discrepancies are a clear indication that an increase in the polarization observable database is essential for the study of resonances.

SAID

The latest SAID fit parametrization uses the 3-channel Heitler K-matrix [66] with the basis of Chew-Mandelstam (CM) K-matrix formalism used in the SAID πN elastic scattering fits [67]. The non-resonant background terms are expanded by the sum of pseudoscalar Born terms and ρ and ω exchange terms. The resonance parameters such as the masses, widths and branching ratios of resonances are determined by fitting the data. In the first step, the hadronic CM K -matrix parameters (πN , $\pi\Delta$, ρN , and ηN) are determined by fitting $\pi N \rightarrow \pi N$ and $\pi N \rightarrow \eta N$ data. Then, pion photoproduction data are fitted by fine-tuning only the parameters of electromagnetic CM K -matrix elements to extract photo-decay couplings. The hadronic parameters extracted in the first step are fixed while fitting the photoproduction data. The SAID PWA is a data-driven technology as it is a model-independent approach.

MAID2007

The MAID2007 unitary isobar model utilizes the t -matrix approach, where a background and a resonance t -matrices are each constructed unitarily and combined afterward [68, 69]. Using the phases shifts and inelasticity parameters obtained from GWU SAID PWA of pion-nucleon elastic scattering, amplitudes are constructed to compute the background contribution's for S -, P -, D -, and F -waves in a unitary way. The MAID2007 approach has its advantage for electroproduction amplitude analyses and all isospin channels up to the limit of $W = 2$ GeV.

BnGa

The BnGa model is based on the K -matrix approach shown in Eq. 47. The latest modification to the K -matrix approach is a dispersion relation approach which is based on the N/D technique [63]; the N/D technique simply takes into account the real parts of the two-body loop diagrams to the K -matrix approach. In BnGa, The t - and u -channel, described in Fig. 13, are included as the resonant parts while parametrizing photoproduction reactions. The model fits πN and γN data simultaneously to extract resonance parameters. When analyzing new resonances with masses above 2.2 GeV, relativistic multi-channel Breit-Wigner amplitudes are used. The multipole amplitudes from πN data are calculated using the GWU SAID technique [73]

1.5 Current challenges in Baryon spectroscopy

The study of baryon resonances requires close collaboration from both theoretical and experimental sides to approach the long standing problem of missing resonances. From the experimental side, acquiring a larger database with reduced uncertainties will aid in resolving discrepancies between partial wave analysis models and help the quark models to better determine correct effective degrees of freedom that reflect internal structures and dynamics at non-perturbative low energy QCD regime. Data

from several experimental facilities around the world contribute to the study of resonances using electron and photon beams, including from Jefferson Lab, Brookhaven National Laboratory, and MIT Bates in the USA; MAMI at Mainz and ELSA at Bonn in Germany; GRAAL at Grenoble in France, and LEPS at Spring-8 in Japan. Among these laboratories, the use of photoproduction reactions (γN) to contribute to the study of resonances is specifically carried out at the CLAS experiment at Jefferson Lab, CBELSA/TAPS experiment at ELSA, and A2 experiment at MAMI. For this thesis, one of the FROST/CLAS experiments at Jefferson Lab designed to extract polarization observable will be analyzed and studied for how the inclusion of this thesis's result into the PWA database will help in the study of baryon resonances.

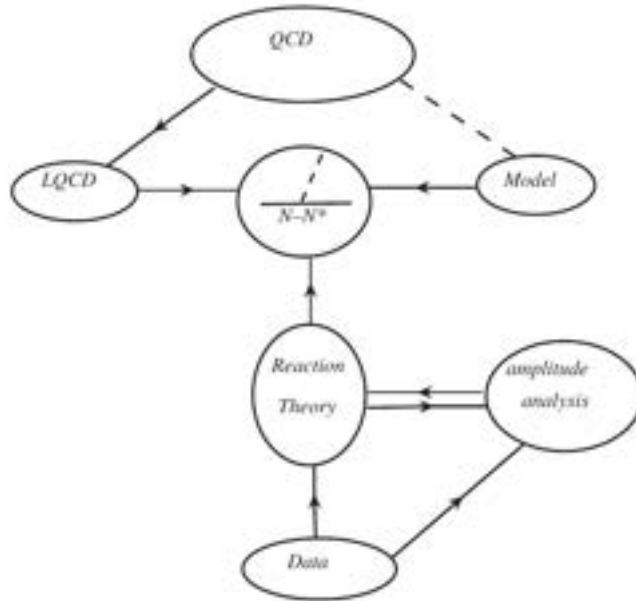


Figure 14: Schematic overview of baryon spectroscopy. Image source: [42]

Missing resonance problem

As discussed in Sec. 1.2.1, the number of predicted resonances by the constituent quark models (CQM) depends heavily on the effective degrees of freedom of the model. Because many of the predicted resonances in the higher invariant mass region

($W \geq 1.7$ GeV) are not observed in experiments, one can say that the CQMs have wrong effective degrees of freedom of QCD at those regions. Hence, CQMs with lesser effective degrees of freedom such as the diquark-quark model or models with different approaches in symmetries [27] could succeed in reproducing the correct resonance spectrum at higher masses [42].

Another possible explanation for missing resonances comes from the possibility that the missing resonances couple weakly to πN elastic scatterings which most of the accumulated data for reconstructing resonances are made up of. Instead, as some CQMs predict, the missing resonances could couple strongly to γN photoproduction reactions [76]. In order to test out this assertion, many different reaction channels that are not kinematically forbidden to excite target nucleons to resonances should be tried for resonance experiments. Until the year 2005, photoproduction experiments (γN) only involved photon beams at low energies $E_\gamma \leq 1$ GeV which limited the resonances to invariant mass of $W < 1.7$ GeV [107]. With the results from FROST/CLAS experiment and CBELSA/TAPS experiments which both utilized real photon beams up to $E_\gamma = 2.4$ GeV for meson photoproductions, we can gain insights on resonances' coupling strengths to electromagnetic channels.

Uncertainties in partial decay widths of resonances

The second long lasting problem in baryon spectroscopy is the large uncertainty values in the partial decay widths of baryon resonances [38]. There may be many contributing factors to large uncertainties. First of which is that some decay channels simply lack the amount of data collected in order for PWA models to extract sensible resonance parameters [42]: ηN , $K\Sigma$, and ωN . The second significant reason is the discrepancies between results from existing PWA methods which all have their own approaches of extracting resonance parameters. In Table. 10, Breit-Wigner masses and decay widths of N^* and Δ^* resonances predicted by five different PWA models

are listed which was put together by Ref. [44] in 2009. This problem could also be resolved by a sufficiently large database that covers large kinematic regions in angles and energies. A larger database will place stronger constraints while extracting the resonance parameters by all models and the model dependence will be diminished.

The result of this thesis on the measurement of the helicity asymmetry E in π^0 photoproduction specifically improves the world database in the energy range of $E_\gamma = [1.73, 2.37]$ GeV. Incorporation of this result into PWA databases, such as SAID, will improve the constraints in the parametrization process of baryon resonances, reducing the uncertainties of resonance decay widths and shed light on the missing resonance problem. This thesis's results have been added to the SAID database to produce a new preliminary SAID fit (discussed in Chapter. 6). This addition showed promising improvements in the higher energy ranges ($E_\gamma = [1.73, 2.37]$ GeV) where the experimental data was previously scarce. The inclusion of more polarization observable measurements with good precision will further reduce the discrepancies between PWA models and provide a more accurate resonance spectrum.

Resonance	Our estimate	Our rating	KH	CM	Kent	GWU	BrGa
$N_{1/2^+}$ (1440)	1450 \pm 32; 300 \pm 100	****	1410 \pm 12; 135 \pm 10	1440 \pm 30; 340 \pm 70	1462 \pm 10; 391 \pm 34	1485 \pm 1; 284 \pm 18	1440 \pm 12; 335 \pm 50
$N_{3/2^-}$ (1520)	1522 \pm 4; 115 \pm 10	****	1519 \pm 4; 114 \pm 7	1525 \pm 10; 120 \pm 15	1524 \pm 4; 124 \pm 8	1516 \pm 1; 99 \pm 3	1524 \pm 4; 117 \pm 6
$N_{1/2^-}$ (1535)	1538 \pm 10; 175 \pm 45	****	1526 \pm 7; 130 \pm 20	1550 \pm 40; 240 \pm 80	1534 \pm 7; 151 \pm 27	1547 \pm 3; 188 \pm 4	1535 \pm 20; 170 \pm 35
$N_{1/2^-}$ (1650)	1660 \pm 18; 165 \pm 25	****	1670 \pm 8; 180 \pm 20	1650 \pm 30; 150 \pm 40	1659 \pm 9; 170 \pm 12	1635 \pm 1; 115 \pm 3	1680 \pm 40; 170 \pm 45
$N_{3/2^-}$ (1675)	1675 \pm 5; 153 \pm 22	****	1679 \pm 8; 120 \pm 15	1675 \pm 10; 160 \pm 20	1676 \pm 2; 159 \pm 7	1674 \pm 1; 147 \pm 1	1678 \pm 5; 177 \pm 15
$N_{3/2^+}$ (1680)	1683 \pm 3; 126 \pm 9	****	1684 \pm 3; 128 \pm 8	1680 \pm 10; 120 \pm 10	1684 \pm 4; 139 \pm 8	1680 \pm 1; 128 \pm 1	1685 \pm 5; 117 \pm 12
$N_{3/2^-}$ (1700)	1725 \pm 50; 190 \pm 110	***	1731 \pm 15; 110 \pm 30	1675 \pm 25; 90 \pm 40	1737 \pm 44; 250 \pm 230	-	1730 \pm 40; 310 \pm 60
$N_{1/2^+}$ (1710)	1713 \pm 12; 220 \pm 180	***	1721 \pm 9; 120 \pm 15	1700 \pm 50; 90 \pm 30	1717 \pm 28; 480 \pm 330	-	1725 \pm 25; 200 \pm 35
$N_{3/2^+}$ (1720)	1730 \pm 30; 320 \pm 210	****	1710 \pm 20; 190 \pm 30	1700 \pm 50; 125 \pm 70	1717 \pm 31; 380 \pm 180	1750 \pm 5; 256 \pm 22	1770 \pm 100; 650 \pm 120
$N_{3/2^-}$ (1860)	1850 \pm 40; 260 \pm 170	**	-	1880 \pm 100; 180 \pm 60	1804 \pm 55; 450 \pm 185	-	1870 \pm 25; 150 \pm 40
$N_{3/2^+}$ (1870)	1880 \pm 40; 270 \pm 180	**	1882 \pm 10; 95 \pm 20	-	1903 \pm 87; 490 \pm 310	1818; 118	1910 \pm 50; 360 \pm 80
$N_{1/2^+}$ (1880)	1890 \pm 50; 210 \pm 100	*	-	-	1885 \pm 30; 113 \pm 44	-	1900 \pm 30; 300 \pm 40
$N_{3/2^+}$ (1900)	1940 \pm 50; 340 \pm 150	*	-	-	1879 \pm 17; 498 \pm 78	-	1960 \pm 30; 185 \pm 40
$N_{1/2^-}$ (1905)	1905 \pm 50; 250 \pm 150	*	1880 \pm 20; 95 \pm 30	-	1928 \pm 59; 414 \pm 157	-	-
$N_{7/2^+}$ (1900)	2020 \pm 60; 410 \pm 110	**	2005 \pm 150; 350 \pm 100	1970 \pm 50; 350 \pm 120	2086 \pm 28; 535 \pm 120	-	-
$N_{3/2^-}$ (2080)	2100 \pm 55; 310 \pm 110	**	2080 \pm 20; 265 \pm 40	2060 \pm 80; 300 \pm 100	-	-	2160 \pm 35; 370 \pm 50
$N_{1/2^-}$ (2090)	-	-	-	2180 \pm 80; 350 \pm 100	-	-	-
$N_{1/2^+}$ (2100)	2090 \pm 100; 230 \pm 200	*	2050 \pm 20; 200 \pm 30	2125 \pm 75; 260 \pm 100	-	-	-
$N_{3/2^-}$ (2200)	2100 \pm 85; 350 \pm 50	**	2228 \pm 30; 310 \pm 50	2180 \pm 80; 400 \pm 100	-	-	2065 \pm 25; 340 \pm 40
			KH	CM	Kent	GWU	Hendry
$N_{7/2^-}$ (2190)	2150 \pm 30; 440 \pm 110	****	2140 \pm 12; 390 \pm 30	2200 \pm 70; 500 \pm 150	2127 \pm 9; 550 \pm 50	2152 \pm 2; 484 \pm 13	2140 \pm 40; 270 \pm 50
$N_{9/2^+}$ (2220)	2260 \pm 60; 490 \pm 115	****	2205 \pm 10; 365 \pm 30	2230 \pm 80; 500 \pm 150	-	2316 \pm 3; 633 \pm 17	2300 \pm 100; 450 \pm 150
$N_{9/2^-}$ (2250)	2255 \pm 50; 420 \pm 150	****	2268 \pm 15; 300 \pm 80	2250 \pm 80; 400 \pm 120	-	2302 \pm 6; 628 \pm 28	2200 \pm 100; 350 \pm 100
$N_{11/2^-}$ (2600)	2630 \pm 120; 650 \pm 250	**	2577 \pm 50; 400 \pm 100	-	-	-	2700 \pm 100; 900 \pm 100
$N_{13/2^+}$ (2700)	2800 \pm 160; 600 \pm 300	**	2612 \pm 45; 350 \pm 50	-	-	-	3000 \pm 100; 900 \pm 150
			KH	CM	Kent	GWU	BrGa
$\Delta_{1/2^+}$ (1232)	1232 \pm 1; 118 \pm 2	****	1232 \pm 3; 116 \pm 5	1232 \pm 2; 120 \pm 5	1231 \pm 1; 118 \pm 4	1233 \pm 1; 119 \pm 1	1230 \pm 2; 112 \pm 4
$\Delta_{1/2^+}$ (1600)	1615 \pm 80; 360 \pm 120	***	1522 \pm 15; 220 \pm 40	1600 \pm 50; 300 \pm 100	1706 \pm 10; 430 \pm 73	-	1640 \pm 40; 480 \pm 100
$\Delta_{1/2^-}$ (1620)	1626 \pm 23; 130 \pm 45	****	1610 \pm 7; 139 \pm 18	1620 \pm 20; 140 \pm 20	1672 \pm 7; 154 \pm 37	1614 \pm 1; 71 \pm 3	1625 \pm 10; 148 \pm 15
$\Delta_{3/2^-}$ (1700)	1720 \pm 50; 370 \pm 200	****	1680 \pm 70; 230 \pm 80	1710 \pm 30; 280 \pm 80	1762 \pm 44; 600 \pm 250	1688 \pm 3; 182 \pm 8	1780 \pm 40; 580 \pm 120
$\Delta_{1/2^+}$ (1750)	-	-	-	-	1744 \pm 36; 300 \pm 120	-	-
$\Delta_{1/2^-}$ (1900)	1910 \pm 50; 190 \pm 100	**	1908 \pm 30; 140 \pm 40	1890 \pm 50; 170 \pm 50	1920 \pm 24; 263 \pm 39	-	-
$\Delta_{1/2^+}$ (1905)	1885 \pm 25; 330 \pm 50	****	1905 \pm 20; 260 \pm 20	1910 \pm 30; 400 \pm 100	1881 \pm 18; 327 \pm 51	1856 \pm 2; 321 \pm 9	1870 \pm 32; 340 \pm 32
$\Delta_{1/2^+}$ (1910)	1935 \pm 90; 280 \pm 150	****	1888 \pm 20; 280 \pm 50	1910 \pm 40; 225 \pm 50	1882 \pm 10; 229 \pm 25	2068 \pm 2; 543 \pm 10	-
$\Delta_{3/2^+}$ (1920)	1950 \pm 70; 260 \pm 100	***	1868 \pm 10; 220 \pm 80	1920 \pm 80; 300 \pm 100	2014 \pm 16; 152 \pm 55	-	1995 \pm 40; 360 \pm 50
$\Delta_{3/2^-}$ (1930)	1930 \pm 30; 350 \pm 170	**	1901 \pm 15; 195 \pm 60	1940 \pm 30; 320 \pm 60	1956 \pm 22; 530 \pm 140	-	-
$\Delta_{1/2^-}$ (1940)	1995 \pm 60; 340 \pm 130	**	-	1940 \pm 100; 200 \pm 100	2057 \pm 110; 460 \pm 320	-	1995 \pm 40; 360 \pm 50
$\Delta_{7/2^+}$ (1950)	1930 \pm 16; 285 \pm 45	****	1913 \pm 8; 224 \pm 10	1950 \pm 15; 340 \pm 50	1945 \pm 2; 300 \pm 7	1921 \pm 1; 271 \pm 1	1928 \pm 8; 290 \pm 14
$\Delta_{3/2^+}$ (2000)	-	-	2200 \pm 125; 400 \pm 125	-	1752 \pm 32; 251 \pm 93	-	-
$\Delta_{1/2^-}$ (2150)	-	-	-	2200 \pm 100; 200 \pm 100	-	-	-
			KH	CM	Kent	GWU	Hendry
$\Delta_{7/2^-}$ (2200)	2230 \pm 50; 420 \pm 100	**	2215 \pm 10; 400 \pm 100	2200 \pm 80; 450 \pm 100	-	-	2280 \pm 80; 400 \pm 150
$\Delta_{9/2^+}$ (2300)	2360 \pm 125; 420 \pm 200	**	2217 \pm 80; 300 \pm 100	2400 \pm 125; 425 \pm 150	-	-	2450 \pm 100; 500 \pm 200
$\Delta_{3/2^-}$ (2350)	2310 \pm 85; 490 \pm 250	***	2305 \pm 26; 300 \pm 70	2400 \pm 125; 400 \pm 150	-	2233 \pm 53; 773 \pm 187	-
$\Delta_{7/2^+}$ (2300)	2390 \pm 100; 300 \pm 200	*	2425 \pm 60; 300 \pm 80	2350 \pm 100; 300 \pm 100	-	-	-
$\Delta_{9/2^-}$ (2400)	2400 \pm 190; 530 \pm 300	**	2468 \pm 50; 480 \pm 100	2300 \pm 100; 330 \pm 100	-	2643 \pm 141; 895 \pm 432	2200 \pm 100; 450 \pm 200
$\Delta_{11/2^+}$ (2420)	2462 \pm 120; 490 \pm 150	***	2416 \pm 17; 340 \pm 28	2400 \pm 125; 450 \pm 150	-	2633 \pm 29; 692 \pm 47	2400 \pm 60; 460 \pm 100
$\Delta_{13/2^-}$ (2750)	2720 \pm 100; 420 \pm 200	**	2794 \pm 80; 350 \pm 100	-	-	-	2650 \pm 100; 500 \pm 100
$\Delta_{15/2^+}$ (2950)	2920 \pm 100; 500 \pm 200	**	2990 \pm 100; 330 \pm 100	-	-	-	2850 \pm 100; 700 \pm 200

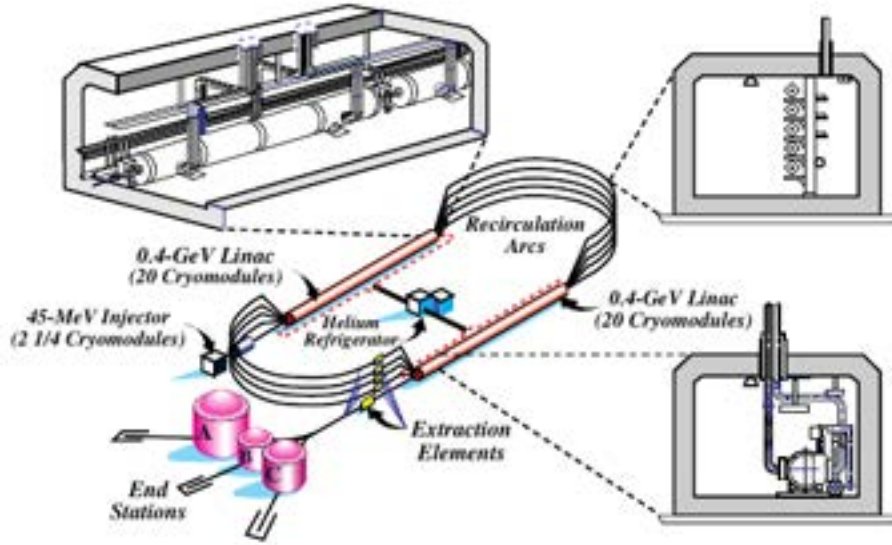
Table 10: Breit-Wigner masses and widths of N^* and Δ^* resonances in units of MeV, given by five different PWA models. The estimates and ratings are from by Ref. [44]. Table is taken from [44]

2 The FROST Experiment at Jefferson Lab

The data used in this analysis were obtained from the 'FROST-g9a' experiment at the Department of Energy's Thomas Jefferson National Accelerator Facility Hall B (Jefferson Lab) in Virginia, USA. In the naming of the experiment 'g9a', 'g9' stands for photon rungroup 9 (i.e. experiments using the FROST targets) and 'a' indicates the first of the 'g9' experiments at Jefferson Lab Hall B. The experimental program of the FROST rungroup was to study the long-standing question of "missing resonances, i.e., experimentally not established baryon states which are predicted by $SU(6) \times O(3)$ symmetric quark models [77], using polarized photon beams and the longitudinally ('g9a') or transversely ('g9b') polarized FROST target. The FROST-g9a experiment sets polarization states of the photon beam (Sec. 2.2) and target proton (Sec. 2.4.1) to allow measurements of double polarization observables H , F , G , and E (Sec. 1.3.4). The actual FROST-g9a experiments were conducted from December 2007 to February 2008 when the beam energy of the Continuous Electron Beam Accelerator Facility (CEBAF) was limited to 6 GeV, prior to the 12 GeV upgrade in 2017. This chapter will mainly cover subsystems of the Jefferson Lab's CLAS detector in Hall B and aids to visualize how the trajectories of outgoing particles are detected and the event kinematics is measured with nearly full 4π solid angular coverage.

2.1 Continuous Electron Beam Accelerator Facility (CEBAF)

The Continuous Electron Beam Accelerator Facility (CEBAF) at Jefferson Lab delivered polarized electron beams up to 6 GeV simultaneously and independently to three experimental Halls A, B and C (prior to the 12 GeV beam energy upgrade in 2014). Simultaneously, each of the Halls could receive electron beam at their desired current, specific to the ongoing experimental programs to probe and study nucleon structures and properties of QCD. As the electrons are injected via a 45-MeV injector as shown in Fig. 15(a), they are accelerated inside a 14 km five pass racetrack shaped



(a)



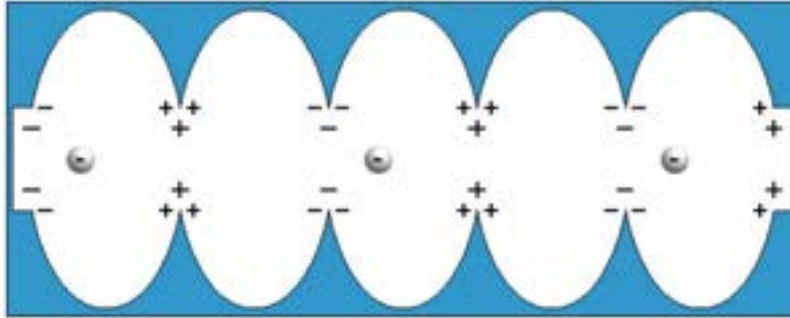
(b)

Figure 15: (a) Schematic layout of the CEBAF accelerator [78] and (b) an aerial view of the CEBAF accelerator with the three experimental Halls A, B, and C prior to 12 GeV upgrade. From the left, the first one is Hall A, the second is Hall B, and the last is Hall C. Image source: [79].

accelerator which consists of 2 anti-parallel linear accelerators (LINACs) and nine recirculation arcs.



(a)



(b)

Figure 16: (a) Picture from Ref. [79] and (b) a diagram of a cryomodule with radio-frequency (RF) cavities showing charge gradient inside an RF cavity [81].

First in the injector, polarized electrons are generated by illuminating a Gallium arsenide photo-cathode (GaAs) with pulsed laser light at the frequency of 499 MHz, which is the 3rd subharmonic of the accelerating cavity frequency of 1497 MHz [82]. To adjust the beams to each of the halls' demands, three independent diode lasers are synchronized and combined to illuminate on the GaAs photo-cathode. To produce

longitudinally polarized electrons, circularly polarized photons are used to strike the GaAs which are polarized via two Pockel cells, consisting of a quarter-wave and a half-wave plate. The resulting longitudinally polarized electron beam attained a polarization level up to 85%. The emitted electrons are accelerated up to 45 MeV inside 9 RF cavities as shown in Fig. 16(b). The electrons are partitioned into 2.004 ns bunches by using an optical chopper before injecting them into the LINACs. One LINAC consists of 20 cryomodules and each cryomodule consists of 8 Niobium superconducting RF cavities as shown in Fig. 16(a). It was capable of accelerating the electrons up to approximately 580 MeV per pass. After 5 passes through each LINAC, the electrons could reach up to the maximum of 5.5 GeV before being delivered into the experimental halls. Submerging the cavities in liquid helium and keeping the temperature at 2 K allows the superconductivity of the cavities, which in turn allows for high voltage difference and strong electric field at the left and right end of the cavity with only tiny amount of energy dissipated on the surfaces. As shown in Fig. 16(b), electric fields inside RF cavities are oriented in such direction (negative/positive on left/right) that accelerates traveling electrons. The electric fields are in fact oscillating and reverting directions periodically, but the oscillations are timed such that the fields are in parallel with the incoming electrons' accelerating direction at the arrival of incoming electron bunches. The microwaves, which are of the same frequency of the electromagnetic waves inside the cavities, causes resonance effect and amplifies the electric fields and acceleration of electrons. After leaving the first LINAC, electrons enter the recirculation arcs [83] and are bent by 180° using strong dipole magnets. Since the entering electrons are comprised of different energy levels depending on the number of passes the electrons made, different magnetic field strength is required to bend all electrons to same radius. An optical spreader is used to differentiate incoming electrons by energies and spread out vertically to steer the electrons to enter specific arcs with the corresponding magnetic field strengths. The

first recirculation arcs are composed of 4 arcs with different magnetic fields and similarly, 5 arcs for the second recirculation arcs. Higher energy electrons enter lower arcs and the lower energies to the upper. As all electrons are bent to same degrees, they are recombined to enter the second LINAC. Then, the RF separator system [84] is used to direct the electrons to the desired halls once desired energies are attained, or otherwise goes through another pass for further acceleration. A system of nine RF separator cavities are located at each arcs of the second recirculation arcs as indicated by yellow boxes with the label “Extraction Elements” in Fig. 15(a). Such separator cavities are capable of providing a $100\ \mu\text{rad}$ kick to any electron passes to deflect the beam to the desired halls.



Figure 17: A picture of recirculation arcs [79] utilizing dipole magnets to bend electron beam by 180° .

2.2 Photon Tagging Spectrometer

As the electrons are delivered to Hall B, photon beams are generated by the bremsstrahlung tagging technique. An overview of tagging system is sketched in Fig. 18. The electrons entering from the CEBAF accelerator interact with a thin radiator (thin gold or carbon foil), where a portion of the electrons interact with the electromagnetic field of the radiator atoms and gets decelerated. As decelerated, the difference in energy is emitted by the bremsstrahlung radiation:

$$E_\gamma = E_0 - E_e, \quad (50)$$

where E_γ , E_0 , and E_e are emitted photon energy, incident electron energy, and outgoing (scattered) electron energy, respectively. The intensities of the photon beam were variable by varying thicknesses of radiator; increasing the radiator thickness increases the photon beam intensity. The photon beam was polarized circularly by a longitudinally polarized electron beam striking the gold foil radiator. Linearly polarized photons beams were obtained via carefully aligning the thin diamond radiator relative to the entering electrons. The alignment technique for producing linearly polarized photon beams is called the Stonehenge technique which is based on series of scans to horizontal/vertical rotations axes of a goniometer. During each scan, the offset between the electron beam and the radiator is measured and fixed by observing the resulting bremsstrahlung radiation energy spectrum. In depth explanation of the Stonehenge technique is given in Ref. [86].

The recoiling electrons and electrons, which did not interact with the radiator, are bent by the magnetic field of a C-shaped dipole magnet, which produced a B-field of up to 1.75 T. The magnet is positioned to direct full energy electrons (non-interacting with the radiator) into a direction toward the beam dump in experimental Hall B floor as shown in Fig. 19. On the other hand, the recoiling electrons are bent stronger,

depending on their residual energy. The recoiling electrons then traverse two scintillator planes placed along the focal plane of tagger magnet to measure their energy (E-counter plane) and arrival times (T-counter plane). As shown in Fig. 18, the E-counters, 384 plastic scintillators of 5 mm thickness, are partially overlaid to provide 767 different energy channels. Depending on which scintillators the energy-degraded electrons passed through, momentum of the electron is calculated. With the measured B-field of tagger magnet. The energy of recoil electrons are calculated in which the resolution of calculated electron energy is approximately 0.1% of the incident electron beam energy (E_0). The T-counters, consisting on 61 scintillators with thickness of 2 cm and are placed parallel to the E-counters but 20 cm downstream of E-counters. as shown by the thick dotted lines in Fig. 18. On both ends of the scintillators, photomultiplier tubes (PMTs) measure the time at which the electrons have crossed the scintillators. Although the arrival time information is entirely determined by T-Counter planes signals, E-counters also records the timing information, which is compared with T-counters' readings to avoid any coincidental readings. This step is carried out after the event was fully recorded in CLAS detectors. For the cases when multiple hits were recorded in the E-counters with only a single hit on the T-counters, the E-counter timing readings could be used to discern the correct hit in the E-counters.

Arrival times of bent electrons can be used to match to the corresponding electron bunches from the CEBAF, hence providing a cross-check on the arrival time of the photons at the target of CLAS detector (minimum of 300 ps of timing resolution is required). Since electron beam bunches are separated by 2.004 ns intervals and the time window of each beam bunches are within a few ps, a better time measurement of the event start time can be obtained by utilizing the RF signal of incident electron beam. Finally, the polarization of the beam photons is further improved as the photons pass through the collimators placed downstream of the tagger magnet, ap-

proximately 14 m from the radiator. The collimator ensures the photon beam achieves the highest degree of polarization by restricting the diameter of the photon beam to be less than 3 cm and removing any charged background particles with inter-spaced sweep magnets [78].

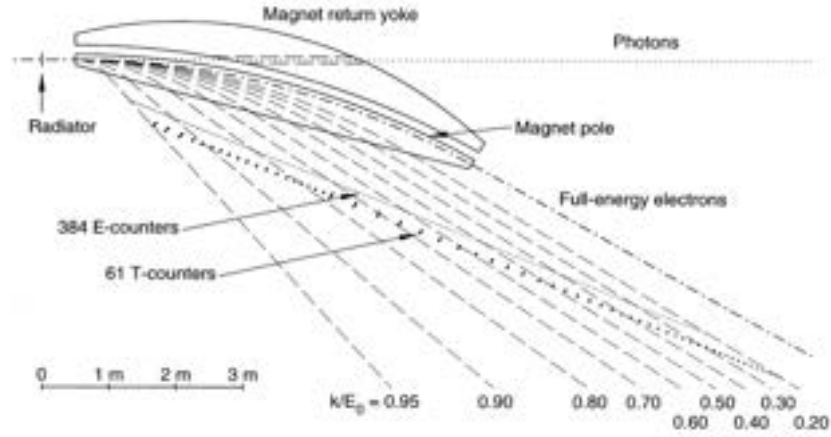


Figure 18: The overall geometry of tagging system. The straight dotted lines indicate electrons entering from left and outgoing photons to the right after interacting with the radiator. Dashed downward lines indicate typical trajectories of bent electrons labeled by the ratio of emitted photon energies over original electron energies [85].

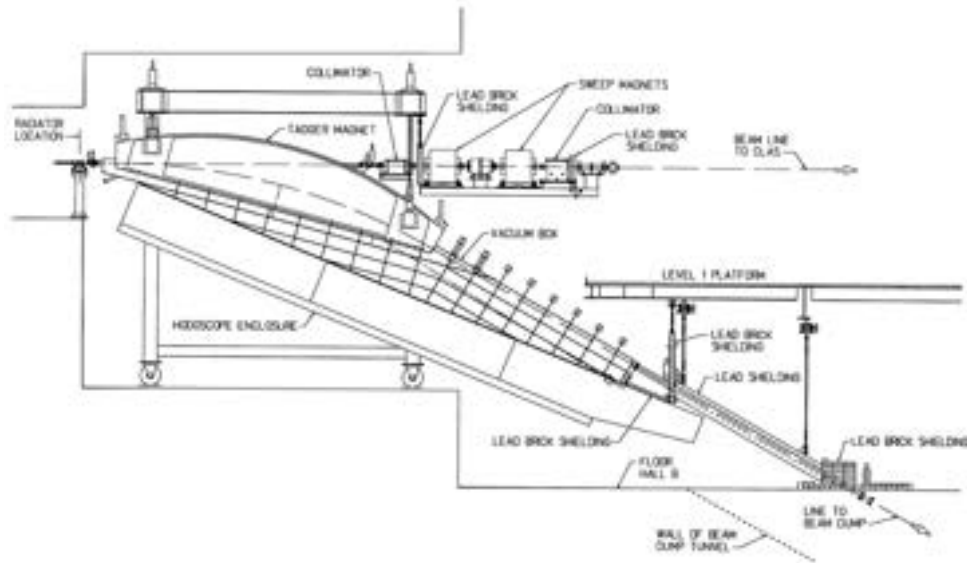


Figure 19: Side view of the tagging system. The tagger magnet is approximately 6 m long [85].

2.3 CLAS Spectrometer

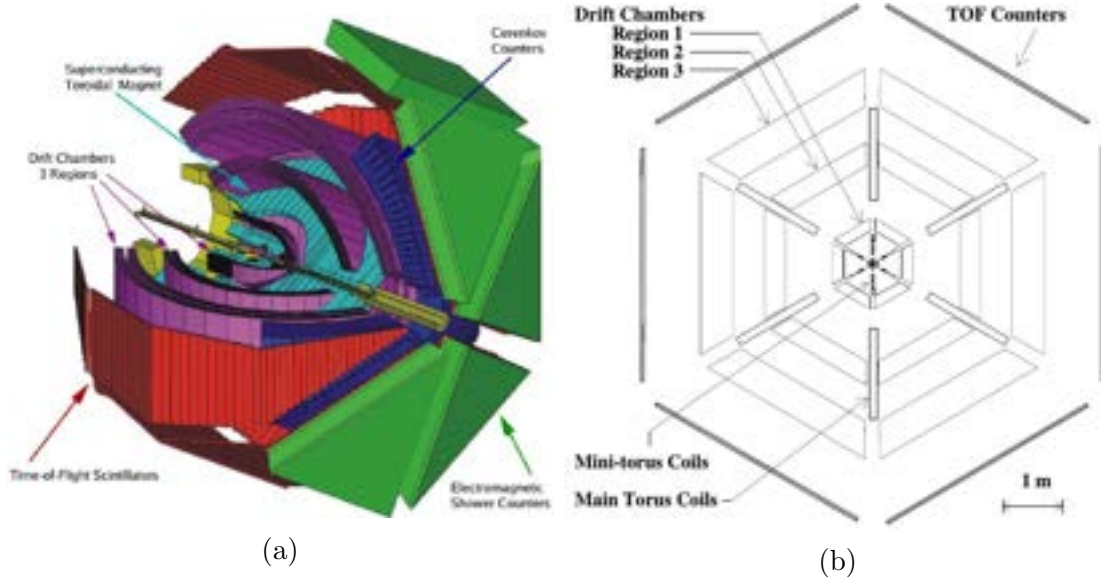


Figure 20: A schematic of the CLAS spectrometer, which is approximately 8 m in diameter, symmetrically designed around the beam axis.

The CEBAF Large Acceptance Spectrometer (CLAS) detector was designed to cover most of 4π angular range to detect charged particles in photo- and electroproduction experiments. The CLAS detector is composed of many sub-detectors arranged azimuthally symmetric around the beamline based on a toroidal magnetic field in ϕ direction generated by six superconducting coils. The detectors are divided symmetrically into six sectors in ϕ direction. The actual range of coverage for charged particles is $8^\circ \leq \theta \leq 140^\circ$ in scattering angle and $-25^\circ \leq \phi \leq 25^\circ$ for each of six sectors. A magnetic field-free region is present around the target to allow polarization of targets by up to 5.0 T magnetic field, unaffected by the toroidal magnetic field. The sub-detectors in each sectors are as follows:

- Drift chambers (DC) determine charged particle momentum by tracing its trajectory,
- Time-of-flight system (TOF) measures the time-of-flight of charged particles,

- Cherenkov counters (CC) identifies recoil electron verses π^- in electroproduction experiments,
- Electromagnetic calorimeter (EC) measures energy of outgoing electrons, photons and neutrons,
- Start counter (SC) measures the start time of every event trigger recorded by the CLAS detector.

The Specifications of the CLAS detector are listed on Table 11 [78]. In the following sections, details of subdetectors as well as the torus magnets, triggering system, data acquisition, and the frozen spin target (FROST) will be discussed.

Capability	Quantity	Range	Capability	Quantity	Range
Coverage	Charged-particle angle	$8^\circ \leq \theta \leq 140^\circ$	Particle ID	π/K separation	$p \leq 2 \text{ GeV}$
	Charged-particle momentum	$p \geq 0.2 \text{ GeV}/c$		π/p separation	$p \leq 3.5 \text{ GeV}$
	Photon angle (4 sectors)	$8^\circ \leq \theta \leq 45^\circ$		π^- misidentified as e^-	$\leq 10^{-3}$
	Photon angle (2 sectors)	$8^\circ \leq \theta \leq 75^\circ$	Luminosity	Electron beam	$L \approx 10^{34} \text{ nucleon } cm^{-2}s^{-1}$
	Photon energy	$E_\gamma \geq 0.1 \text{ GeV}$		Photon beam	$L \approx 5 \times 10^{31} \text{ nucleon } cm^{-2}s^{-1}$
Resolution	Momentum ($\theta \leq 30^\circ$)	$\sigma_p/p \approx 0.5\%$	Data acquisition	Event rate	4 kHz
	Momentum ($\theta \geq 30^\circ$)	$\sigma_p/p \approx (1 - 2)\%$		Data rate	22 MB/s
	Polar angle	$\sigma_\theta \approx 1 \text{ mrad}$	Polarized target	Magnetic field	$B_{max} = 5 \text{ T}$
	Azimuthal angle	$\sigma_\phi \approx 4 \text{ mrad}$			
	Time (charged particles)	$\sigma_t \approx (100 - 250) \text{ ps}$			
	Photon energy	$\sigma_E/E \approx 10\%/\sqrt{E}$			

Table 11: Summary of the CLAS detector specifications [78]

2.3.1 Start Counter

The first detector the particles encounter after interacting with the FROST target is the Start counter (SC). The purpose of the SC is to measure the time at which the reaction has occurred, hence the SC being the first of all other sub-detectors. Reaction start time measurements are crucial in computing $\beta = \frac{v}{c}$ of the outgoing particles by using the fixed distance between the SC and the Time-of-Flight system (TOF) and

particles' flight time measured at TOF which is placed near the end of the CLAS detector. As shown in Fig. 21, the SC is composed of six sector, matching the six sector design of other CLAS sub-detectors and each sector is composed of three scintillator paddles of 50.2 cm in length and 3 mm thick [87]. Each scintillator paddles has a straight rectangular section in parallel with the beam axis positioned 10.2 cm away from the beam axis and a “nose” section shaped inward to cover the forward angle. At the opposite upstream side of the SC, photomultiplier tubes (PMTs) are placed in a specific angle away from the direction of outgoing particles to avoid interacting. The light signals are induced as charged particles interact with the scintillator bars and directed by light guides to PMTs. Then at the PMTs, the light signals are first converted into electrical signals which later are converted into readable digital ADC and TDC values. The ADC and TDC values are translated into physical quantities of interest to be used in the analysis. The time measurement of the SC has a resolution of about 290 ps at the straight parallel section and about 320 ps in the “nose” tip section, providing a far better time measurement than the 2.004 ns separation of beam bunches. The acceptance range of the SC is $7^\circ < \theta < 145^\circ$ in polar angles and $-29^\circ < \phi < 29^\circ$ in azimuthal angles for each sectors designed to cover the same solid angle as the TOF system.

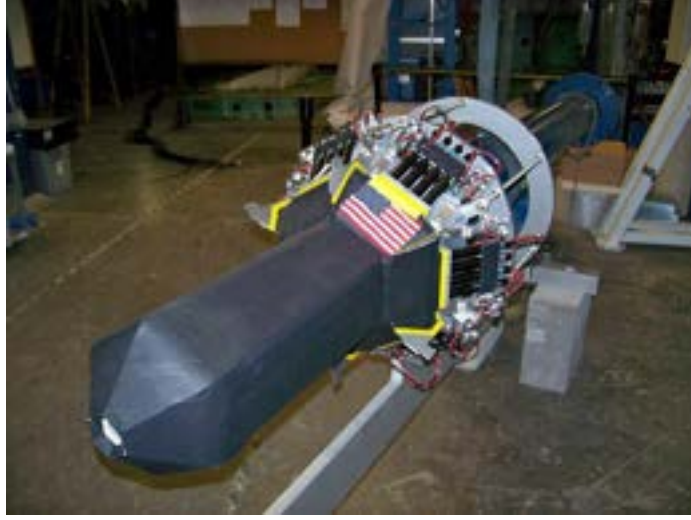
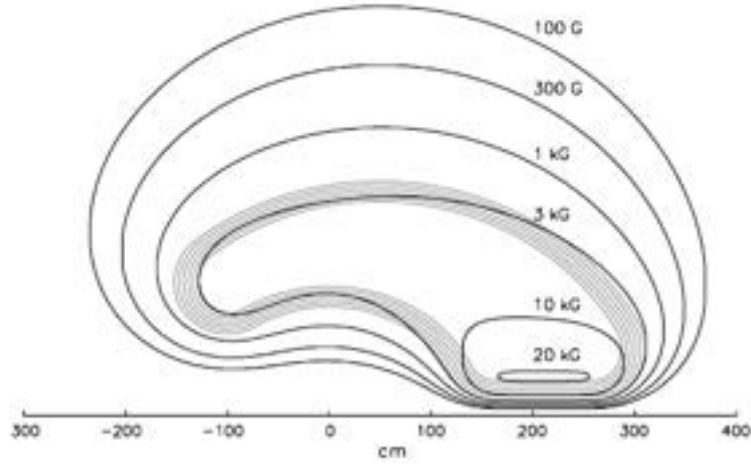


Figure 21: The CLAS start counter [79]. The straight portion of the scintillator paddles are in parallel with the beam axis positioned 10.2 cm away radially.

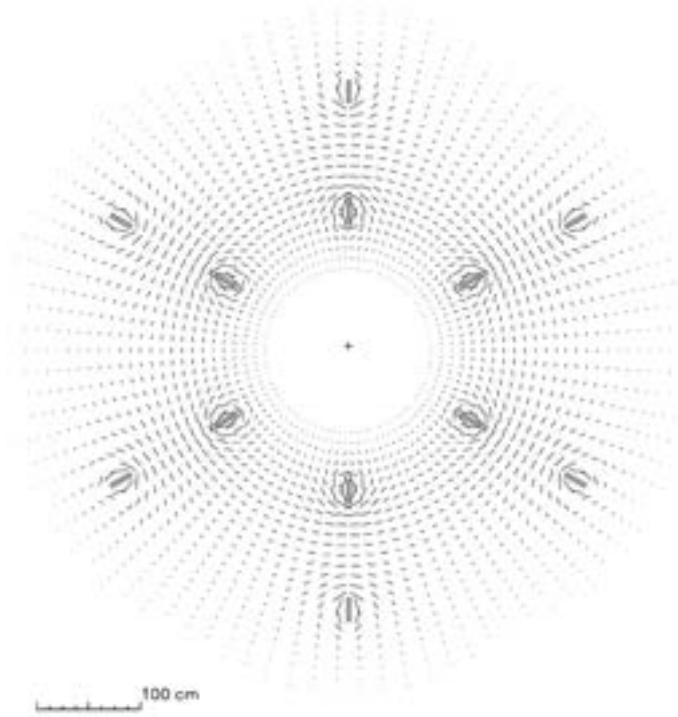
2.3.2 Torus magnets

The torus magnets provide a magnetic fields, generated by six superconducting coils in toroidal geometry around the beam axis, that bends the outgoing charged particles to analyze their momentum. The torus magnet system does not have an iron return yoke, so magnetic fields are purely induced by currents in the coils [78]. The coils are configured specifically to provide magnetic field in the azimuthal ϕ direction. The field can be negative or positive depending on the polarity of the current as shown in Fig. 22(a). The field's vector map (Fig. 22) shows that the field is almost perfectly in φ direction except in close vicinity of coils. To minimize such discontinuity in overall field direction, the inner shape of the coil are designed to be circular. The whole magnet is about 5 m in diameter and 5 m in length, composing coils laid out in shapes of a kidney as shown in Fig. 22(a). The kidney shape allows higher field integral for high momentum forward-going particles whereas particles outgoing at larger angles experience lower field integral. To allow polarization of targets with different magnetic fields, a small region near the center of CLAS was designed to be

field free. The maximum current is designed to be 3560 A at which forward angle regions achieve magnetic fields of up to 2.5 T and a particle with a scattering angles around 90° experiences a field of 0.6 T. To provide the in-bending (out-bending) curvature toward (away from) the beam axis for negatively charged particles, positive (negative) current is provided. For the g9a/FROST experiment a current of 1920 A was provided in in-bending configuration.



(a)



(b)

Figure 22: (a) Contour map of CLAS torus magnet's constant field in the midplane between two coils. For reference, the layout of superconducting coils is projected onto the midplane. (b) Magnetic field vectors of the CLAS torus magnet shown in the plane perpendicular to the beam axis, centered at the target position. The superconducting coils are laid out to provide magnetic field vectors in direction of ϕ [78].

2.3.3 Drift Chambers

Under the influence of the magnetic field generated by the torus magnet, the curved trajectories of charged particles (Fig. 23(a)) and their momentum ($p = q \cdot B \cdot r$) are measured in the drift chambers (DC). The DC are composed of three separate regions: Regions 1, 2, and 3 (R1, R2, and R3) as shown in Fig. 23(b), where each section is also partitioned into six sectors, corresponding to the six sector design of the CLAS detector. The R1 (Fig. 25(a)) enclosed the area where magnetic field is lowest and closest to the FROST cryogenic target. The R2 (Fig. 25(b)) is a larger drift chamber positioned in between superconducting coils of the torus magnet and thus experiences the strongest magnetic field. The R3 are placed just outside of the torus magnetic field and utilized to capture the end part of the particles' trajectories.

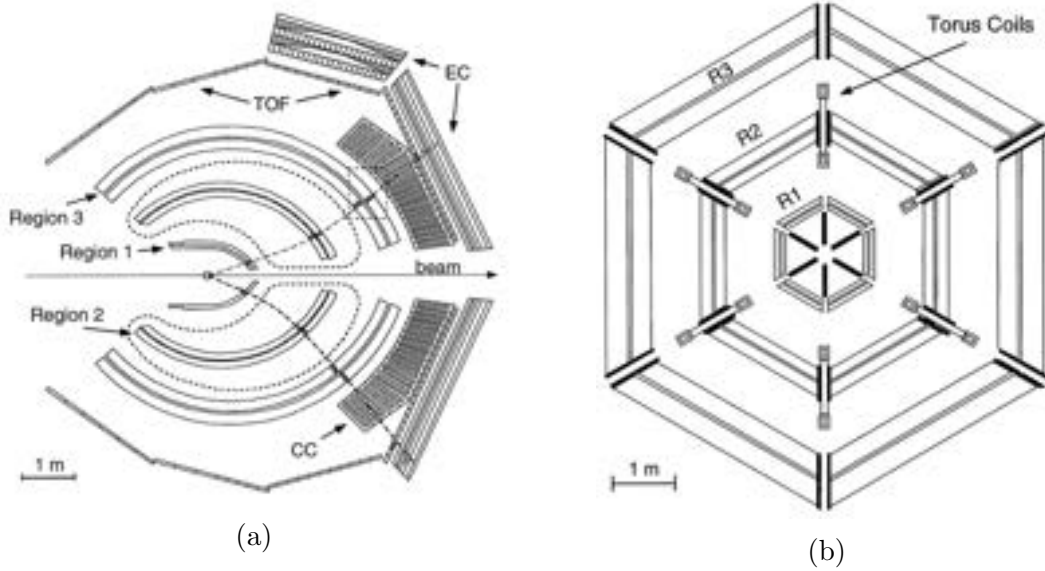


Figure 23: (a) Top view of CLAS detector in horizontal plane. Two charged particles under influence of torus magnet are shown. (b) Cross section view of CLAS in parallel with the beam axis showing hexagonal layout of R1, R2, and R3 of the drift chamber [78].

Each region is composed of two separate superlayers which in turn consists six layers of hexagonal drift cells as shown in Fig. 24, except for R1 having 4 layers of

drift cells. For each of the hexagonal drift cells, one sense wire positioned at the center of the cell while kept at a positive potential and six field wires are positioned at each of six vertices with negative potential. The sense wires are composed of $20\ \mu\text{m}$ diameter gold-plated tungsten whereas the field wires are composed of $140\ \mu\text{m}$ diameter gold-plated aluminum [88]. The choice for drift chamber gas was 90% argon and 10% CO_2 to sustain non-flammability, low multiple scattering, and better ionization processes. As charged particles pass and interact with the gas, they produce ion pairs where negative ions move towards sense wire which are kept at positive potential, triggering a signal. The signal is converted and digitized in TDCs and marks the times at which the passing of charged particles happened.

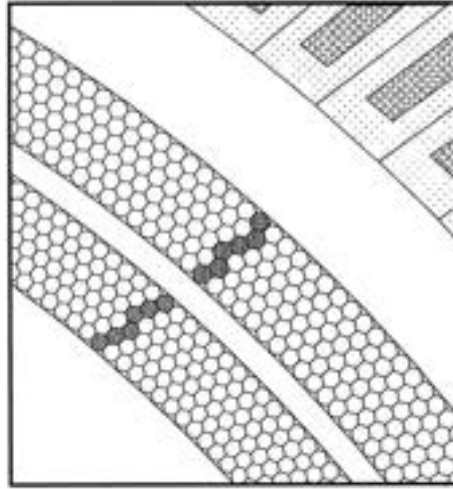


Figure 24: A diagram of R3 superlayers of the drift chambers. The highlighted cells indicate ionization occurred as charged particles passed through. There are no physical walls between the drift cells. The perimeters of the hexagons are only drawn in the figure to outline the shape of each cell [88].

As for the performance and specifications of the drift chambers, individual layers achieved efficiencies greater than 98% which is the probability that a good hit is accurately tracked and recorded in the wire layer [88]. The drift chambers covers $8^\circ \leq \theta \leq 142^\circ$ in polar angles and approximately 80% of the azimuthal angles. The sources for tracking uncertainty are multiple scattering in the DC, geometrical

misalignment of DC chambers, incorrect mapping of the magnetic field, background hits in the DC, and single-wire resolution.

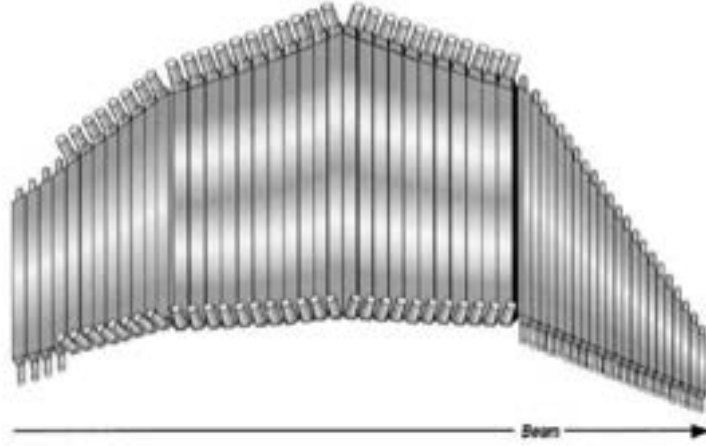


Figure 25: (a) A photograph of R1 of the drift chamber with all sectors assembled. (b) A photograph showing one sector of R2 [80].

2.3.4 Time-of-Flight System

The time at which the outgoing particles cross the panels of the time-of-flight system (TOF) is recorded and used to compute $\beta = \frac{v}{c}$ with the start time measurements from the SC (Sec. 2.3.1) and particle travel distance obtained from the drift chamber's tracking (Sec. 2.3.3). Furthermore, the charged particles could be identified by solving for its mass using momentum calculated from the drift chambers ($\beta = p/\sqrt{m^2 + p^2}$): electrons, pions, kaon, protons, *etc.* As shown in Fig. 26(a), each of TOF's six sectors are divided into four panels which in total contains 57 scintillator bars with PMTs attached at both ends of the bars. The TOF scintillator panels are positioned in between Cherenkov counters and the calorimeters, approximately 1 m – 1.5 m away from the R3 of the drift chambers as shown in Fig. 23(a). Also, such positioning of TOF allowed the PMTs to be shielded from the magnetic field of the torus magnet [89]. As for the angular coverage, the TOF covers $8^\circ \leq \theta \leq 142^\circ$ in polar angles and nearly all azimuthal angles from which 23 scintillators are positioned in forward-

angle panel to capture angles of $8^\circ \leq \theta \leq 45^\circ$ and the remaining scintillators in larger-angle panels covering $46^\circ \leq \theta \leq 142^\circ$ [89]. Each scintillator is placed specifically to be perpendicular to the direction of average incoming particle trajectories with forward-angle counters having 15 cm width and the large-angle counters with 22 cm width in $\Delta\theta$ direction [78]. As charged particles pass through the scintillators, signals are collected by PMTs to be converted into readable ADC and TDC values. TDC values contain timing measurements and ADC values, recording magnitude of the signal, are then used to calibrate each TOF counter (attenuation length, energy loss, time-walk corrections, *etc*) to better compute the exact time when the particles hit TOF scintillators. The TOF system is able to provide timing resolution of 120 ps in the forward-angle counters and 250 ps in the large-angle counters, with a maximum count rate of about 100 kHz at forward-angle counters, as achieved in electron-beam experiments at a luminosity of $10^{34} \text{ cm}^{-2}\text{s}^{-1}$ [89].



(a)



(b)

Figure 26: (a) One sector of TOF counters consisting of four panels covering polar angles of $8^\circ \leq \theta \leq 142^\circ$. (b) A photograph of two panels of TOF counters with PMTs on both ends [89].

2.3.5 Electromagnetic Calorimeters

The forward electromagnetic calorimeters (ECs), which cover scattering angle of $0 \leq \theta \leq 45^\circ$, are placed behind the forward-angle panels of TOF system to detect electrons and neutral particles by measuring its energy deposited. Electrons of energy above

0.5 GeV are detected with the EC and provide information at the trigger level to reject minimum ionizing particles or to set a specific limit on the range of scattered electron energy [90]. Photons are detected with the EC and allow reconstructions of π^0 by assuming the 2γ decay. At least two neutral hits (hits without matched DC tracks) in any of six sectors is required to reconstruct π^0 . The measured neutrons are differentiated from photons by considering the particle's flight time. The flight time of the neutral particle is calculated by using the EC's TDC timing readings, length of the particle trajectory from the target to the hit position in the EC scintillator, and the propagation velocity of the light inside the EC scintillator [91].

The forward EC is partitioned into six modules to correspond to the six sector design of the overall CLAS detectors. Shown in Fig. 27 is the layout of one EC module which contains 39 layers. Each scintillator layer is of 10 mm thickness and one lead sheet of 2.2 mm thickness is placed between each layer and the next. Each scintillator layer has a shape of an equilateral triangle which consists of 36 strips parallel in the direction of one side of the triangle. Each successive layer is rotated by 120° setting three different orientations (U, V, and W), hence, 13 layers of each of three layer orientations in one EC module. The layers are again partitioned into inner and outer stacks, allowing longitudinal sampling of the shower for better hadron identification. For three orientations each with 36 strips and 2 stacks, 216 PMTs are used per one module, which totals up to 1296 PMTs in all 6 EC modules. The EC has an energy resolution of about 4% and a time resolution of 200 ps over the entire detector [78].

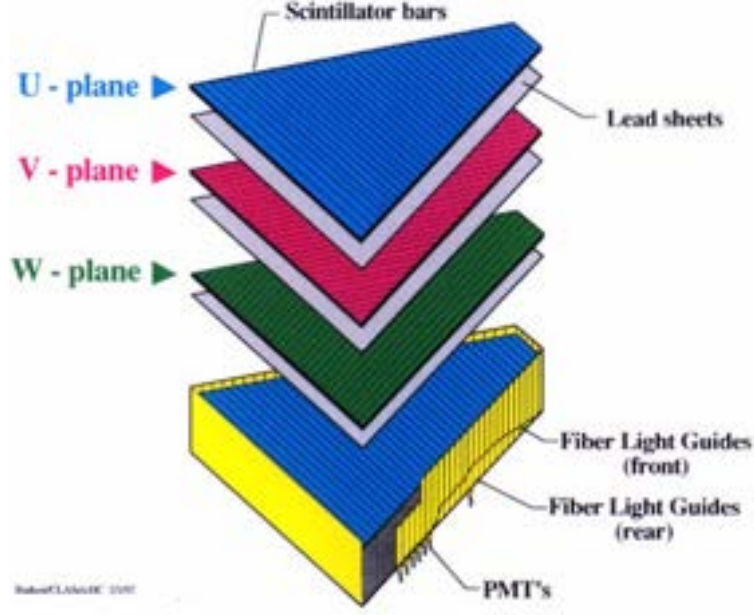


Figure 27: An illustration of the layer structure of one of the Forward electromagnetic calorimeter's module [90].

The large angle calorimeter (LAC), which covers two of the six sectors of CLAS (120° in ϕ), are implemented in addition to the forward EC to further provide detection of scattered electrons and neutral particles (neutrons and photons) in scattering angle of $45^\circ \leq \theta \leq 75^\circ$. The LAC consists of two modules in rectangular shape with a sensitive area of $(217 \times 400) \text{ cm}^2$ [91] as shown in Fig. 28. As with the forward EC, the LAC module has 33 stacks of layers with alternating types: 0.20 cm thick lead foil, 1.5 cm thick scintillator bars, and thin Teflon foils to prevent scintillator bars from touching the lead foil. Each successive scintillator layer is rotated by 90° , setting two different orientations. The layers are further divided into inner (17) and outer (16) layers to improve better classification between pions and electrons. Similar to the forward EC, the light signals produced from the particle shower are collected at both ends of the scintillator layers by PMTs where its amplitude and timing are converted and recorded into ADC and TDC values. Each module in total has 128 stacks and 256 PMTs. As for the performance, energy resolution is about 7.5% for

1 GeV electrons and improves with increasing momentum. The timing resolution is 260 ps for neutrons with momentum higher than 0.5 GeV/c and the efficiency for neutron detection is about 30% [78].

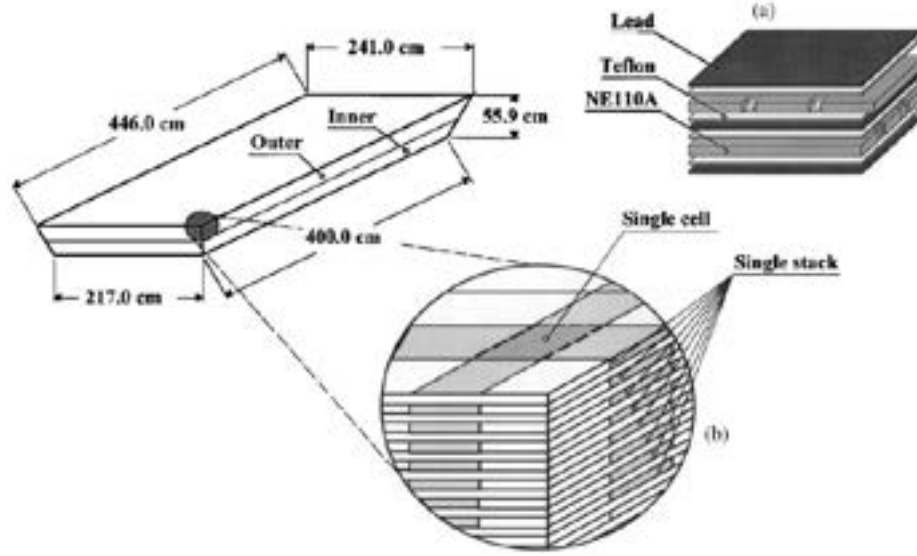


Figure 28: An illustration of the internal structure of the electromagnetic calorimeter at large angles [91].

2.3.6 Trigger System

Main goals of triggering system are to only record interested physics events and minimize the dead-time of the data acquisition system. The signals read by CLAS sub-detectors that are not from interactions of the target and the beam possibly source from cosmic rays, malfunctioning electronics, multiple scattering, *etc.* To reject such unwanted events, a two-level hierarchical trigger system was employed in CLAS experiments [92]. The Level 1 trigger selects hits which have interacted with the same sector of both the start counter and the TOF system, hence, only events with reasonable flight time remain. Moreover, the Level 1 trigger is dead-time-less, meaning all prompt PMT signals for such filtered events are rendered through a pipelined memory lookup within 90 ns [78]. Such filtered triggers from the Level 1 are forwarded to a trigger supervisor (TS) where common start and end signal for

PMT ADCs and TDCs are generated as shown in Fig. 29(a). The Level 2 trigger then filters out events which do not have hits at least four out of six superlayers (R1, R2, and R3) of the drift chamber to ensure the remaining events have good tracking from the drift chambers. To further tailor set of events to our interest physics events, the events undergoes skimming routine as described in Sec. 3.2 and Sec. 3.3.

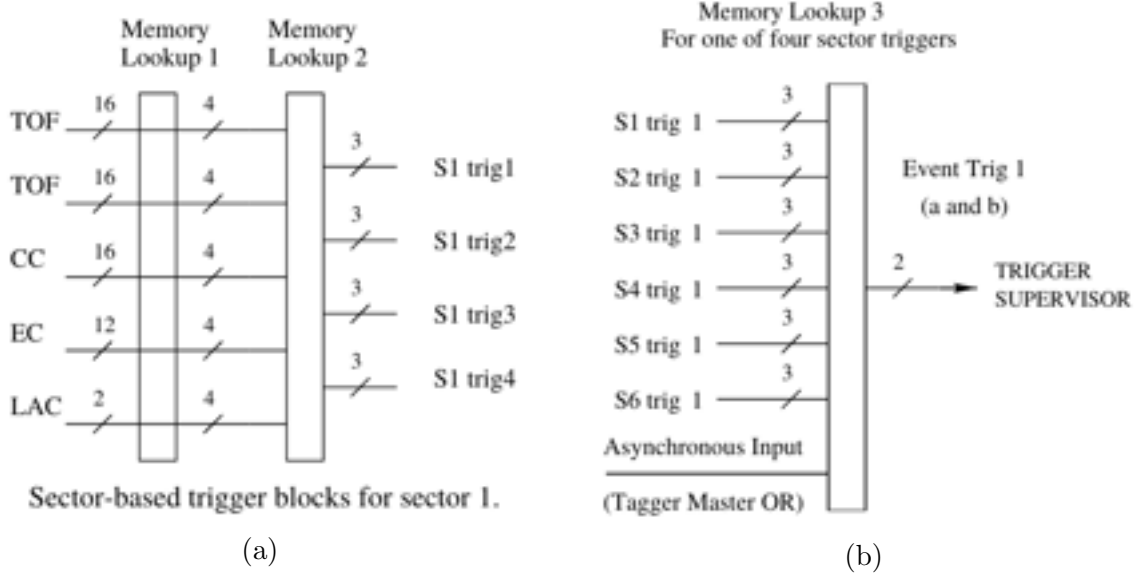


Figure 29: (a) Schematic diagram of four sector-based trigger blocks in a single sector (Level 1). (b) Schematic diagram of trigger electronics (Level 1) which combine information from each sectors and inputs into a event trigger [78].

2.4 CLAS Frozen Spin Target (FROST) Experiment

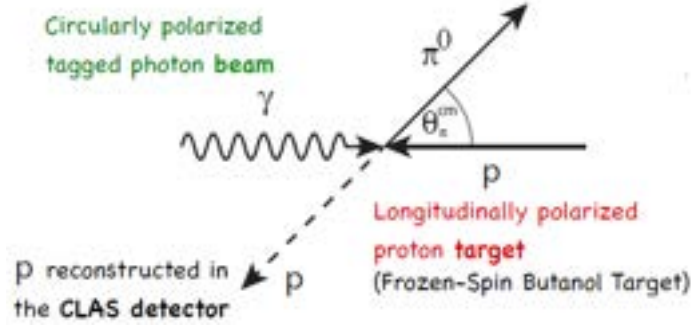


Figure 30: Kinematics for $\gamma p \rightarrow \pi^0 p$

The g9a/FROST (FROzen Spin Target) experiment was performed at the Thomas Jefferson National Accelerator Facility (JLab) using CLAS in Hall B. The FROST experiment for the $\gamma p \rightarrow \pi^0 p$ reaction scattered longitudinally polarized protons with circularly polarized photons at energies between 0.4 GeV and 2.4 GeV enabling the extraction of double polarization observables. Approximately three billion events were recorded during FROST/g9a experiments as shown in Table 12.

Two different electron beam energies were used (1.645 and 2.478 GeV) since there is a kinematical limit on the photon energy that can be tagged by the Hall B Photon tagger for a given electron beam energy. For example, the tagger cannot tag photons with energy below 1.6 GeV when using a 2.4 GeV electron beam. Therefore, additionally a 1.6 GeV electron beam was needed to make photon beams in the energy region of $[0.35, 1.6]$ GeV.

The main goal of the proposed research is the extraction of helicity asymmetry E where it can be utilized with other observables from different polarization experiments to perform the complete experiment to determine the helicity amplitudes [70].

Electron Beam Energy (GeV)	Photon Beam Polarization	# of Events (M)	Observable
1.645	Circular	~ 1000	E
2.478	Circular	~ 2000	E
2.751	Linear	~ 1000	G
3.538	Linear	~ 2000	G
4.599	Linear	~ 3000	G

Table 12: Hall B g9a/FROST run from 12/2007 - 2/2008

2.4.1 Frozen Spin Target (FROST) - Longitudinal Polarization

The main target material utilized in FROST/g9a experiment was butanol C_4H_9OH in which its covalently bonded protons in hydrogen atoms are polarizable using a technique called the Dynamic Nuclear Polarization (DNP), simply transferring spin polarization from the electrons to the nucleons. The events scattered off of the protons in the carbon and oxygen part of the butanol target were considered as the dominant background contributions due for their non-polarizable nature. Through the slits of the target cup (Fig. 33(a)), $^3He/^4He$ filled between the butanol beads, giving the packing fraction of the butanol beads in the target cup of about 60 \sim 65%. Although the scattering events from $^3He/^4He$ are significantly smaller (due to the density difference) than the events from the bound nucleon portions of the butanol target, they also contribute to the background events in the butanol target region. Therefore the non-polarizable bound nucleons in the butanol target region include: bound nucleons in hydrogen, carbon, and oxygen part of the butanol, bound nucleons in $^3He/^4He$ coolant, and bound nucleons in any other materials in the target system.

To study the background events of butanol target and use for background subtraction, two additional targets, carbon and polythene (CH_2), were placed downstream of the main target as illustrated in Fig. 54.

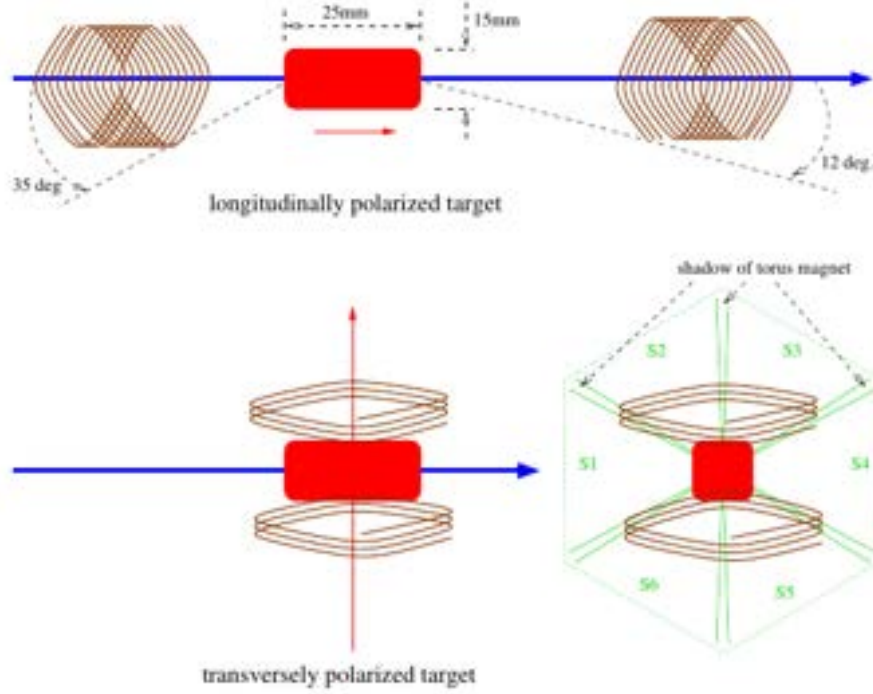


Figure 31: Schematic of a frozen-spin target with holding coils for longitudinal and transverse polarization; red arrows indicate the polarization direction and blue arrows indicate the beam direction. [77].

The frozen spin target is polarizable both longitudinally and transversely; in this analysis, the target was longitudinally polarized as shown in Fig. 31(a). DNP applies the brute force polarization:

$$P = \tanh\left(\frac{\vec{\mu} \cdot \vec{B}}{kT}\right), \quad (51)$$

where P , $\vec{\mu}$, \vec{B} , k , and T are polarization, magnetic moment of ensemble of free electrons, magnetic fields, Boltzmann constant and temperature, respectively [93]. To achieve the highest polarization possible, one should aim to maximize the field, \vec{B} and minimize the temperature, hence the name “FROzen Spin Target (FROST)”. Major components of the FROST polarizing system are a 5 T superconducting polarizing magnet, a dilution refrigerator with high cooling capacity, an inserting device to load the target into the dilution refrigerator, a superconducting holding magnet, a

140 GHz microwave system for DNP technique, and a nuclear magnetic resonance (NMR) system to measure the target polarization [93]. The polarizing system, apart from the 5 T polarizing magnet, was mounted on an insertion cart, which could be inserted into CLAS to have the target positioned at the CLAS center.

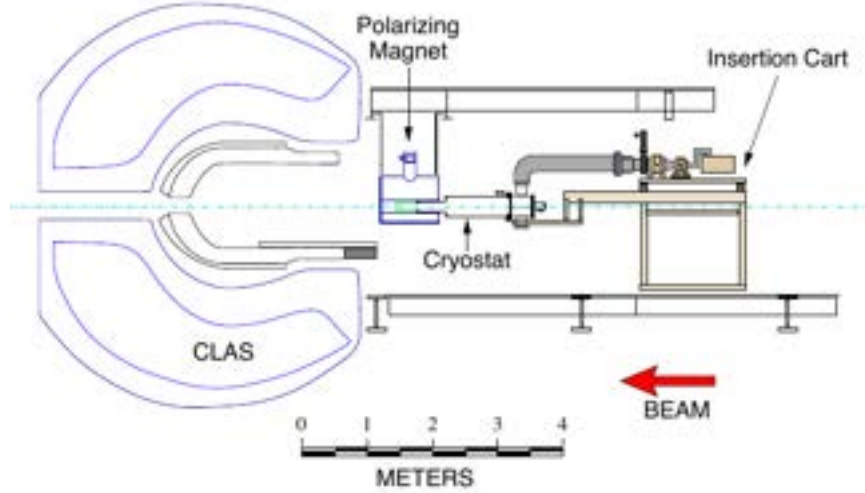


Figure 32: Schematic diagram of the target polarization process with the 5 T superconducting magnet before insertion into the center of CLAS [93].

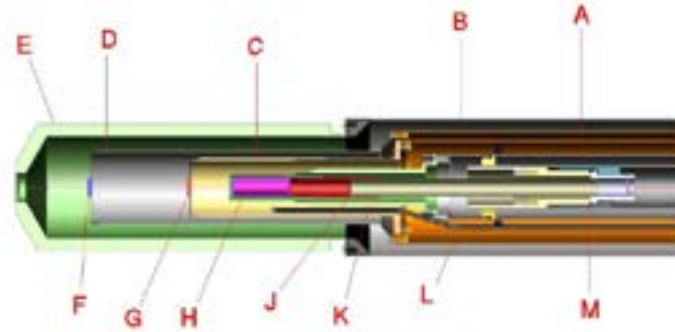
First step of the DNP is to maintain the FROST target at 0.3 K using dilution refrigerator and under magnetic field of 5.0 T using the polarizing magnet (Fig. 34(a)) which is placed 0.57 m away from the center of the CLAS as shown in Fig. 32. At this stage, target's electron spins are completely polarized. Secondly, the polarized butanol target is placed under microwaves near the Electron Spin Resonance (ESR) frequency, allowing the transfer of polarization from the electron's spin to the nucleon spin. Depending on whether the frequency is set slightly below or above ESR frequency, nucleon's spin are polarized either parallel or anti-parallel to direction of the magnetic field. After polarization is complete, the target is further cooled down to about 30 mK to improve the relaxation time of the polarization. Additionally a holding magnet of 0.5 T field in beam axis direction (Fig. 35(b)) is assigned to improve the relaxation time. The dilution refrigerator was continuously turned on during the experimental

runs to ensure the temperature of 30 mK, which operated at 800 μ W. With lowered temperature and holding magnetic field, polarization decay was less than 1% per day [96]. In Fig. 34(b), a picture of the holding magnet coils is shown which was inserted into the CLAS center with the target as its width is thin enough to not interfere with scattered particles from the reactions.

The target polarization is measured via the Nuclear Magnetic Resonance (NMR) technique. Under the influence of the polarizing magnet, a proton's spin will precess, like a spinning top, but at a characteristic resonant frequency. When a radio wave is swept in the frequency over this resonance, The polarized protons will depolarize and begin precessing inphase, which can be detected with an antenna. The total response on the antenna, integrating over the frequency sweep, is proportional to the target polarization [93]. The measurements on the target polarization during the FROST experiments are plotted in Fig. 35 where the relaxation time was about 2,000 hours as indicated by the downward slope over the experiment runs in 7 separate run periods.



(a)



(b)

Figure 33: (a) Photograph of butanol target cup where butanol beads are placed. (b) Side view of FROST target where beam enters from left to right. (A) Primary head exchanger, (B) 1 K heat shield, (C) Holding coil, (D) 20 K heat shield, (E) Outer vacuum cup, (F) Polyethylene target, (G) Carbon target, (H) Butanol target, (J) Target insert, (K) Mixing chamber, (L) Microwave waveguide, and (M) Kapton cold seal. [94].

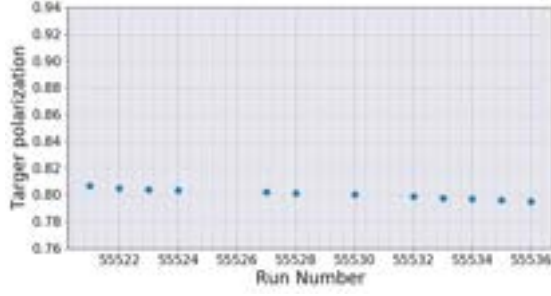


(a)

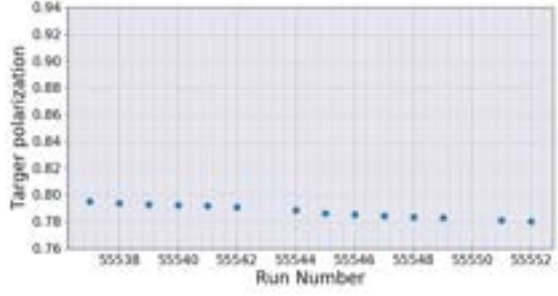


(b)

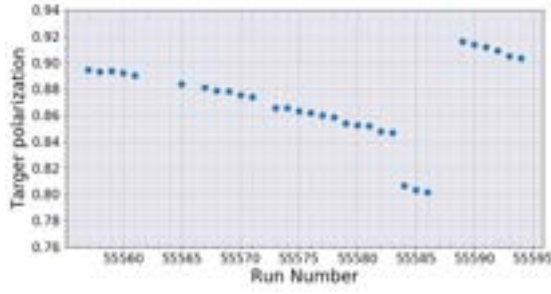
Figure 34: (a) The polarizing magnet with magnetic field of $\vec{B} = 5.1 \text{ T}$ and the bore size of 127 mm. (b) The holding magnet with magnetic field of $\vec{B} = 0.32 \text{ T}$ and dimensions of $\text{Ø}(40 \times 355) \text{ mm}$ [94].



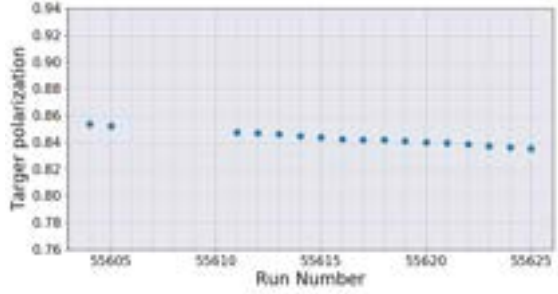
(a) Run period 1: 55521 - 55536



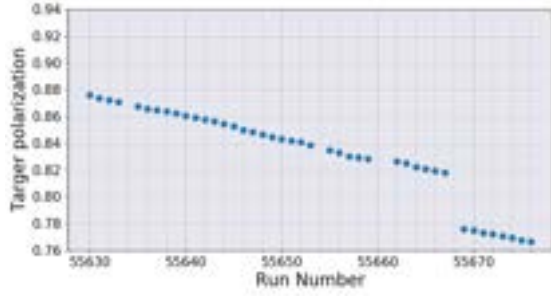
(b) Run period 2: 55537 - 55552



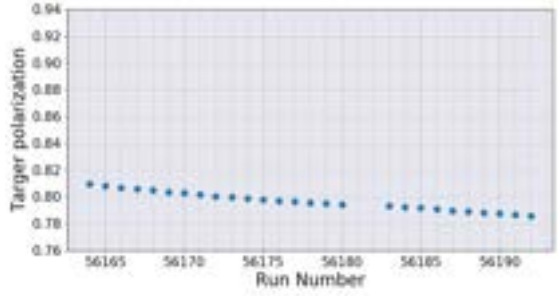
(c) Run period 3: 55557 - 55594



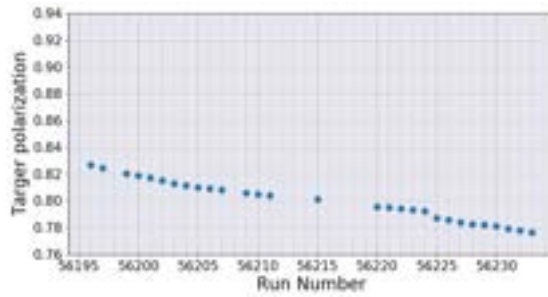
(d) Run period 4: 55604 - 55625



(e) Run period 5: 55630 - 55678



(f) Run period 6: 56164 - 56193



(g) Run period 7: 56196 - 56233

Figure 35: Target polarization versus the run number in each of run periods. The sudden drops of target polarization in (c) and (e) indicate the pause of the experiment for a brief period of time and resuming without re-polarizing the target.

2.4.2 Circularly Polarized Photon Beam

Circularly polarized photon beams with energy E_γ are produced as longitudinally polarized electron beam of energy E_e from the CEBAF interacts with a thin gold foil bremsstrahlung radiator. The degree of photon's circular polarization P_γ depends on the degree of electron polarization P_e and the ratio of photon and electron energy $x = \frac{E_\gamma}{E_e}$ [95]:

$$\begin{aligned} P_\gamma &= P_e \frac{4x - x^2}{4 - 4x + 3x^2}, \\ \sigma_{P_\gamma}^2 &= \sigma_{P_e}^2 \left[\frac{4x - x^2}{4 - 4x + 3x^2} \right]^2. \end{aligned} \tag{52}$$

Therefore, to achieve highly polarized photons for the experiment, incoming photons with less energy transferred x needed to be filtered out. As a way to refine the photon beam, the existing collimator (radius = 1 mm), positioned 16 m from the CLAS center, is used to remove unwanted charged particles and reduce photon flux cross section [77]. Also, the angular spread of unfiltered bremsstrahlung photon beam is larger than the size of our target, hence, photon beam aperture could be reduced without losing good physics events. As a result, the collimation reduced the flux of initial bremsstrahlung photon beam by 32% for $E_e = 1.6$ GeV and 47% for $E_e = 2.4$ GeV.

The electron beam polarization measured by Møller polarimeter in the function of experiment run numbers are shown in Fig. 37 and Table 13. The details of Møller polarimeter can be found in Ref. [105]. The fluctuations in each measurement were larger than their statistical uncertainties due to unknown systematic effects or significant changes in the electron beam polarization [108]. For this analysis, the standard deviation of all Møller measurements ($\sigma(P_e) = 0.033$), as indicated by the shaded regions in Fig. 37, are used as an estimate of the uncertainty in electron beam polarization.

In order to perform a Møller measurement, the experiment had to be stopped

completely which resulted in a loss of good beam delivery time. The reasoning behind the frequency of Møller measurements performed during the FROST experiments were not provided in the experiment database.

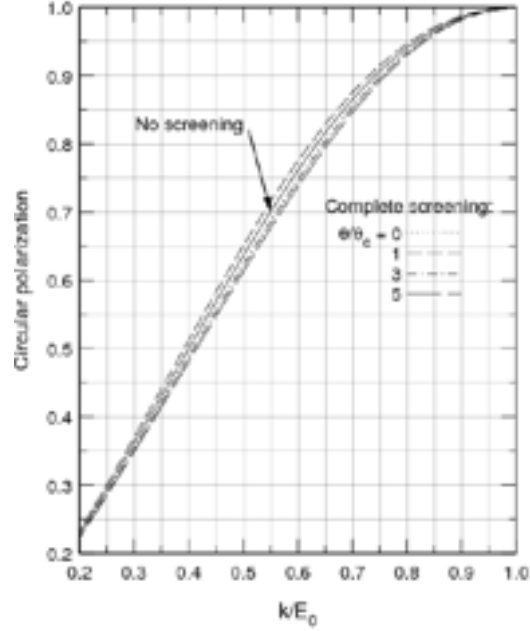


Figure 36: Circular polarization as a function of the photon energy k and electron energy E_0 [95].

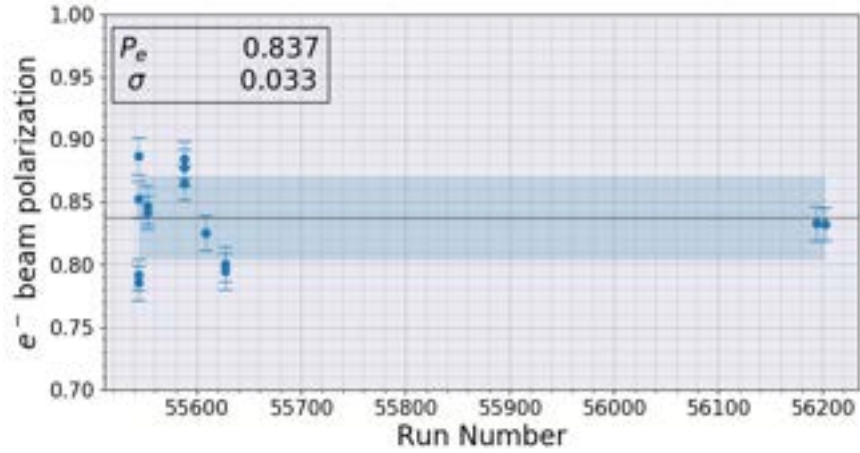


Figure 37: Electron beam polarization measured by the Møller polarimeter. Indicated by a black solid line is the average and shaded region indicates one standard deviation. The run numbers in between 55700 to 56100 are empty runs with no beams.

Beam Energy	Run Number	Møller Measurement (%)	Run Range
1.645 GeV	55544	85.228 ± 1.420	55521 - 55552
		-78.523 ± 1.350	
		-79.150 ± 1.26	
		88.700 ± 1.480	
	55552	84.167 ± 1.330	55537 - 55552
		-84.725 ± 1.530	
	55588	-86.531 ± 1.380	55557 - 55594
		88.409 ± 1.440	
		87.753 ± 1.480	
2.478 GeV	55608	-82.534 ± 1.400	55604 - 55625
	55627	-79.450 ± 1.410	55627 - 55678
		80.060 ± 1.400	
	56194	-83.267 ± 1.380	56164 - 56194
	56202	-83.248 ± 1.320	56196 - 56233

Table 13: Degree of circularly polarized photon beam polarization measured by Møller polarimeter for 7 run periods with different target polarization and beam helicity setups [96].

Run Period	Avg. BCA	σ
1, 2, 3	7×10^{-4}	1×10^{-3}
4, 5	3×10^{-5}	3×10^{-3}
6, 7	1×10^{-3}	4×10^{-3}

Table 14: The average of the beam charge asymmetry (BCA) for each experiment period [96].

3 Data Analysis I - Event Selection

The CLAS g9a/FROST data consists of multiple channels (Fig. 38) and its feature of measuring everything under the same controlled conditions allows for better constraints for PWA. Among other double polarization observables from FROST experiments, we will extract the helicity asymmetry E in the $\gamma p \rightarrow \pi^0 p$ reaction with circularly polarized photon beam of $E_\gamma = 0.4 - 2.4$ GeV and longitudinally polarized proton targets [75]. The extracted helicity asymmetry E will be compared to experimental results from CBELSA/TAPS Collaboration and PWA predictions from the SAID, MAID, and BnGa groups.

Approximately three billion physics events were collected on circularly polarized photons during the FROST/g9a experiment, and the analysis of such a huge amount of data was partitioned into four main steps to minimize the computational cost and maximize the purity of the data: raw data reconstruction (Sec. 3.2), event selections (Sec. 3.4 – Sec. 3.10), Machine Learning applications (Sec. 4), and finally determination of helicity asymmetry E (Sec. 5).

3.1 Overview of Event Selection

Of the measured three billion physics events, two body reactions $\gamma p \rightarrow pX$ where only one outgoing proton is measured, are selected for further analysis. The hypothetically undetected particle X 's missing mass squared (M_X^2) are reconstructed using the kinematics of incoming photons and outgoing protons. Considering the conservation of the 4-momentum, M_X^2 is expressed via:

$$(p_X)_u(p_X)^u = M_X^2 = (E_\gamma + m_{p1} - E_{p2})^2 - (\vec{p}_\gamma - \vec{p}_{p2})^2, \quad (53)$$

where p_X , M_X , E_γ , m_{p1} , E_{p2} , and \vec{p}_{p2} are the undetected particle's four-momentum, reconstructed missing mass of the undetected particle, incoming photon energy, mass of a proton, energy of the recoil proton, and momentum of the recoiling proton. The

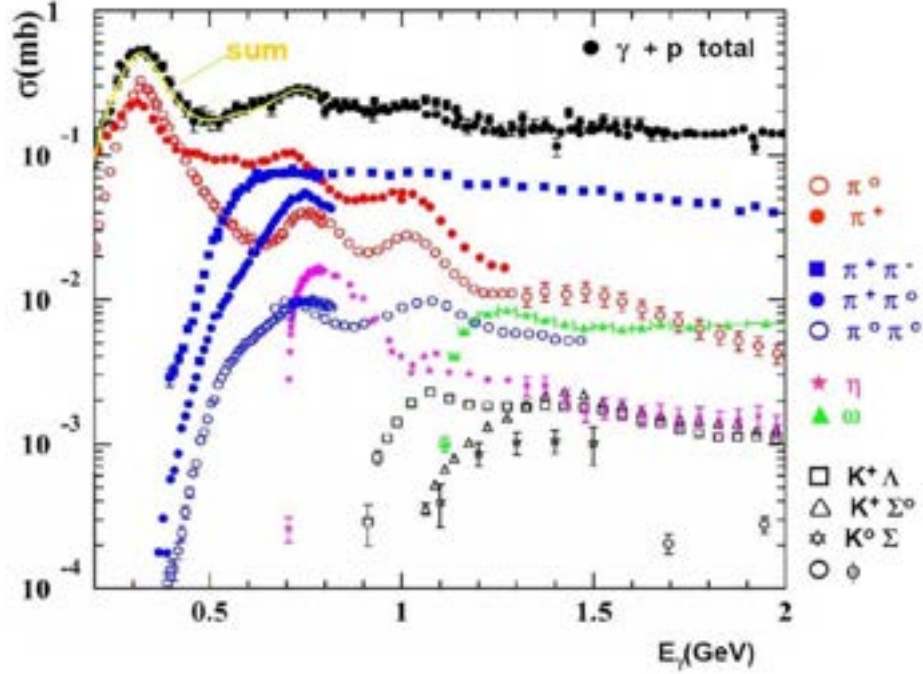


Figure 38: Cross sections for all channels of γp reactions. Image source: [39].

procedures of selecting physics events relevant to our $\gamma p \rightarrow \pi^0 p$ reaction channel are outlined below in the order of its implementations:

1. Raw Data Reconstruction (Sec. 3.2)
 - Choose which variables (Table 15) are needed for the analysis and which data banks (specific data structure for CLAS) are suitable for $\gamma p \rightarrow \pi^0 p$
2. Initial reaction channel filtering (Sec. 3.3).
3. Energy loss correction - Account for particles' loss of energy while traveling inside the butanol target, target wall, carbon cylinder, and the start counter (Sec. 3.4).
4. Momentum correction - Account for misalignment in drift chambers and uncertainties in magnetic field-map (Sec. 3.4).
5. Fiducial selections (Sec. 3.5).

- Inactive CLAS regions - Remove events which have reconstructed event vertex positions in inactive regions of the CLAS detector such as gaps in between sectors and the beam hole.
 - Low momentum selection - Exclude recoiling protons with $\mathbf{p} \leq 350 \text{ MeV}/c$ for $\theta_{lab} > 35^\circ$ and $\mathbf{p} \leq 400 \text{ MeV}/c$ for $\theta_{lab} < 35^\circ$.
 - Inefficient Time-of-Flight paddles - Remove events detected in malfunctioning paddles of time-of-flight detector.
6. Proton selection - Remove all charged particles except protons (Sec. 3.6).
 7. Photon Identification - Among tagged photons, choose the best photon that has the arrival time at the target location closest to the event reaction time (Sec. 3.7).
 8. Hydrogen Contamination - Classify and remove the build up of ice in carbon target via Machine Learning techniques (Sec. 4).
 9. Transverse event vertex selection - Exclude events in ^3He bath far outside of the target cup ($\geq 2 \text{ cm}$) (Sec. 3.8).
 10. Z -vertex selection - Select only events within tight ranges of each target to safely deduce the target type of the reaction (Sec. 3.8).
 11. π^0 missing mass squared selection - Compute the missing mass squared and identify the undetected neutral pions by using measured kinematics of detected photons and outgoing protons (Sec. 3.10).

Software Tools for FROST Data Analysis

- ROOTBEER (ROOT-based) software [115] for initial data skimming and filtering out unwanted reaction channels.

- ELOSS package [121] for particle energy loss calculations.
- Momentum correction routine from [123] for misalignment in drift-chamber and magnetic field-map uncertainties.
- Uproot package [116] for converting root files into python environments.
- Pandas [117], numpy [118], and scipy [119] packages for data wrangling.
- Tensorflow [120] for application of Machine Learning.

3.2 Raw Data Reconstruction

As outgoing particles interact with the CLAS detectors, the raw signals are read in whichever form each detector subsystem outputs. The raw signals consisted of the TDC (time to digital converter), ADC (analog to digital converter), QCD (charge to digital converter) channels IDs and values, and any other sub-detector specific information. The first task, so called “cooking”, is the process of converting these raw signals into physical quantities (E_γ , \vec{p} , \vec{x} , PID, *etc.*) for further analysis. After filtering out unwanted hits in detectors, readings from each detector subsystem are matched to find candidates of particles that belong to the same physics events. To account for misalignment within and between detectors, the data obtained from each detector undergo calibration processes. The raw signals then undergo calibration from each sub-detectors to account for any misalignment within the sub-detector and the alignments of signals passed between each sub-detectors. The calibration is an iterative procedure where any improvement of one sub-detector requires corresponding changes in the next sub-detector’s calibration values. For the FROST experiment, the order of calibration performed was as follows:

- Photon tagging system aligns timing from T- and E-counters to RF beam signal [99, 100].

- The Time-of-flight system corrects time and hit positions at which the outgoing particle interacted with the scintillator bars [102].
- Start counter corrects the timing signals for each paddle [101].
- Drift chambers optimize the reconstruction of charged particles' tracks [103].
- Electromagnetic calorimeter optimizes reconstruction of energy and time measurements of detected electrons and neutral particles [104].

After calibrations and reconstruction of particle kinematics, the cooking phase is complete and the converted physical quantities of each particle interaction are stored in various data banks (CLAS data structure) as shown in Table 15. Different kinds of data banks are designed to store specific information; for example, TAGR bank stores information about incoming photons and SCPB bank stores outgoing particle's information from the Time-of-Flight detector. The following analysis utilized *HEAD*, *EPIC*, *EVNT*, *MVRT*, *GPID*, *TAGR*, *SCPB*, and *TESC* banks.

The MVRT bank reconstructs event vertex positions by using the drift chamber hit positions and time information. A 5 dimensional linear fit with the following parameters are done to extrapolate the trajectory toward the center of CLAS: position in the beam axis (z), perpendicular distance from the beamline (d_0), charge/momentum (q/p), deflection away from the midplane in beam axis (azimuthal), and deflection towards or away from the beam line (polar angle). For single track events, MVRT then calculates the distance of the extrapolated trajectory's closest approach to the measured center of the beam.

The GPID bank identifies particles on a track by track basis [122]. First, the particle's measured momentum (p_{dc}) from the drift chambers with all possible particle identities (m_X) are used to compute possible values of $\beta_c = \frac{p_{dc}}{\sqrt{p_{dc}^2 + m_X^2}}$. Each value of β_c is compared to the measured value of β_m from the Time-of-flight system (Eq. (59a)) to identify the particle. The GPID algorithm then attempts to find a photon which

have interacted with the particle by going through the tagging system. The required banks to build GPID bank are the following: TAGR, STR, TDPL, SCRC, PART, TBID, and TBTR.

Quantity	Bank	Min/Max	Description
E_γ (GeV)	<i>TAGR</i>	[0, 12]	Closest photon energy
PID	<i>GPID</i>	[0, 100]	Particle ID (GEANT)
E (GeV)	<i>GPID</i>	[0, 16]	Energy of outgoing particle
p_x (GeV/c)	<i>GPID</i>	[-16, 16]	Momentum in x (lab frame)
p_y (GeV/c)	<i>GPID</i>	[-16, 16]	Momentum in y (lab frame)
p_z (GeV/c)	<i>GPID</i>	[-16, 16]	Momentum in z (lab frame)
β_c	<i>GPID</i>	[-1, 1]	$\frac{ \vec{p} }{E}$
β_m	<i>GPID</i>	[-1, 1]	Beta from Time-of-Flight detector
mass (GeV)	<i>GPID</i>	[0, 1000]	Mass from Time-of-Flight detector
sc_time (ns)	<i>GPID</i>	[-1000, 1000]	Arrival time at Time-of-Flight detector
sc_len (cm)	<i>GPID</i>	[-1000, 1000]	Distance between event vertex to TOF counter
ntrk	<i>MVRT</i>	[-100, 100]	Number of tracks used to make event vertex
x -vertex (cm)	<i>MVRT</i>	[-1000, 1000]	X position of event vertex
y -vertex (cm)	<i>MVRT</i>	[-1000, 1000]	Y position of event vertex
z -vertex (cm)	<i>MVRT</i>	[-1000, 1000]	Z position of event vertex
ScPdHt	<i>SCPB</i>	[0, 100000]	10000*sector + 100*SC_PD_ID + HitID in SCR
TRIGBITS	<i>HEAD</i>	[0, 9999999]	Trigger Latch Word (16 bits)
NRUN	<i>HEAD</i>	[0, 100000]	Run Number
DCstat	<i>EVNT</i>	[0, 50]	Pointer to DCPB banks (=0 if drift chamber not involved)
SCstat	<i>EVNT</i>	[0, 50]	Pointer to SCPB banks (=0 if TOF not involved)

Table 15: The physical quantities derived from raw signals and associated data bank names.

3.3 Initial Reaction Channel Filter

Among all possible reaction channels produced from $\gamma + p$ as seen in Fig. 38, initial selection for $\gamma p \rightarrow \pi^0 p$ was carried out by ruling out events that have particle kine-

matics and identifications that are less likely from $\gamma p \rightarrow \pi^0 p$. The initial skimming routine contains the following:

1. Select only events with good photon candidates that might have initiated the photoproduction; good photon candidates contain reading from both E- and T-counters of the tagger in agreement that one or more unambiguous hits are reconstructed in the tagging system [99]. Keep good photon candidates for further photon identification step to choose the most likely photon that is involved in the reaction (Section 3.7).
2. Select only the events with positively charged outgoing particles which will include e^+ , π^+ , K^+ , and protons.
3. Select events with valid readings in the Time-of-Flight system and drift chambers to ensure the events' timing measurements and hit position measurements (x -, y -, and z -vertex positions). Events with invalid readings refer to events from miscalibration or malfunctioning parts of the subdetector.
4. Compute or extract needed kinematics (momentum, energy, angles, *etc.*) of incoming photons and outgoing particles from selected data banks.

3.4 Energy Loss and Momentum Correction

Energy Loss Correction

The charged particles lose energy while moving through matter by interacting with the electrons of atoms in the target or any other materials. The interaction either excites or ionizes the atoms, hence, the energy loss of the traveling charged particles. The measured four-momentum of protons in drift chambers (DC) does not account for the energy loss while traveling inside the butanol target, target cell wall, mixing chamber, holding coils, the start counter and the air gap between DC Region 1.

The unaccounted energy loss could be substantial in determining the π^0 missing mass, especially for low momentum particles. For example, a heavy dependence of z event vertex positions on the missing mass squared distribution was present inside the butanol target region which is shown by a downward slope in Fig. 41(a). Additionally, the uncorrected missing mass squared of the π^0 calculated from kinematics of incoming photons and outgoing protons is off to about $\sim 0.02 \text{ GeV}^2$ as seen in Fig. 39(c).

The energy loss was corrected by the standard CLAS ELOSS package [121] developed by Pasyuk and is applicable to any charged particles with an electrical charge of 1 and heavier than an electron. Below lists the input and output parameters required to run the ELOSS package:

- Input parameters
 - 3-vector of particle momentum after the Start Counter
 - Particle mass
 - Target material
 - Target thickness
- Output parameters
 - 3-vector of particle momentum at the event vertex

The ELOSS routine first computes the pathlength that the particle traveled in each of the materials (absorber) along the trajectory. Then by using the momentum at which the particle came out of the absorber, computes the energy loss to estimate the momentum at the event vertex by using the Bethe-Block equation [38]:

$$-\frac{dE}{dx} = Kz^2 \frac{Z}{A} \frac{1}{\beta} \left[\frac{1}{2} \ln \left(\frac{2m_e c^2 \beta^2 \gamma^2 T_{max}}{I^2} \right) - \beta^2 - \frac{\delta}{2} \right], \quad (54)$$

where $\frac{dE}{dx}$, A , K , z , Z , T_{max} , I , δ , $x = \rho s$, ρ , and s are mean rate of energy loss (stopping power), atomic mass of the absorber, $4\pi N_A r_e^2 m_2 c^2 = 0.307075 \text{ MeV mol}^{-1} \text{ cm}^2$,

atomic number of incident particle, atomic number of absorber, maximum transferable energy, mean excitation energy, density effect correction to ionization energy loss, mass per unit area, density of absorber, and the length, respectively.

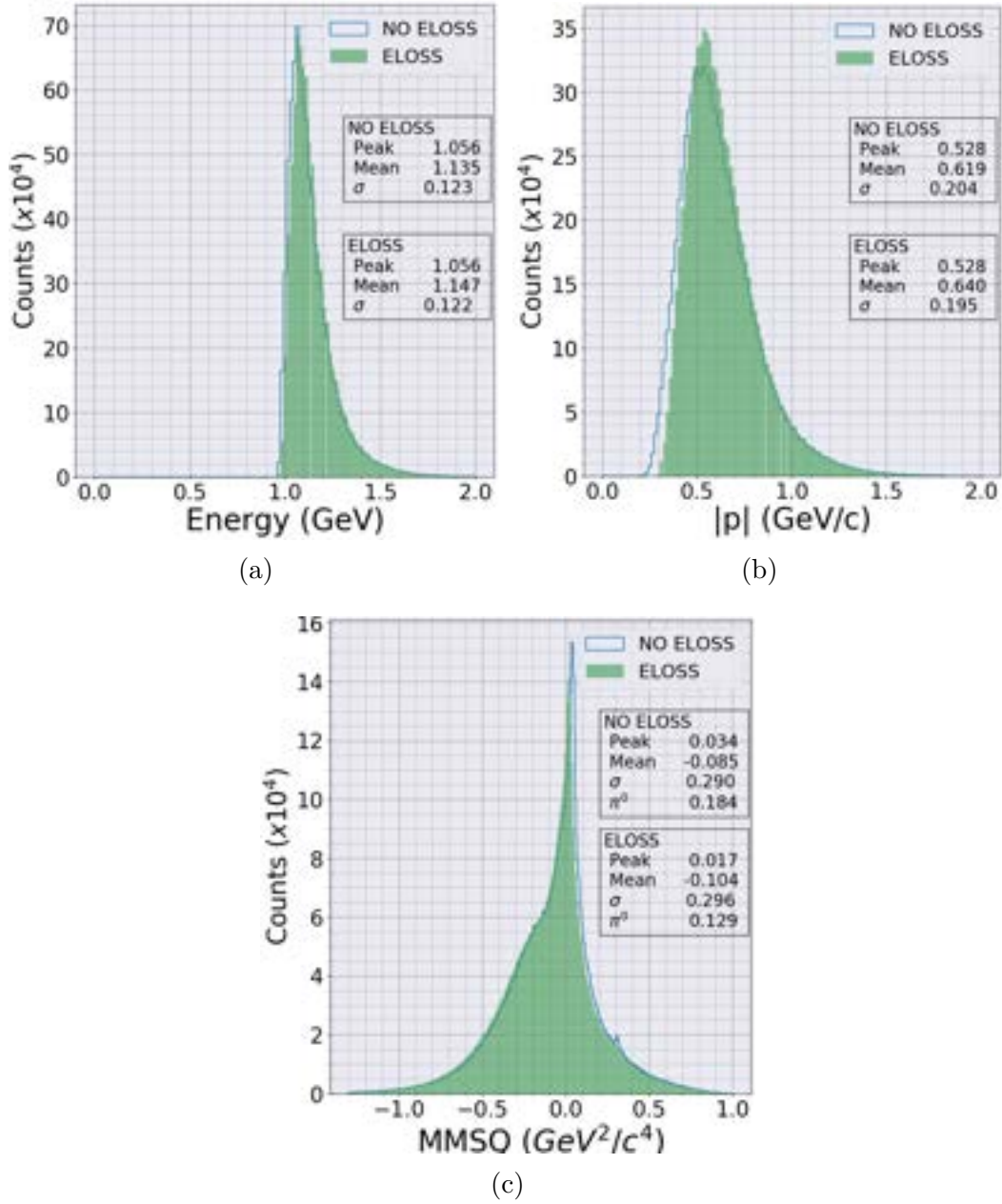


Figure 39: Before (green) and after the energy loss correction (blue) on the protons of $\gamma p \rightarrow Xp$ for (a) Energy of outgoing protons, (b) Momentum magnitude of outgoing protons, and (c) Missing mass squared (M_X^2) of undetected particles

The peak position of missing mass squared distribution has shifted from 0.034 GeV^2 to 0.017 GeV^2 after the correction, which is closer to the actual $M_{\pi^0}^2$ value of 0.018 GeV^2 [38]. As shown in Fig. 40, the most significant changes were applied to particles with momentum less than $\sim 350 \text{ MeV}/c$ which in turn are selectively filtered out depending on their scattered laboratory angles in Sec. 3.5. The energy loss corrections have successfully amended the downward slope inside the butanol target region of the missing mass squared distribution as shown in Fig. 41. Although the corrected missing mass squared distribution in Fig. 41(b) might appear to have a broader width, we can be assured that the actual change in the width of the missing mass squared distribution is negligible as shown in Fig. 39(c)

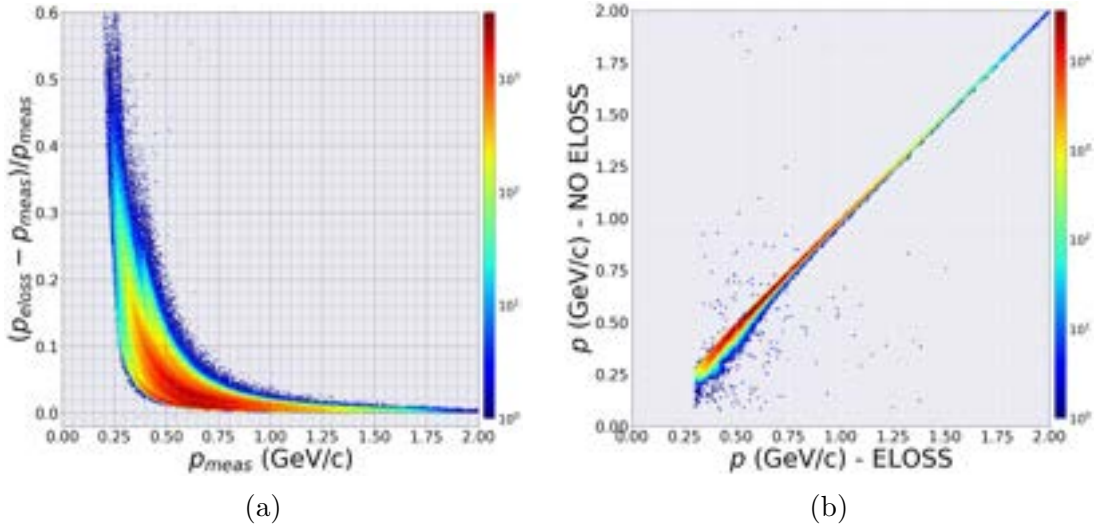


Figure 40: (a) Relative momentum difference after energy loss correction. Particles with momentum less than $\sim 350 \text{ MeV}/c$ are corrected to a greater extent than higher momentum protons during the energy loss corrections. (b) Measured momentum versus energy loss corrected momentum. Particles with momentum higher than $\sim 750 \text{ MeV}/c$ showed insignificant changes after the energy loss corrections.

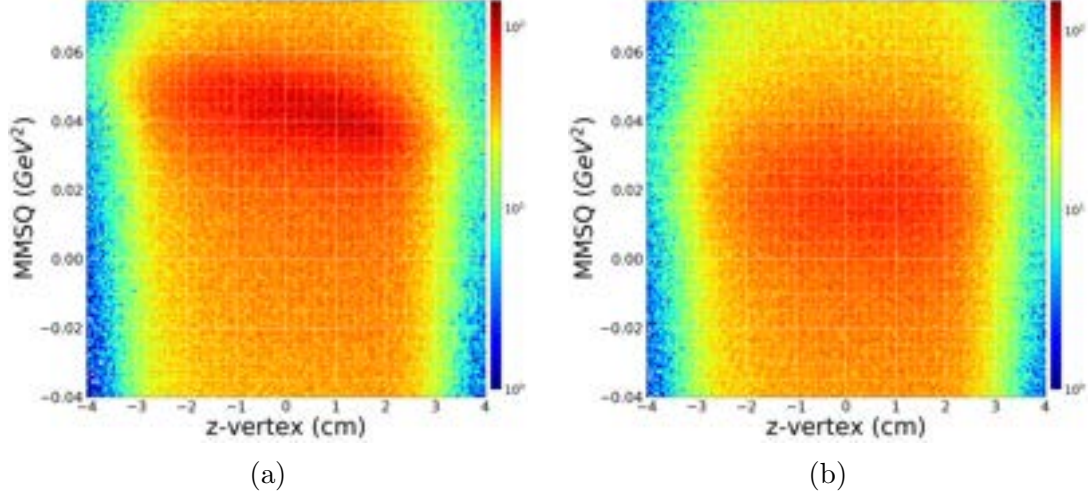


Figure 41: Missing mass squared (M_X^2) of $\gamma\mathbf{p} \rightarrow X\mathbf{p}$ (a) before and (b) after the energy loss correction.

Momentum Correction

A slight dependence on the azimuthal angle was observed in the missing mass squared distribution of $\gamma\mathbf{p} \rightarrow X\mathbf{p}$ as shown in Fig. 42(a, c). Since the reaction should be azimuthally symmetric, such dependence indicates a slight azimuthally-dependent bias in the proton reconstruction. Investigated by a collaborator [108], the azimuthal dependence was present due to uncertainties in magnetic field maps (rapid $\Delta\mathbf{B}$ at sector edges) and misalignment in drift chambers. The momentum correction package discussed here was developed by Ref. [123] using the same data set as ours, but for a different reaction channel, $\gamma p \rightarrow \pi^+ n$. The package corrected for the ϕ dependence of π^+ particles. In the future, the momentum correction package will be updated to correspond to recoiling protons for our reaction $\gamma p \rightarrow \pi^0 p$. This section only serves to present the application of the correction routine to our data set.

The measured momentum of outgoing particles obtained from drift chambers using the curvature of particle trajectories under the torus magnetic field is:

$$p_{dc} = qBR, \quad (55)$$

where q , B , and R are electric charge, magnitude of torus magnet, and radius of curvature.

Another comparable measurement on momentum ($p(\theta_{lab})$) could be carried out by using the outgoing particle's polar angle θ_{lab} , flight time and pathlength between the start counter and time-of-flight system. If we assume the proton's polar angle θ_{lab} is reconstructed correctly, the correction terms for azimuthal angle offsets in π^0 missing mass square distribution could be calculated by the difference of differently obtained momentum:

$$\Delta p = p(\theta_{lab}) - p_{dc}. \quad (56)$$

For a similar reaction channel $\gamma \mathbf{p} \rightarrow \pi^+ \mathbf{n}$, Δp was fitted by Strauch [108] and the same extracted correction terms were used for our analysis. It was evident that two differently measured momentum have significant offsets arising from multiple sources of error. The correction term for such difference was estimated by performing a fit to Δp with a polynomial function [108]:

$$\Delta p = \sum_{n=0}^5 \sum_{m=0}^2 \sum_{l=0}^2 a_{n,m,l}^{n_{sec}} \left(\frac{\theta_{lab}}{180^\circ} \right)^n \left(\frac{\phi_{lab}^{sec}}{30^\circ} \right)^m \left(\frac{p_{dc}}{2 \text{ GeV}} \right)^l. \quad (57)$$

A χ^2 minimization routine was performed to obtain coefficients $a_{n,m,l}^{n_{sec}}$ that minimized Δp and good fits were chosen whose χ^2 values per degrees of freedom were between 1.2 to 1.6. The azimuthal angle ϕ_{lab}^{sec} in each sector ($n_{sec} = 1, \dots, 6$) was defined by:

$$\phi_{lab}^{sec} = \begin{cases} \phi_{lab} - 60^\circ(n_{sec} - 1), & \text{if } \phi_{lab} < 330^\circ \\ \phi_{lab} - 360^\circ, & \text{otherwise.} \end{cases} \quad (58)$$

After applying the correction, although the difference is subtle, one can spot a slight adjustment in azimuthal and scattering angle at $M^2 \approx 0.02 - 0.03 \text{ GeV}^2$ in Fig. 42(b, d) and Fig. 43(b, d). The momentum range, where the corrections were most significant, was $p = [0.40, 0.85] \text{ GeV}$ as seen in Fig. 44. More importantly, the missing mass squared distribution peak was sharpened which allows better extraction of π^0 (Fig. 45).

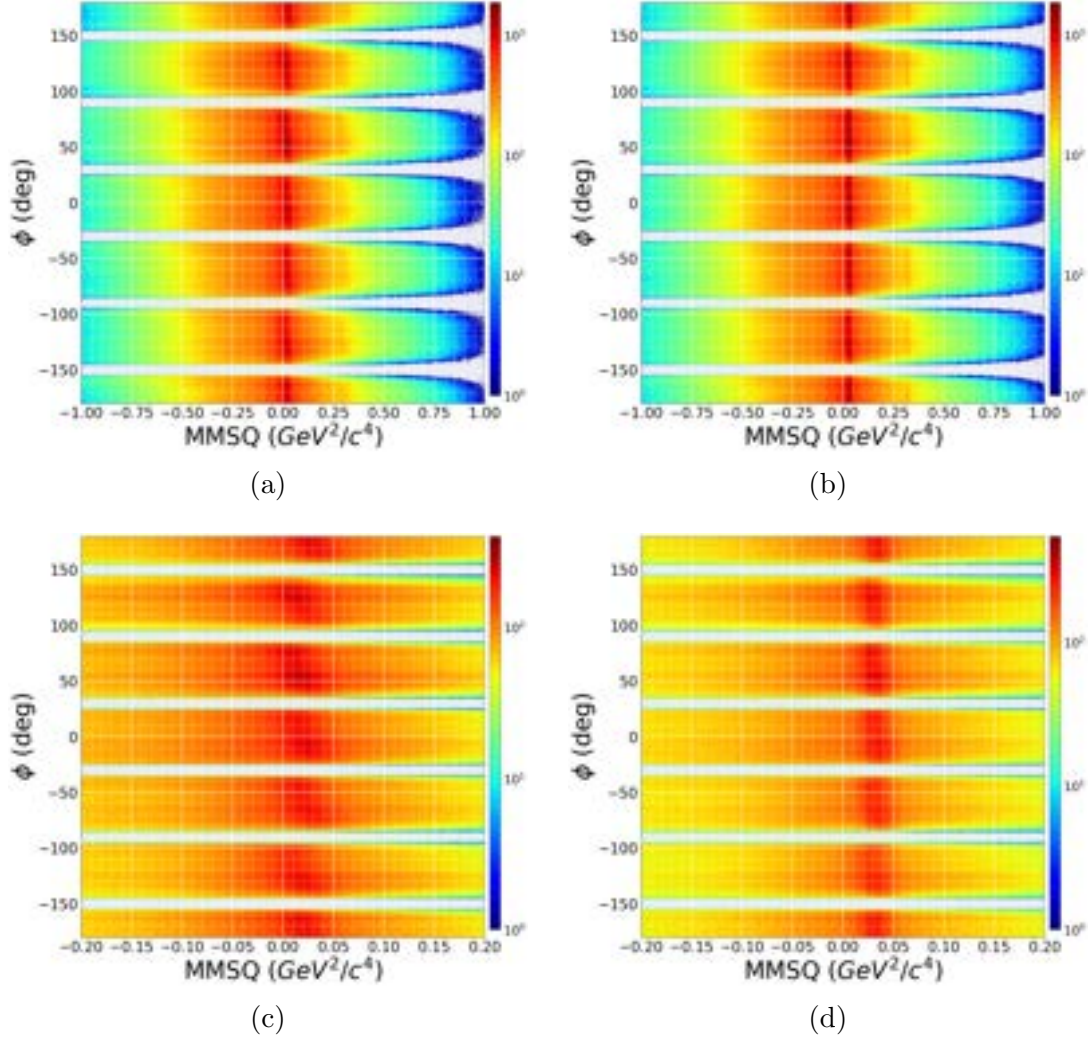


Figure 42: M_X^2 distribution vs azimuthal (ϕ) angle (a, c) before and (b, d) after the momentum correction applied. (c) and (d) show zoomed-in views of (a) and (b) where most corrections were visible.

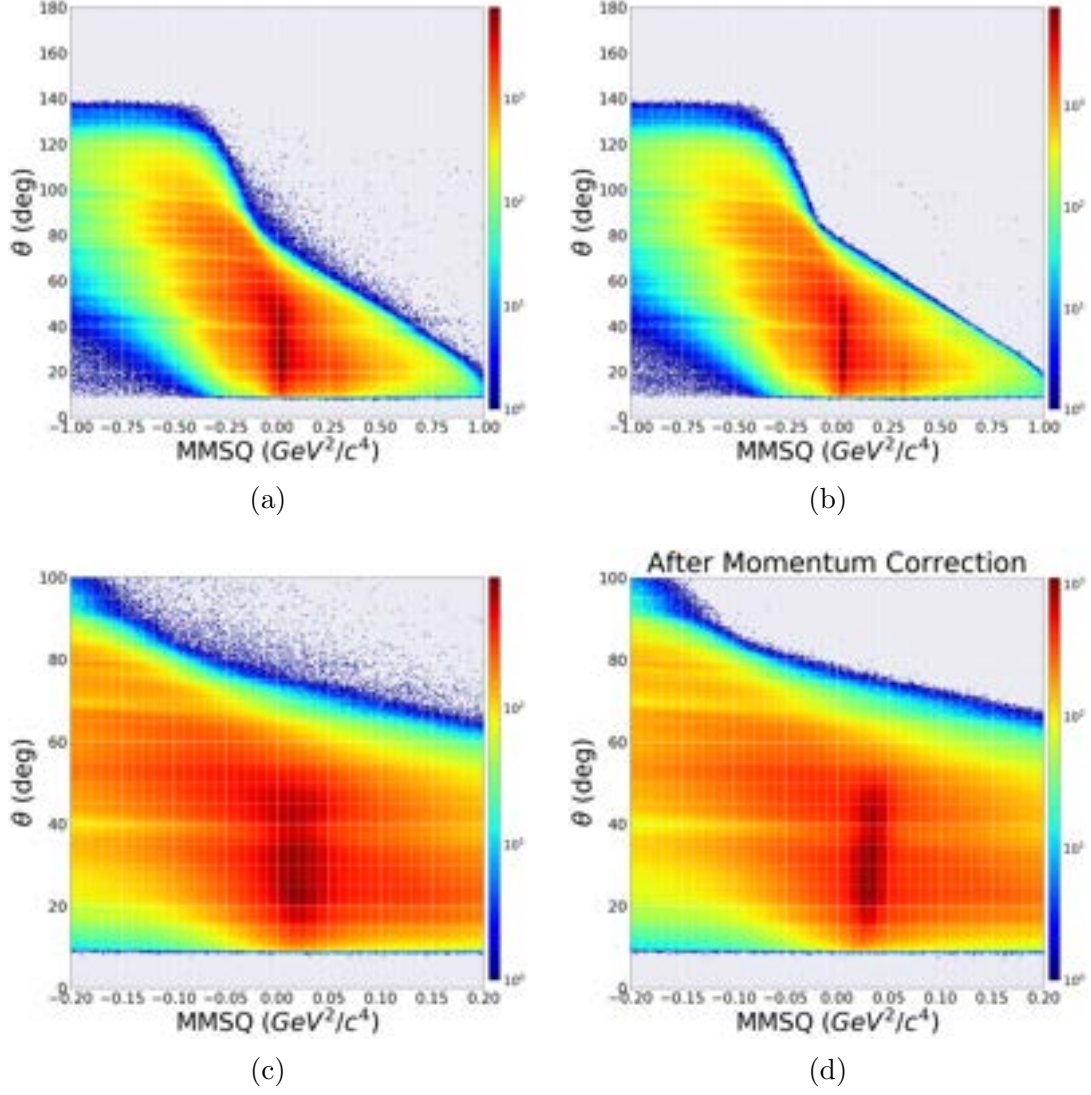


Figure 43: M_X^2 distribution vs scattering (θ) angle (a, c) before and (b, d) after the momentum correction applied. (c) and (d) show zoomed-in views of (a) and (b) where most corrections were visible.

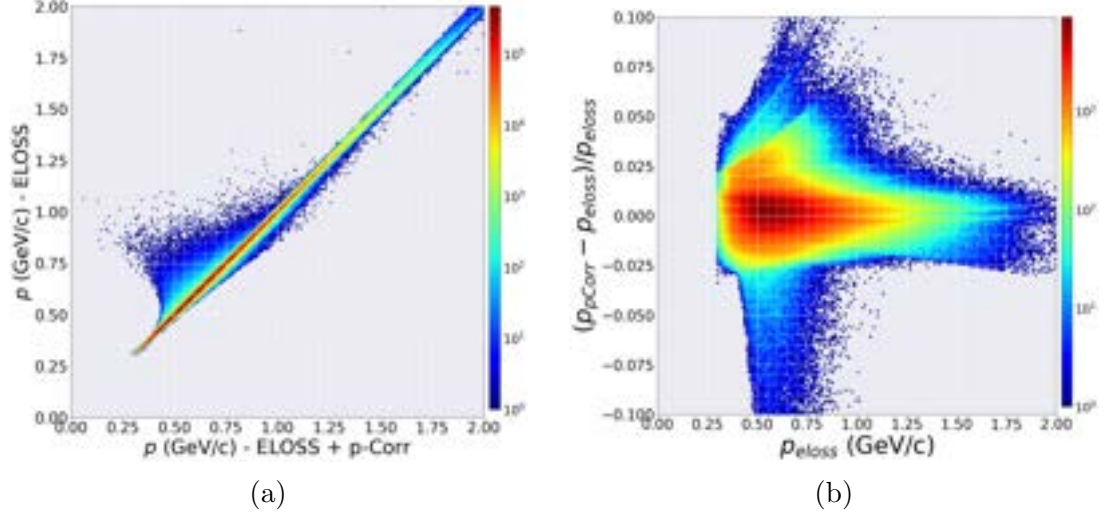


Figure 44: (a) The corrected momentum with ELOSS alone versus corrected momentum with ELOSS and momentum correction. (b) Relative momentum difference between ELOSS and momentum correction and ELOSS.

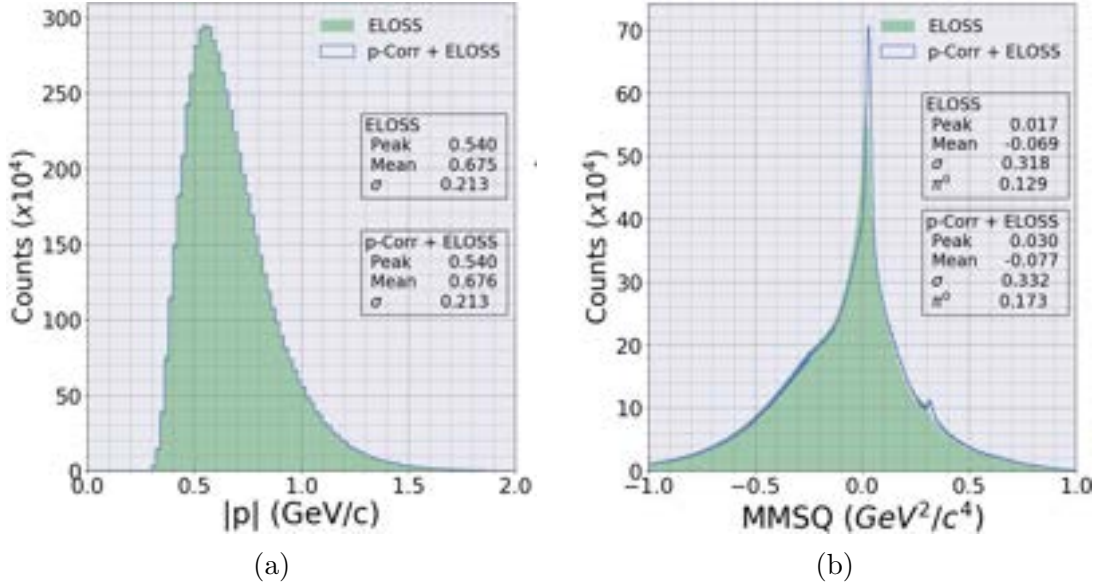


Figure 45: Before and after momentum corrections on the protons of $\gamma p \rightarrow X p$ for (a) momentum magnitude and (b) missing mass squared of X .

3.5 Fiducial Selections

Inactive CLAS region

Regions near superconducting torus coils experience strong magnetic field changes which results in the inaccurate mapping of the field. Events from such regions are removed due to their large systematic uncertainty. In addition, a small opening of the beam line ($\theta_{lab} \leq 7^\circ$) where most events result from interactions are with coils, is removed (Fig 46). The overall removed inactive regions of detectors are:

- $\theta_{lab} \leq 7^\circ$,
- $\phi \in [-155^\circ, -145^\circ] \cup [-95^\circ, -85^\circ] \cup [-35^\circ, -25^\circ] \cup [25^\circ, 35^\circ] \cup [85^\circ, 95^\circ] \cup [145^\circ, 155^\circ]$.

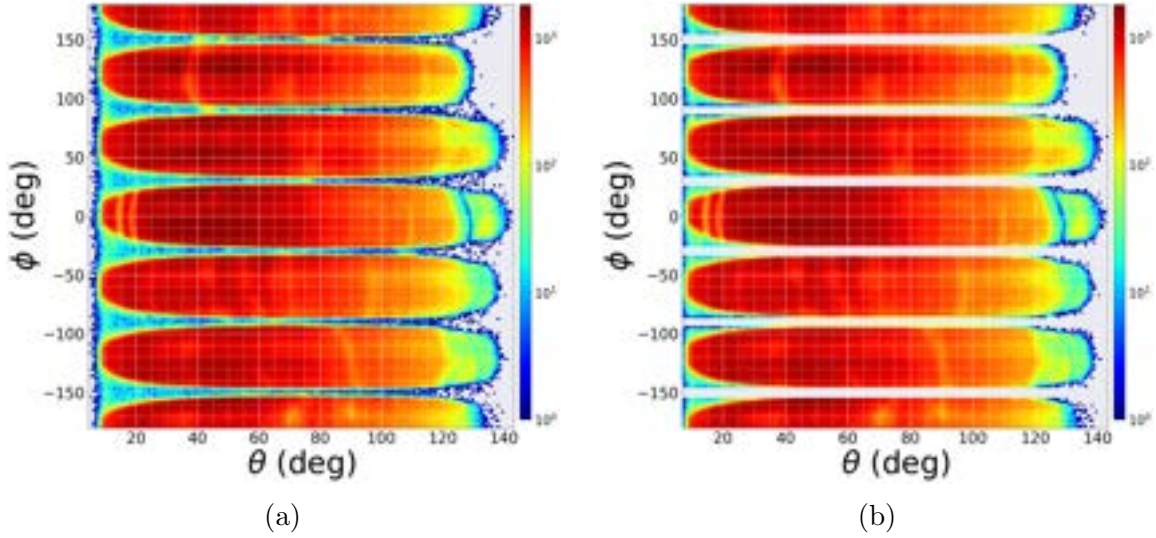


Figure 46: The angular distribution (a) before and (b) after the removal of inactive CLAS regions.

Low Momentum Selection

For protons to reach drift chambers in the CLAS detector, their momentum must exceed $\sim 300 \text{ MeV}/c$. Due to the angular dependence of the detector, such low momentum thresholds varied for different ranges of scattering angles. From Fig. 47, one

can spot sharp discontinuities near $p = 350 \text{ MeV}/c$ and $p = 400 \text{ MeV}/c$ for $\theta_{lab} \geq 35^\circ$ and $\theta_{lab} \leq 35^\circ$, respectively in all energy bins. Also, multiple curved horizontal bands across all distributions are visible, which are a clear indication of malfunctioning in one of the sub-detectors as a significantly low number of events are measured in those bands. One can also notice that the curved bands are initiated where discontinuities are present. Because Time-of-flight system (TOF), Drift chambers (DC), and Start counters (SC) are the only sub-detectors which are involved in measuring charged particles velocity, momentum, and trajectories, one of these sub-detectors is the source of the problem.

If the problem stemmed from malfunctioning TOF scintillator paddles, the bands should have been horizontally straight in θ axis for all momentum values. If any of the SC's scintillator paddles were the source of the problem and if events that interacted with those paddles were discarded, the bands' widths should have been much wider since SC is placed closest to the target and the effects should have been dispersed. Since we know that particles momentum must exceed $p \approx 300 \text{ MeV}$ in order to reach the drift chambers, the discontinuities are the result of low momentum particles failing to reach drift chambers. But for $\theta \geq 35^\circ$, particles with momentum well below $350 \text{ MeV}/c$ reached the drift chambers. The main reason why low momentum protons in forward direction don't get through DC and reach TOF is the stronger magnetic field in that region. Particles with low velocity under stronger magnetic field will deflect stronger: $r = mv/qB$. Additionally, FROST experiment had a holding magnet for the target system that caused a slight deflection in ϕ . If the angle of deflection for these low momentum particle is greater than TOF system's coverage angle of $8^\circ \leq \theta \leq 142^\circ$, they do not have the timing information. Hence, tracking of trajectories of these particles are absent. As for the curved empty bands in horizontal directions shown in Fig. 47, they are known to be the cause of malfunctioning and miscalibrated TOF paddles.

Additionally, the missing mass squared (M_X^2) values for different ranges of momentum values are plotted in Fig. 48 and one can see for events with proton momentum below $p = 300 \text{ MeV}/c$ shows completely difference distributions than the rest of the momentum ranges. In low momentum bins, the major peak locations are positioned approximately at $M_x^2 = 1.4 \text{ GeV}^2$ and π^0 peaks near $M_{\pi^0}^2 = 0.018 \text{ GeV}^2$ were less dominant. According to such observations, low momentum selection ranges were set for two separate polar angle ranges and events under these thresholds were removed:

- $p \leq 350 \text{ MeV}/c$ for $\theta_{lab} \geq 35^\circ$,
- $p \leq 400 \text{ MeV}/c$ for $\theta_{lab} \leq 35^\circ$.

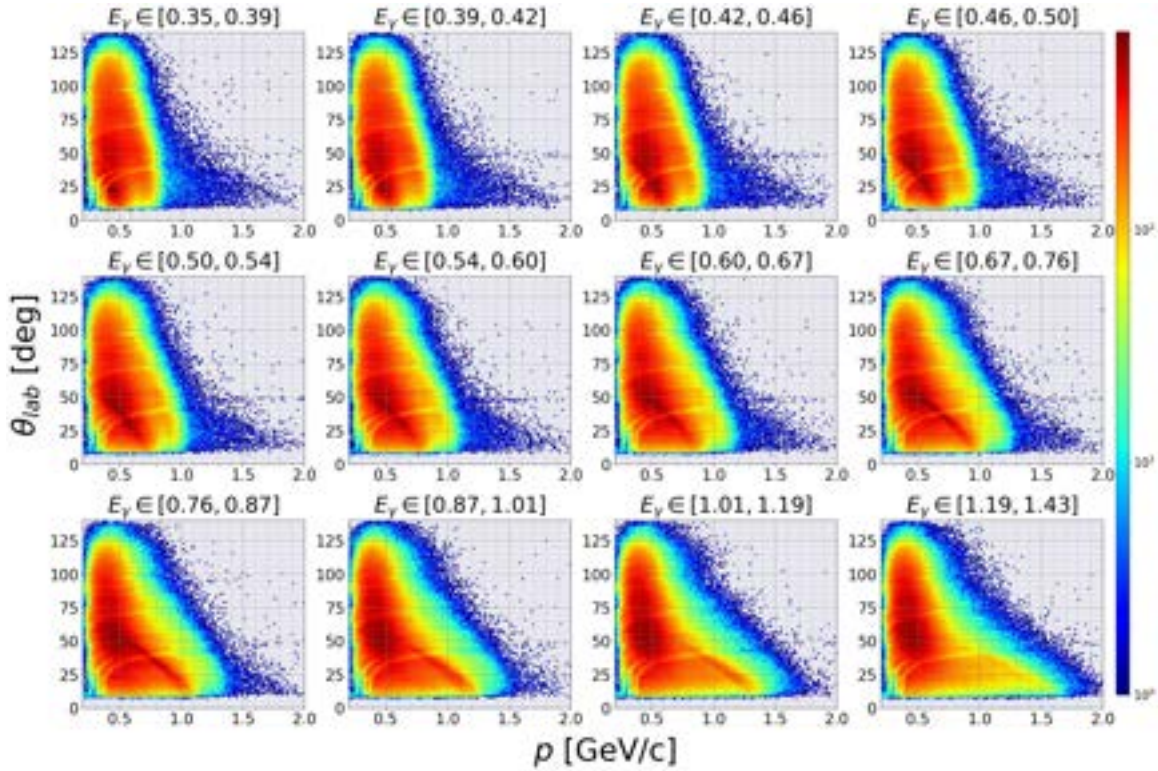


Figure 47: Momentum versus lab angle in partitions of energy bins. The events plotted are prior to applying energy and momentum corrections. E_γ is in units of GeV .

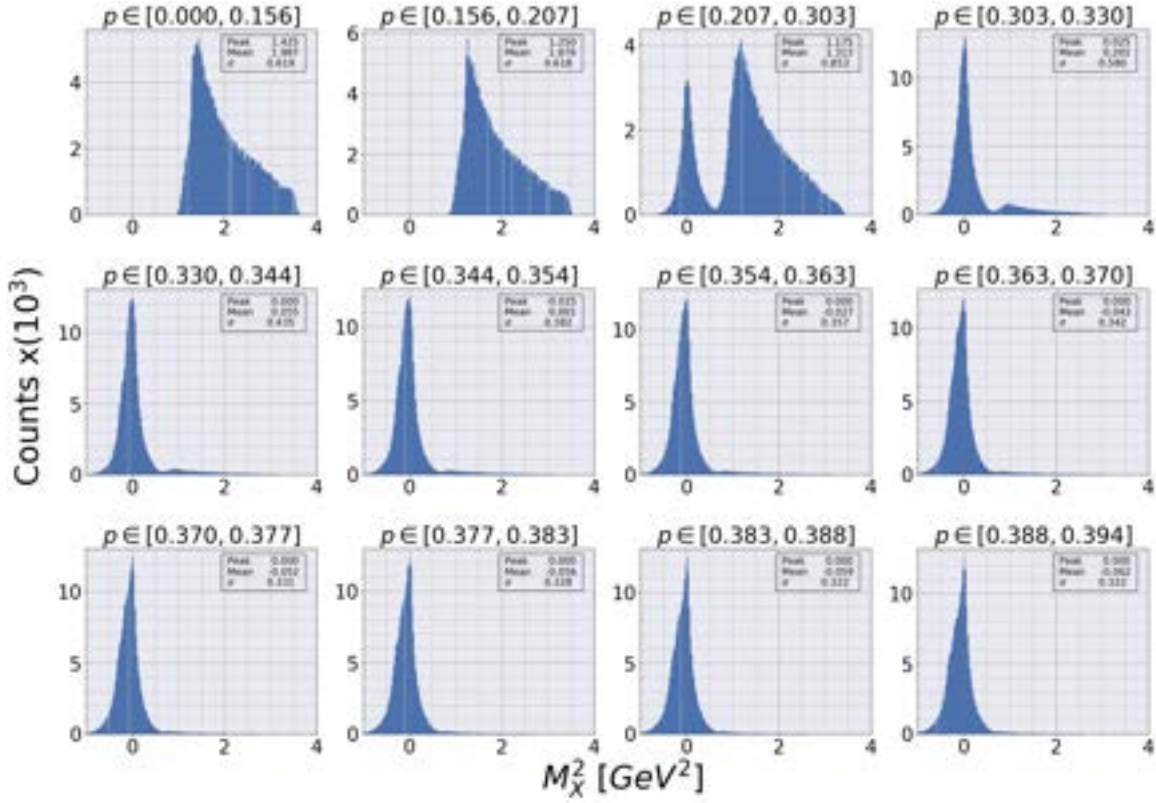
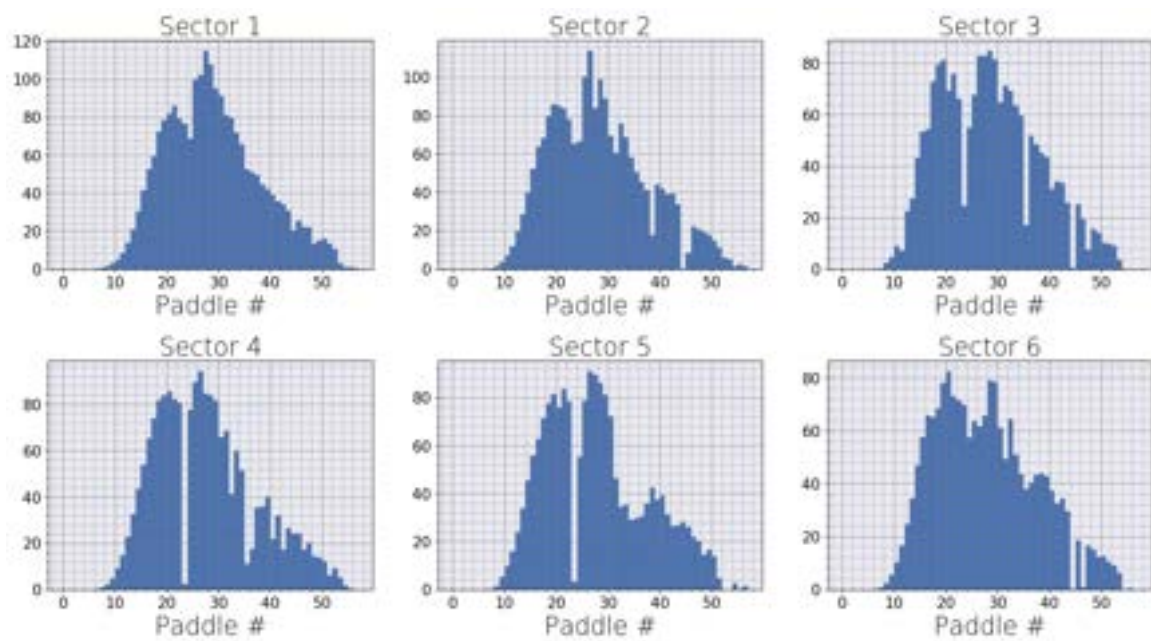


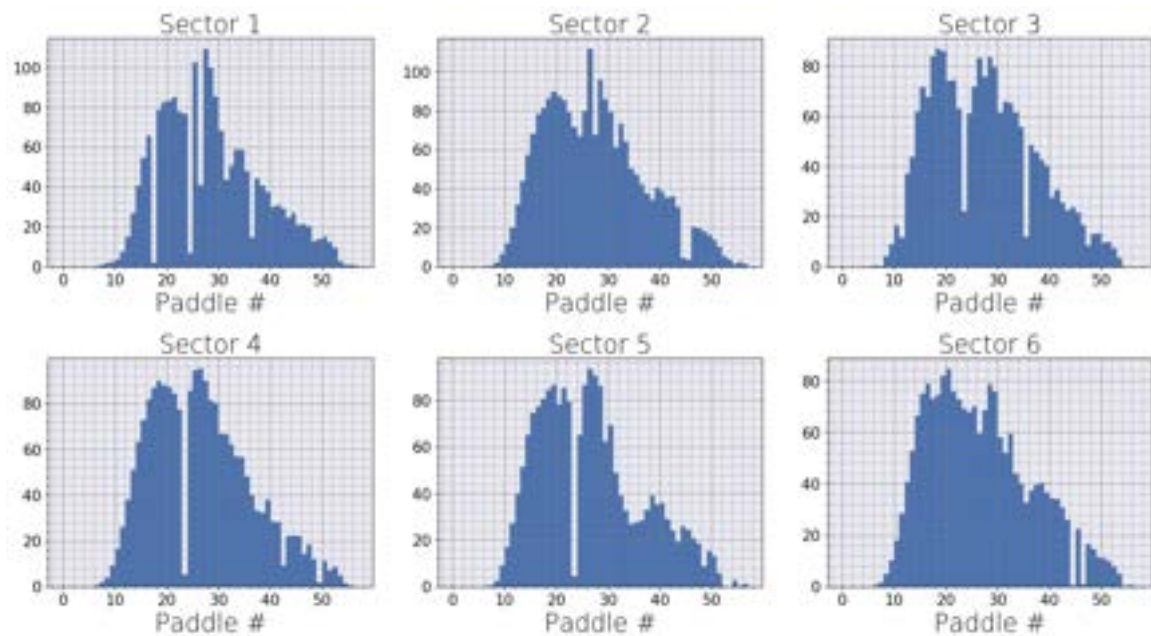
Figure 48: Missing mass squared distribution in partitions of momentum bins. p is in units of GeV/c.

Inefficient Time-of-flight Paddles Selection

Some paddles in the time-of-flight (TOF) system were malfunctioning or even dead, causing events from such paddles to have higher systematic uncertainty. Higher uncertainty in TOF contributes significantly to particle misidentifications by measuring inaccurate β_{meas} . The selection of malfunctioning paddles is determined manually by comparing the event counts of each paddle to the neighboring paddles' event counts. If the event count of a paddle was significantly lower than the neighboring paddles as indicated by empty strips in the distributions shown in Fig. 49, the events having TOF timing measurements from these specific paddles are discarded from further analysis.



(a)



(b)

Figure 49: The event counts in each paddle for 6 sectors of the time-of-flight system: (a) run period 2 and (b) run period 6.

Sector	Removed TOF Paddle	Sector	Removed TOF Paddle
1	None	1	17, 24, 26, 36
2	38, 44	2	44, 46
3	23, 35, 44	3	23, 35
4	23, 32, 35, 36, 40, 42	4	23, 42, 49
5	23	5	23, 52, 53
6	44, 46	6	44, 46

(a) Run periods 1, 2, 3, 4, and 5

(b) Run periods 6 and 7

Table 16: Malfunctioning TOF paddles with low statistics which are removed in the analysis.

3.6 Particle ID: Proton Selection

Particle velocity ($\beta_{meas} = \frac{v}{c}$) was measured by using information from the Time-of-flight system (TOF) and the Start counters (SC) whereas another particle velocity β_{calc} was calculated using the invariant mass of the proton $m_p = 0.93827$ GeV and measured proton momentum from the drift chambers. The difference between these two proton velocities is used for filtering out charged particles other than protons. First, β_{meas} (Eq. (59a)) was calculated by dividing the pathlength between the hit position of SC to the hit position of TOF over the time-of-flight in-between them. β_{calc} (Eq. (59b)) was computed using measured momentum from drift chambers and assuming the particles to be protons.

$$\beta_{meas} = \frac{\text{pathlength between hit positions of SC and TOF}}{\text{flight time between SC and TOF}}, \quad (59a)$$

$$\beta_{calc} = \frac{p}{E} = \frac{p_{dc}}{\sqrt{p_{dc}^2 + m_p^2}}, \quad (59b)$$

where m_p^2 is the proton mass and p_{dc} is measured momentum from the drift chambers. The $\Delta\beta$ distribution ($\beta_{meas} - \beta_{calc}$) provides a way to sort out positively charged single track events that are not protons. Since β_{calc} was calculated with proton mass, events further away from $\Delta\beta = 0$ are less likely to be protons. Events within $|\Delta\beta| < 0.06$ were chosen as proton candidates for the next steps of analysis as shown in Fig. 50(a). As a result (Fig. 50(c)), we can see clear extraction of protons among all other positively charged single track events (e^+ , π^+ , deuteron, *etc.*). As an alternative method, one could have set upper and lower bounds to the middle curve in Fig. 50(b) and select out non-proton events outside of the set bounds. Such method requires two manually set bounds which adds an additional systematic uncertainty in setting the bounds.

The resolution for reconstructing path length was dependent on the drift chamber tracking resolution and the accuracy of the mapping of the magnetic field, but independent of the timing resolutions from the TOF and Start counter system. The CLAS achieved a path length resolution of ≈ 1 cm, and this is less significant than the impact of timing resolution on the particle identification. Nevertheless, the β selection in determining the particle identification was based on the total β resolution, factoring in contributions from all sources.

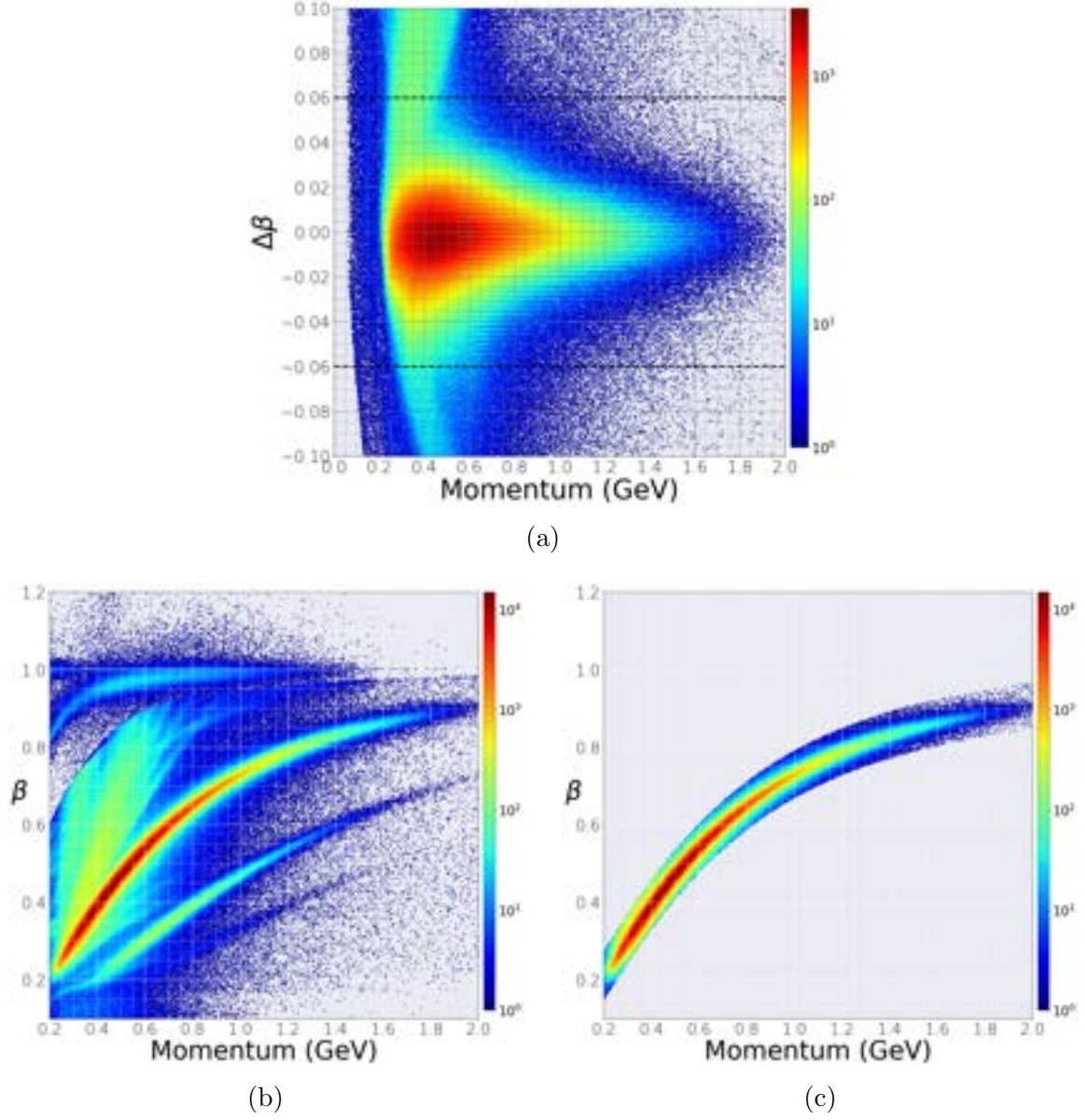


Figure 50: (a) $\Delta\beta$, (b) β before selection, and (c) β after selection as a function of momentum of the positively charged particles assuming proton mass.

3.7 Photon identification

Photons that most likely have caused the measured π^0 photoproduction reaction are identified by observing the time difference of the arriving photons and recoil protons at reconstructed z -vertex positions. Since electron beam bunches are separated by

2.004 ns intervals, we need to filter out photons (Section 2.2) whose arrival time lies outside of a ± 1 ns interval of the reaction time of the proton at the reaction vertex. For each triggered event, the tagger information is stored for all photon candidates, which have coincident hits in E- and T-counters. Such photon candidates are marked by a 7 or 15 in the status variable of the TAGR bank to indicate good quality photons. The initial photon filtering, which is done at the skimming stage to reduce the file size, computes the time differences, Δt , of all good photon candidates relative to the reaction time and selects the photon with the smallest Δt :

$$\Delta t = t_{v,\gamma} - t_{v,p} = \left(t_\gamma + \frac{z}{c}\right) - \left(t_{p,sc} - \frac{l_{sc}}{\beta_{calc}c}\right), \quad (60)$$

where $t_{v,\gamma}$, $t_{v,p}$, t_γ , z , $t_{p,sc}$, l_{sc} , and β_{calc} are arrival time of photon at the event vertex, reaction time of recoil proton at the event vertex, arrival time of photon at the CLAS center, z -vertex position from MVRT bank, arrival time of recoil proton at TOF counter, distance from the event vertex to the hit position on TOF counter, and calculated β assuming proton mass (Eq. (59b)), respectively.

Even after initial photon filtering, about 2% of the selected photons that fit best to the event time are from incorrect electron beam bunches. Fig. 51(a) shows Δt for the best selected photons as a function of the recoiling proton momentum, and the neighboring peaks outside of ± 1 ns interval indicate events with incorrect photon selections. Such events are removed from further analysis.

In addition, about 3% of the total events had multiple good photons that all reside inside ± 1 ns interval, belonging to the same correct electron beam bunch. In this analysis, we simply discarded those events which resulted in the loss of approximately 3% of the total data, following the same approach taken by two previous FROST analyses [97, 108]. One thing to be assured about the method of simply discarding 3% of the total events is that the discarded events are evenly distributed for each of the helicity states since the helicity flip occurred at a high frequency of 30 Hz.

For high rates of tagged-photon pile-up, the standard approach is to use off-time photons ($\pm > 1$ ns) to estimate and subtract on-time background. Since the pile-up rate in this experiment was small, such an approach was not used. Again, the background contribution of the main peak is evenly distributed between two helicity states due to frequent helicity flips during the experiment.

The tagging ratio, which is the fraction of tagged photon in the tagger that have actually reached the target position, was about 0.8, measured by a device called the total absorption shower counter (TASC); the efficiency of TASC is reported to be essentially 100% [85]. However, TASC only operated at low beam currents (< 100 pA). During higher beam currents, the secondary monitor was used to measure the tagging efficiency and they were cross-calibrated against the TASC at low beam currents. The secondary monitoring was reported to provide absolute efficiency of only a few percent [78].

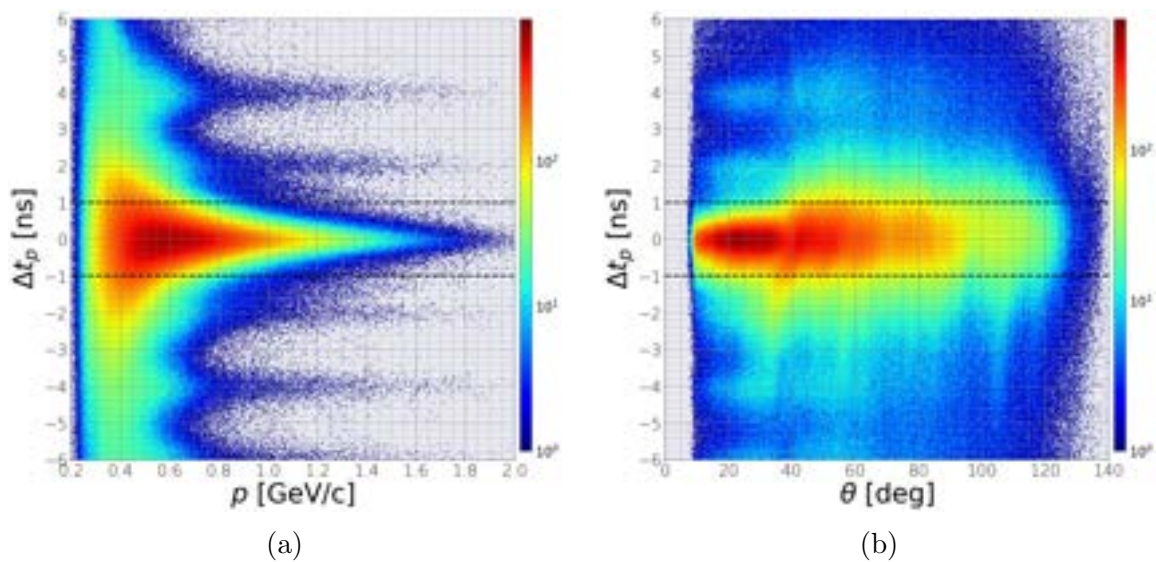


Figure 51: Δt as a function of (a) momentum and (b) scattering angle in laboratory frame before removal of any events with bad photon selections. The dotted black lines indicate at which the selections are made.

3.8 Event vertex selection

To correctly reconstruct the event vertex position of π^0 photoproduction, many algorithms have been developed by the g9a/FROST collaborators. For this analysis, MVRT (multi-track vertex fitting) bank is utilized for event vertex coordinates where all tracks in the corresponding events are used. For our reaction $\gamma p \rightarrow \pi^0 p$ only the four-momentum of the recoiling proton is used and the four-momentum of the π^0 is reconstructed. Thus the MVRT routine for single charged tracks is utilized. In this case, MVRT calculates the distance of the closest approach (tracks from drift chambers) to the measured center of the beam, which also accounts for small beam offset.

3.8.1 Transverse vertex selection

The butanol, in the form of 2 mm diameter beads, is contained within a 1.5 cm diameter target cup as shown in Fig. 52(b). Hence, any events lying outside of the target cup region are from the photons scattering on $^3\text{He}/^4\text{He}$ solution in the dilution refrigerator which is used for cooling the butanol target (Fig. 53). Another possible source for the events outside the target cut is simply from the incorrect event vertex tracking.

As seen in Fig. 52(a), a substantial number of events lie outside of the physical geometry of the target cup which amounts to approximately 3% of the total events. To safely account for possible uncertainties in the reconstruction of event vertex positions from MVRT bank, a selection range slightly larger than the actual target cup size is used; events within a circle of 1 cm radius, $((x - x_{max})^2 + (y - y_{max})^2) < (1 \text{ cm})^2$, are kept for further analysis. The location of the bin that contained the largest number of events in the 2 dimensional histogram of x and y hit positions shown in Fig. 52(a) was estimated to be at $x_{max} = -0.13 \text{ cm}$ and $y_{max} = -0.18 \text{ cm}$.

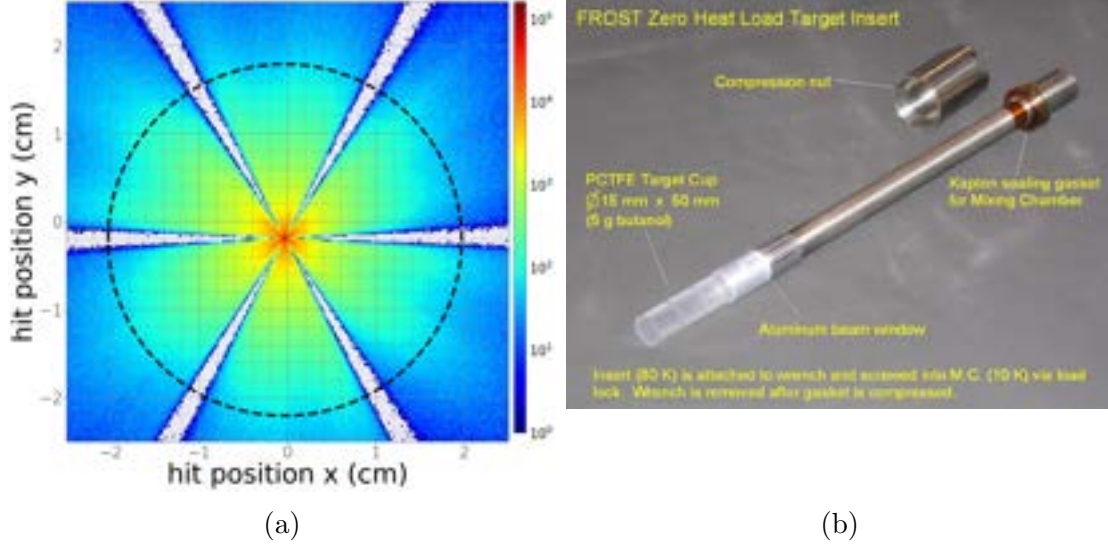


Figure 52: (a) Reconstructed (x, y) event vertex positions for run period 1. The maximum of the distribution is at $(-0.13 \text{ cm}, -0.18 \text{ cm})$ and the events outside of the circle of radius $r = 1 \text{ cm}$ are removed from further analysis. (b) Picture of butanol target cup of 1.5 cm diameter [93].

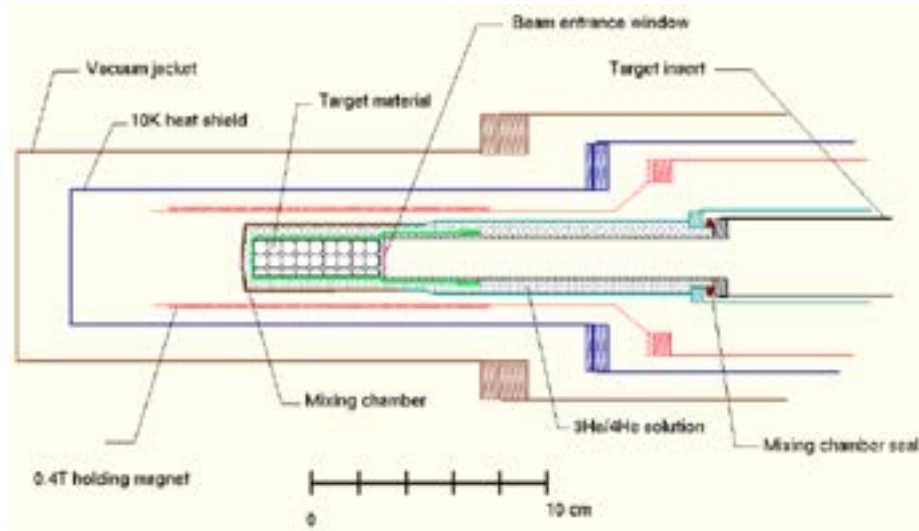
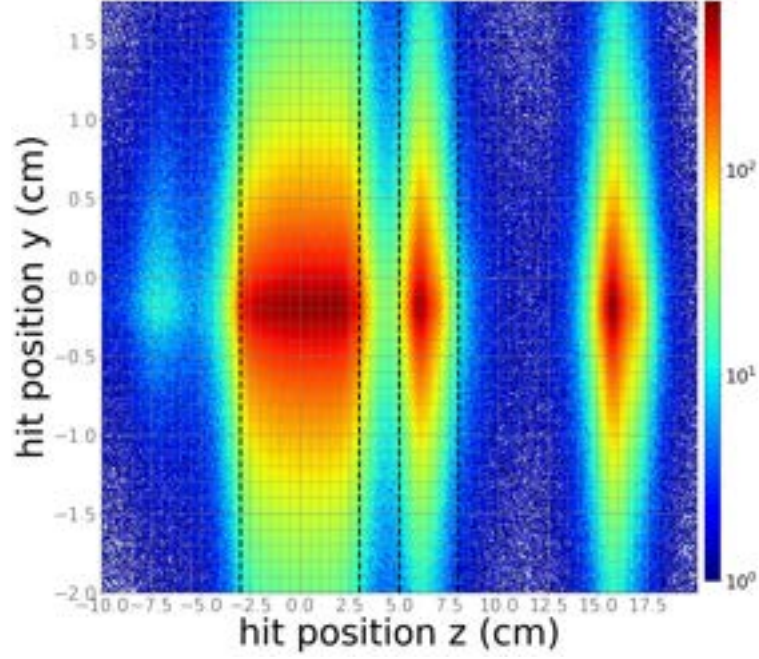


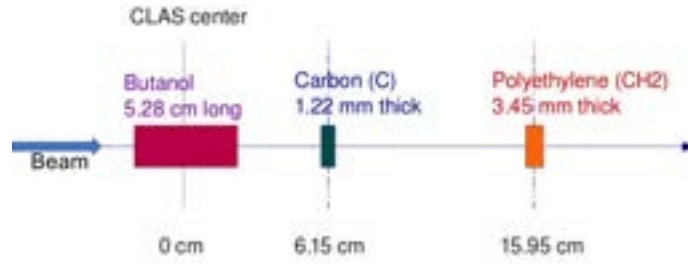
Figure 53: Schematic of FROST target side view where the $^3\text{He}/^4\text{He}$ solution surrounds the butanol target cup (highlighted in green). Image source: [94].

3.8.2 Z -vertex selection

To correctly identify the target types (butanol (C_4H_9OH), carbon (C), or polythene (CH_2)) that photons interacted with, z event vertex locations from tracking need to be matched to actual target locations. From Fig. 54(a), one can see three dense areas which we can associate to physical target locations (Fig. 54(b)). For the purpose of the current analysis, only butanol and carbon events will be utilized. Since the purpose of placing carbon targets was to scale it to butanol events and to correspond it to the nonpolarizable bound nucleon part of butanol targets for background subtraction (Sec. 5.1), it is essential to have only the carbon events without any mixture of butanol events or contamination with any free nucleon sources (Sec. 4).



(a)



(b)

Figure 54: (a) The reconstructed y and z event vertex positions. (b) The schematic picture of FROST target layout.

Target	z -vertex min	z -vertex max
Target	(cm)	(cm)
Butanol	-3	3
Carbon	5	8

Table 17: Z -vertex selection range for butanol and carbon targets.

Butanol z -vertex selection range

The target cup, in which the butanol target in the form of small beads ($r = 1$ mm) were placed, was about 5.28 cm in length. However, to account for possible uncertainty in tracking, a range slightly larger than the actual target size was selected to filter out events not originated from butanol. The objective of the study was to find the z -vertex position at which raw asymmetry and known kinematic values start to diverge from the expected values: all events within $z_{vtx} = [-4, 4]$ are partitioned into $\Delta z = 0.1$ cm bins for the following study. With respect to the z -vertex positions, raw helicity asymmetry E was calculated which is prior to any background subtraction done, as shown in Fig. 55(a). Raw asymmetries are, therefore, expected to have been heavily diluted with background, but an overall sign of the asymmetry was expected to match the theoretical predictions and other experimental results. It is known that in the ranges of $E_\gamma \in [0.84, 1.27]$ GeV and $\cos \theta_{cm} \in [-0.97, 0.]$, the asymmetry is expected to yield a negative value of E ; such negative results are also confirmed in the final result, see Fig. 84. One can see from Fig. 55 that at roughly about $z = -3$ cm and $z = 3$ cm, raw asymmetry E converges to zero, indicating the absence of polarized free nucleons. Additionally, the mean of M_X^2 are examined and as shown in Fig. 55(b), the M_X^2 mean starts to deviate from the mode value approximately at $z = -3$ cm and $z = 3$ cm. We could have selected a tighter region for butanol to achieve a higher free nucleon ratio to bound nucleons for the expense of a good amount of statistics. More systematic studies on the choice of selection range will be conducted in the future.

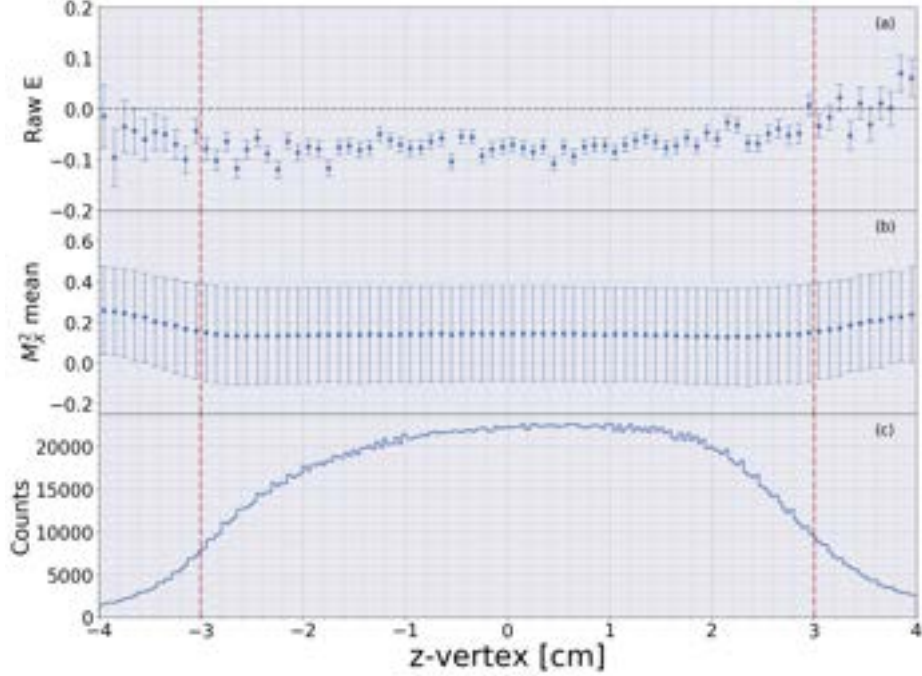


Figure 55: The reconstructed z event vertex positions for $\gamma p \rightarrow p\pi^0$ candidates vs (a) raw asymmetry E , (b) Missing mass squares (M_X^2) mean, and (c) hit counts on z -vertex positions. Plotted events are in photon energy range $E_\gamma \in [0.84, 1.27]$ GeV and angular range of $\cos\theta_{cm} \in [-0.97, 0.0]$.

Carbon z -vertex selection range

For carbon events, a selection range of $z = [5, 8]$ cm is chosen. Even though, the carbon target was only 1.22 mm thick, a significant portion of carbon events were dispersed in the region $z = [5, 8]$ cm as shown in Fig. 57. As discovered in other analyses on the same carbon data, hydrogen contamination was spotted on the carbon data and diluting the carbon target with unwanted free nucleon targets [123]. The location of hydrogen contamination was examined by comparing M_X^2 distributions of events in various ranges of z -vertex positions. Ice, having a characteristic of a sharp peak in M_X^2 distribution, was visible in events in z -vertex ranges of $[6, 7.5]$ cm, suggesting potential formation of ice on the carbon target. See Fig. 56 for details. Such evidences on the possible location of hydrogen contamination will be used in Sec. 4, where a Machine Learning technique will be employed to classify ice from

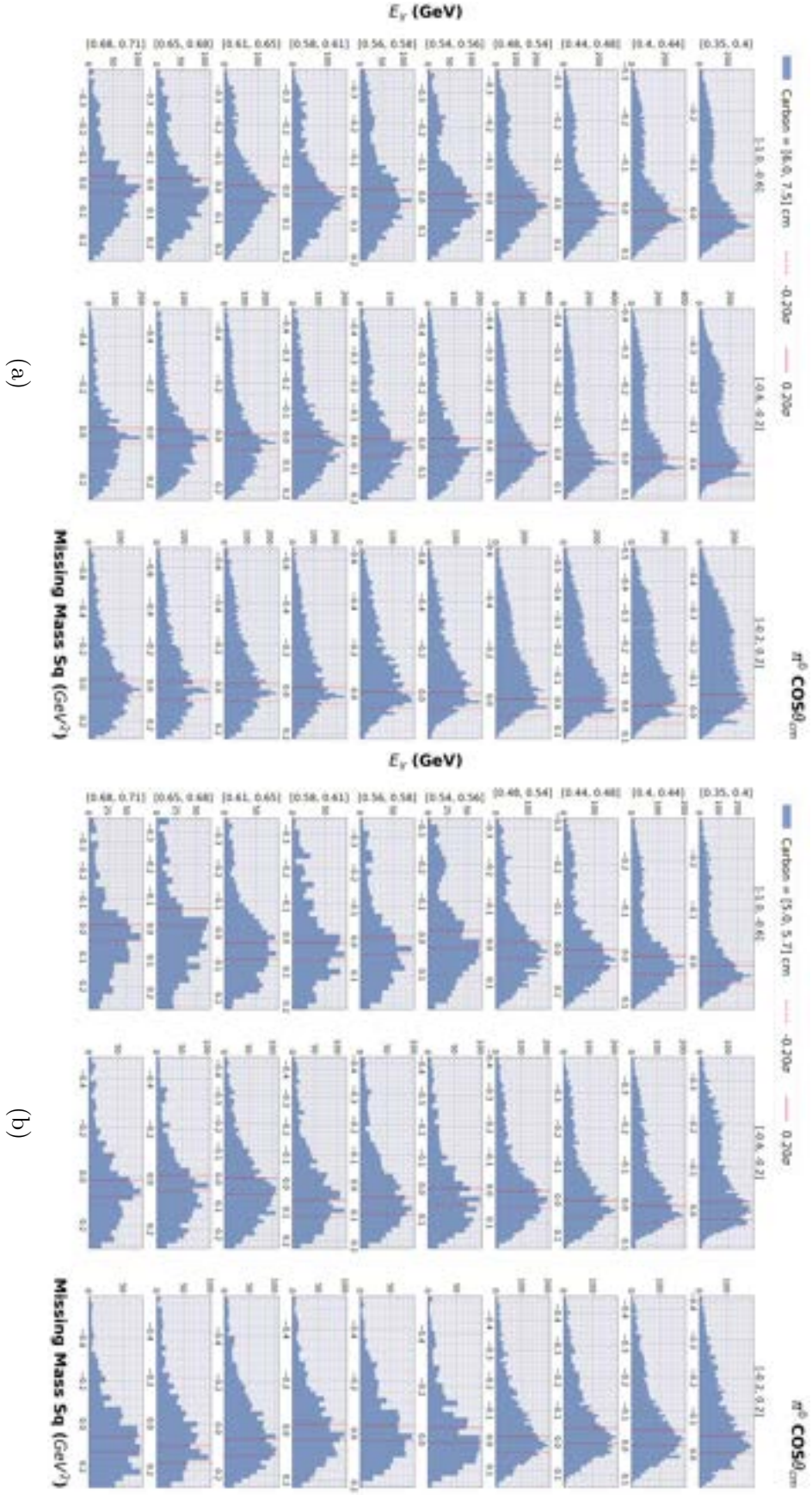
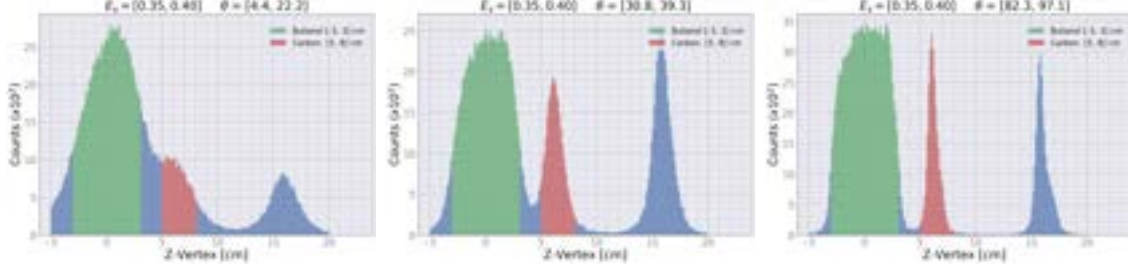


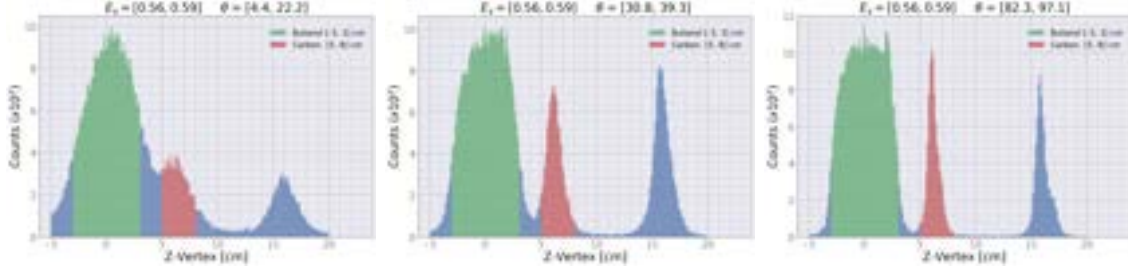
Figure 56: Carbon M_X^2 distribution partitioned in photon energies E_γ and $\cos \theta_{cm}$ for events in z -vertex range of (a) $[5.0, 7.5]$ cm and (b) $[5.0, 6.0]$ cm.

carbon events.

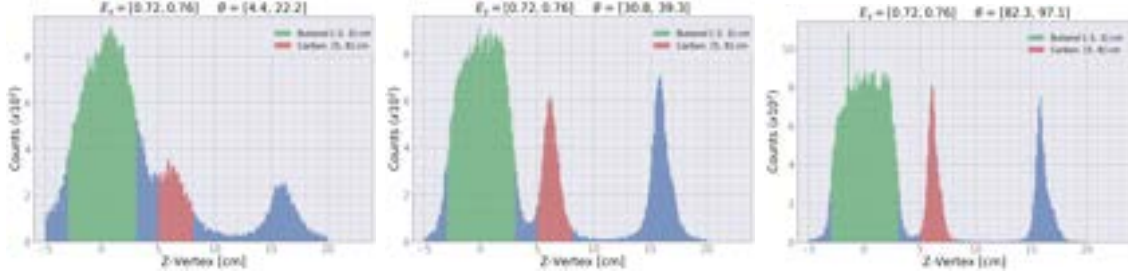
A tighter selection range for the carbon data could have been used to minimize the hydrogen contamination. However, due to the significant loss of statistics, the fit results on the carbon distribution were severely worsened. Since the quality of fit on the carbon data had a considerable impact on the calculation of scale factors and the dilution factors, the current carbon z-vertex selection range was used.



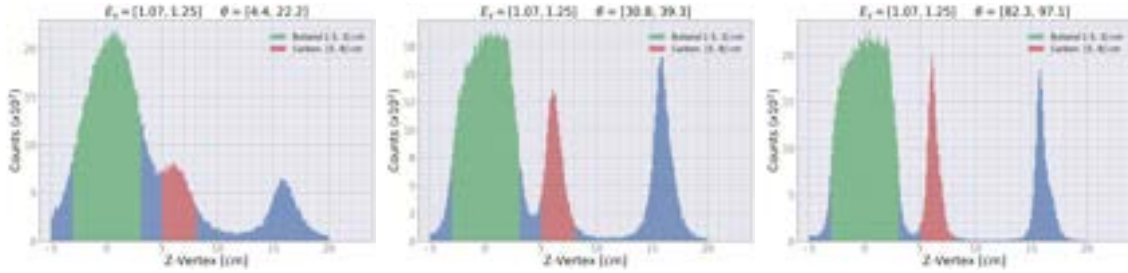
(a)



(b)



(c)



(d)

Figure 57: The reconstructed z -vertex positions in selected bins of E_γ and recoiling proton's θ_{lab} . The forward angles show poor vertex resolutions in all photon energy bins whereas resolution improves as θ_{lab} increases.

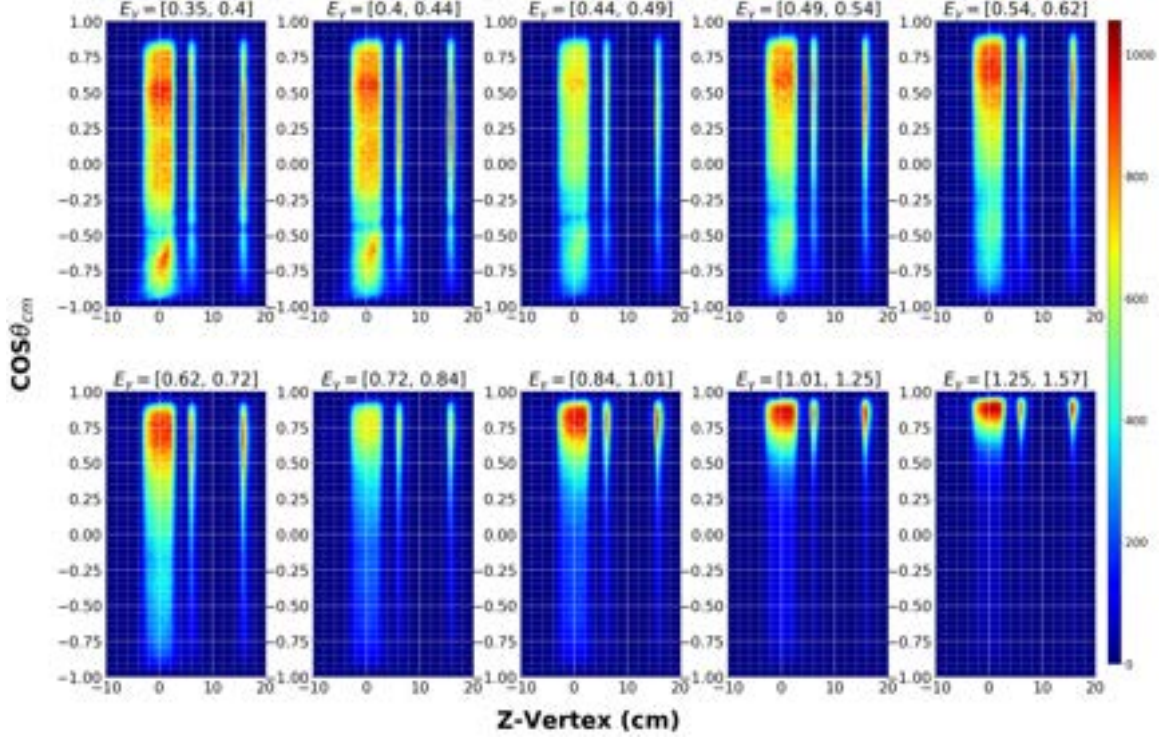


Figure 58: The reconstructed z -vertex positions versus $\cos\theta_{cm}$ in partitions of E_γ .

3.9 Binning

Determination of photon energy and $\cos\theta_{cm}$ bins were carried out separately for lower ($E_e = 1.6$ GeV) and higher energy ($E_e = 2.4$ GeV) data sets due to different concentration of events in those two data sets. For the 1.6 GeV data set, forward angle bins were much less concentrated than the 2.4 GeV data set and π^0 peaks were significantly more distinctive as background contribution was lesser, as shown in Fig. 70 and Fig. 71. For 2.4 GeV data set (Fig. 72), the populated forward angles consisted of mostly unwanted background events and only small π^0 peaks were visible in $\cos\theta_{cm} \approx [0.0, 0.9]$. Also, the counts in the π^0 peaks for the 2.4 GeV data set were only about 5% of the total counts in the π^0 peaks for both data sets combined. Hence, if two data sets were combined to determine the binning, the region where π^0 peaks were visible in 2.4 GeV would not have been binned sufficiently. Additionally,

only a subset of events whose M_X^2 values are close to π^0 peaks, as indicated by red vertical lines in Fig. 59, are used for determining the binning in order to have π^0 events evenly spaced throughout the bins. For higher energy bins, a much tighter selection was chosen to allow free nucleon events to have more weight than background events while maximizing the number of bins. Bins are constructed such that each bin contains approximately the same number of selected events, including the background and π^0 events.

The resolution of photon energy measurement from the tagger was about $\sigma_E/E \approx 10\%/\sqrt{E}$, which is roughly 2 to 5 MeV for our data sets [78]. On the other hand, the resolution of polar angle was about $\sigma_\theta \approx 1$ mrad (0.057°). Hence the narrow angular binning was not problematic. Moreover, the narrow bins shown in forward direction for $E_e = 2.478$ GeV runs were discarded when computing the E asymmetry due to the absence of π^0 signals in those bins.

A tighter M_X^2 selection range for lower energy runs was not attempted simply because the current selection range was able to declare bins that adequately partitioned events with good π^0 signals in $\cos\theta_{cm} \in [-1, 0.5]$ region. However, tighter selection ranges could be tried to further investigate any possible improvements on our final result. As for the forward angle bin edges which contained the region where no events were present, no adjustments were made since all forward angle bins with no π^0 signals were discarded in the final calculation of E .

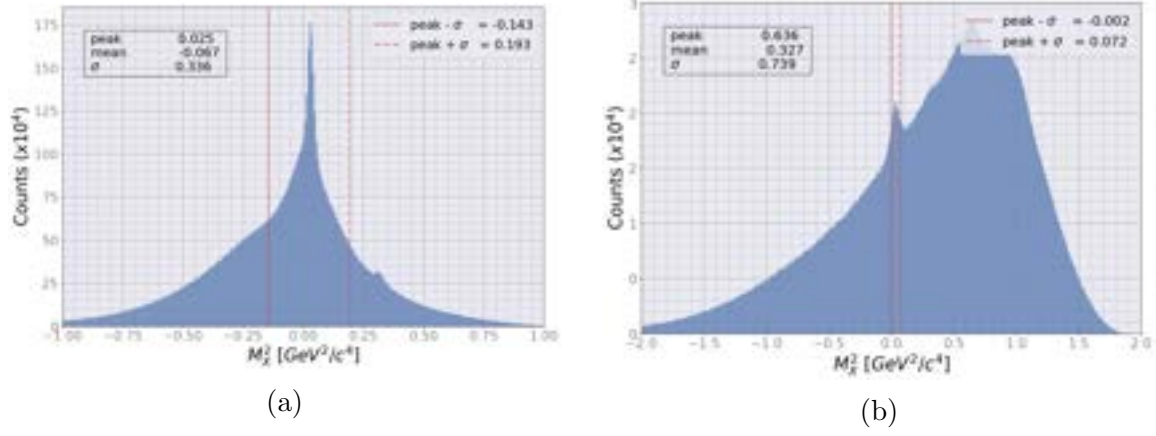


Figure 59: M_X^2 distribution from all 7 run periods where events in between red lines are used for determination of bins: (a) $E_e = 1.6$ GeV runs and (b) $E_e = 2.64$ GeV runs.

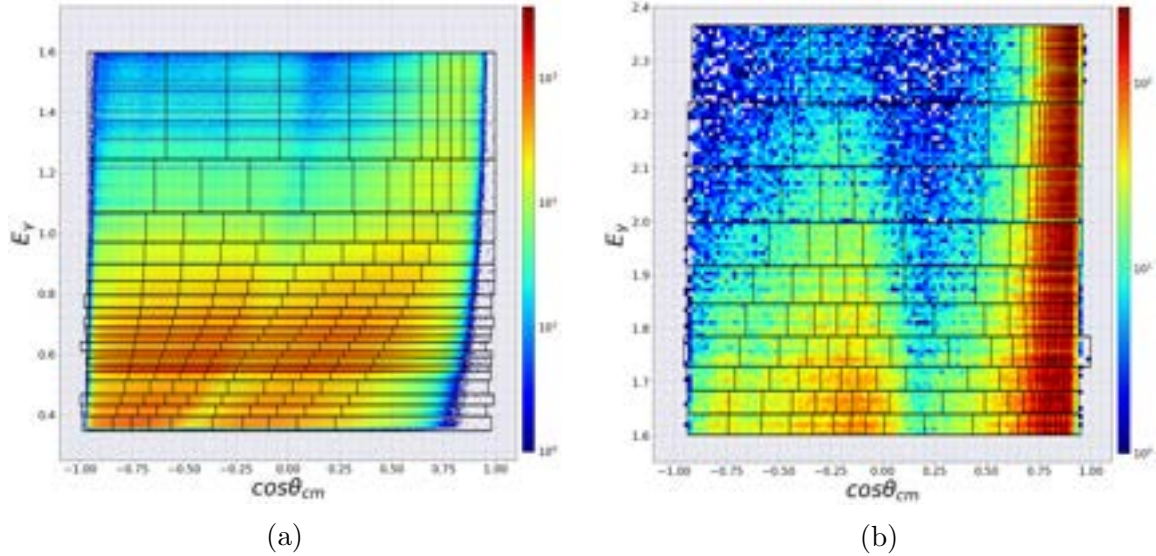


Figure 60: E_γ vs $\cos \theta_{cm}$ with black solid lines to indicate the binning used for the analysis. Each bins determined to ensure approximately same number of events in each bins: (a) $E_e = 1.6$ GeV run and (b) $E_e = 2.64$ GeV run.

3.10 M_X^2 Selection

We want to select out only a subset of events which has the highest ratio of free polarized nucleon events over non-polarized background events in order to measure

helicity asymmetry E as accurately as possible. The region at which such ratio happens varies bin-by-bin, thus, the M_X^2 selection is carried out separately for each bins; Sec. 5.1 discusses the procedures of determining these butanol free nucleon regions. If the selection range is widened further than the π^0 peak width, more contribution from the background events will contribute in calculating the asymmetry E , which will dilute the result further and increase the uncertainty of E . The second reason that these extracted free nucleon peak regions impact our final result is the quality of the fitting on the butanol distribution varied significantly. The tail part of the butanol free nucleon peaks varied a lot for each bin because the shape of the background contribution varied a lot bin by bin. If the range is too wide that it contained neighboring background events, fit quality was worsened significantly.

Any events lying outside of the butanol free nucleon regions, as indicated by red vertical lines in Fig. 80 and Appendix. A Fig. 100 – Fig. 102, are removed for our final computation of helicity asymmetry E . This M_X^2 selection step is carried out after all steps in Sec. 5 are implemented.

As Fig. 62 shows, the scattering angular coverage is dependent on the photon energy and recoil proton momentum; as photon energy increases, the maximum scattering angle θ_{p_2} of the recoiling proton increases. The change of allowed scattering angle can be verified by a simple relativistic kinematics of a two-body interactions where four-momentum conservation leads to a scattering angle limit dependent on photon energy and proton momentum:

$$\cos(\theta_{p_2}) = \frac{E_\gamma - [(E_\gamma + m_{p_1} - E_{p_2})^2 - m_{\pi^0}^2]^{1/2} \cos(\theta_{\pi^0})}{|\vec{p}_{p_2}|}, \quad (61)$$

where $\cos \theta_\pi$ are set to 1 to allow maximum proton production angle θ_{p_2} . Such limit on production angle for our reaction $\gamma p \rightarrow \pi^0 p$ is also visible in Appendix. A Fig. 100 – Fig. 102. Additionally, one can see that widths of free nucleon peaks vary as photon energy increases, emphasizing the need for M_X^2 step to be carried out separately for

each bin.

On the other hand, the reconstructed M_X^2 will not only depend on E_γ and \vec{p}_2 , but also on the azimuthal angle ϕ due to various systematic effects. The systematic effects include (a) DC misalignments, (b) beam and/or target offsets since it results in different material thickness in ϕ and different solenoidal magnetic field, (c) mis-calibrations, mainly Start counter, DC, and TOF, (d) the asymmetric B-field caused by changes of the torus magnet position during the cooling process and potential systematic uncertainties. A further systematic uncertainty analysis on such segments causing ϕ dependence will be conducted in the future.

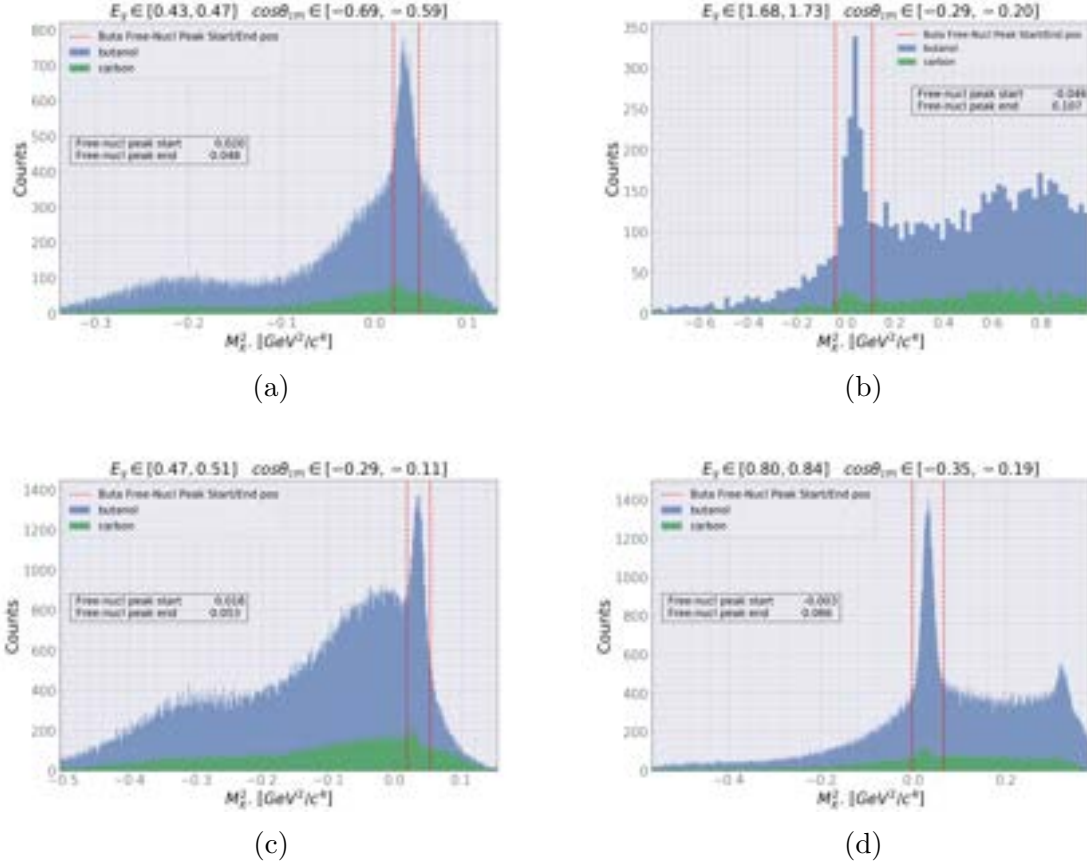
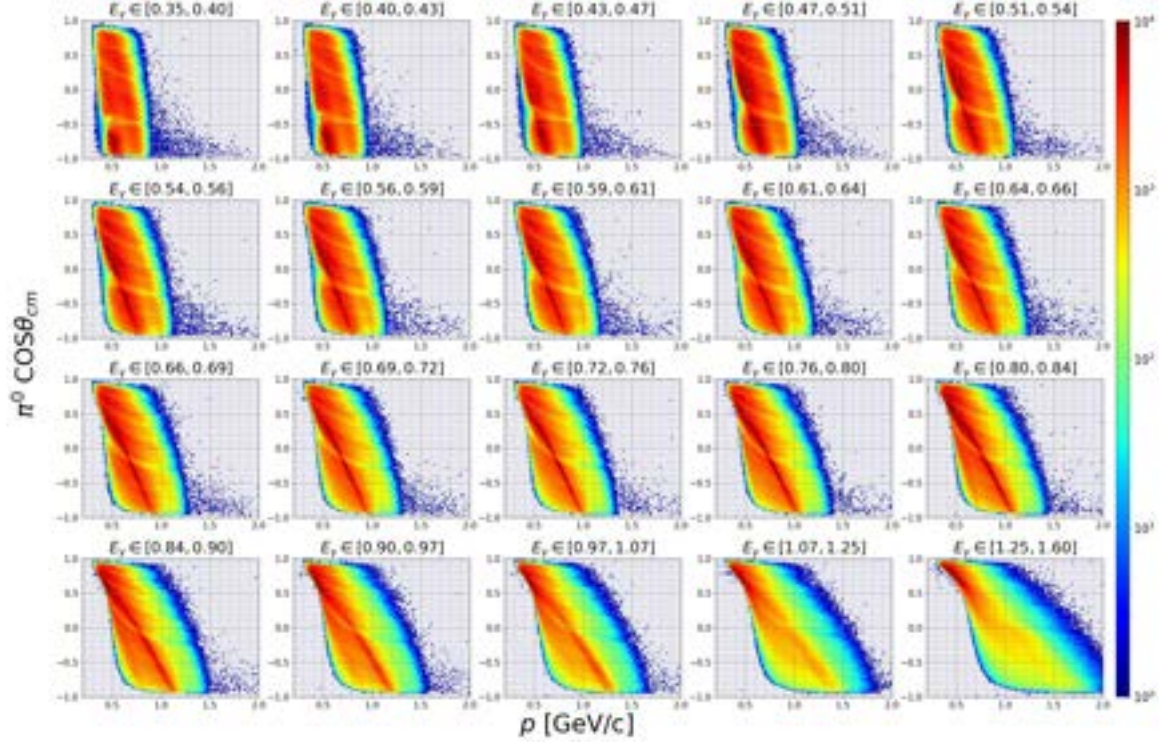
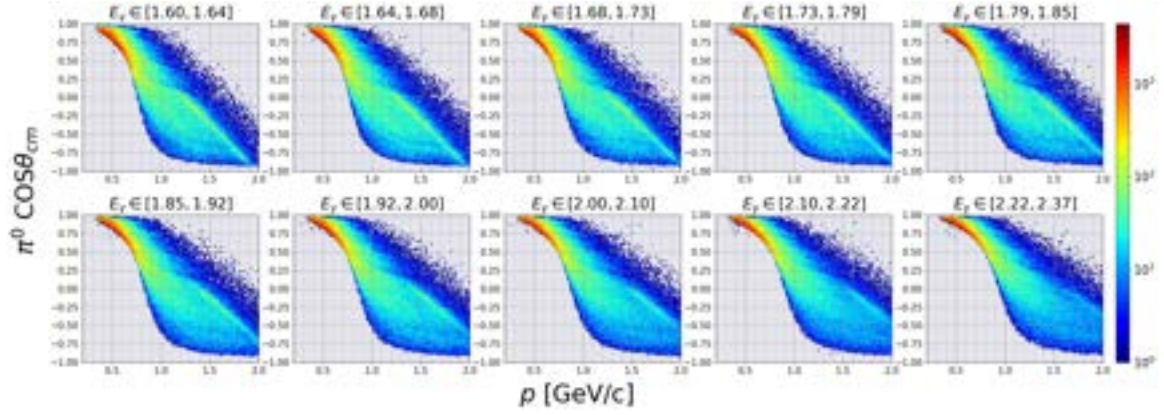


Figure 61: Selection range of butanol M_X^2 distributions in four kinematic bins. Events within red dotted vertical lines are used for calculation of helicity asymmetry E . The determined selection ranges are the final results of Sec. 5.1. Selection ranges for all bins are shown in Appendix. A Fig. 100 – Fig. 102.



(a)



(b)

Figure 62: Momentum versus $\cos \theta_{cm}$ in partitions of E_γ for (a) low energy data set ($E_e = 1.6$ GeV) and (b) high energy data set ($E_e = 2.4$ GeV)

4 Data Analysis II - Application of Deep Learning

The application of Machine Learning for regression and classification tasks in nuclear physics experiments has become commonplace in recent years. Such popularity was driven by recent developments of many open-source Machine Learning libraries: TMVA [113] for ROOT based analysis, Tensorflow [120] for python based analysis, *etc.* However, there still remain numerous obstacles in validating the results from Machine Learning algorithms, mainly in the handling of the uncertainties associated with the training data and prediction results. This section will discuss the application of a multi-layered feed-forward neural network, along with the problems it faced. The ultimate objective was to minimize the loss of valid data by classifying and filtering out contaminated data points in our data set [114].

As encountered in many previous analysis steps and Sec. 5.1, hydrogen contamination on the carbon target inhibited the usage of many simple and effective methods of separating the background events from the π^0 signals. In Fig. 63, one can see a small bump in the carbon M_X^2 distribution from the hydrogen contamination, which is amplified significantly when scaled to match butanol background events. Our aim is to classify and remove those hydrogen contaminated events (ice) from carbon bound nucleon events.

For the training data, randomly selected events from a subset of our total data are used, which has a low likelihood of having uncontaminated events. A generated training data from Monte Carlo simulation could have been used as well; however, this leads to another obstacle as the accuracy of the simulation relative to the real experiment has to be quantified and included in the uncertainty of the training data. The final result of our neural network contains uncertainties stemming from having an impure training data set, hence, will be omitted from the calculation of our final observable E . In the future, a probabilistic neural network [129] will be studied to quantify such uncertainties in attempts to include results of deep learning into our

calculation of E .

This chapter encloses the feature selection procedures, general problems encountered in applications of ML in nuclear physics experiments, setup of the applied neural network, and possible solutions for ML applications in nuclear physics experiments. An excellent introduction of ML and neural networks is given by Ref. [128, 127] which this study is based on.

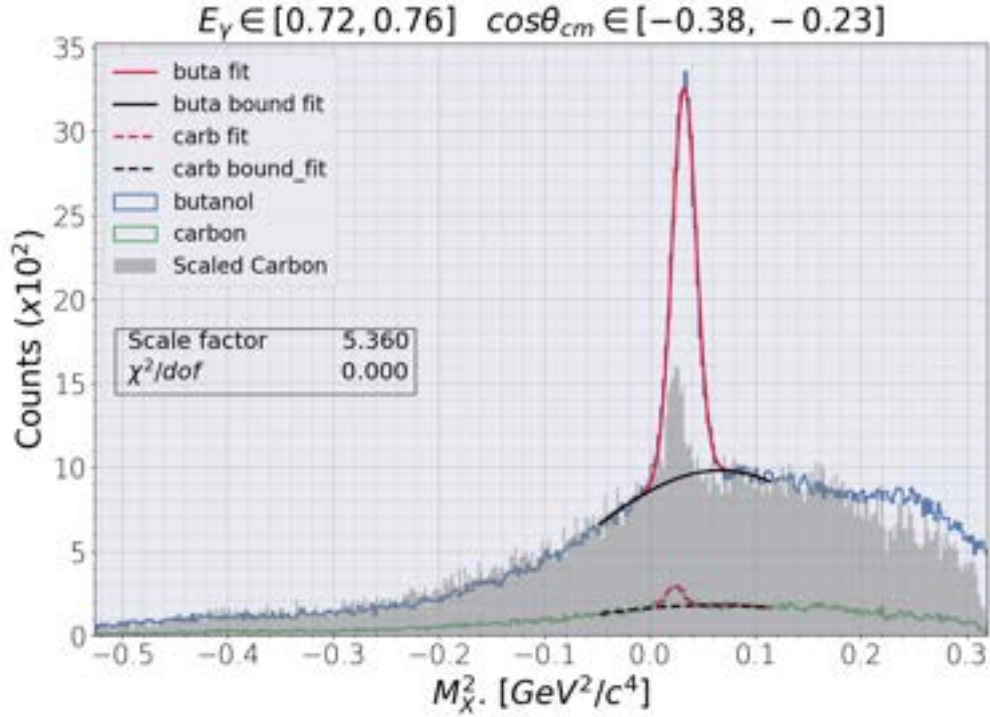


Figure 63: An exemplary evidence of strong hydrogen contamination (red dotted line) on the M_X^2 distribution of carbon events, causing scaled carbon (gray histogram) to fail to match to butanol background events (blue histogram without $M_{\pi^0}^2$ peak)

4.1 Feature Selection

In the field of Machine Learning, the term “feature selection” refers to the process of selecting parameters that are fed into the neural network model for the purpose of obtaining successful predictions. Prior knowledge of the parameters is the most crucial factor in setting up the neural network; study of distributions of the parameters and

any physical and meaningful underlying relations between parameters are far more important than implementing any sophisticated versions of neural networks. Our employed neural network model consists of two fully-connected dense neural layers and takes as inputs 10-15 classifying parameters such as E , β , E_γ , \vec{p} , x , y , z , *etc*; the procedure of selecting classifying parameters plays a crucial role in minimizing irrelevant systematic effects and avoiding overfitting. Overfitting refers to the case when the model performs successfully on training data sets, but fails on any other data. A correlation matrix between the variables for each $\gamma p \rightarrow \pi^0 p$ event is shown in Fig. 64. There are no theoretically established conditions or bounds on the number of classifying parameters which guarantee the success of classifications. Hence, many combinations of parameters were tested and the final set of classifying parameters was selected through trial and error while considering the following list as general guidelines:

- Excessively high number of classifying parameters with insufficient training data leads the model to overfit.
- Parameters with significantly low variances will cause all the training events to have the same or too similar values for all events, leading to less contribution to the classification at the expense of additional computational costs.
- If two of any chosen variables are too highly correlated, as indicated by white or black squares on Fig. 64, they contribute less to classification and cause overfitting, hence, one of them is omitted. This process is continued until no two variables with $+1$ or -1 correlation values were present.
- If too many number of uncorrelated parameters are chosen as classifying parameters, the classification will fail to capture the relations that the user first intended to discover. For example, using event vertex positions (x , y , and z) with experiment run number or TOF paddle number will not contribute to

classifying whether the event's missing mass squared (M_X^2) resides in the region of hydrogen contamination or carbon bound nucleon. On the other hand, if the event vertex positions are chosen with variables (E_γ , E_p , $|p|$, and p_z) that are used to compute M_X^2 values, the classification result is more likely to make predictions based on the physical location of the hydrogen contamination and M_X^2 values.

- There has been strong scattering angular dependence for butanol and carbon targets, hence, any variables which contains angular information are included and their weights are increased.

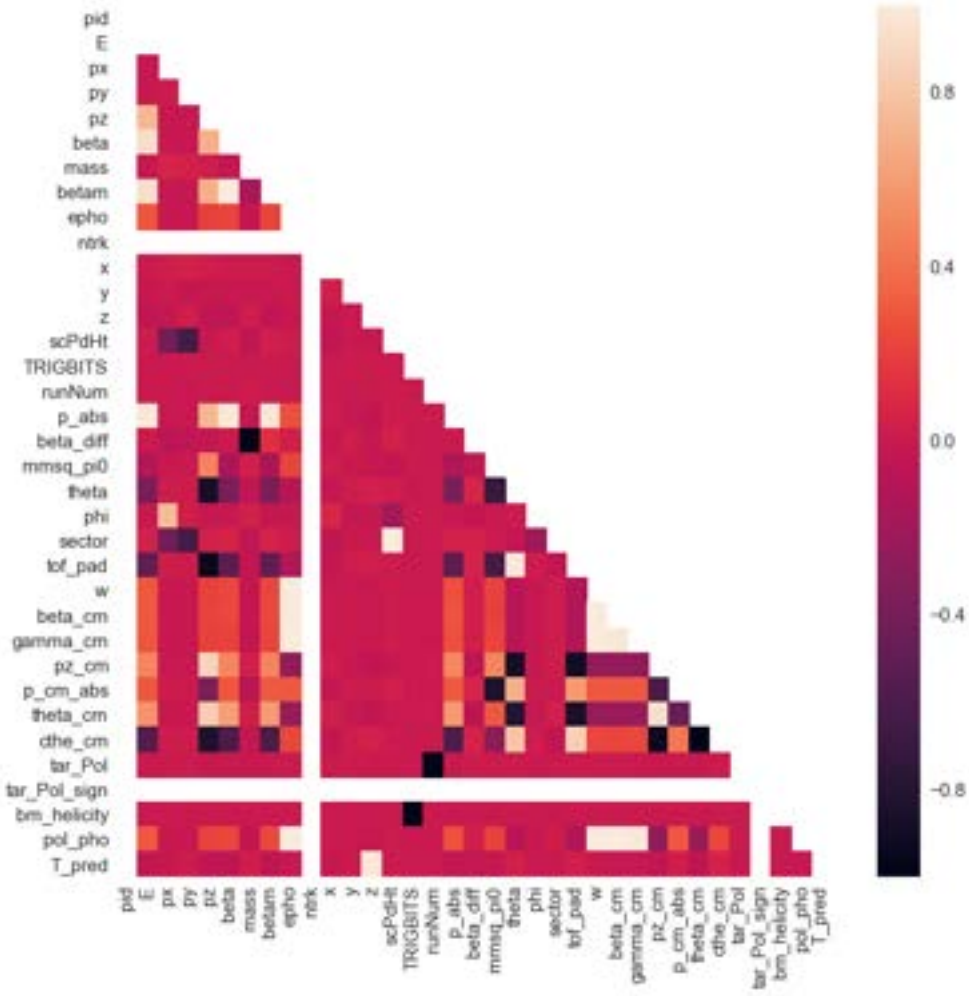


Figure 64: A heatmap showing correlation values between all the variables associated with each $\gamma p \rightarrow \pi^0 p$ event. Definitions of these variables are given in Table. 15.

The list below contains feasible classifying parameters of combinations that are tested to yield good results for our initial target classification and ice versus carbon classification. However, more robust studies on feature selection could be carried out by studying uncertainties associated with each parameter and implementing them into a Bayesian neural network [129], which is planned to be conducted after the approval of this analysis.

- Initial target classification: $E_\gamma, x, y, z, p_x, p_y, p_z, E_p, M_X^2, \theta, \phi, \beta_{meas}$, sector number, target polarization;
- Ice versus carbon classification: $E_\gamma, x, y, z, p_x, p_y, p_z, E_p, M_X^2, \theta, \phi, \beta_{meas}$, sector number, target polarization, experiment run number.
- The experimental run number is estimated to be a key classifying parameter because the ice buildup was due to air residues (humidity) on some surface, which wasn't pumped out when evacuating and cooling the target system. Therefore, if the ice was formed, the amount of ice must not have fluctuated much in consecutive experimental runs until the next target re-polarization process began.

Problems

For the initial target classification problem, the only pieces of knowledge we have are (1) carbon events will have a broader M_X^2 distribution, (2) larger $|\mathbf{p}|$ than butanol's free nucleon events due to the addition of Fermi momentum to bound nucleons of carbon events, and (3) the carbon target is placed at 6.15 cm. Therefore, training will impose conditions such as events near $z = 6.15$ cm (z is needed as a classifier) whose M_X^2 values belonging to broader ends of the M_X^2 distribution will likely be carbon events, if and only if butanol's M_X^2 distribution is completely different from that of carbon. Hence, this is an ill-posed classification problem because butanol events also contain bound nucleon events whose M_X^2 values also reside on the broader ends of the distribution. Fig. 66(b) shows the result of the initial target classification. Even though the results appear to have classified butanol versus carbon successfully, a careful study on how the model arrived at such results is needed to validate the Machine Learning approach in this problem.

For the ice versus carbon classification problem, the two pieces of information

we have are (1) for events that occurred in $z = [6, 7.5]$ cm and (2) events whose M_X^2 values are near π^0 signal $M_{\pi^0}^2 = 0.018 \text{ GeV}^2$ have large number of ice events as shown in Fig. 56. If we were to choose training data based on these two conditions, we have to consider what percentage of these events are actually ice events which means we need the uncertainty value for the impure training data. The percentage of ice events can be calculated by the same method that we will use in dilution factor calculations in Sec. 5.3. From Fig. 56, we can fit the whole distribution including the ice peaks with the background and also fit the background separately. Integrating the fit function for the whole distribution (N_{tot}) and for the background only (N_{bkg}), we can obtain the dilution factor of the hydrogen contamination in our training data (D_{HC}):

$$D_{HC} = \frac{N_{tot} - N_{bkg}}{N_{tot}}. \quad (62)$$

Currently, a probabilistic deep learning model is under development in order to include this uncertainty into the final predictions.

4.2 Setup of Applied Neural Network

A simplified flowchart of the three layered feed-forward neural network model used in this analysis is shown in Fig. 65 [127] [128]. The layers with purple nodes are called the hidden layers which refer to any layers between the input and the output layers that perform nonlinear transformations of the inputs from the previous layers. In our neural network model, the first and second hidden layers contain 15 nodes with each node containing a nonlinear function of a linear combination of the previous layer's inputs. The third hidden layer contains 2 nodes (3 for the first target classification problem) which returns probability scores (ice or carbon) that sums to one.

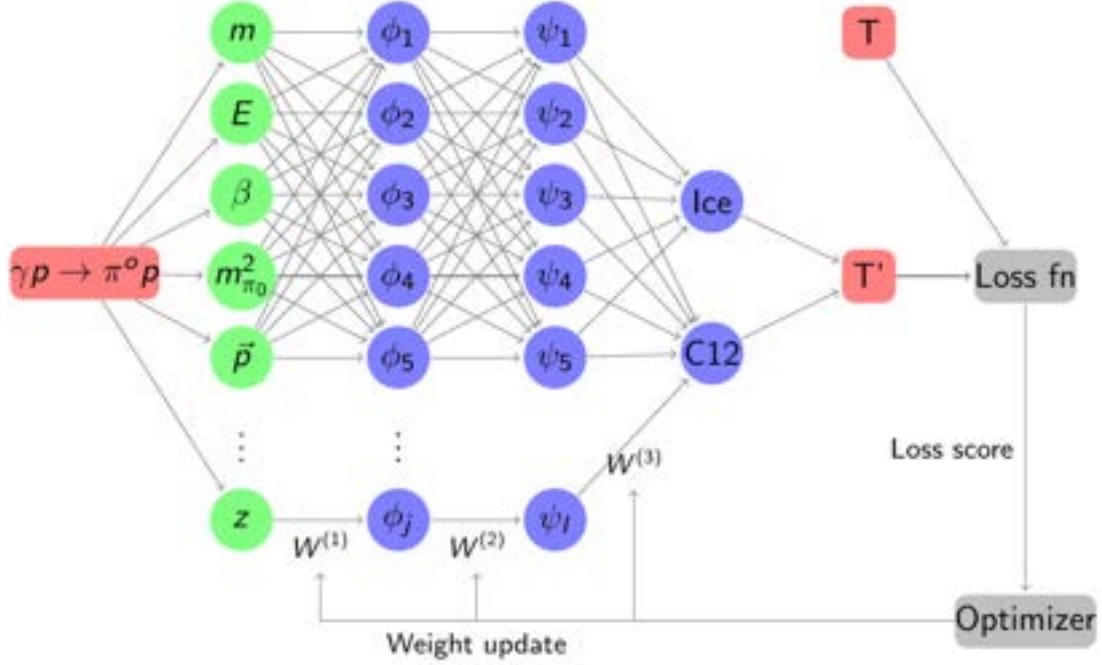


Figure 65: A schematic flowchart of a three-layered feed-forward neural network used in hydrogen contamination classification. T' and T denote the prediction and truth value of the event being classified.

For each $\gamma p \rightarrow \pi^0 p$ event, the chosen parameters (x_i, \dots, x_D) are fed into the first layer of the model as indicated by green nodes in Fig. 65. Then, J ($=15$) linear

combinations (ϕ_j) of the input variables are constructed:

$$\phi_j = \sum_{i=1}^D w_{ji}^{(1)} x_i + w_{j0}^{(1)}, \quad (63)$$

where subscript (1) denotes the weights ($w_{ji}^{(1)}$) from the input layer and $w_{j0}^{(1)}$ indicated the biases. The initial value of weights is chosen to any arbitrary number depending on the choice of the optimizer and starts to vary in a succession of steps while optimization iterates through the model. For our choice of the optimizer (Adam Optimizer [126]), the initial weights are set to zero.

Before entering into the second hidden layer, the outputs from the first hidden layers are refined by a specific activation function called the Rectified Linear Unit (ReLU) to ensure no negative values are passed:

$$z_j(\phi_j) = \begin{cases} 0 & \text{if } \phi_j < 0 \\ \phi_j & \text{otherwise.} \end{cases} \quad (64)$$

The same steps are repeated as the results from the first layer get passed to the second hidden layer. The second hidden layer introduces another nonlinear function of a linear combination of the first hidden layer outputs. Therefore, adding more layers allows the network to learn additional combinations of functions that help to make better classifications. If the classification result shows signs of overfitting, this additional hidden layer could be removed or its nodes removed to make the model less specific only to the training data. Similarly, L ($=15$) linear combinations (ψ_l) of the output from first hidden layer are constructed:

$$\psi_l = \sum_{j=1}^J w_{lj}^{(2)} z_j + w_{l0}^{(2)}, \quad (65)$$

where subscript (2) denotes the weights ($w_{lj}^{(2)}$) from the first hidden layer to the second

hidden layer and $w_{l0}^{(2)}$ are the biases. Again, negative output from the second hidden layers are filtered out:

$$z_l(\psi_l) = \begin{cases} 0 & \text{if } \psi_l < 0 \\ \psi_l & \text{otherwise.} \end{cases} \quad (66)$$

The third hidden layer consists of two nodes each with a probability score (a_k) that corresponds to the probability that the $\gamma p \rightarrow \pi^0 p$ event came from the ice or the carbon targets:

$$a_k = \sum_{l=1}^L w_{kl}^{(3)} z_l + w_{k0}^{(3)}, \quad (67)$$

where $k \in \{0, 1\}$ for ice and carbon. The final probability score is refined using a softmax function to ensure normalization:

$$y_k = \sigma(a_k) = \frac{\exp(a_k)}{\sum_{i=1}^2 \exp(a_i)}. \quad (68)$$

Combining all stages to give the overall neural network function in terms of \mathbf{x} and \mathbf{w} gives:

$$y_k(\mathbf{x}, \mathbf{w}) = \sigma \left[\sum_{l=1}^L w_{kl}^{(3)} \left(\sum_{j=1}^J w_{lj}^{(2)} \left(\sum_{i=1}^D w_{ji}^{(1)} x_i + w_{j0}^{(1)} \right) + w_{l0}^{(2)} \right) + w_{k0}^{(3)} \right]. \quad (69)$$

For the obtained result y_k , a loss score is calculated by a selected loss function which describes the result's accuracy to the known truth value, denoted as T in Fig. 65. The truth value T refers to the correct identity of the event (from the training data) that the network is training to correctly identify.

In deep learning practices, cross entropy is often used as a measure of accuracy in classification results. Entropy ($-\mathbb{E}[\log p(x)]$) in statistics is an average of negative log of probability distribution function which could be interpreted as the amount of

available information given the outcome of the measurement. For example, if we repeatedly measure unlikely events, it is an indication that the probability density function (PDF) that we are using to describe the system is wrong. In other words, there are other factors at play that are not accounted for. The amount of these unaccounted factors corresponds to the size of information that is not yet discovered. When we have two separate probability distributions $p(x)$ and $q(x)$ over the same random variable x , the likeness of these two distributions can be obtained by computing a quantity called the cross entropy:

$$E(p, q) = - \sum_x p(x) \log q(x), \quad (70)$$

where minimizing $E(p, q)$ is equivalent to narrowing the difference of two distributions. Hence cross entropy was chosen as the loss function in our neural network model to assess the correctness of the computed weights ($w_{ji}^{(1)}$, $w_{lj}^{(2)}$, and $w_{kl}^{(3)}$) by comparing $y(\mathbf{x}, \mathbf{w})$ to the known truth values.

We can obtain individual the cross entropy (E_n) for each data point (x_n) in the training data in function of the weights and input values by taking the negative logarithm of the likelihood function ($p_n(\mathbf{t}|\mathbf{x}, \mathbf{w})$):

$$\begin{aligned} E_n(\mathbf{x}, \mathbf{w}) &= -\ln p_n(\mathbf{k}|\mathbf{x}, \mathbf{w}), \\ p_n(\mathbf{k}|\mathbf{x}, \mathbf{w}) &= y_n^k (1 - y_n)^{1-k}, \end{aligned} \quad (71)$$

where n refers to the specific data point being classified and $k \in \{0, 1\}$ denotes two possible classification outcomes. Since we are considering a binary classification problem, the probability distribution is the *Bernoulli* distribution. The overall loss score can then be summed over all E_n : $E(\mathbf{w}) = \sum_{n=1}^N E_n(\mathbf{w})$.

The weights are then continuously altered by small increments in the direction of the negative gradient of the loss function until the minimum of the loss function is

reached:

$$\mathbf{w}^{\tau+1} = \mathbf{w}^{\tau} - \eta \nabla E_n(\mathbf{w}^{\tau}), \quad (72)$$

where τ indicates the iteration step at which the gradient of the loss function has been computed and η is the learning rate that we can freely set to optimize the result. Such approach is called *gradient descent optimization* (SGD). The specific SGD optimization algorithm used is *Adam Optimizer*. It utilizes ∇E of not only the current value, but also the past values to allow the determination of local minimum and global minimum of the loss function [126].

Most importantly, minimization of the error function in the feed-forward neural network involves an iterative procedure where adjustments to the weights are made while back-propagating from the last layer to the initial layer of the model. The chronological order of network flows is indicated by the arrows in Fig. 65 where an input of one $\gamma p \rightarrow \pi^0 p$ event is the beginning and updating the first hidden layer's weights is the last process. The computation of the gradient of the error function with respect to the weights is given by:

$$\begin{aligned} \frac{\partial E_n}{\partial w_{ji}} &= \frac{\partial E_n}{\partial \phi_j} \frac{\partial \phi_j}{\partial w_{ji}} \\ &= \left[\sum_l \frac{\partial E_n}{\partial \psi_l} \frac{\partial \psi_l}{\partial \phi_j} \right] \frac{\partial \phi_j}{\partial w_{ji}} \\ &= \left[\sum_l \left[\sum_k \frac{\partial E_n}{\partial a_k} \underbrace{\frac{\partial a_k}{\partial \psi_l}}_{\propto w_{kl}} \right] \underbrace{\frac{\partial \psi_l}{\partial \phi_j}}_{\propto w_{lj}} \right] \underbrace{\frac{\partial \phi_j}{\partial w_{ji}}}_{\propto x_i}, \end{aligned} \quad (73)$$

where $\frac{\partial E_n}{\partial a_k}$ can be calculated using Eq. (71) and Eq. (68). As shown in Eq. (72), the gradients are then used to compute the needed adjustments to the weights in the direction of the minimum of the error function.

4.3 Initial Target Classification

Before applying any deep learning classification for hydrogen contamination caused by ice build up on carbon targets, we need to make sure the carbon events are free of any butanol events since free nucleon events from butanol are indistinguishable from ice events within the scope of our measured kinematic quantities. In the region $z = [2, 5]$ cm, as shown in Fig. 54(a), the events are indistinguishable whether the photons hit the butanol or carbon targets. The three-layer feed-forward neural network model, described above, was used to classify carbon versus butanol events. Since both of our butanol data and contaminated carbon data consist of both bound and free nucleons, the most contributing classifying parameters were z -vertex positions and scattering angles. The scattering angles played a big role since carbon and butanol targets had different acceptance rates simply due to carbon being placed further downstream of the beam axis.

For the initial selection of training data, events within $z = [-3.0, 3.0]$ cm were selected for butanol training data and events within $z = [5.5, 7.0]$ cm were selected for carbon training data as shown in Fig. 66(a). The selection ranges were determined to ensure the identities of the target types of training data could be assumed with good confidence. However, we will have to place a constraint on the classifying parameter z such that the network will not depend its classifications too much on z values but rather studies other classifying parameters in relation to z . This process of putting constraints is called L1 and L2 regularization methods in the field of machine learning. The ratio of butanol over carbon training data was matched with the ratio of butanol over carbon testing data to minimize biased training; a subset of training data were randomly selected to maintain the ratio.

The result of classification seemed to successfully classify carbon events and butanol events in the region $z = [2, 5]$ cm as shown in Fig. 66(b). However, as will be discussed later in the section, the biggest problem is the unknown uncertainty in the

truth values of the training and testing data. In other words, even though we selected the training data with a strong belief that they correctly represent their known target types, we have no methods to achieve 100% certainty in knowing the true identities of target types at subatomic scales.

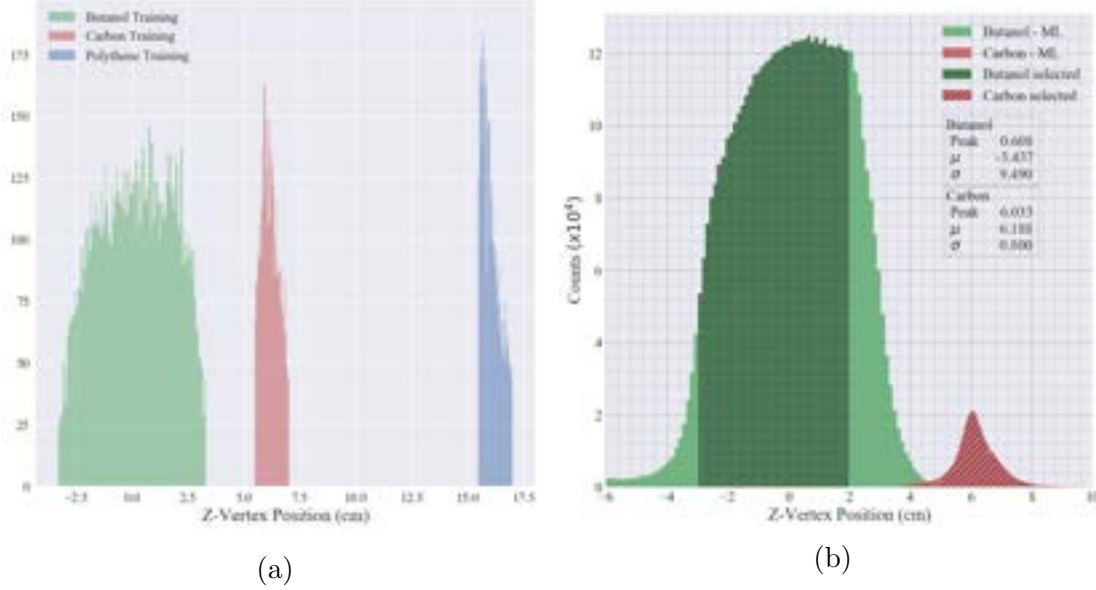


Figure 66: (a) Events within selection range for each target's training data. (b) Result of classification between butanol and carbon events in region $z = [3, 5]$ cm.

4.4 Ice versus Carbon Classification

From previous initial target classification results, only the events that are classified as carbon events, will be used in this step from which ice events will be predicted and filtered out for further analysis steps. Unfortunately, none of our measured physical quantities of each event is a solid classifying parameter that can directly distinguish the ice from carbon events. The only parameter that could remotely distinguish ice events would be the missing mass squared M_X^2 values in which events with ice targets will result in M_X^2 values close to π^0 ($m_{\pi^0}^2 \sim 0.018 \text{ GeV}^2$) peaks and carbon events will result in broader M_X^2 distributions due to the addition of Fermi momentum. In Fig. 67, M_X^2 distribution of all events previously classified as carbon

events are plotted and the red shaded portion of the distribution indicates the chosen events for ice training data. This selected range was determined by π^0 peak $\pm\sigma/10$, where σ is a standard deviation of the carbon M_X^2 distribution. One can see from Fig. 67 that majority of the selected ice training events are already dominated by carbon background, which causes the classification of ice and carbon events to be less effective. We have tightened the selection ranges to increase ice proportions in the training data, as far as possible while still retaining sufficient statistics for unbiased training. For selecting carbon training data, we could attain more certainty by selecting events in regions that belonged to carbon events with good confidence. As shown in Fig. 68 events satisfying three criterion were selected as carbon training data: $M_X^2 \in [-0.073, 0.27] \text{ GeV}^2$, $z \in [5.5, 6.5] \text{ cm}$, and $(x-x_{max})^2+(y-y_{max})^2 < (0.8 \text{ cm})^2$.

The results are shown in Fig. 69, where M_X^2 values are plotted against z -vertex positions. From the classified ice, we can attest that they are events with $M_X^2 \sim 0.018 \text{ GeV}^2$ which mostly lie in between $z = [6.5, 7.7] \text{ cm}$. However, we certainly cannot conclude that these events are from ice targets. In Sec. 3.8.2, free nucleon peaks in the carbon target region were studied and build up of ice was suspected to reside in the vicinity of $z = [6, 7.5] \text{ cm}$. Therefore, the prediction of ice in regions left of $z = 6 \text{ cm}$ raises doubts whether the model actually selected events stemming from ice targets or merely selected out events with $M_X^2 \approx M_{\pi^0}^2$ which consists of both carbon and ice events. The latter scenario seems more plausible since our training data was heavily diluted with carbon background events.

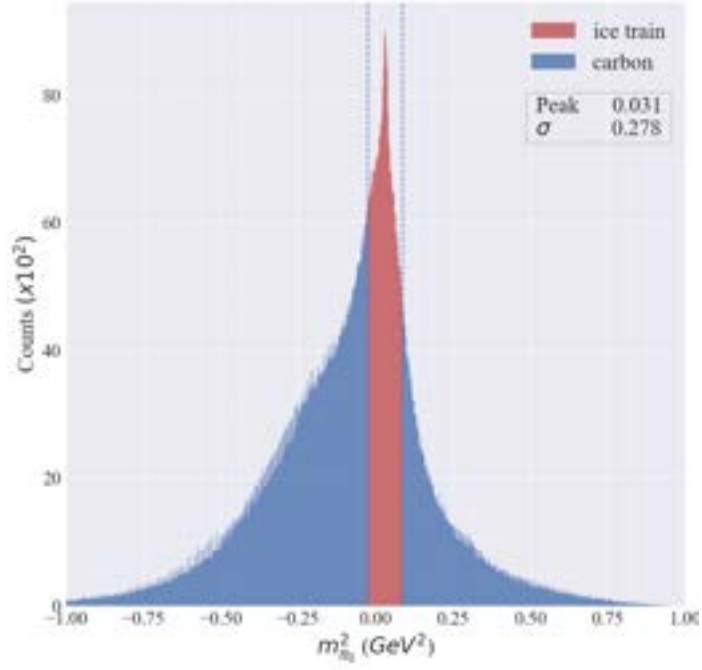


Figure 67: Selection of ice training data. From carbon M_X^2 distribution, events within $[peak - \sigma/10, peak + \sigma/10]$, were selected as ice training events.

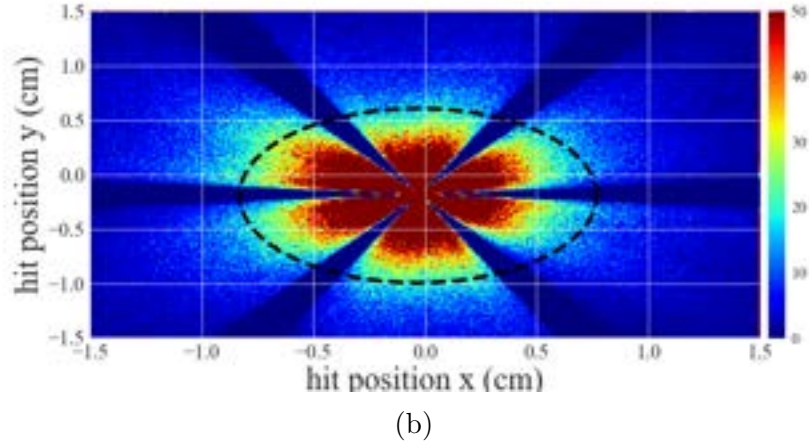
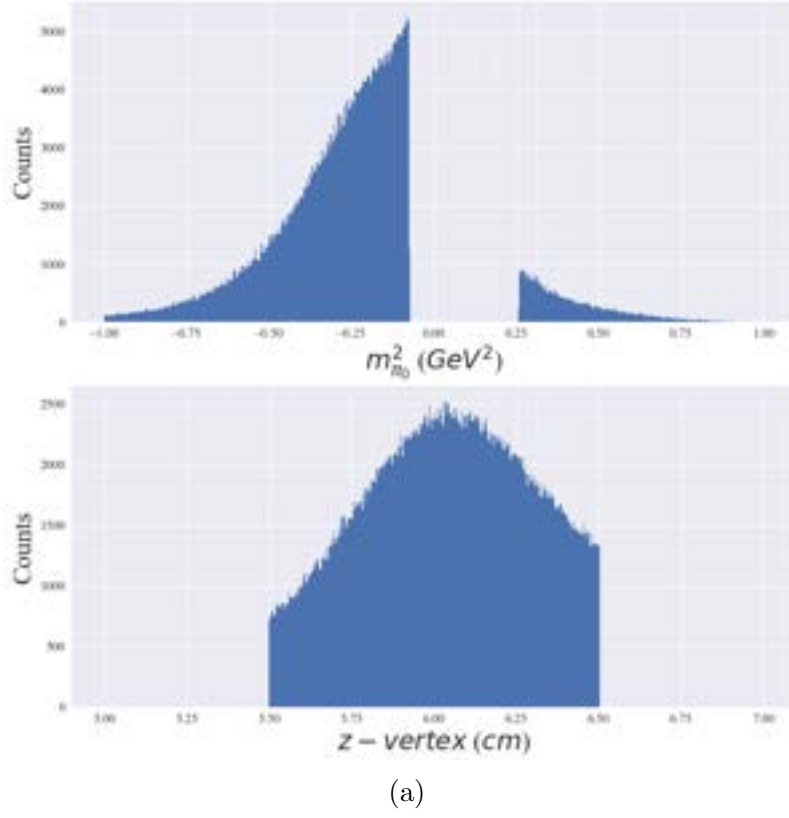


Figure 68: Selection of carbon training data. Events satisfying three criterion were selected as carbon training data: $M_X^2 \in [-0.073, 0.27] \text{ GeV}^2$, $z \in [5.5, 6.5] \text{ cm}$, and $((x - x_{max})^2 + (y - y_{max})^2) < (0.8 \text{ cm})^2$.

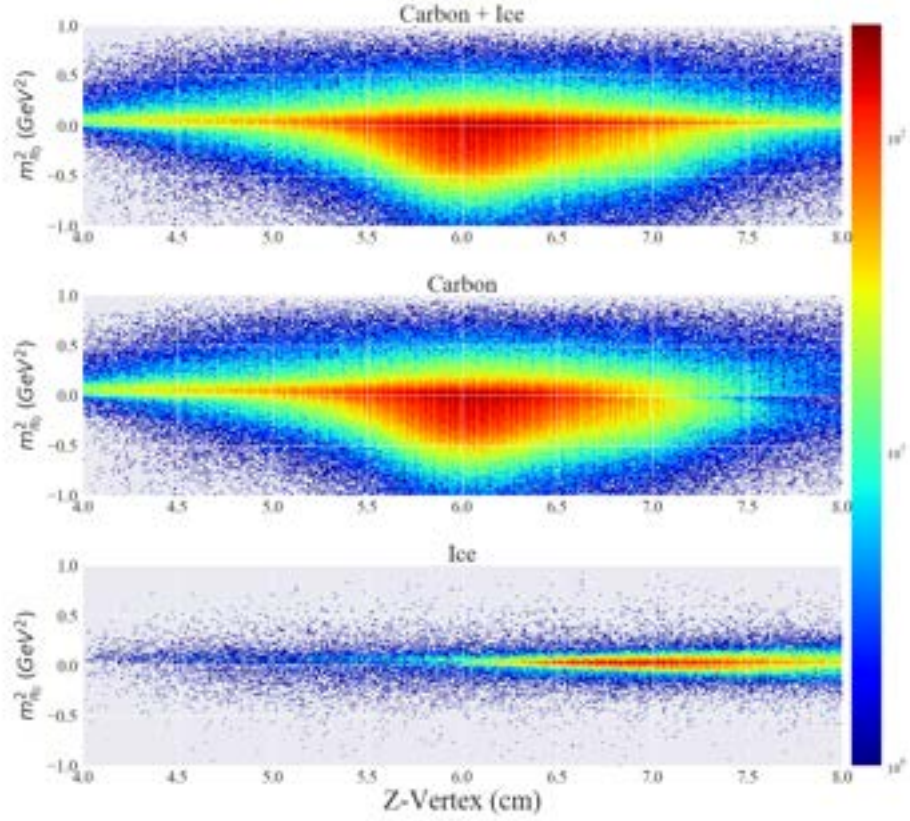


Figure 69: Results of classification between ice and carbon events in $z = [4, 8]$ cm.

4.5 Possible Solutions

In conclusion, the application of Machine Learning algorithms in nuclear physics experiments, especially for classification problems, requires well defined training data. To further minimize the uncertainty in the training data, one might choose the following approaches.

- Use of simulated data as training data will provide truth values with certainty. But accuracy of the simulation to the real experiments needs to be assessed and included as the uncertainty of training data. Detector acceptance, tracking

resolution, momentum correction, and energy loss correction cause that the distributions are skewed. Thus, even careful simulations will not match the real experimental data. As a result, a mixture of real and simulated data for our training data might be a solution.

- The proceeding g9b/FROST experiment had the carbon targets placed further downstream and had no hydrogen contamination. The g9b/FROST experiments' carbon data could be used as carbon training data. However, it is impossible to mimic the exact experimental conditions of the g9a/FROST experiment, in particular the acceptance rate of each sub-detector.
- Extract ice training data separately in each of angle and photon energy bins' M_X^2 distributions because visibility of free nucleon peaks in carbon events varied at different angle and energy ranges. As shown in Fig. 57 or Fig. 90, the event vertex resolution of the CLAS detector varied heavily depending on the scattering angle. We can limit the selection of training data to only be drawn from bins with good event vertex resolutions: $\theta_{lab} \geq 39^\circ$. This approach will help in increasing ice proportions in ice training data.
- Implement various regularization methods such as early stopping, drop-out, or L1 and L2 parameter norm penalties methods. These methods help to avoid possible overfitting. Although acceptance studies are not required for our final result of this analysis, in order to place correctly emphasized or constrained weights on certain classifying parameters, further acceptance studies could be beneficial.
 - L1 and L2 regularizations suppress the weights on certain classifying parameters. This method is useful when the user has prior knowledge of specific classifying parameters that can potentially induce a bias.

- Drop-out regularization randomly selects and removes some nodes in the hidden layers at every iteration of training. This method is useful when the network is large and the user wants to introduce some randomness.
- Early stopping regularization involves monitoring of the error while training on the training data and testing on the testing data simultaneously. If the error from the testing data reaches certain value that the user preset, the training stops at the moment.
- Implement a Bayesian neural network model where the uncertainty in inputs is accounted for and probability distribution functions are passed between neural layers instead of scalar weights. The overall uncertainty in using impure training data could be quantified.

5 Data Analysis III - Helicity Asymmetry E

To correctly measure E from the events where photons interacted with the polarized free nucleons of the butanol target (C_4H_9OH), the ratio of bound nucleons to free nucleons in our butanol target (Sec. 2.4.1) needs to be estimated. A carbon target, consisting of only bound nucleons, was placed about 6 cm downstream of the CLAS center to study and correlate to the nature of background events of butanol events. A scale factor to estimate the ratio of carbon events to butanol background events and a dilution factor to estimate for the ratio of butanol background events to total butanol nucleon events are computed in upcoming sections. However, some of carbon events in certain energy and angle bins were contaminated by the formation of ice which diluted the carbon events with some free nucleon events, hindering the background subtraction process. Therefore, the carbon data is not utilized in computation of the dilution factor, but only utilized in computing the scale factor. The scale factor is then used for the extraction of the free nucleon peak ranges.

In Sec. 4, a deep learning classification model, which was employed to classify hydrogen contamination from carbon events, is discussed. But without a reasonable method to estimate the uncertainty of the classification, the significance of the results was unclear. Hence, to further minimize the effects from such hydrogen contamination, two separate methods were tried in computing the scale factor (Sec. 5.1 and Sec. 5.2). The steps of calculating scale factors and dilution factors for each scattering angle and photon energy bin are the following:

1. The initial scale factor is obtained by directly comparing butanol and carbon events in side-bands of missing mass squared (M_X^2) distribution (Fig. 70 and Fig. 71).
2. Using the initial scale factor, the carbon M_X^2 distribution is scaled up to correspond to the background of the butanol M_X^2 distribution. The butanol M_X^2

distribution is then subtracted by the scaled carbon M_X^2 distribution. Then from the remaining M_X^2 distribution, start and end positions of butanol free nucleon peaks were extracted for the first time. At this stage, bins with non-distinctive free nucleon peaks were selected and omitted from further analysis. The determination of the distinctiveness of free nucleon peaks was based on whether the fitting of the free nucleon peak was successful or not.

3. Two separate methods are attempted in calculating the final scale factors: using standard fitting routine (Sec. 5.1) and cubic spline interpolation (Sec. 5.2). The method listed in Sec. 5.1 is ultimately chosen for our analysis.
4. Using the finalized scale factors, start and end positions of butanol free nucleon peaks were extracted again for improvement.
5. Using the fit results from butanol events only, the dilution factor (D_f) is obtained over the range of estimated butanol free nucleon region (Sec. 5.3):

$$D_f = \frac{B_{tot} - B_{bnd}}{B_{tot}}, \quad (74)$$

where B_{bnd} is the number of bound nucleon events and B_{tot} is the total number of events (free and bound).

5.1 Scale Factor

5.1.1 Initial Scale Factor

Reactions on bound nucleons are subject to Fermi motion. This momentum can only be inferred by measuring the π^0 in coincidence. Since this was inclusive (proton only), I could only assume each struck proton was initially stationary when calculating M_X^2 . Such assumption will cause the Fermi momentum to be included in M_X^2 value:

$$E_{p1,\text{bound}} = \sqrt{m_p^2 + p_{\text{Fermi}}^2}, \quad (75)$$

$$M_{\pi^0}^2 = (E_\gamma + m_{p1} - E_{p2})^2 - (\vec{p}_\gamma + \vec{p}_{\text{Fermi}} - \vec{p}_2)^2.$$

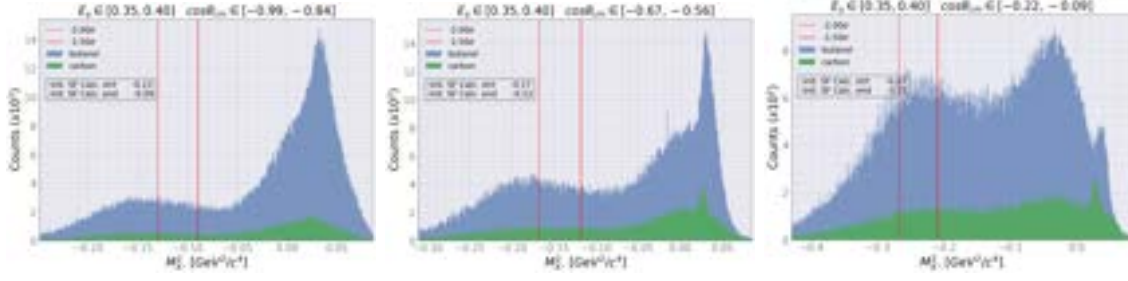
In our calculation where we have assumed the initial proton to be stationary, the bound nucleon events contribute to the broader side-bands of M_X^2 distribution than free nucleon events.

Regions selected for computing initial scale factors need to be absent of any free nucleon events to obtain a ratio of butanol and carbon bound nucleon events. From the butanol distributions, events in between $[\pi^0 \text{ peak} - 2.0\sigma, \pi^0 \text{ peak} - 1.5\sigma]$ for $E_e = 1.6$ GeV data and $[\pi^0 \text{ peak} + 1.0\sigma, \pi^0 \text{ peak} + 1.5\sigma]$ for $E_e = 2.4$ GeV data, where free nucleon events are supposedly absent, were chosen for each kinematic bin as marked with red vertical lines in Fig. 70, Fig. 71, and Fig. 72. The σ denotes the standard deviation of the butanol distribution. The selection ranges for all bins in both low and high energy runs are displayed in the Appendix A Fig. 91 - Fig. 93. Also, the missing mass squared distributions for both butanol and carbon events are binned identically to use uniformly chosen m_X^2 ranges and bins for computing a ratio. Eq. (76) was minimized to obtain the initial scale factors, α , in each bin:

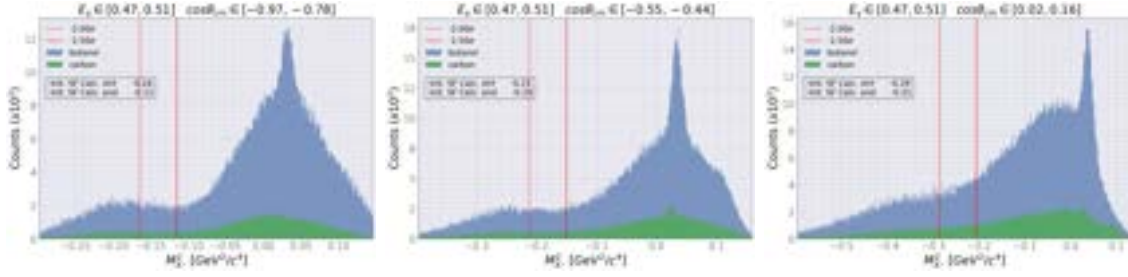
$$\begin{aligned} \chi^2 &= \sum_i \frac{(N_i^B - \alpha N_i^C)^2}{N_i^B + \alpha^2 N_i^C}, \\ N_i^B &= \int_{\mu-2\sigma}^{\mu-1.5\sigma} n_b \, dm_x^2, \\ N_i^C &= \int_{\mu-2\sigma}^{\mu-1.5\sigma} n_c \, dm_x^2, \end{aligned} \quad (76)$$

where n_i^b and n_i^c are factors of butanol and carbon events in each bins of m_X^2 extraction regions, respectively. Fig. 73 and shows scaled carbon distributions using obtained initial scale factors to check whether the values are within sensible ranges; the bins shown are examples of a few special cases where unwanted angular dependence, hydrogen contamination, or no free-nucleon peak is visible. Since only rough

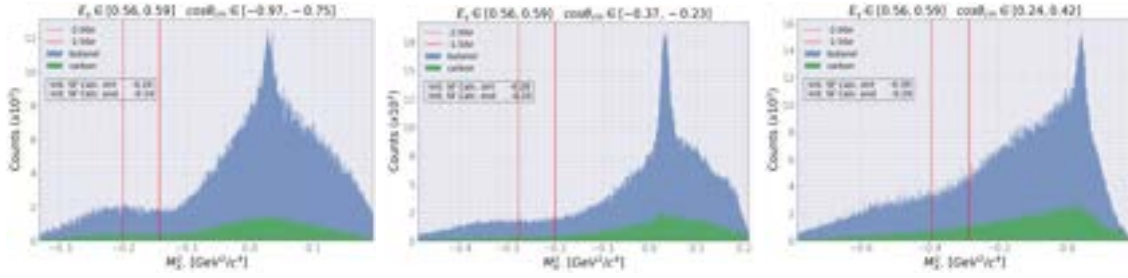
estimates on scale factors are needed for the next steps, fitting parameters were not fine-tuned.



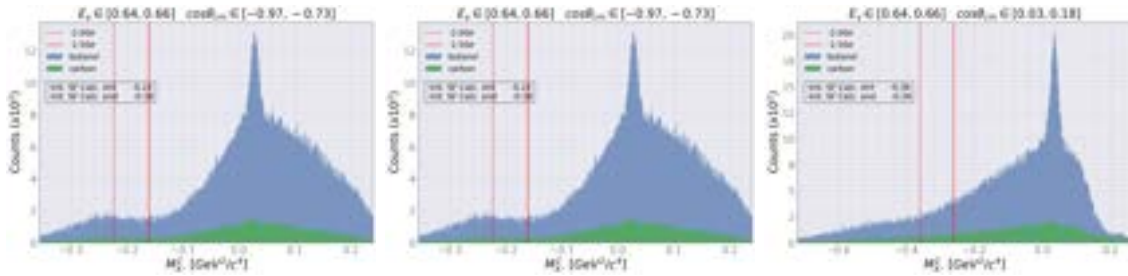
(a) $E_\gamma \in [0.35, 0.40]$



(b) $E_\gamma \in [0.47, 0.51]$

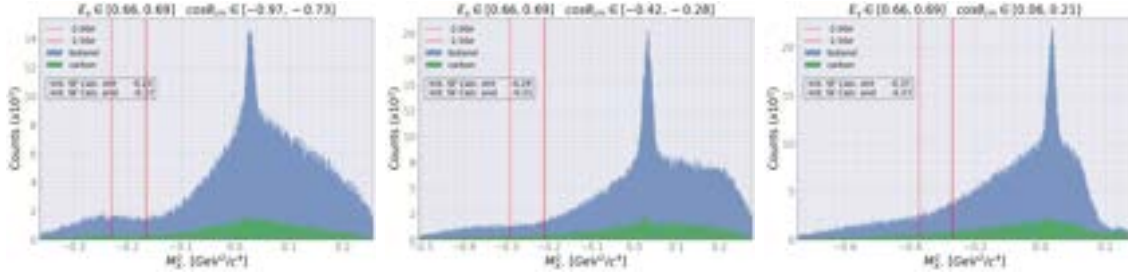


(c) $E_\gamma \in [0.56, 0.59]$

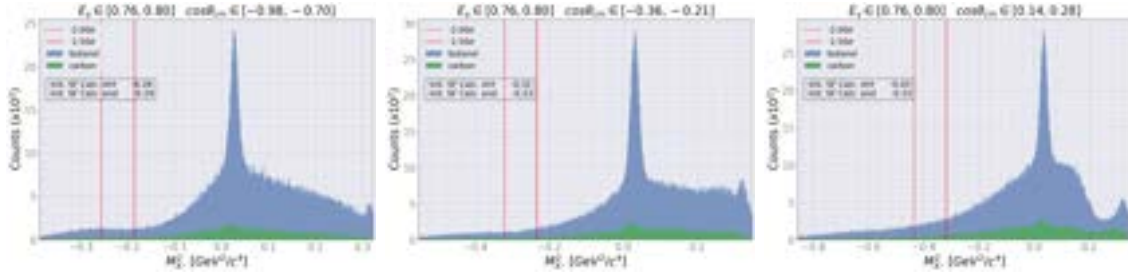


(d) $E_\gamma \in [0.64, 0.66]$

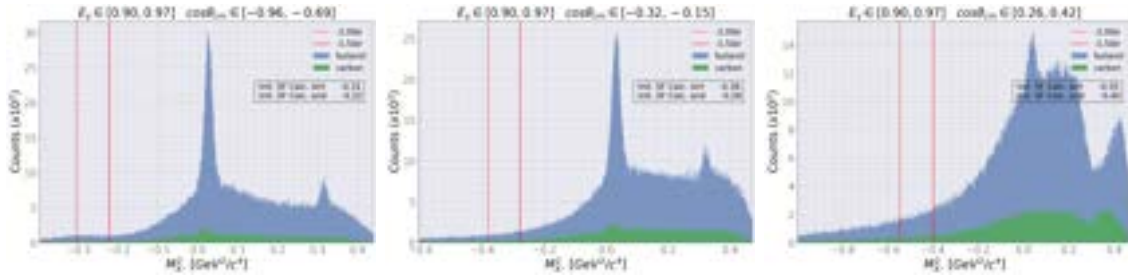
Figure 70: π^0 missing mass squared distributions in selected bins of photon energies E_γ and $\cos\theta_{cm}$ for $E_\gamma \leq 0.71$ GeV. Dotted lines to indicate the regions used for initial scale factor calculation



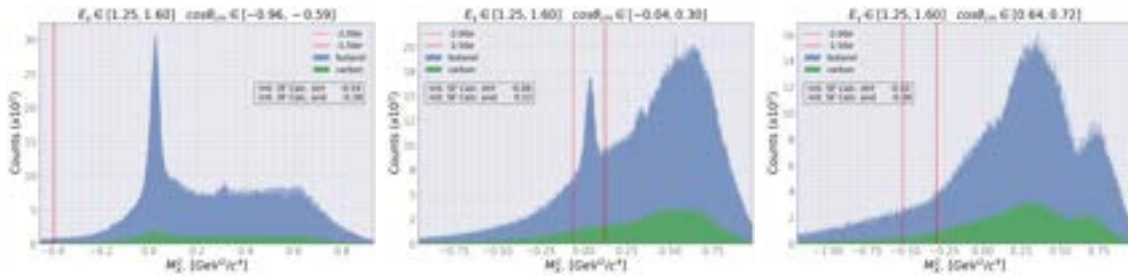
(a) $E_\gamma \in [0.66, 0.69]$



(b) $E_\gamma \in [0.76, 0.80]$

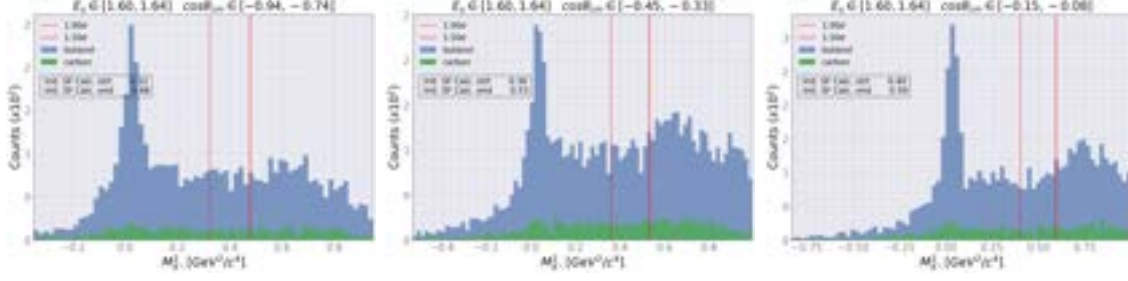


(c) $E_\gamma \in [0.90, 0.97]$

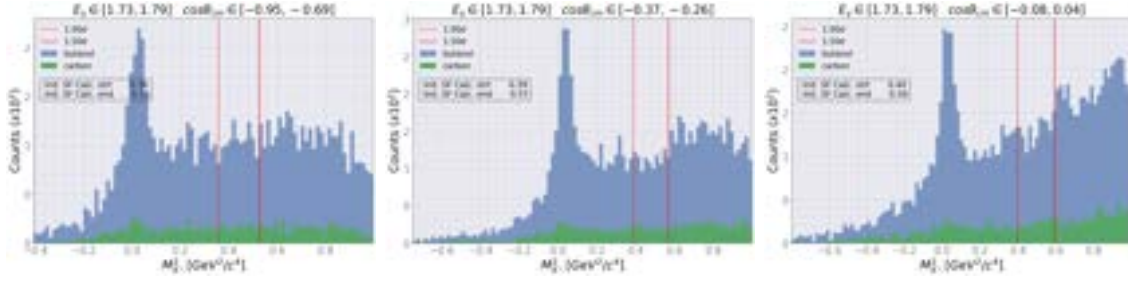


(d) $E_\gamma \in [1.25, 1.60]$

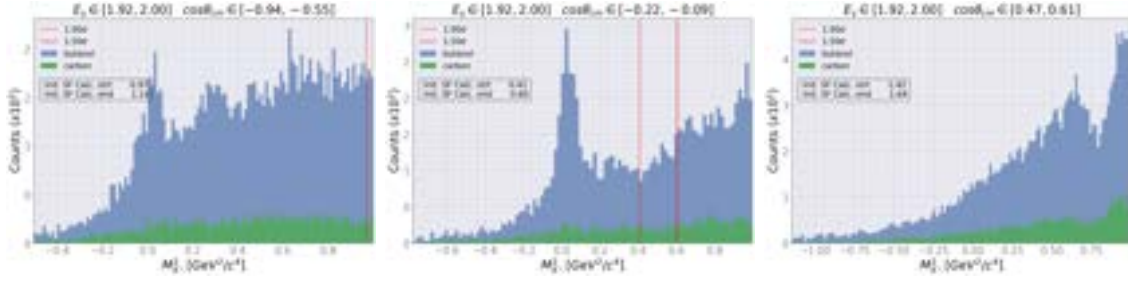
Figure 71: π^0 missing mass squared distributions in selected bins of photon energies E_γ and $\cos \theta_{cm}$ for $E_\gamma = (0.66, 1.6)$ GeV. Dotted lines to indicate the regions used for initial scale factor calculation



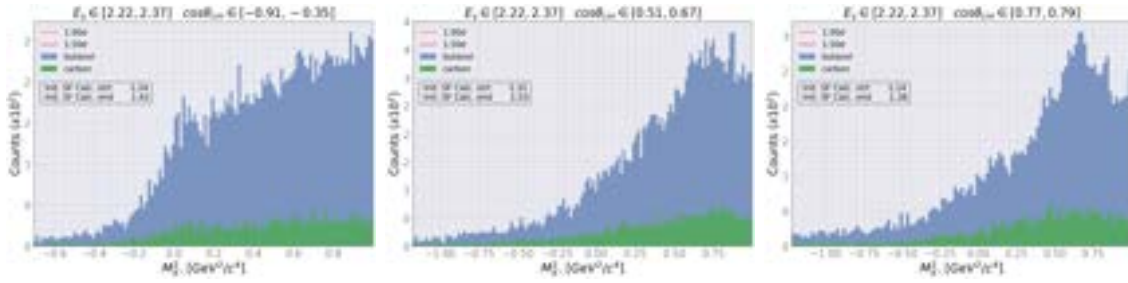
(a) $E_\gamma \in [1.60, 1.64]$



(b) $E_\gamma \in [1.73, 1.79]$

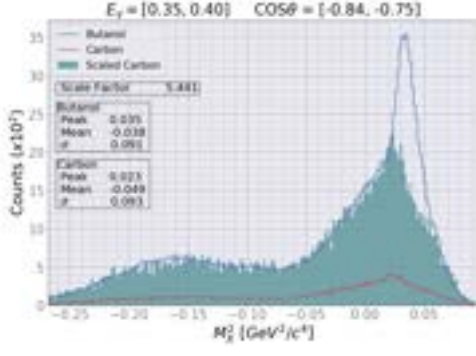


(c) $E_\gamma \in [1.92, 2.00]$

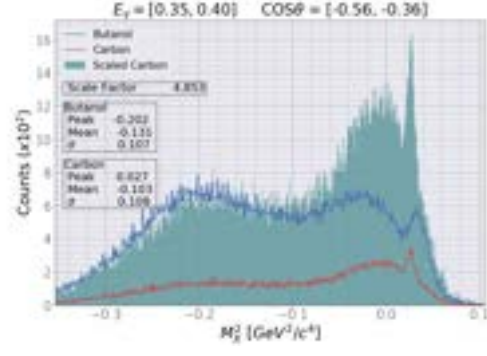


(d) $E_\gamma \in [2.22, 2.37]$

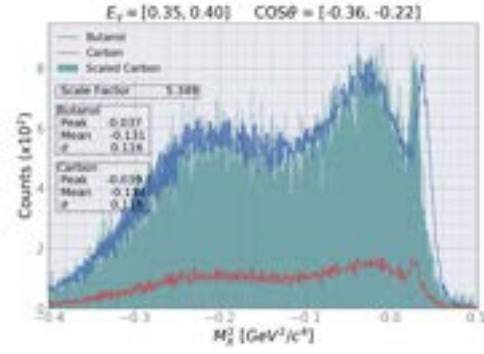
Figure 72: π^0 missing mass squared distributions in selected bins of photon energies E_γ and $\cos \theta_{cm}$ for $E_\gamma = (1.6, 2.4)$ GeV. Dotted lines to indicate the regions used for initial scale factor calculation



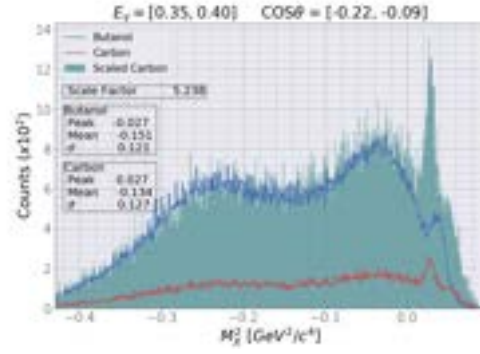
(a)



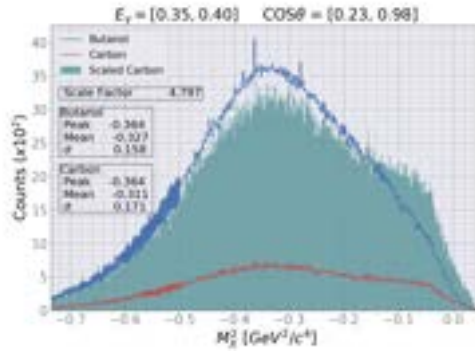
(b)



(c)



(d)



(e)

Figure 73: Example of scaled carbon events using initial scale factors overlaid with butanol distributions for 4 different kinematic bins: (a) shows an example of bins where scaled carbon M_X^2 distribution correctly represents butanol background events, (b) shows an example of bins with unwanted angular dependence, causing discrepancies in M_X^2 distributions for butanol and carbon targets, (c) shows an example of bins where background contribution far exceeds free nucleon signals, but still usable if free nucleon ranges are selected out manually, (d) shows an example of hydrogen contamination on carbon target where free nucleon peak is visible in carbon distribution, (e) is an example of bins in which no apparent free nucleon peaks are observed.

5.1.2 First free proton peak extraction

Free nucleon peaks in M_X^2 distribution of butanol events in each kinematic bin have differing sharpness and peak locations. The start and end points of free nucleon peaks are extracted to be utilized in two of the next steps: to be set as knot positions in splines interpolation as was discussed in Sec. 5.2, improving the fit quality significantly and to be set as limits of integration for dilution factor calculations. Using the initial scale factor, the difference of butanol and scaled carbon distributions for each kinematic bin is computed and the residual is fitted (Fig. 74) using a Gaussian. The start and end positions of the free proton peaks are chosen to be $\pm 3\sigma$ from the peak location, where σ is the standard deviation of the Gaussian used to fit the residual.

When observing the free nucleon peaks, a strong angular dependence of π^0 acceptance is evident in the difference of butanol and scaled carbon distributions. Such dependence is shown by the indistinct shape of the free nucleon peak, in particular at the forward angles in the lower E_γ bins. Such difference in angular dependence for two targets emerges from the different physical target positions along the beam line. If two targets were placed closer to avoid such problems, the classification of the event target would have been compromised and more events would have been discarded. Bins with such non-distinct free nucleon peaks and low statistics (plotted in red in Appendix A Fig. 94 and Fig. 95) have been removed from further analysis. The determination of distinctiveness of free nucleon peaks was based on whether the fitting of the free nucleon peak was successful or not. Therefore, these selections could change as we improve on the fitting procedures. One can easily see the inaccuracy of the extracted free nucleon peak regions as shown in Appendix A Fig. 94 9th column or last row of Appendix A Fig. 95. Free nucleon peak regions will be extracted again and discussed in the next sections with improved scale factors.

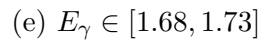
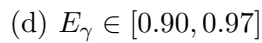
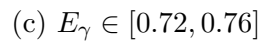
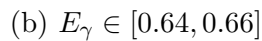
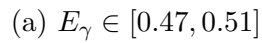


Figure 74: Difference between butanol and initially scaled carbon M_X^2 distributions in selected bins of E_γ and $\cos \theta_{cm}$. Red dotted vertical lines indicate our first estimation on start and end positions of free-nucleon peaks.

5.1.3 Final Scale Factor

Scale factors (α) were improved by using fit results of butanol and carbon M_X^2 distributions, instead of using the number of counts for butanol and carbon events as done in the initial scale factor step. The reasoning is that in most of the bins, a small bump was visible in carbon M_X^2 distribution and even a sharper peak in scaled carbon events as shown in Fig. 75(d). Therefore, scaled carbon data was not a good representation of butanol background events. One possible solution would be to use outer regions far away from free nucleon peaks to guarantee the absence of any hydrogen contamination; for example, using $M_X^2 \in [-3.0\sigma, -2.0\sigma]$ would have excluded free nucleon events for both butanol and carbon. However, as shown in Fig. 78, this solution was not possible due to shifted carbon M_X^2 distributions in certain angular bins; the boxed column shows heavily shifted carbon M_X^2 distributions. To circumvent the usage of such unwanted free nucleon peaks or unnaturally shifted distributions due to unresolved angular dependence, both butanol and carbon M_X^2 distributions were fitted simultaneously to specifically capture and differentiate the background from the signal. Both butanol and carbon free nucleon peaks (μ_{pk}) were fitted with a Gaussian whereas their bound nucleon contributions (f_{bnd}) were fitted with either a fourth order polynomial or a Gaussian [97]:

$$f(m_X^2) = A_1 \cdot \exp\left(-\frac{(m_x^2 - \mu_{pk})^2}{2\sigma_{pk}^2}\right) + f_{bnd}(m_x^2). \quad (77)$$

As shown in Fig. 76 and Fig. 77, the shape of background contribution differs greatly between $E_e = 1.6$ GeV and $E_e = 2.4$ GeV data; results on all angular and energy bins are shown in Appendix A Fig. 97 - Fig. 99. With higher photon energy, events with higher M_X^2 than π^0 peak dominate more on the forward angles and π^0 signals become less apparent; From Sec. 3.10, it was anticipated that π^0 peaks would be reduced in such forward angles. To correspond to such background changes, a

Gaussian ($f_{bnd}(m_x^2) = A_2 \cdot \exp\left(-\frac{(m_x^2 - \mu_{bnd})^2}{2\sigma_{bnd}^2}\right)$) was tried to fit butanol background for lower energy bins and a fourth order polynomial ($f_{bnd}(m_x^2) = p_0 + p_1(m_x^2) + p_2(m_x^2)^2 + p_3(m_x^2)^3 + p_4(m_x^2)^4$) on higher energy bins. For carbon background, a Gaussian sufficed to fit the background for both low and high energy bins. As for the hydrogen contamination in carbon events, none was visible on the higher energy bins. After acquiring a fitting functions for butanol and carbon background, the χ^2 defined below was minimized to obtain final scale factors [108]:

$$\chi^2 = \sum_i^N \frac{[B_{bnd}(i) - \alpha C_{bnd}(i)]^2}{B_{bnd}(i) - \alpha^2 C_{bnd}(i)}, \quad (78)$$

where $B_{bnd}(i)$ and $C_{bnd}(i)$ are fitting functions for butanol and carbon background, evaluated at midpoint of an i^{th} bin of butanol and carbon distributions. The statistical uncertainties in the final scale factors were obtained from the χ^2 minimization routine, combined with the uncertainties in fitting background of butanol and carbon M_X^2 distributions.

The resulting scale factors were used to obtain scaled carbon M_X^2 distributions; some examples are shown in Fig. 75. The overall scale factors ranged roughly between 4 to 8 as shown in Fig. 79. The observed oscillating pattern in Fig. 79 is an indication of angular dependence due to unresolved systematic effects; the tracking resolution varied depending on the polar angle. There are many possible sources for this angular dependence and the most likely candidate is the momentum correction that induced angular dependence in certain angular bins as indicated in Fig. 78. This, however, does not have an impact on the final result of E since the missing mass selection routine (Sec. 3.10) was carried out bin by bin.

When carbon events are scaled up to match the butanol background, many underlying effects become visible: shifting of the whole carbon M_X^2 distribution in certain bins, level of hydrogen contamination, and lack of carbon data points to allow scaled carbon to be used as a representation of butanol background. In this analysis, the

scale factor was only used to extract butanol free nucleon ranges which are used for missing mass squared selection step in Sec. 3.10.

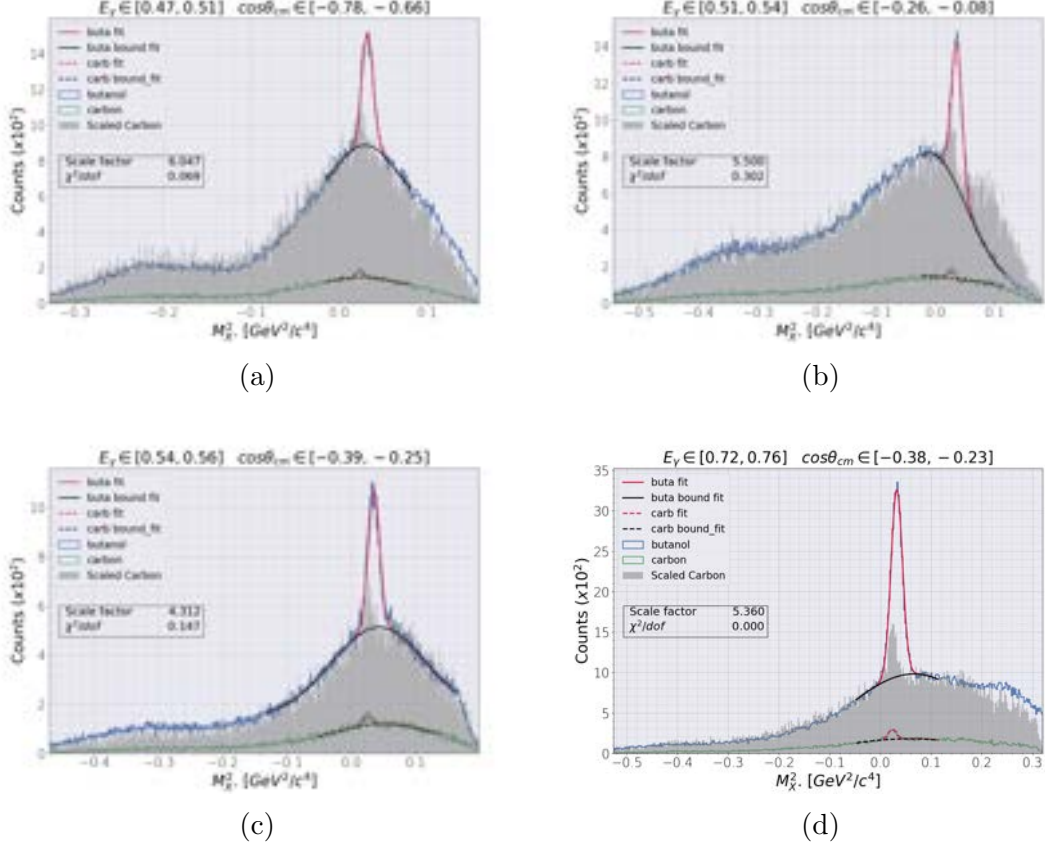
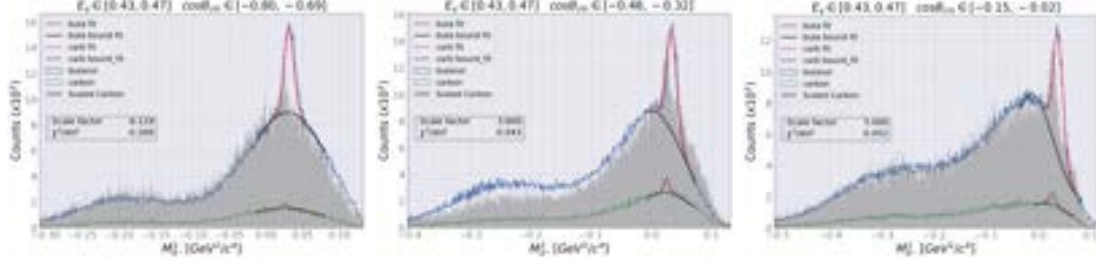
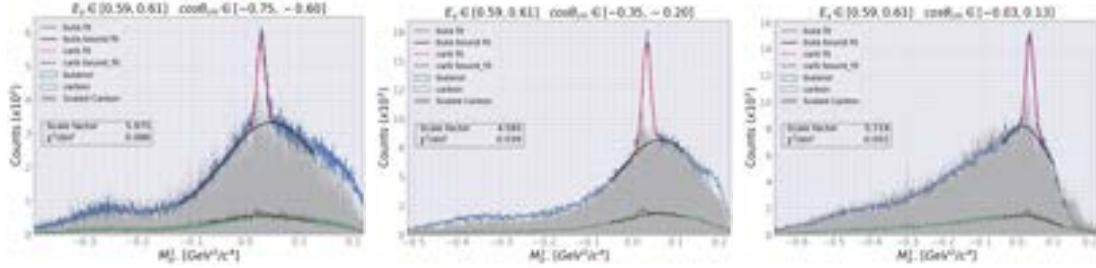


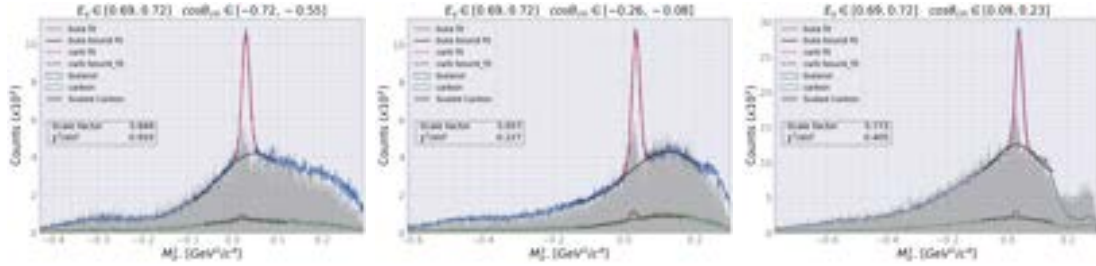
Figure 75: Example of scaled carbon events using final scale factors overlaid with butanol distributions for four distinctive kinematic bins. (a) shows an example of bins where scaled carbon M_X^2 distribution correctly represent butanol background events. (b) shows an example of bins with unwanted angular dependence, causing discrepancies in M_X^2 distributions for butanol and carbon targets. (c, d) show an example of strong hydrogen contamination on carbon target where scaled carbon fails to correspond to butanol background events.



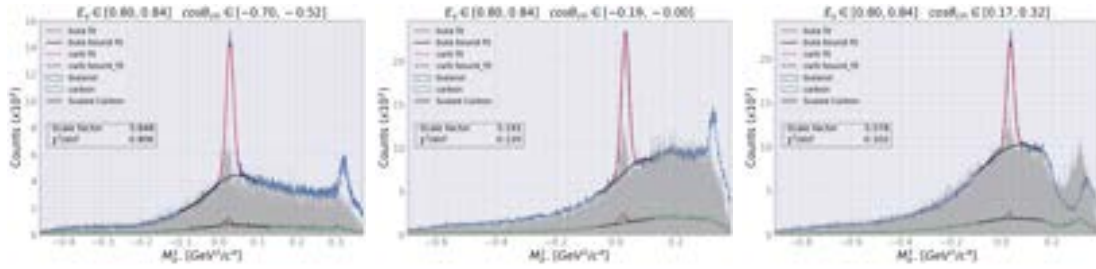
(a) $E_\gamma \in [0.43, 0.47]$



(b) $E_\gamma \in [0.59, 0.61]$



(c) $E_\gamma \in [0.69, 0.72]$



(d) $E_\gamma \in [0.80, 0.94]$

Figure 76: Scaled carbon M_X^2 distribution overlaid over butanol and carbon distribution with fitting results on butanol and carbon distributions for $E_\gamma \leq 0.94$ GeV and $\cos\theta_{cm} \in [-1, 1]$.

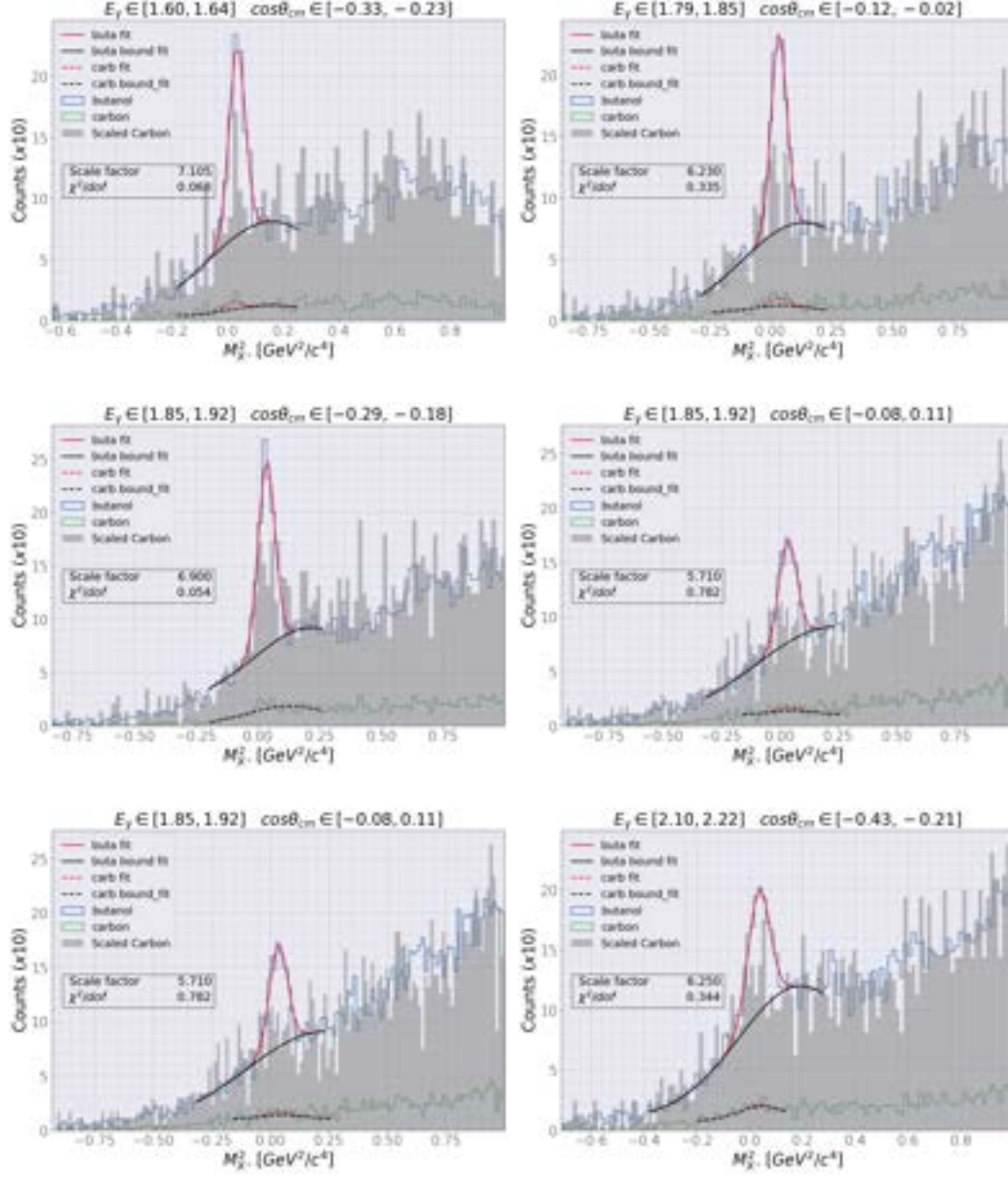


Figure 77: Scaled carbon M_X^2 distribution overlaid over butanol and carbon distribution with fitting results on butanol and carbon distributions for $1.6 \leq E_\gamma \leq 2.4$ GeV and $\cos\theta_{cm} \in [-1, 1]$.

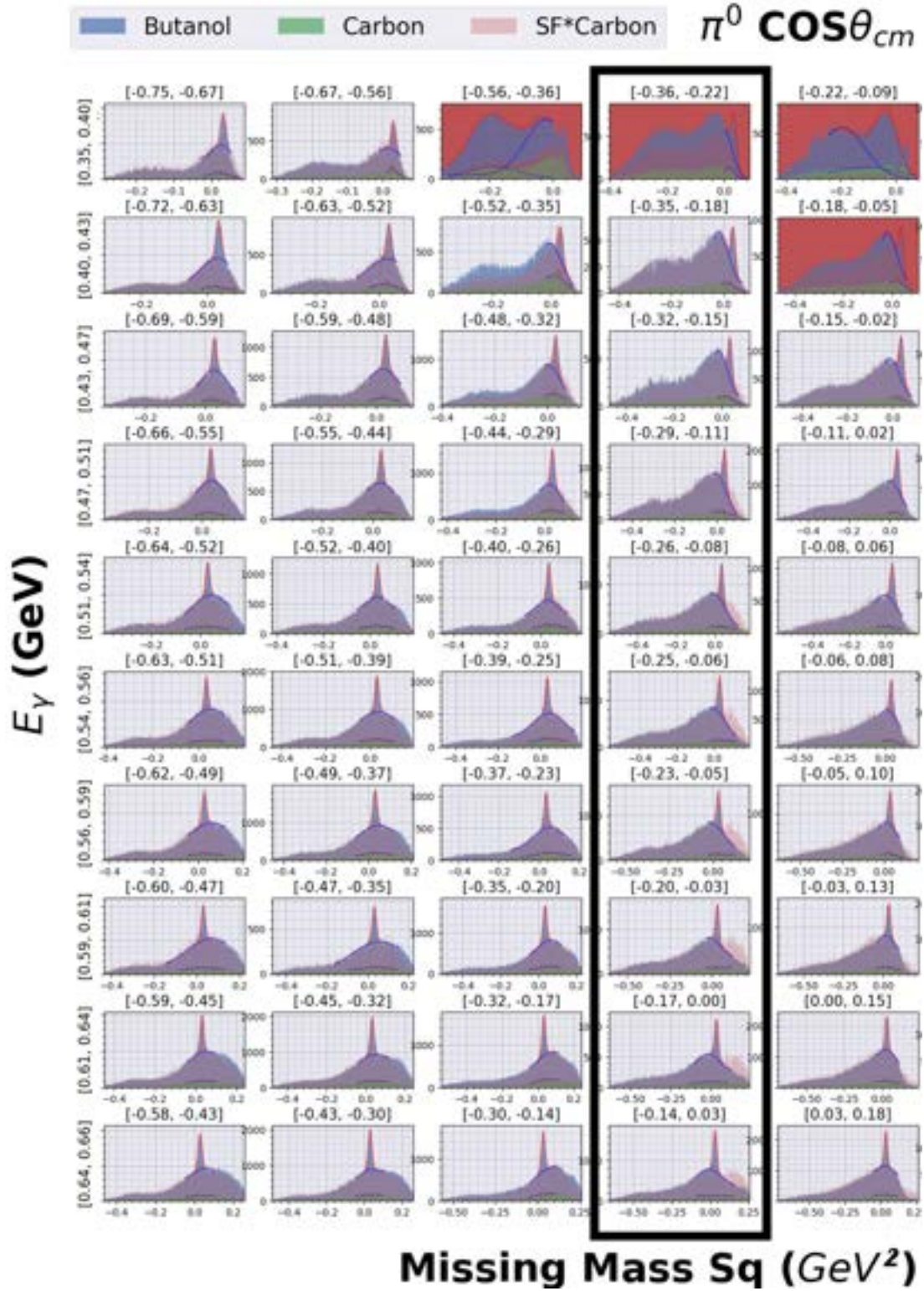


Figure 78: Scaled carbon M_X^2 distribution overlaid over butanol and carbon distribution with fitting results on butanol and carbon distributions for $E_\gamma \in [1.6, 2.4]$ GeV and $\cos\theta_{cm} \in [-1, 0.2]$. Bins with negligible free nucleon peaks are plotted out in red.

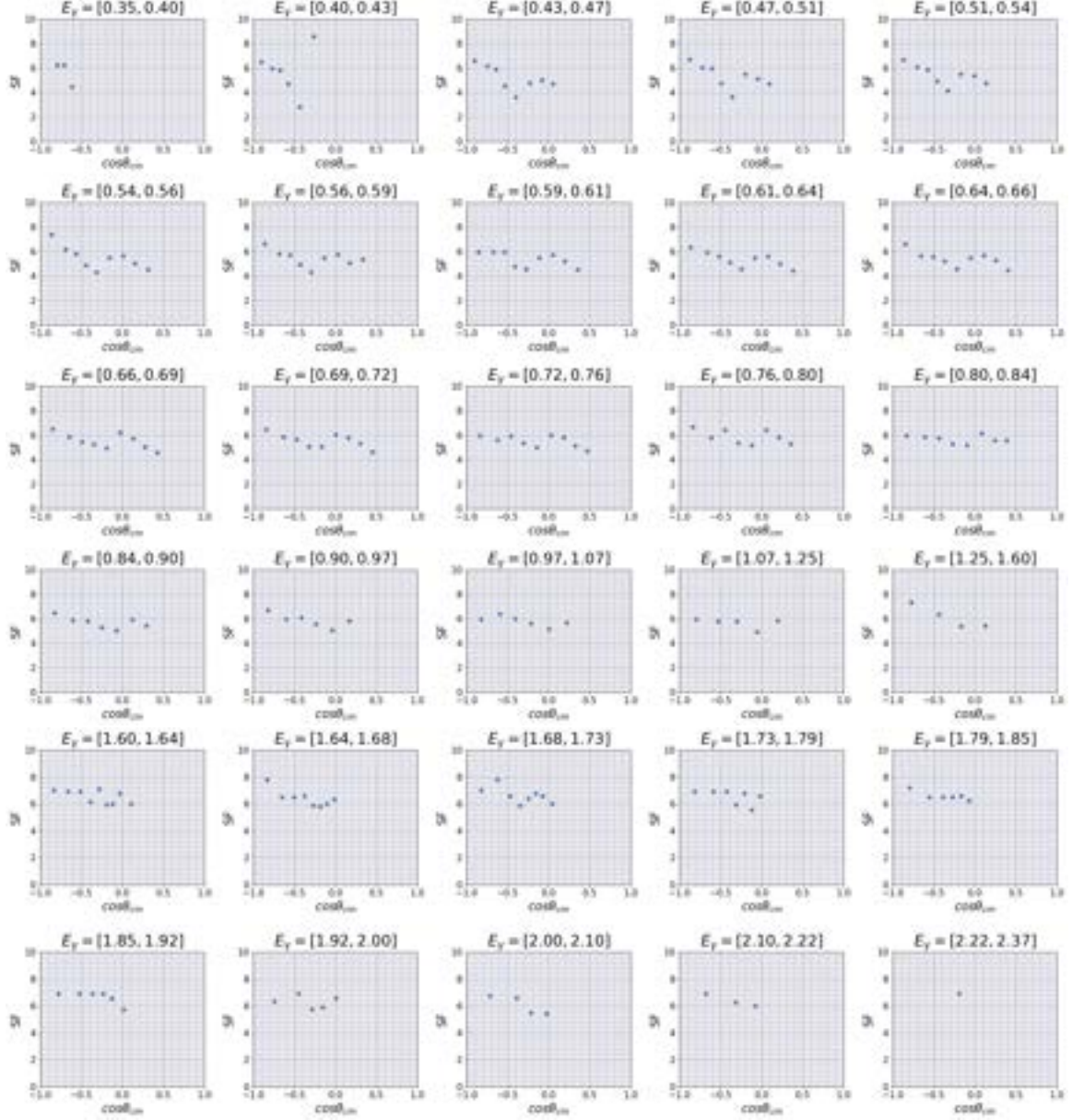
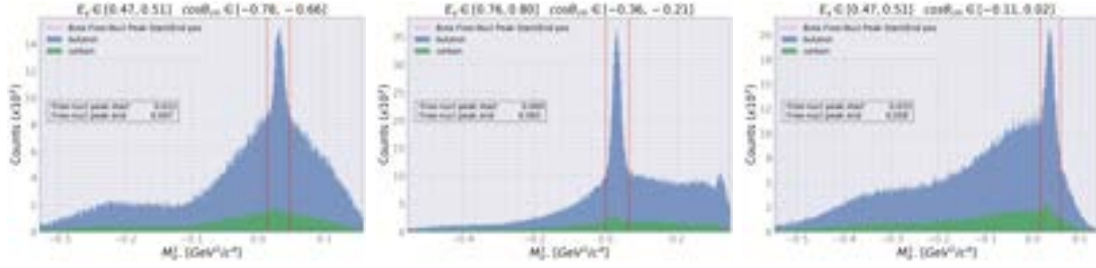


Figure 79: Final scale factor obtained by χ^2 minimization for each kinematic bin.

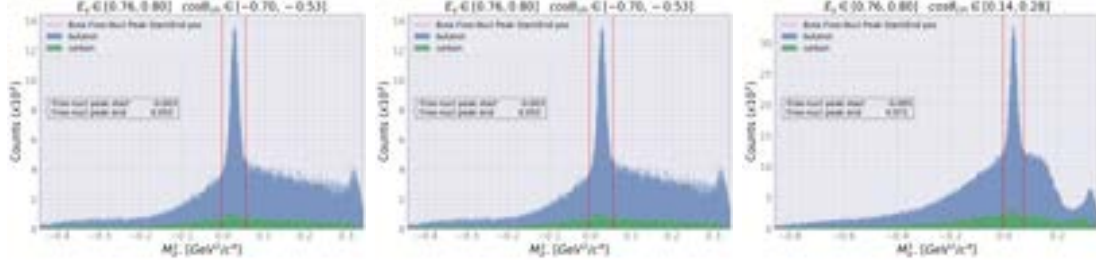
5.1.4 Second free proton peak extraction

The butanol free nucleon ranges were again extracted using the improved scale factor from the previous step. Exactly the same steps were taken as in the initial extraction step where butanol M_X^2 distributions were subtracted by scaled carbon M_X^2 distributions and the residuals are fitted with a Gaussian. The range of the free nucleon region

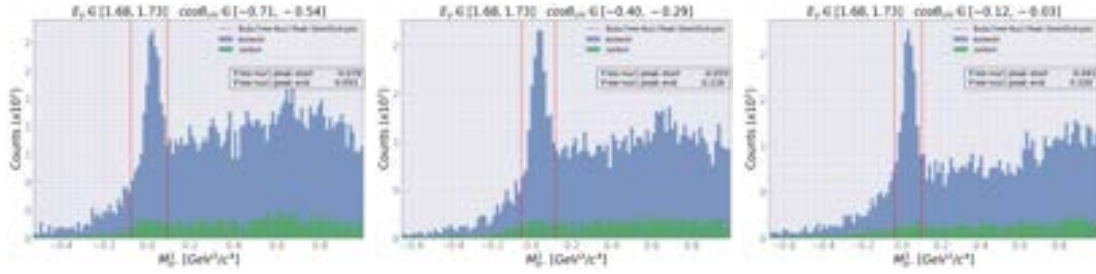
was chosen to be $\pm 3\sigma$ from the peak location, where σ is the standard deviation of the Gaussian used to fit the residual. In certain bins, the range was set manually due to effects from hydrogen contamination causing excessively subtracted yields due to amplified free nucleon events in the scaled carbon yields, leading to failure in fitting the residual distribution. The finalized free nucleon ranges are indicated by dotted red vertical lines in Fig. 80. The final extraction ranges for all angular and energy bins are shown in Appendix A Fig. 100 - Fig. 102. In higher energy bins, free nucleon ranges were set slightly wider than in the low energy bins because π^0 peak widths were larger in general as seen in Fig. 81. The π^0 peaks were widened due to detector resolution and applied corrections. Determining the free nucleon range was the most important step in this analysis as it directly sets the range for the computation of the dilution factor (Sec. 5.3) and the missing-mass-squared selection (Sec. 3.10). For future systematic studies on the selection of the free nucleon range, the final extraction range of the free nucleon range will be varied in small increments to study its effect on our final results of the helicity asymmetry E .



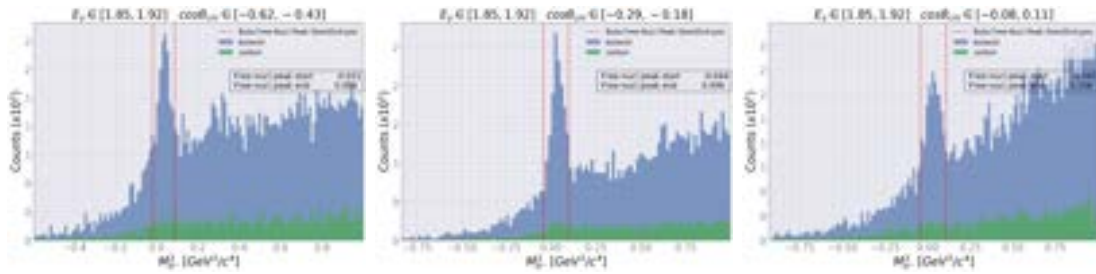
(a) $E_\gamma \in [0.47, 0.51]$



(b) $E_\gamma \in [0.76, 0.80]$



(c) $E_\gamma \in [1.68, 1.73]$



(d) $E_\gamma \in [1.85, 1.92]$

Figure 80: Final extraction of butanol free nucleon ranges in M_X^2 distributions. Red dotted lines indicate extracted start and end positions of free nucleon events.

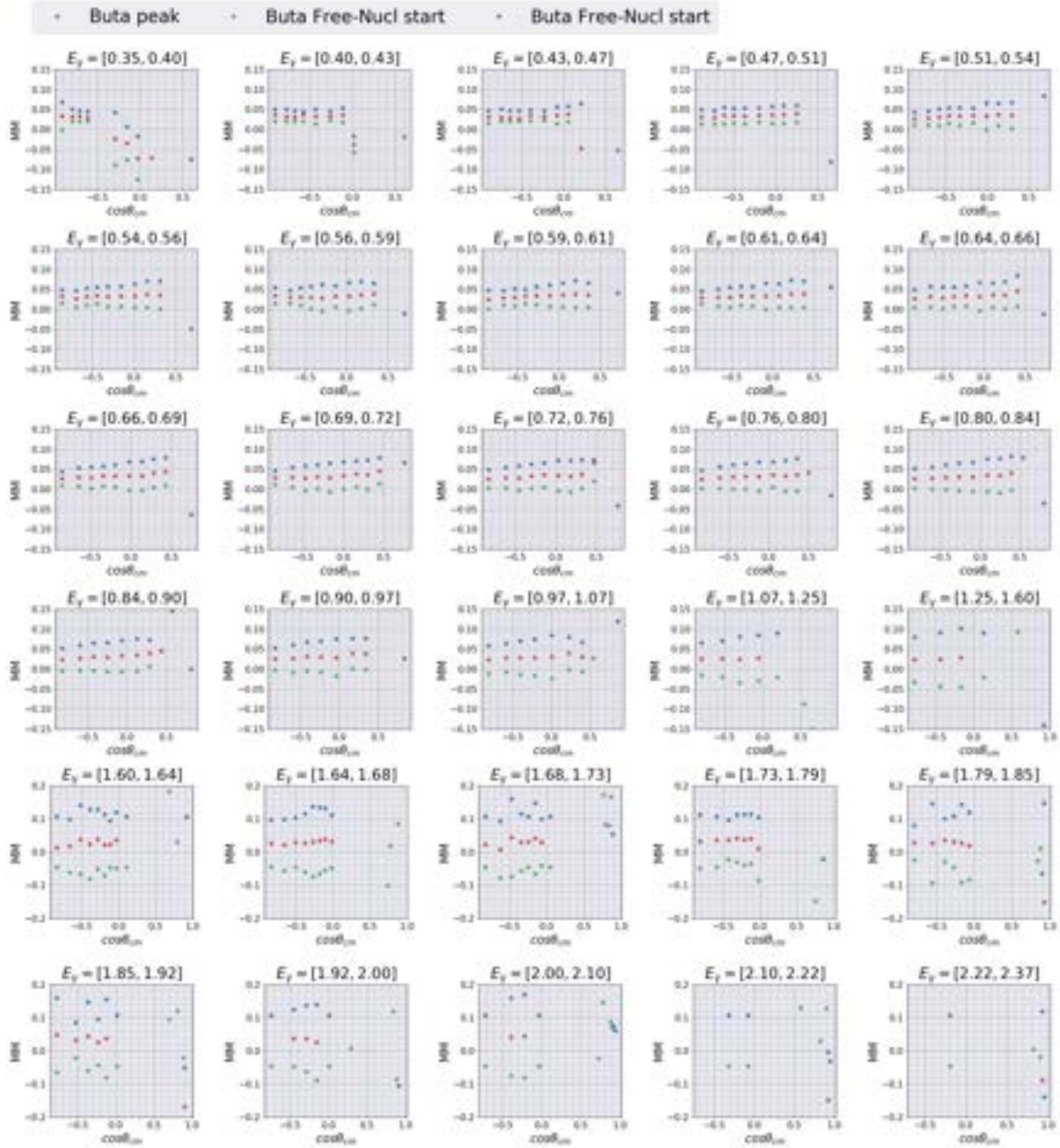


Figure 81: Overview of final butanol free nucleon peak ranges. Red dots are peak locations and green/blue dots are left/right ends of the butanol free nucleon peaks

5.2 Scale Factor: Alternative Method

Another approach attempted to obtain scale factors to be used for background subtraction in butanol M_X^2 distribution was the use of cubic spline interpolation to fit the

carbon M_X^2 distribution. Carbon events in each kinematic bin were fitted by a cubic spline interpolation method, following previous studies done by collaborators [98], for which the obtained spline polynomials are to be multiplied by a scale factor to represent bound nucleon backgrounds of butanol M_X^2 distributions. Splines interpolation is basically a piecewise function consisting of fit functions defined between each knot positions. The only constrain is that the polynomials and the first and second derivatives of the polynomials must have identical values at the knot positions. This method was attempted to better fit the carbon distribution in a wider range of M_X^2 distribution. The aspects that determined the quality of fitting by splines polynomials were the number of knots, positions of knots, fitting ranges, and appropriate constraints on fitting parameters. The start and end positions of the butanol free-nucleon peak, obtained from the previous section, were set as fixed knot positions for spline interpolation and none between these endpoints. Fit functions for butanol ($B(m_x^2)$), carbon ($C(m_x^2)$), and butanol free-nucleon peak ($F(m_x^2)$) are described as below:

$$\begin{aligned}
C(m_x^2) &= \begin{cases} p_1(m_x^2) &= a_1 + b_1(m_x^2) + c_1(m_x^2)^2 + d_1(m_x^2)^3, & m_x^2 \in [x_0, x_1] \\ \vdots & \\ p_i(m_x^2) &= a_i + b_i(m_x^2) + c_i(m_x^2)^2 + d_i(m_x^2)^3, & m_x^2 \in [x_i - 1, x_i] \\ \vdots & \\ p_n(m_x^2) &= a_n + b_n(m_x^2) + c_n(m_x^2)^2 + d_n(m_x^2)^3, & m_x^2 \in [x_n - 1, x_n] \end{cases} \\
F(m_x^2) &= A \exp\left(\frac{-(m_x^2 - \mu_0)^2}{2\sigma^2}\right) \\
B(m_x^2) &= \alpha C(m_x^2) + F(m_x^2),
\end{aligned} \tag{79}$$

where α , x_i , μ_0 , and σ , are scale factor, knot positions, butanol free-nucleon peak position, and standard deviation, respectively. Final scale factors were obtained by

minimizing the χ^2 function:

$$\chi^2 = 2 \left[\sum_i [B(m_i^2) - N_i^B \ln B(m_i^2)] + \sum_j [C(m_j^2) - N_j^C \ln C(m_j^2)] \right], \quad (80)$$

where N_i^B and N_i^C are number of events in i^{th} bin of butanol and carbon distributions, respectively. The χ^2 function (Eq. (80)) is the negative logarithm of the likelihood functions for butanol and carbon distributions which yield the least biased estimates of the scale factor [124], also known as Cash C-statistic [125]. Fig. 82 shows successful cases where splines polynomials fitted carbon M_X^2 distribution successfully while ignoring the small bumps caused by hydrogen contamination. However, in most bins, the effects of hydrogen contamination could not be ignored and worsened the fit quality dramatically, leading to inaccurate scale factors. Hence, this approach was discarded in this analysis and the previously described scale factor method (Sec. 5.1) was employed in our analysis.

The next FROST experiment (g9b) was designed to place the carbon target further downstream from the butanol target, avoiding the formation of ice and providing better separation between butanol and carbon events. As a result, this method yielded much improved results for extracting correct scale factors [98] in g9b experiments.

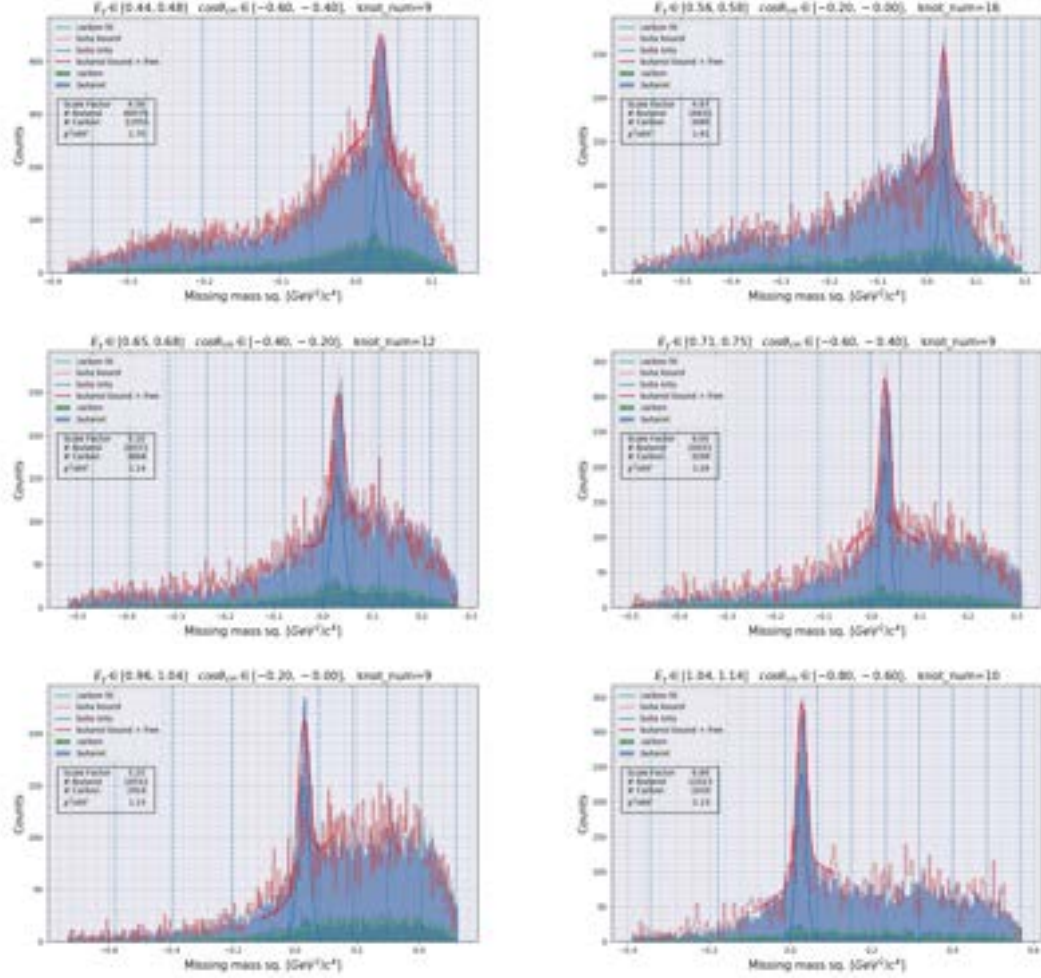


Figure 82: Selected examples of successfully obtained scale factors by fitting carbon M_X^2 distribution by cubic splines interpolation. Cases with $\chi^2/dof \lesssim 2.0$ were selected to be a criterion for good fits. Dotted blue vertical lines show knots positions defined for cubic splines interpolation.

5.3 Dilution Factor

Because we are determining the helicity asymmetry E over both free nucleon events and bound nucleon events combined, we apply the dilution factor to our final result of E to correspond to only free nucleon interactions; The dilution factor is a ratio of

how many free nucleon events occurred to the total number of events:

$$D_f = \frac{B_{tot} - B_{bnd}}{B_{tot}}, \quad (81)$$

where B_{bnd} is the number of bound nucleon events and B_{tot} is the total number of events (free and bound). The value of B_{bnd} was obtained by integrating the fitting function $B_{bnd}(x)$ that describes background contribution of butanol M_X^2 distribution, discussed in the Sec. 5.1 [97]. Few functions have been attempted to fit the butanol background and for this part of the analysis, a Gaussian is used since the range of the integration is very small: the start and end positions of butanol free nucleon peak as shown in Fig. 80. On the other hand, the value of B_{tot} was obtained directly by multiplying the number of counts in each bin by the width of the bins. The results on the dilution factors over all bins are shown in Fig. 83 and one can notice a common maximum in $\cos\theta_{cm} \in [-0.5, 0]$ and a smooth downward concavity in bins with reasonable statistics. Such downward concavity is an indication of how the free proton interactions have scattering angle limitation depending on the incoming photon energies as discussed in Sec. 3.10. Simply by dividing the number of free protons (10) in butanol over total nucleons (74) in butanol, a theoretical low limit of dilution factor is set to 0.135 as indicated by dotted horizontal lines in Fig. 83.

In utilizing the dilution factor to account for the background contribution, an assumption was made such that the background events yield the helicity asymmetry value of zero. In other words, the background events consist of only the bound nucleon events and are free of any other reaction channels that might cause the asymmetry to fluctuate. To test this assumption, one can calculate the asymmetry E from the events in the outer bands of the M_X^2 distributions where there exist no π^0 events. If this measured asymmetry comes out to be zero, we can safely assume that the background events only contain bound nucleon events. For example, there could be a

probability that our measured proton is from the double pion channel ($\gamma p \rightarrow p\pi^+\pi^-$) and it is included in the background contribution. Since there is one more pion to consider when calculating the M_X^2 , the M_X^2 value from double pion channel will reside on the right side of the π^0 peak. One way to address this is to widen the M_X^2 selection range incrementally to the right of the π^0 peak and measure the asymmetry E . If the asymmetry fluctuates and becomes larger, then it is indicated that some contribution from the double pion channel is present. These studies were not included in this thesis, but will be conducted in near future.



Figure 83: Dilution factors for each kinematic bin obtained by using the Gaussian fit on the background events of butanol M_X^2 distributions. Dotted black horizontal lines indicate a low limit (0.135) of dilution factors.

5.4 Extraction of Helicity Asymmetry E

After obtaining dilution factors, our final helicity asymmetry E is determined in each kinematic bin via:

$$E = \frac{1}{D_f P_z P_\gamma} \left[\frac{N_{1/2} - N_{3/2}}{N_{1/2} + N_{3/2}} \right], \quad (82)$$

where D_f , P_z , P_γ , $N_{3/2}$, and $N_{1/2}$ are dilution factor, target polarization, photon polarization, number of events with helicity 3/2, and number of events with helicity 1/2, respectively. The derivation of the E equation is explained in more detail in Sec. 1.3.5. The target and electron beam polarization values in each experiment run are plotted in Fig. 35 and presented in Table 13 whereas the signs of target polarization and half-wave plate status are listed in Table 18.

The event selection routines (Sec. 3) were carried out individually for each of seven runs. For the scale and dilution factors (Sec. 5), the run periods with the same electron beam energy were grouped together for the calculation.

The half-wave plate was occasionally inserted to reverse the helicity states by 180° . The purpose of the half-wave plate was to provide a systematic check to make sure there was no helicity-dependent performance change of the laser at the injector.

Run Period	Run Number	e^- beam energy (GeV)	Half-wave Plate	Target pol. sign
1	55521-55536	1.645	OUT	—
2	55537-55552	1.645	IN	—
3	55557-55594	1.645	OUT	+
4	55604-55625	2.478	OUT	—
5	55630-55678	2.478	OUT	+
6	56164-56193	2.478	OUT	+
7	56196-56223	2.478	OUT	—

Table 18: The polarization states of each run period. The signs (—) and (+) denote anti-parallel and parallel to the beam axis.

As for the statistical uncertainties in E , a generic error propagation equation is used:

$$\begin{aligned}
\sigma_E^2 &= \sigma_{N_{1/2}}^2 \left(\frac{\partial E}{\partial N_{1/2}} \right)^2 + \sigma_{N_{3/2}}^2 \left(\frac{\partial E}{\partial N_{3/2}} \right)^2 + \sigma_{P_T}^2 \left(\frac{\partial E}{\partial P_T} \right)^2 + \\
&\quad \sigma_{P_\gamma}^2 \left(\frac{\partial E}{\partial P_\gamma} \right)^2 + \sigma_{D_f}^2 \left(\frac{\partial E}{\partial D_f} \right)^2 \\
&= E^2 \left[\left(\frac{\sigma_{D_f}}{D_f} \right)^2 + \left(\frac{\sigma_{P_\gamma}}{P_\gamma} \right)^2 + \left(\frac{\sigma_{P_T}}{P_T} \right)^2 + \frac{4N_{1/2}N_{3/2}}{N_{tot}(N_{3/2} - N_{1/2})^2} \right],
\end{aligned} \tag{83}$$

where $\sigma_{N_{1/2}} = \sqrt{N_{1/2}}$ and $\sigma_{N_{3/2}} = \sqrt{N_{3/2}}$ since counting statistics follow Poisson distributions. The statistical uncertainties in determining dilution factor (D_f) come from fitting butanol and carbon M_X^2 distributions and integration of the bound nucleon fit function over butanol in the free nucleon regions. The photon polarization statistical uncertainty ($\sigma_{P_\gamma}^2$) is determined using Eq. (52).

6 Results and Discussion

The following chapter encloses a discussion on the final results on the helicity asymmetry E in comparison to CBELSA/TAPS results [112] and PWA predictions from SAID [110], MAID2007 [111], and BnGa [71] groups. This thesis's result has been added to the SAID PWA database and a new SAID prediction has been generated. I examine how the addition of my results into the SAID database will aid our understanding of the missing resonance problem. Lastly, the prospects for successfully incorporating machine learning in event selection to improve future works are considered.

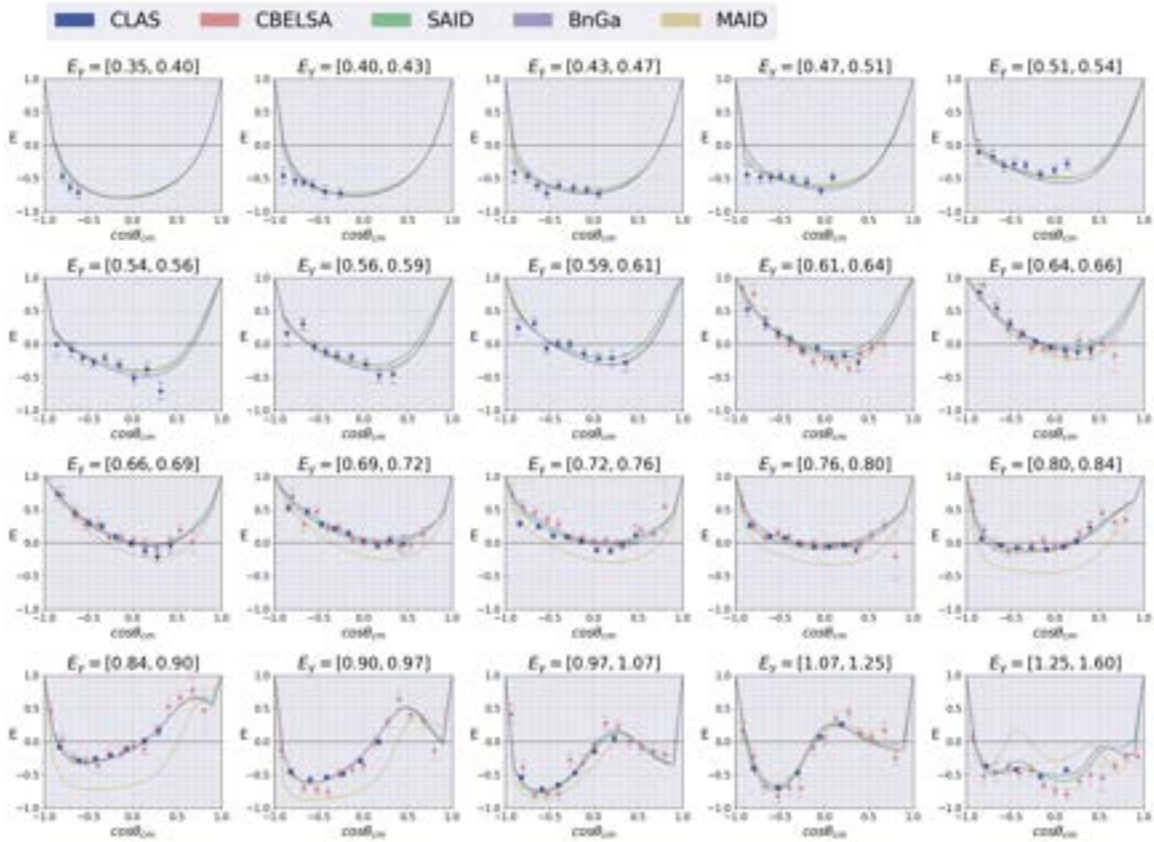


Figure 84: Helicity asymmetry E for $E_\gamma \in (0.35, 1.6)$ GeV. The result of this analysis is shown in blue dots (HAE) whereas CBELSA/TAPS [112] experimental results, SAID [110], BnGa [71], and MAID2007 [111] predictions are shown in red, green, purple, and yellow, respectively. Only statistical uncertainties are included for the results of this analysis.

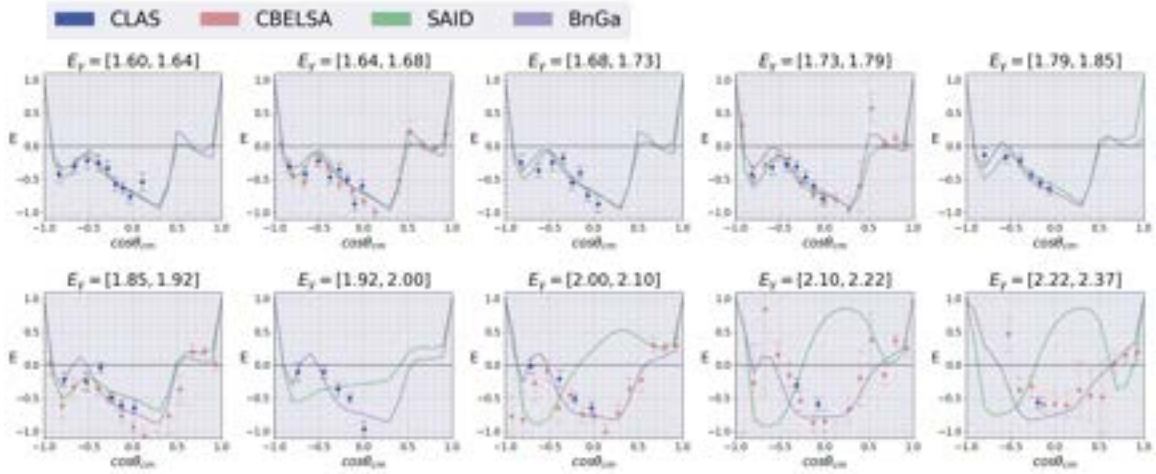


Figure 85: Helicity asymmetry E for $E_\gamma \in (1.60, 2.4)$ GeV. The result of this analysis is shown in blue dots (HAE) whereas CBELSA/TAPS [112] experimental results, SAID [110], and BnGa [71] predictions are shown in red, green, and purple, respectively. MAID2007 [111] predictions are only valid under $E_\gamma \leq 1.6$ GeV. Only statistical uncertainties are included for the results of this analysis.

6.1 Results Interpretation

The new measurements are compared to the experimental data from CBELSA/TAPS [112] and partial-wave analysis (PWA) predictions from SAID [110], MAID2007 (for $E_\gamma < 1.6$ GeV) [111], and BnGa2014 [71]. The results for the helicity asymmetry E for $\gamma p \rightarrow \pi^0 p$ channel from the g9a/ FROST experiment are shown in Fig. 84 for $E_\gamma \in [0.35, 1.6]$ GeV and Fig. 85 for $E_\gamma \in [1.60, 2.4]$ GeV. The results are shown in the π^0 production center-of-mass (cm) frame angle and the photon energy binning with only statistical uncertainties. Since much of the forward angle bins were heavily populated with background events and insignificant π^0 signals, bins were determined specifically to ensure a similar number of π^0 signals in each bin (Sec. 3.9). The statistical uncertainties included uncertainties from counting event numbers ($N_{1/2}$ and $N_{3/2}$), photon and target polarization, and computation of dilution factors. For the measurement of photon beam polarization via Møller polarimeter, there were unknown systematic uncertainties which caused each measurement's fluctuation to be

larger than their overall statistical uncertainties (Fig. 37). Because the origin of such systematic effects was unknown, a standard deviation of all Møller measurements was used instead [123]. Although the systematic uncertainty study is not included in this thesis, one can speculate that the dominant sources of systematic uncertainties stem from the electron beam and target polarization, the hydrogen contamination of the carbon target, and the scale and dilution factors.

In $E_\gamma \in [0.35, 0.80]$ GeV ($W \in [1.23, 1.54]$ GeV) region, the distribution of E shows a single global minimum without any oscillatory behavior which suggests only a small number of resonances are involved. The possible resonances involved in this energy range are $\Delta(1232)3/2^+$, $N(1440)1/2^+$, $N(1520)3/2^-$, and $N(1535)1/2^-$. The zero crossing behavior starts to shift from $\cos(\theta_{cm}) = -0.9$ to $\cos(\theta_{cm}) = 0$ and the global minimum shifts from $E = -0.7$ to $E = 0$ which indicates more resonances coming into effect; one can see from Fig. 38 that the $\Delta(1232)$ peak becomes insignificant at $E_\gamma \approx 0.5$ GeV and non-resonant terms (u- and t-channels) start to become stronger as well as more resonances. If only $N(1535)1/2^-$ was contributing, measured E should have been a constant in all $\cos \theta_{cm}$ bins; $N_{3/2}$ would vanish and $E \propto 1/(D_f P_z P_\lambda)$.

By contrast, in $E_\gamma \in [0.80, 1.25]$ GeV ($W \in [1.54, 1.79]$ GeV) region, our E distribution starts to show oscillatory behaviors, suggesting the emergence of more resonances. The allowed resonances in these regions are all the resonances whose mass falls into $W \in [1.54, 1.79]$ GeV: $N(1650)1/2^-$, $N(1675)5/2^-$, $N(1680)5/2^+$, $N(1700)3/2^-$, $N(1710)1/2^+$, $N(1720)3/2^+$, $\Delta(1600)3/2^+$, $\Delta(1620)3/2^+$, $\Delta(1700)3/2^-$, and $\Delta(1750)1/2^+$. Also, resonances whose masses are near $m \approx 1.8$ GeV are allowed in this region since baryon resonances have broad widths and the tail of some other resonance may contribute in this energy range. In this energy range the PWA predictions show two local minimum. Our agreement with CBELSA/TAPS data in $\cos \theta_{cm} = [-1.0, 0.2]$ confirms the validity of our result.

Finally, in $E_\gamma \in [1.25, 2.4]$ GeV ($W \in [1.79, 2.31]$ GeV) region, the oscillatory behavior changes and zero crossing is not observed in this region. The global minimum starts to appear at $\cos(\theta_{cm}) \approx 0$ and deepens as E_γ increases and more resonances emerge.

6.2 Comparison to CBELSA/TAPS Data

The CBELSA/TAPS experiment at the ELSA facility in Bonn measured the helicity asymmetry E for the reaction channel $\gamma p \rightarrow \pi^0 p \rightarrow \gamma \gamma p$ with circularly polarized photons beams and longitudinally polarized targets. CBELSA had an angular coverage for photon detection of $2^\circ \leq \theta \leq 156^\circ$ whereas the CLAS detector covered $8^\circ \leq \theta \leq 140^\circ$ for detecting charged particles. The main difference to our approach was that CBELSA/TAPS reconstructed π^0 events from two reconstructed final state photons from electromagnetic showers that photons induced while interacting with the Crystal Barrel calorimeter; outgoing protons were considered as missing particles whose mass was calculated using the kinematics of incoming photons and two reconstructed final state photons. Reconstructing π^0 signals from two reconstructed final state photons allowed CBELSA/TAPS to have more data points in the $\cos \theta_{cm} = [0.5, 1.0]$ region, whereas in the CLAS FROST experiment reconstruction, reconstructing π^0 events by measuring outgoing protons allowed us to have more statistics in the $\cos \theta_{cm} = [-0.97, 0.25]$ region. In the angular region $\cos \theta_{cm} > 0$, our effective dilution factors tend downwards (Fig. 83) which suggests decreasing π^0 peaks and larger background contributions. The CBELSA/TAPS data covered photon energy ranges of $E_\gamma = [0.6, 2.31]$ GeV and our photon range was $E_\gamma = [0.35, 2.4]$ GeV. Our new FROST measurements extended the experimental information on the E asymmetry down to $E_\gamma = 0.35$ GeV and reached the $\Delta(1232)$ $3/2^+$ region, where CBELSA data is absent. Even with a difference in angular coverage and detector acceptances, the agreement with the CBELSA/TAPS result above $E_\gamma = 0.61$ GeV

for helicity asymmetry E confirms the validity of the result obtained in this analysis.

6.3 Comparison to PWA Predictions

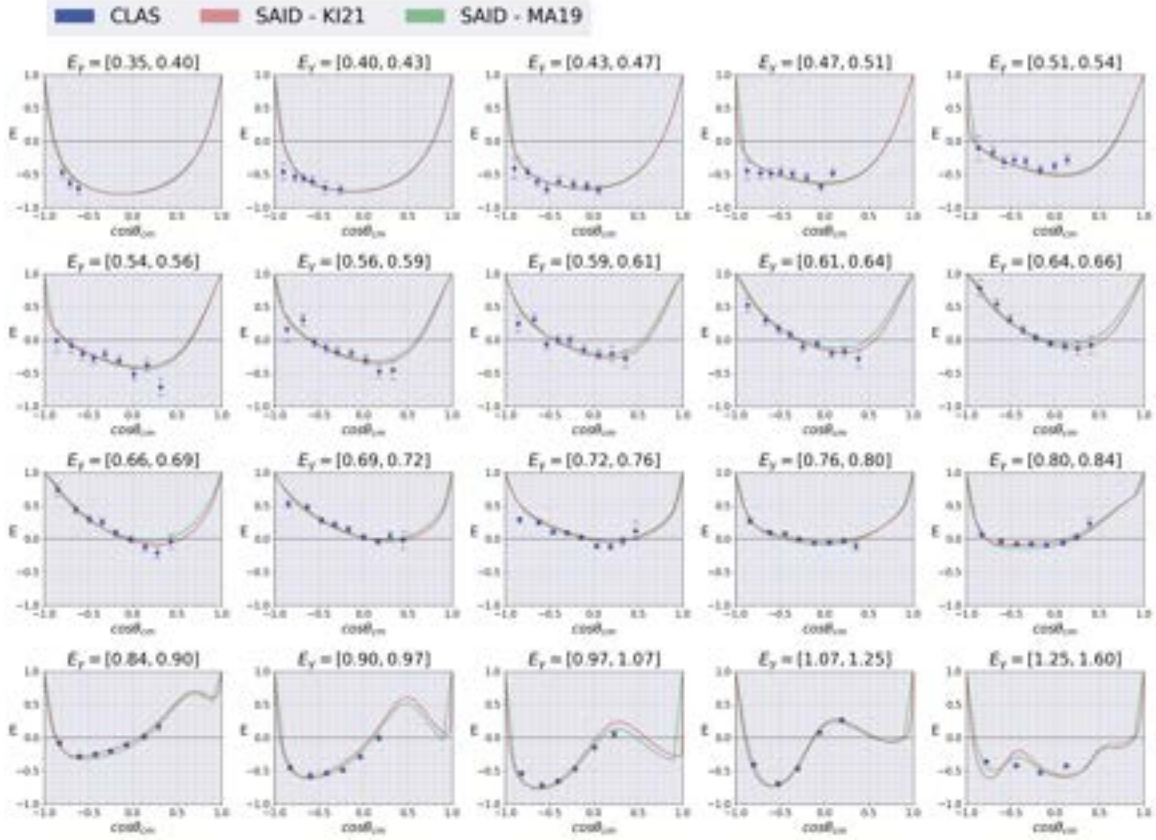


Figure 86: The comparison of the helicity asymmetry E predictions from the new SAID solution KI21 (with the inclusion of this thesis's results) and the previous SAID solution MA19 [110] for $E_\gamma \in (0.35, 1.6)$ GeV. This thesis's result is denoted as HAE.

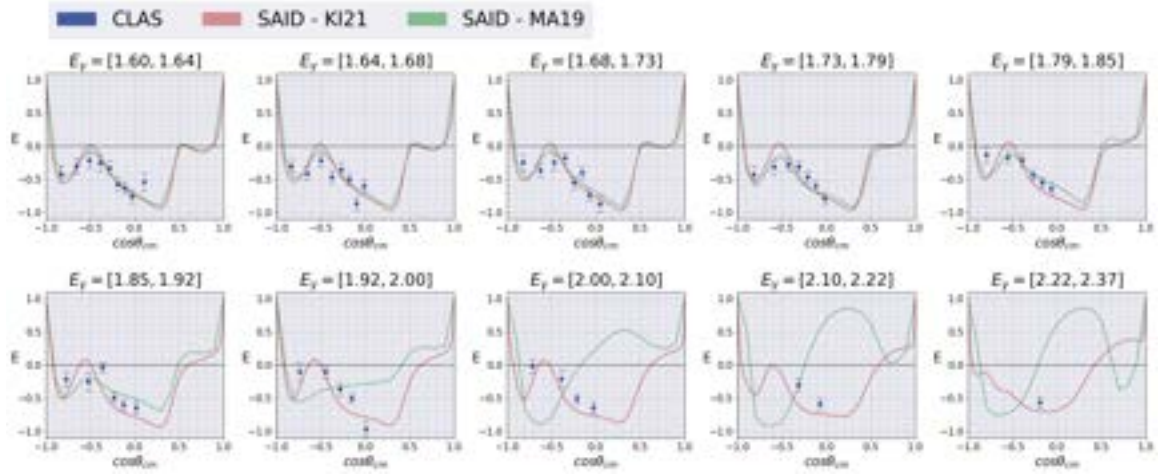


Figure 87: The comparison of the helicity asymmetry E predictions from the new SAID solution KI21 (with the inclusion of this thesis's results) and the previous SAID solution MA19 [110] for $E_\gamma \in (1.60, 2.4)$ GeV. This thesis's result is denoted as HAE.

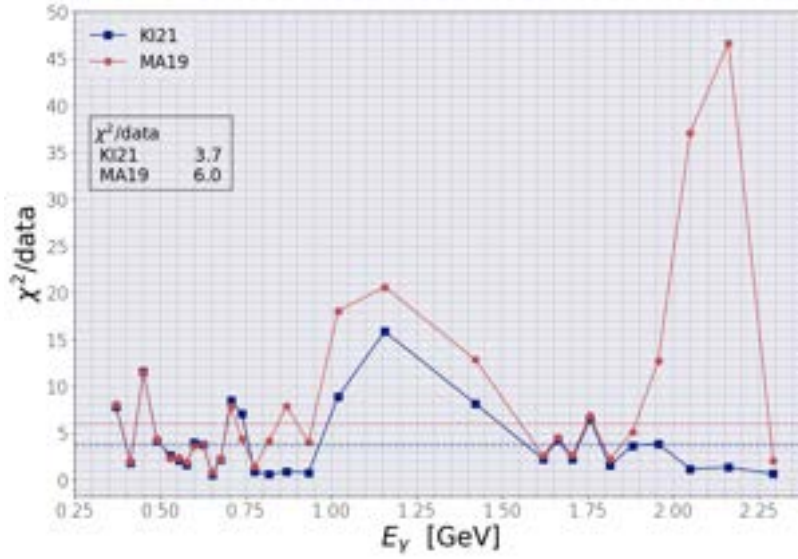


Figure 88: The comparison of χ^2 per data point for the new SAID solution KI21 (with the inclusion of this thesis's results) and the previous SAID solution MA19 [110]. The χ^2 per data point values are averaged over all photon energy E_γ bins: the blue dotted line for KI21 ($\langle \chi^2/data \rangle = 3.7$) and the red dotted line for MA19 ($\langle \chi^2/data \rangle = 6.0$).

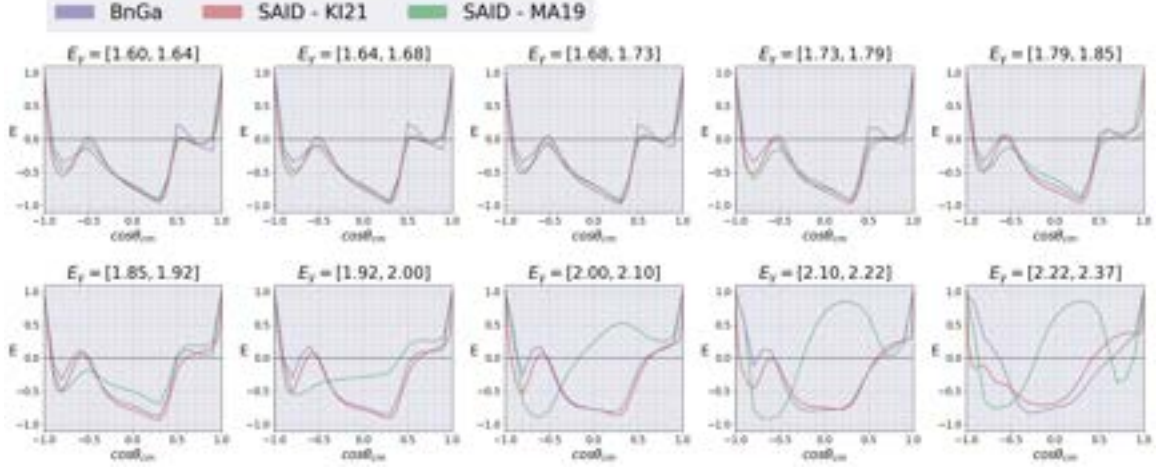


Figure 89: The comparison of the helicity asymmetry E predictions from the new SAID solution KI21 (with the inclusion of this thesis's results) and the BnGa prediction for $E_\gamma \in (1.60, 2.4)$ GeV.

In the $E_\gamma \in [0.35, 1.92]$ GeV region, SAID and BnGa predictions showed promising agreements with our results. However, in $E_\gamma \in [1.92, 2.10]$ GeV region, SAID starts to deviate from our result and BnGa predictions. Since SAID aims to be as model-independent as possible and is a primarily data-driven PWA, the inclusion of our new E measurements into the world database will improve SAID fits in higher energy ranges.

MAID's predictions matched our results at lower energy bins of $E_\gamma \in [0.35, 0.64]$ GeV, but began to deviate at higher energies. The global minimum were deepened as photon energy increased in $E_\gamma \in [0.64, 0.97]$ GeV region and started to rise above our measurement and other PWA predictions in $E_\gamma \in [0.97, 1.60]$ GeV. MAID2007 predictions were not valid above $E_\gamma \geq 1.6$ GeV.

This thesis's result has been added to the SAID PWA database and a new SAID prediction (KI21) has been generated as shown in Figs. 86 – 87. The previous SAID prediction (MA19) includes CBELSA data, but not this thesis's result. One can see that the impact of our results in the SAID prediction starts to become significant at the photon energy $E_\gamma \geq 1.79$ GeV. Even with a small number of measurements in

those high energy bins, our result is very impactful to SAID predictions because a relatively wide angle bin is chosen in those energy bins to reduce the statistical uncertainty. By comparing the BnGa predictions and the new SAID (KI21) predictions in Fig. 89, it is clear that the discrepancies between these two PWA models have been significantly reduced in the energy ranges $E_\gamma = [1.85, 2.4]$ GeV.

The quality of the SAID fits can be assessed by considering a form of χ^2 which can quantify the difference between the data points and the new fits. During the fitting process in PWA, the data points become weighted and go through a normalization process which introduces a normalization constant (X) for each angular distribution. The χ^2 function that is minimized during the fit is given by:

$$\chi^2 = \sum_i \left[\frac{X\theta_i - \theta_i^{expt}}{\epsilon_i} \right]^2, \quad (84)$$

where i , θ_i^{expt} , θ_i , and ϵ_i denote the label for each data point within the angular distribution, an individual measurement (E in this case), the corresponding SAID PWA prediction, and the statistical uncertainty for the measurement, respectively. The total χ^2 per data point in all energy bins is plotted in Fig. 88. It is evident that our result has reduced the overall χ^2 per data point and specifically improved the SAID predictions in the energy ranges of $E_g = [0.75, 1.65]$ GeV and $E_g = [1.79, 2.4]$ GeV.

Since SAID's Chew-Mandelstam (CM) K-matrix approach uses the fit results of the πN and ηN elastic scattering data to form the resonance spectrum, the inclusion of our result into the SAID database will not introduce new resonances in SAID predictions. However, the pion photoproduction data are used explicitly in SAID to fine-tune the photo-decay couplings of CM K-matrix which ultimately results in reduced uncertainties of resonance parameters and better predictions on polarization observables. On the other hand, MAID and BnGa PWA methods can form new resonances with the new pion photoproduction data.

6.4 Future Works

The angular dependence (θ and ϕ) of π^0 missing mass squared distributions were the main challenges in extracting π^0 signals accurately. The visibility of π^0 signals varied significantly in different scattering angular bins. Such dependence was minimized by determining the angular bins based on the amount of π^0 events present in each $\cos\theta_{cm}$ range (Sec. 3.9). A finer angular binning in $\cos\theta_{cm} = [0.5, 1.0]$ could have been attempted for events in $E_\gamma = [0.35, 1.6]$ GeV at the expense of increasing uncertainties. However, given the lack of π^0 signals in those regions (Appendix A Fig. 100 – Fig. 102), no such attempt was made in this thesis.

For azimuthal angular (ϕ) dependence, the offsets were corrected by applying momentum corrections (Sec. 3.4), developed by Strauch [108]. Although, the momentum corrections seemed to correct π^0 peaks' ϕ dependence (Fig. 42), it also introduced some θ dependence (Fig. 43) which might have caused the uniform shifting of carbon M_X^2 distributions in certain angular bins. Such unstable carbon M_X^2 distributions along with the hydrogen contamination on carbon targets prohibited the usage of carbon events for background subtraction of butanol events. As an alternative, only the fit results on butanol events' background and π^0 peaks were used for computing the dilution factors in this analysis.

Our π^0 missing mass squared values were found to be around 0.025 GeV^2 for the low energy runs ($E_e = 1.6 \text{ GeV}$) and 0.03 GeV^2 for the high energy runs ($E_e = 2.4 \text{ GeV}$) (Fig. 59), which deviated significantly from the actual value of $m_{\pi^0}^2 = 0.018 \text{ GeV}^2$. Two possible explanations would be the order of how energy loss and momentum corrections were applied and the use of the momentum correction package that was built for recoiling π^+ instead of a proton. In this analysis, energy loss corrections, which assume the direction of the photon beam to be aligned with the z -axis and no ϕ dependence, were applied first. Afterward, momentum corrections were applied to correct ϕ and θ dependence. One can study the impact of correcting

the ϕ dependence via the momentum correction on the effectiveness of the energy loss correction simply by reversing the order at which these two corrections were applied. The momentum correction will be revisited and improved to correspond to recoiling protons rather than π^+ as done in Strauch [108] momentum correction package.

One of the key findings of this analysis was the testing of the deep learning algorithms in nuclear physics experiments, which in our case, was attempted to minimize hydrogen contamination in the carbon data. If successful, it would allow a significant increase in the body of the E data missed in previous FROST analyses [106, 109]. It was found that well defined training data are mandatory for classification tasks in nuclear physics experiments. The reason lies in the inability to obtain absolute certainties in truth values of any training data containing identifications of subatomic particles. A list of possible solutions to circumvent such problems are listed in Sec. 4.4. For our case of classifying events with photons interacting with free nucleons versus bound nucleons, an application of probabilistic deep learning to quantify and include the uncertainties in training data in the final predictions would be the next feasible step. Although acceptance studies were not required to compute the helicity asymmetry E , in order to place a correctly emphasized or constrained weights on certain classifying parameters, further acceptance studies are also needed.

After corrections on event selection methods and the development of probabilistic deep learning are complete, systematic studies on each of the event selection steps will be conducted. The findings will then be reported to the FROST/g9a run group and will work towards publication of this analysis in a peer-review journal.

6.5 Summary

The presented results on helicity asymmetry E for $\gamma p \rightarrow \pi^0 p$ reaction channel with circularly polarized photons and longitudinally polarized protons show a promising agreement with the PWA predictions in $E_\gamma = [0.35, 1.92]$ GeV and with CBELSA/

TAPS data in $E_\gamma = [0.35, 2.4]$ GeV. The reduced discrepancies between PWA models by the inclusion of this thesis's result into the SAID database and the agreement with CBELSA/TAPS' data show that the results of this work are consistent with previous findings. The addition of our results into the world database will then further improve PWA fits in extracting the resonance contribution and reducing the uncertainties in the parameters of known resonances, especially in the energy ranges of $E_\gamma = [1.79, 2.4]$ GeV.

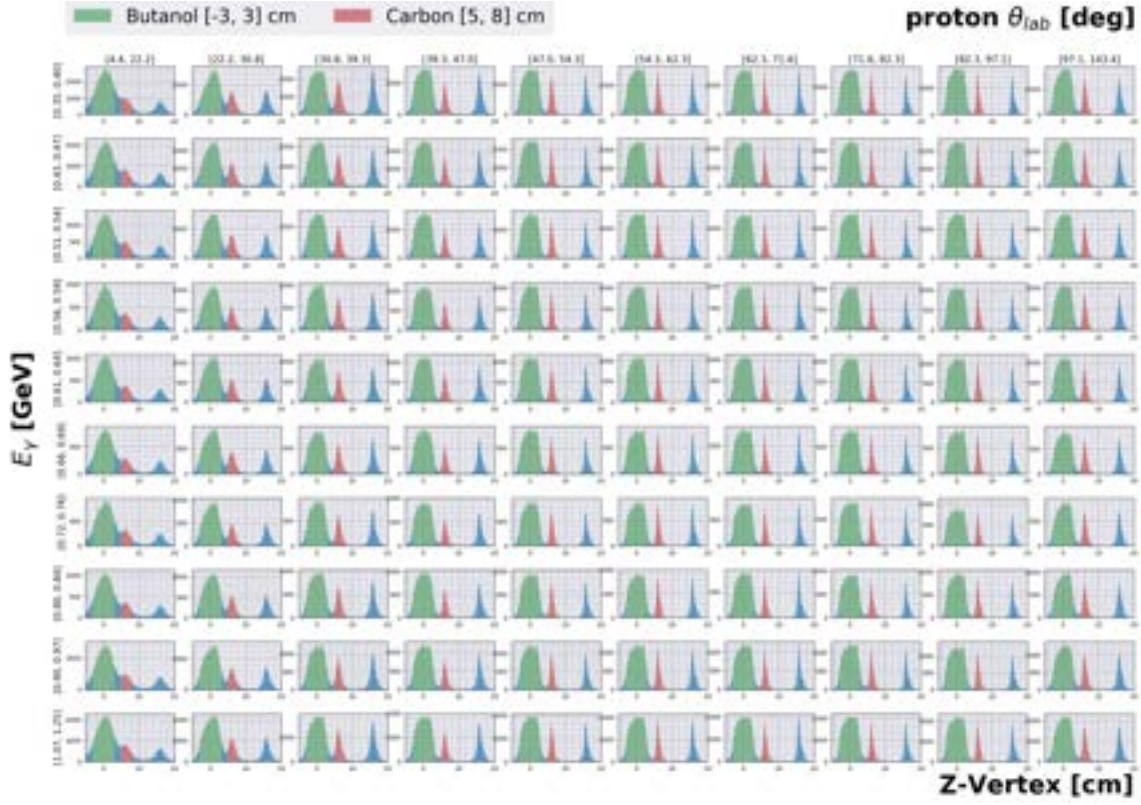
The possibility of using machine learning techniques to accomplish event selection and background subtraction was thoroughly investigated. A robust development in handling uncertainties in contaminated data is especially needed when machine learning algorithms are to be utilized in nuclear physics experiments.

Appendix A Additional plots

This section is dedicated for additional plots to display the kinematic values over all ranges of angles and energies as an overview. One can see where the interested quantities start to become distinct and at which angular and energy ranges the detector has good resolutions.

Z event vertex resolution

The tracking information provided the z event vertex positions of all $\gamma p \rightarrow \pi^0 p$ events. However, the detector's resolution was heavily varied at different angular ranges. Fig. 90 gives an overview of z event vertex positions of all events and the highlighted areas (in green for butanol and red for carbon) indicate the selection range for each of the target types. This plot is used for Z vertex event selection in Sec. 3.8.2 and for training data selection in Sec. 4.3



Initial scale factor selection ranges

Fig. 91 - Fig. 93 show the ranges in missing mass squared (M_X^2) distribution at which the initial scale factor calculations were performed in Sec. 5.1.1.

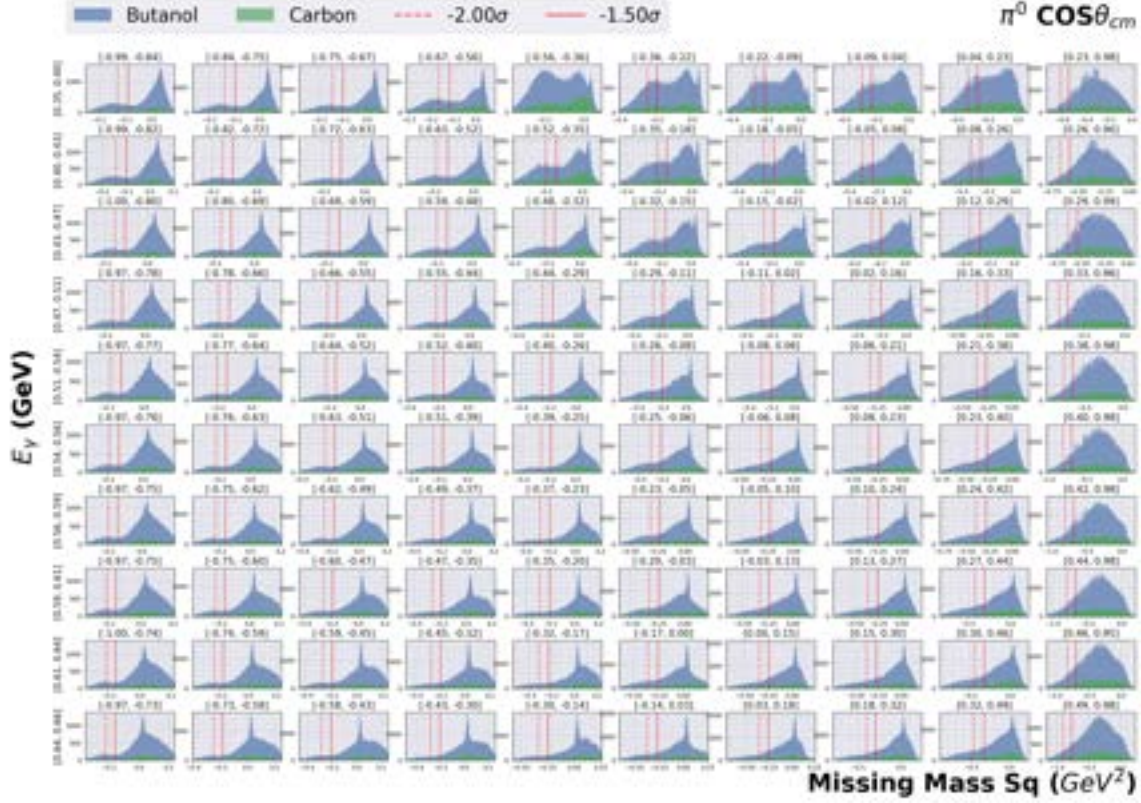


Figure 91: π^0 missing mass squared distribution partitioned in photon energies E_γ and $\cos\theta_{cm}$ for $E_\gamma \leq 0.71$ GeV. Dotted lines to indicate the regions used for initial scale factor calculation

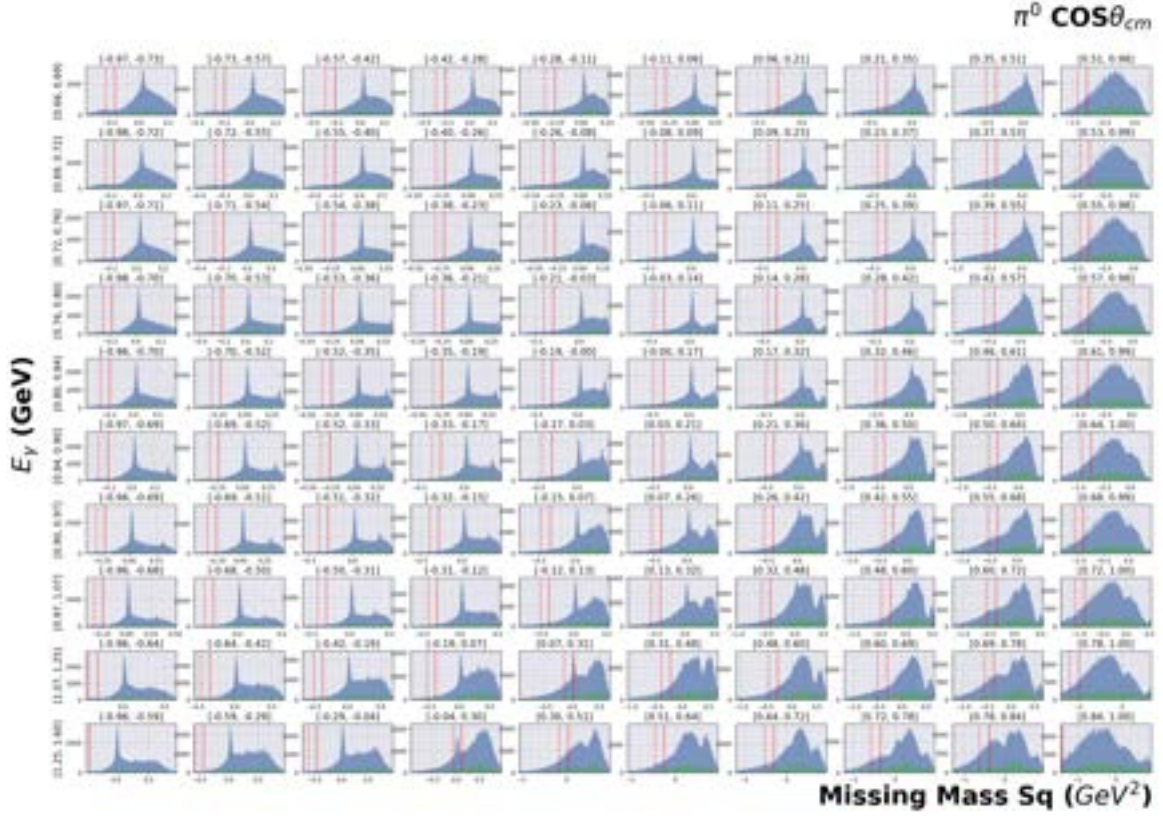


Figure 92: π^0 missing mass squared distribution partitioned in photon energies E_γ and $\cos\theta_{cm}$ for $E_\gamma = [0.71, 1.6]$ GeV. Dotted lines to indicate the regions used for initial scale factor calculation.

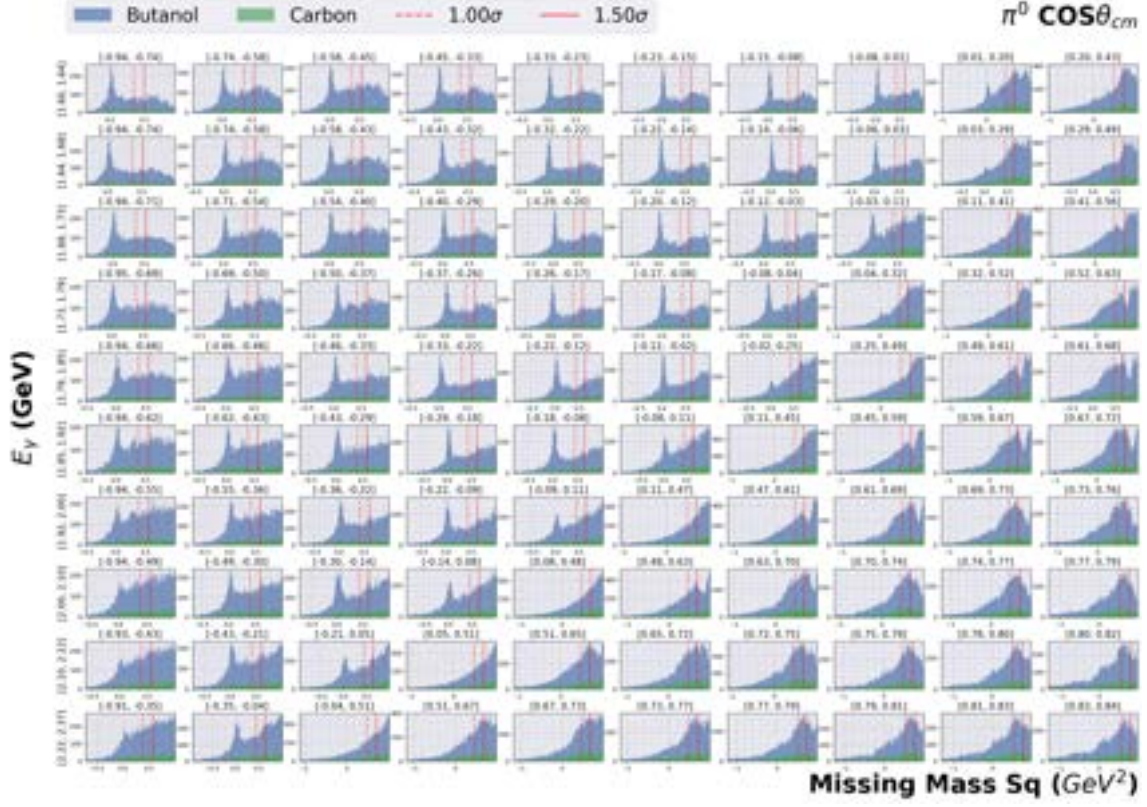


Figure 93: π^0 missing mass squared distribution partitioned in photon energies E_γ and $\cos\theta_{cm}$ for $E_\gamma = 2.4$ GeV. Dotted lines to indicate the regions used for initial scale factor calculation

First free proton peak extraction range

Fig. 94 - Fig. 96 show the first extraction of free proton events ranges in missing mass squared (M_X^2) distributions in all angular and energy bins. This event selection process is discussed in Sec. 5.1.2.

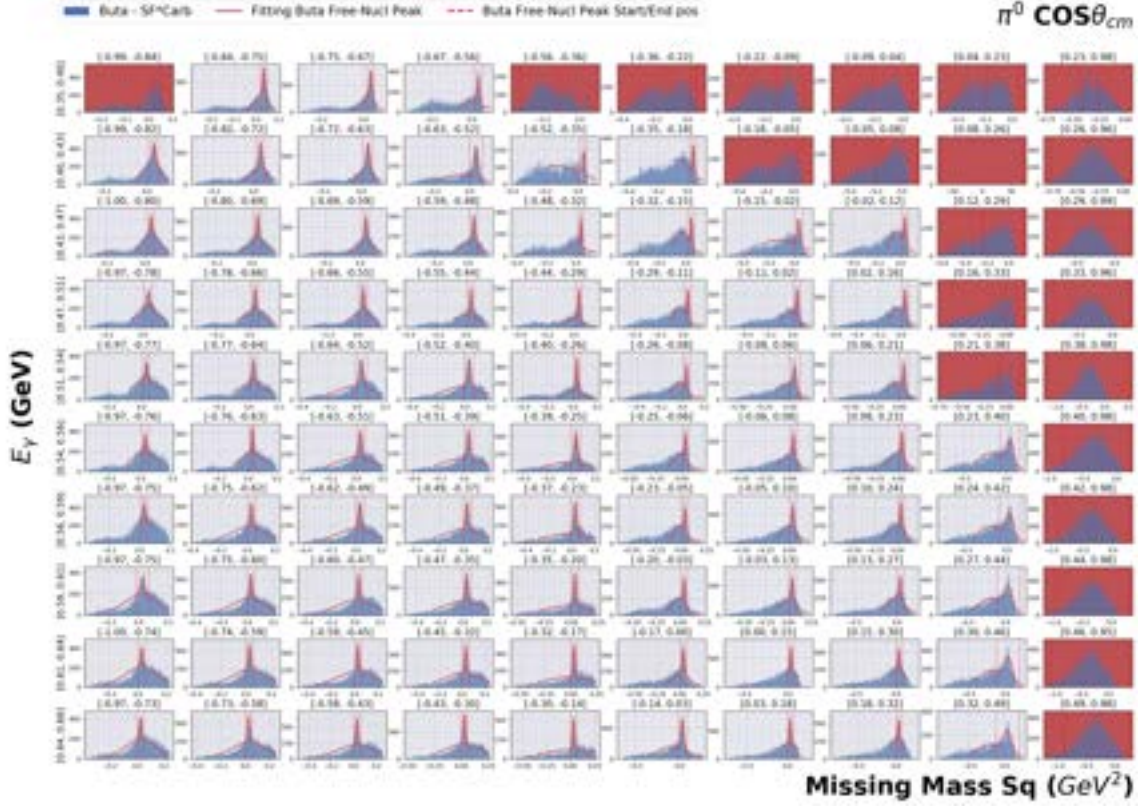


Figure 94: Difference between butanol and initially scaled carbon missing mass distributions partitioned in photon energies E_γ and $\cos\theta_{cm}$ for $E_\gamma \leq 0.66$ GeV. Red solid lines are fits on free nucleon peaks and red dotted vertical lines indicate estimated start and end positions of free-nucleon peaks. Bins with low statistics and no distinct free nucleon peaks are plotted in red.

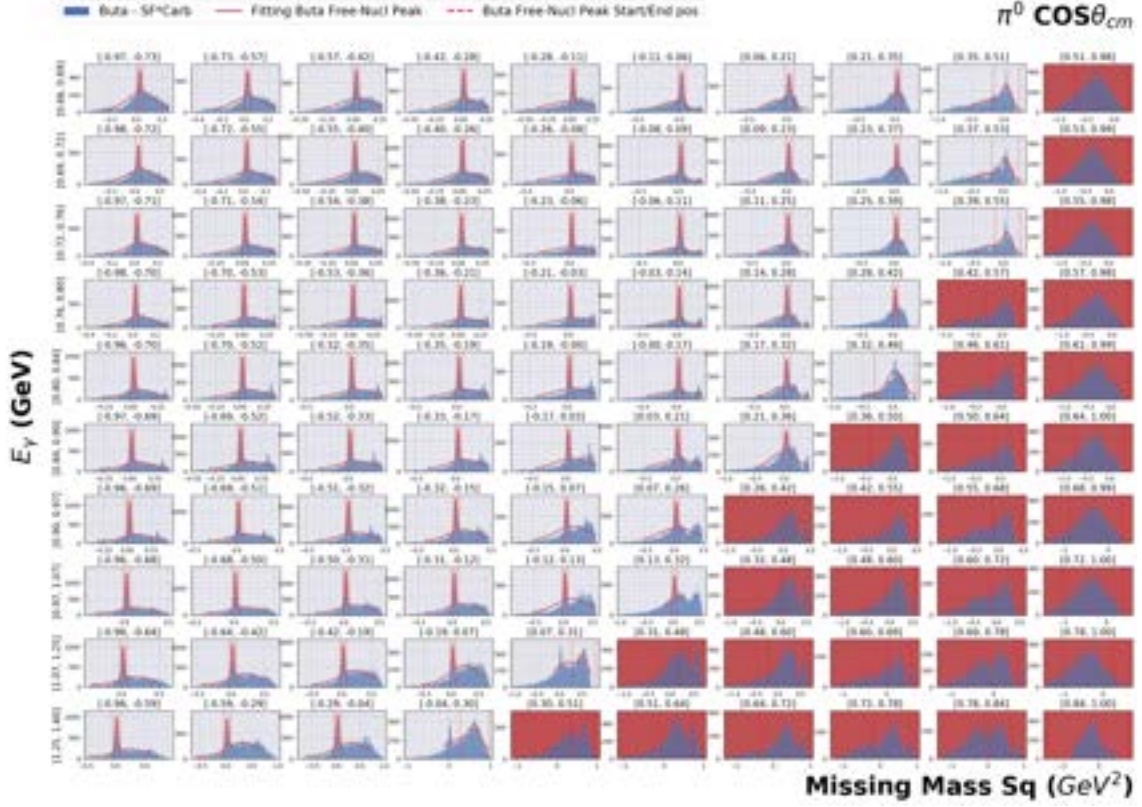


Figure 95: Difference between butanol and initially scaled carbon missing mass distributions partitioned in photon energies E_γ and $\cos\theta_{cm}$ for $E_\gamma = (0.66, 1.6)$ GeV. Red solid lines are fits on free nucleon peaks and red dotted vertical lines indicate estimated start and end positions of free-nucleon peaks. Bins with low statistics and no distinct free nucleon peaks are plotted in red.

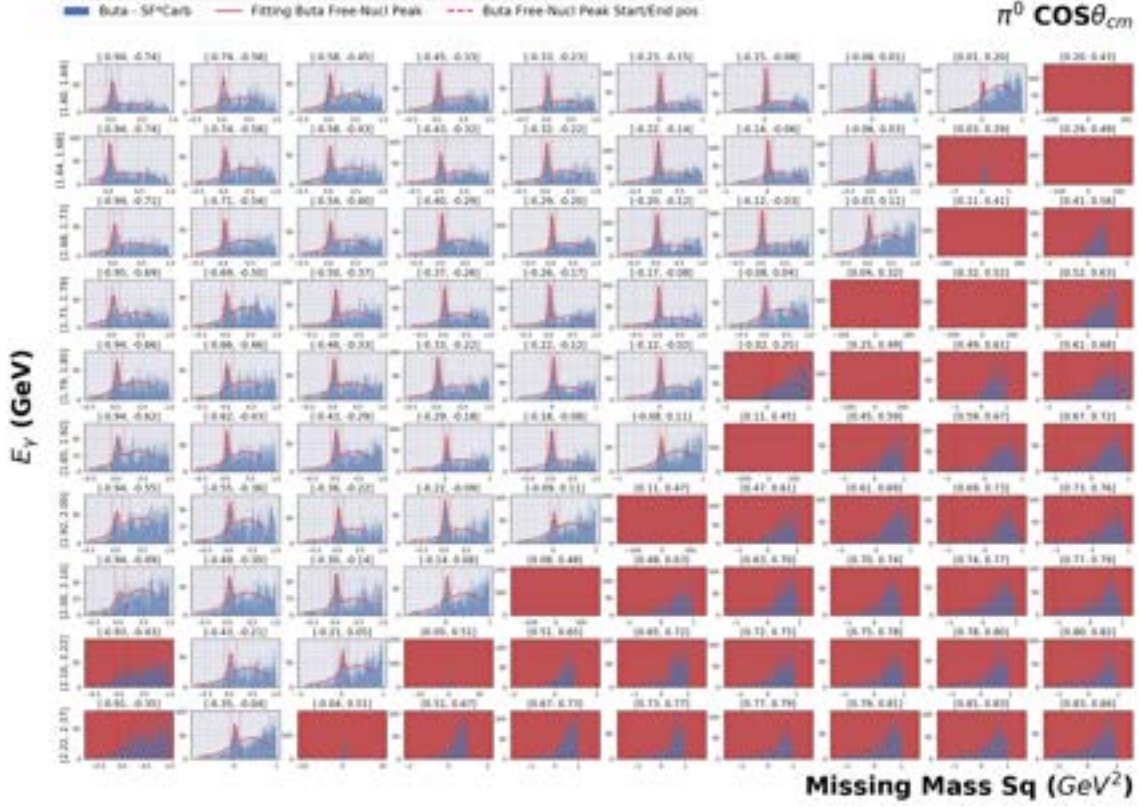


Figure 96: Difference between butanol and initially scaled carbon missing mass distributions partitioned in photon energies E_γ and $\cos \theta_{cm}$ for $E_\gamma = (1.6, 2.4)$ GeV. Red solid lines are fits on free nucleon peaks and red dotted vertical lines indicate estimated start and end positions of free-nucleon peaks. Bins with low statistics and no distinct free nucleon peaks are plotted in red.

Final scale factor

Fig. 97 - Fig. 99 show the results of final scale factors as carbon events are scaled to butanol background events. This event selection process is discussed in Sec. 5.1.3.

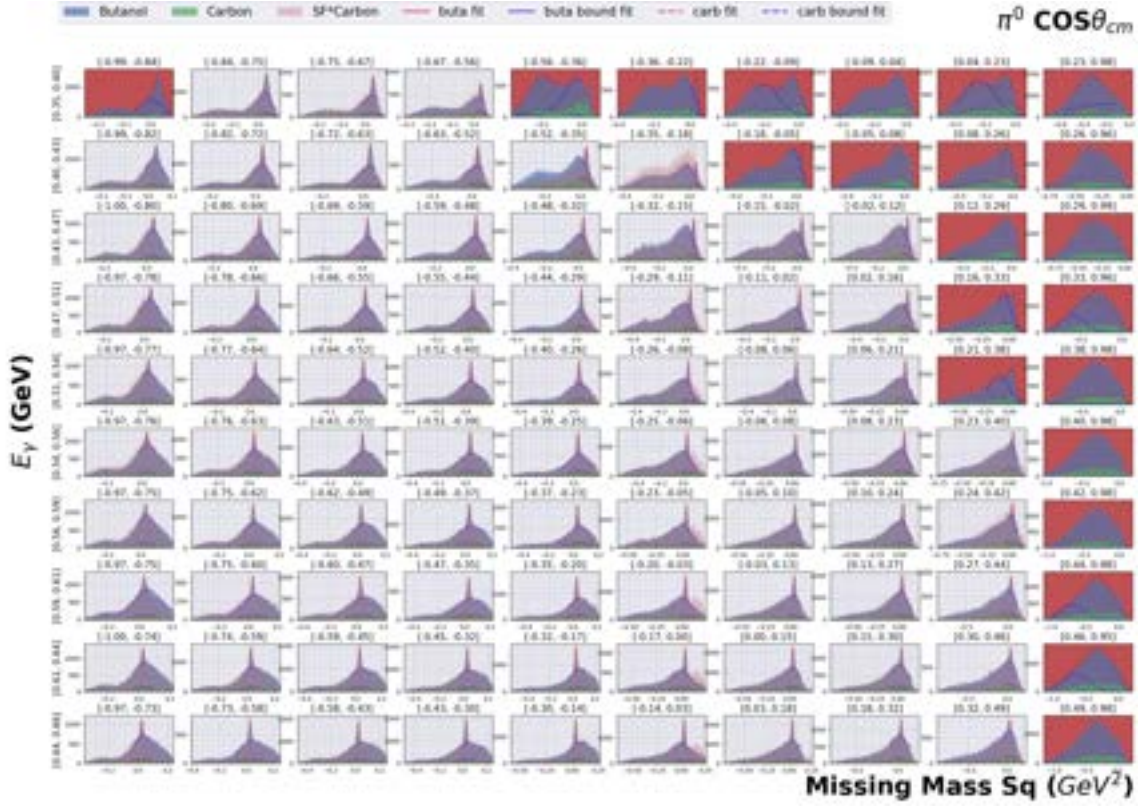


Figure 97: Scaled carbon M_X^2 distribution overlaid over butanol and carbon distribution with fitting results on butanol and carbon distributions for $E_\gamma \leq 0.66$ GeV and $\cos \theta_{cm} \in [-1, 1]$. Bins with negligible free nucleon peaks are plotted out in red.

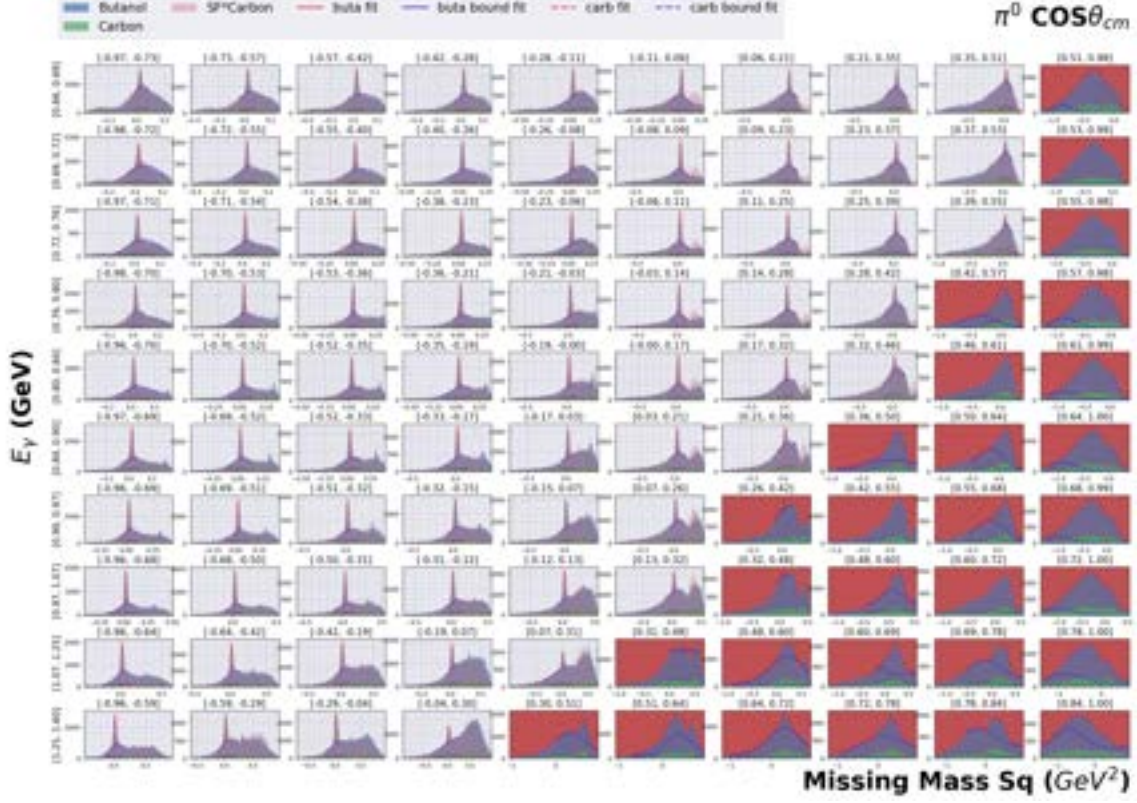


Figure 98: Scaled carbon M_X^2 distribution overlaid over butanol and carbon distribution with fitting results on butanol and carbon distributions for $E_\gamma = (0.66, 1.6)$ GeV and $\cos\theta_{cm} \in [-1, 1]$. Bins with negligible free nucleon peaks are plotted out in red.

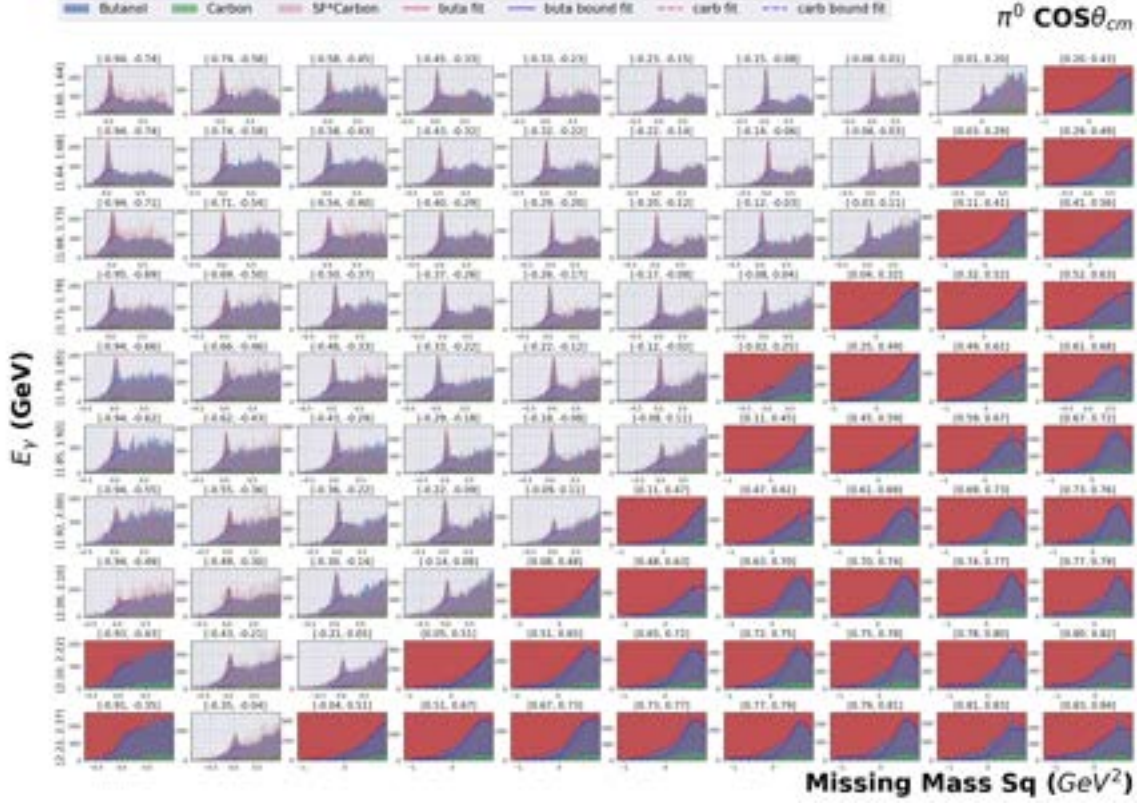


Figure 99: Scaled carbon M_X^2 distribution overlaid over butanol and carbon distribution with fitting results on butanol and carbon distributions for $E_\gamma \in [1.6, 2.4]$ GeV and $\cos \theta_{cm} \in [-1, 0.2]$. Bins with negligible free nucleon peaks are plotted out in red.

Second free proton peak extraction range

Fig. 100 - Fig. 102 show the final extraction of free proton events ranges in missing mass squared (M_X^2) distributions in all angular and energy bins. This event selection process is discussed in Sec. 5.1.4.

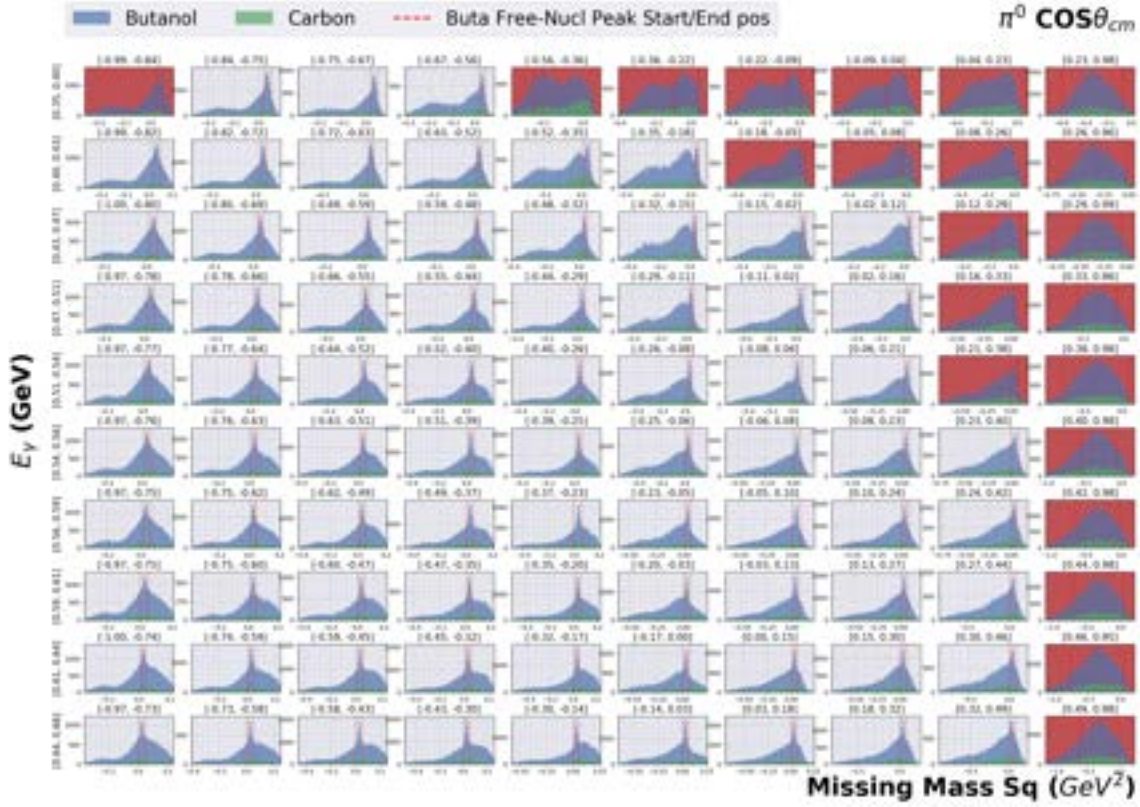


Figure 100: Final butanol free nucleon ranges (dotted red vertical lines) for $E_\gamma \leq 0.66$ GeV and $\cos \theta_{cm} \in (-1, 1)$. Bins with negligible free nucleon peaks are plotted out in red.

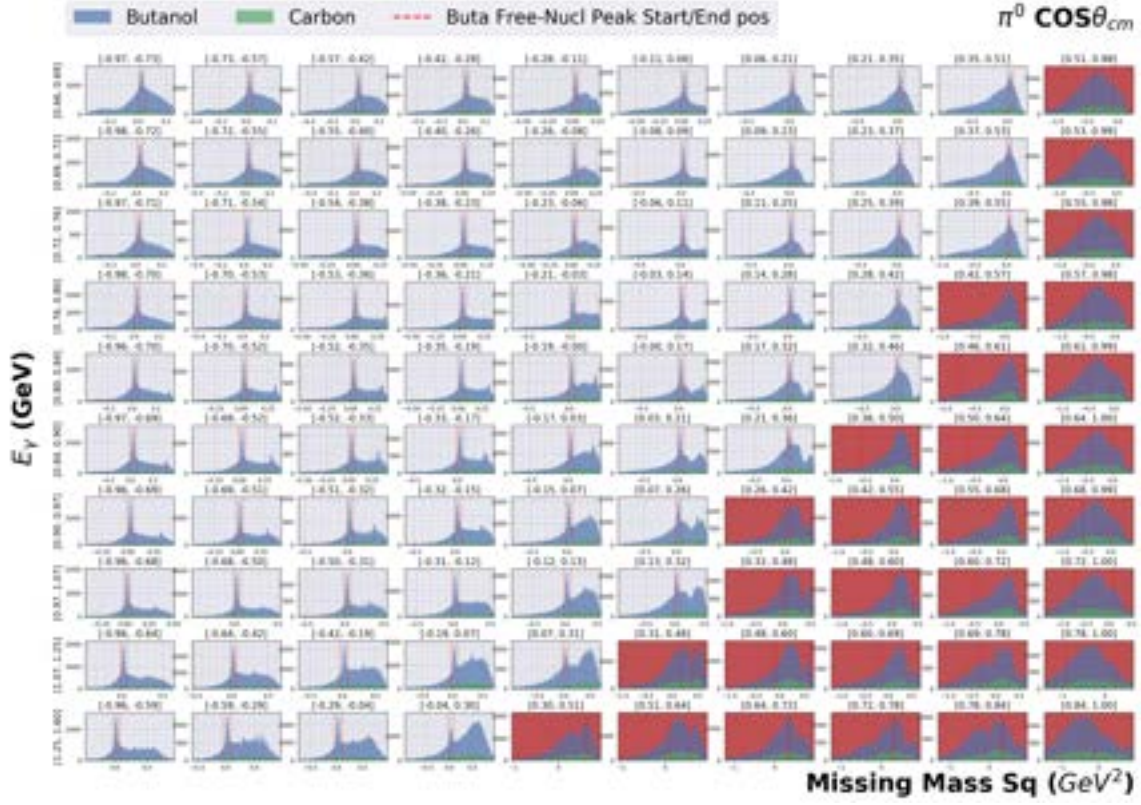


Figure 101: Final butanol free nucleon ranges for $E_\gamma = (0.66, 1.6)$ GeV and $\cos \theta_{cm} \in (-1, 1)$. Bins with negligible free nucleon peaks are plotted out in red.

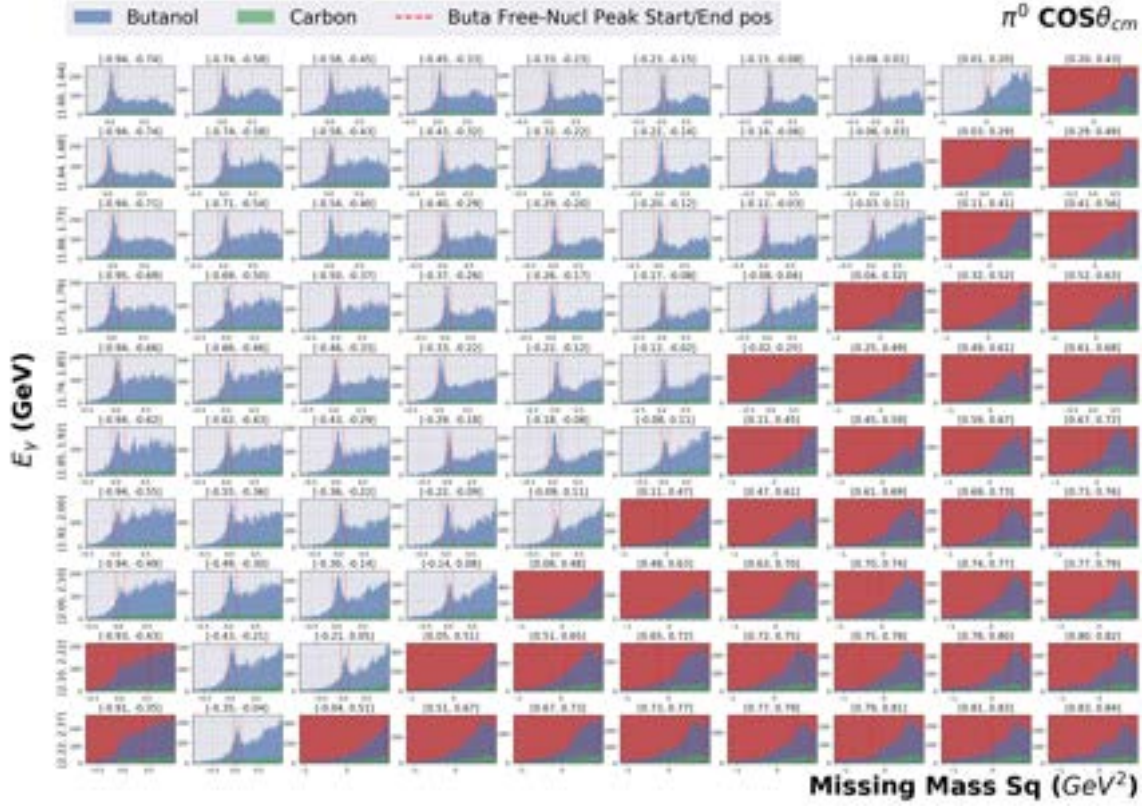


Figure 102: Final butanol free nucleon ranges (dotted red vertical lines) for $E_\gamma \in (1.6, 2.4)$ GeV and $\cos\theta_{cm} \in (-1, 0.2)$. Bins with negligible free nucleon peaks are plotted out in red.

References

- [1] E. E. Chambers and R. Hoffstadter, Phys. Rev. **103**, 1454 (1956).
- [2] M. Gell-Mann and Y. Ne'eman, "The Eightfold way: a review with a collection of reprints," (W. A. Benjamin, 1964).
- [3] C. M. G. Lattes *et al.*, Nature, **159**, 694 (1947).
- [4] D. Griffiths, "Introduction to Elementary Particles," (Wiley, USA, 1987).
- [5] V. Barnes *et al.*, Phys. Rev. Lett. **12**, 204 (1964).
- [6] J. J. Aubert *et al.*, Phys. Rev. Lett. **33**, 1404 (1974).
- [7] S. Herb *et al.*, Phys. Rev. Lett. **39**, 252 (1977).
- [8] S. Abachi *et al.*, Phys. Rev. Lett. **74**, 2632 (1995).
- [9] E. D. Bloom *et al.*, Phys. Rev. Lett. **23**, 930 (1969).
- [10] H. Gao, Nature **590**, 559 (2021).
- [11] S. Bethke, Prog. Part. Nucl. Phys. **58**, 351 (2007).
- [12] P. Achard *et al.*, Phys. Lett. B **623**, 26 (2005).
- [13] A. De Rujula, H. Georgi, and S. L. Glashow, Phys. Rev. D **12**, 147 (1975).
- [14] N. Isgur and G. Karl, Phys. Lett. **B72**, 109 (1977).
- [15] S. Capstick and N. Isgur, Phys. Rev. D **34**, 2809 (1986).
- [16] L. Ya. Glozman and D.-O. Riska, Phys. Rep. **268**, 263 (1996).
- [17] B. F. Wagenbrunn *et al.*, Phys. Lett. B **511**, 33 (2001).
- [18] G. t Hooft, Phys. Rev. D **14**, 3432 (1976); **18**, 2199(E) (1978).
- [19] M. A. Shifman, A. I. Vainshtein, and V. I. Zakharov, Nucl. Phys. B **163**, 46 (1980).
- [20] R. Bijker, F. Iachello, and A. Leviatan, Ann. Phys. (N.Y.) **236**, 69 (1994).
- [21] H. B. Nielsen and A Patkos, Nucl. Phys. B **195**, 137 (1982).
- [22] A. Chodos *et al.*, Phys. Rev. D **9**, 3471 (1974); *ibid* D **10**, 2599 (1974).
- [23] G. E. Brown and M. Rho, Phys. Lett. **82B**, 177 (1979).
- [24] R. Friedberg and T. D. Lee, Phys. Rev. D **15**, 1694 (1977); *ibid* D **16**, 1096 (1977).

- [25] G. Eckart and B. Schwesinger, Nucl. Phys. A **458**, 620 (1980).
- [26] P. Maris and C. D. Roberts, Int. J. Mod. Phys. E **12**, 297 (2003).
- [27] M. Kirchbach, M. Moshinsky, and Yu. F. Smirnov, Phys. Rev. D **64**, 114005 (2001).
- [28] U. Loring, B. C. Metsch. and H. R. Petry, Eur. Phys. J. A **10** (2001), 447-486.
- [29] R. G. Edwards *et al.* [Hadron Spectrum Collaboration], Phys. Rev. D **87** (2013) no.5, 054506.
- [30] A. Ukawa, J. Stat. Phys. **160**, 1081 (2015).
- [31] C. T. H. Davies *et al.*, Phys. Rev. Lett. **92**, 022001 (2004).
- [32] S. Dürr *et al.*, Science, **322**, 1224 (2008).
- [33] P. Hagler, Proc. Sci., **LAT2007**, 013 (2007).
- [34] F. X. Lee *et al.*, Nucl. Phys. B Proc. Suppl. **106-107**, 248 (2002).
- [35] D. B. Leinweber, A. W. Thomas, K Tsushima, and S. V. Wright, Phys. Rev. D **61**, 074502 (2000).
- [36] S. Aoki *et al.*, Phys. Rev. D **60**, 114508 (1999).
- [37] D. B. Leinweber, D. H. Lu, and A. W. Thomas, Phys. Rev. D **60**, 934014 (1999).
- [38] P. A. Zyla *et al.* [Particle Data Group], “Review of Particle Physics,” PTEP **2020**, 083C01 (2020).
- [39] K. Hagiwara *et al.* [Particle Data Group], Phys. Rev. D **66**, 010001 (2002).
- [40] R. Koniuk and N. Isgur, Phys. Rev. Lett. **44** (1980), 845.
- [41] T.-S. H. Lee, A. Matsuyama, and T. Sato, Phys. Rep. **439**, 193 (2007).
- [42] F. Close, S. Donnachie, and G. Shaw, “Electromagnetic Interactions and Hadronic Structure” (Cambridge University Press, Cambridge, 2007).
- [43] V. D. Burkert and T. S. H. Lee, Int. J. Mod. Phys. E **13**, 1035 (2004).
- [44] E. Klempt and J.-M. Richard, arXiv:0901.2055 [hep-ph] (2009).
- [45] D. Sokhan, “Beam Asymmetry Measurement from Pion Photoproduction on the Neutron,” Ph.D. dissertation, University of Edinburgh (2009).
- [46] F. Tabakin, C. Fasano, and B. Saghai, Phys. Rev. C **46**, 2430 (1992).
- [47] F. Tabakin and W. Chiang, Phys. Rev. C **55**, 2054 (1997).

- [48] G. F. Chew, M. L. Goldberger, F. E. Low, and Y. Nambu, Phys. Rev. **106**, 1345 (1957).
- [49] G. F. Chew, M. L. Goldberger, F. E. Low, and Y. Nambu, Phys. Rev. **106**, 1337 (1957).
- [50] A. Nagl *et al.*, Springer Tracts in Modern Physics, **120**: “Nuclear Pion Photo-production”, (Springer-Verlag, Berlin Heidelberg, 1991).
- [51] A. Thomas and W. Weise, “The Structure of the Nucleon”, (Wiley, Berlin, 2001).
- [52] T. Ericson and W. Weise, “Pions and Nuclei”, (Clarendon Press, Oxford, 1988).
- [53] R. L. Walker, Phys. Rev. **182**, 1729 (1969).
- [54] M. Jacob and G. C. Wick, Ann. Phys. **7**, 404 (1959).
- [55] G. Knochlein, D. Dreschel, and L. Tiator, Z. Phys. A **352**, 327 (1995).
- [56] I. S. Berker, A. Donnachie, and J. K. Storrow, Nucl. Phys. B **95**, 347 (1975).
- [57] B. Krusche and S. Schadmand, Prog. Part. Nucl. Phys. **51**, 399 (2003).
- [58] R. Shankar, “Principles of Quantum Mechanics”, (Springer Science Business Media. Inc., 1994).
- [59] S. U. Chung *et al.*, Ann. der Phys. **507**, 404 (1995).
- [60] E. P. Wigner, Phys. Rev. **70**, 15 (1946).
- [61] E. P. Wigner and L. Eisenbud, Phys. Rev. **72**, 29 (1947).
- [62] K. L. Au, B. Morgan. and j. R. Pennington, Phys. Rev. D **35**, 1633 (1987).
- [63] A. V. Anisovich *et al.*, Eur. Phys. J. A **52**, 284 (2016).
- [64] J. Hadamard, *Sur les problmes aux drives particles et leur signification physique*, (Princeton University Bulletin, 1902) pp. 49-52.
- [65] A. N. Tikhonov and V. Y. Arsenin. *Solutions of ill-posed problems* (New York: Winston, 1977).
- [66] R. L. Workman, M. W. Paris, W. J. Briscoe, and I. I. Strakovsky, Phys. Rev. C **86**, 015202 (2012).
- [67] R. L. Workman, R. A. Arndt, W. J. Briscoe, M. W. Paris, and I. I. Strakovsky, Phys. Rev. C **86**, 035202 (2012).
- [68] L. Tiator, D. Drechsel, S. S. Kamalov, and M. Vanderhaeghen, Eur. Phys. J. ST **198**, 141 (2011).
- [69] L. Tiator, Few Body Syst. **59**, 21 (2018).

- [70] A. M. Sandorfi, B. Dey, A. Sarantsev, L. Tiator, and R. Workman, AIP Conf. Proc. **1432**, 219 (2012).
- [71] A. V. Anisovich, R. Beck, E. Klempt, V. A. Nikonov, A. V. Sarantsev, and U. Thoma, Eur. Phys. J. A **48**, 15 (2012).
- [72] A. V. Anisovich, E. Klempt, V. A. Nikonov, M. A. Matveev, A. V. Sarantsev, and U. Thoma, Eur. Phys. J. A **44**, 203 (2010).
- [73] R. A. Arndt, I. I. Strakovsky, and R. L. Workman, Phys. Rev. C **53**, 430 (1996).
- [74] C. G. Fasano, F. Tabakin, and B. Saghai, Phys. Rev. C **46**, 2430 (1992).
- [75] “Pion photoproduction from a polarized target,” Spokespersons: N. Benmouna, W. J. Briscoe, I. I. Strakovsky, S. Strauch, and G. V. O’Rially [CLAS Collaborations], JLab Proposal E-03-105, Newport News, VA, USA, 2003.
- [76] B. Metsch, Eur. Phys. J. A **35**, 275 (2008).
- [77] “Search for missing nucleon resonances in the photoproduction of hyperons using a polarized photon beam and a polarized target,” Spokespersons: F. J. Klein and L. Todor [CLAS Collaborations], JLab Proposal E-02-112, Newport News, VA, USA, 2002.
- [78] B. A. Mecking *et al.* [CLAS Collaboration], Nucl. Instrum. Meth. A **503**, 513 (2003).
- [79] <https://www.flickr.com/photos/jeffersonlab/>.
- [80] <https://www.jlab.org/Hall-B/album/>.
- [81] S. Gagnon, <http://education.jlab.org/sitetour/guidedtourt05.l.alt.html>.
- [82] M. Crofford *et al.*, “The RF system for the CEBAF polarized photoinjector,” Technical Report, Thomas Jefferson National Accelerator Facility (1993).
- [83] C. W. Leemann, D. R. Douglas, and G. A. Krafft, Ann. Rev. Nucl. Part. Sci. **51**, 413 (2001).
- [84] C. Hovater, G. Arnold, J. Fugitt, L. Harwood, R. Kazimi, G. Lahti, J. Mammoser, R. Nelson, C. Piller, and L. Turlington, Conf. Proc. C **9608262**, 77 (1996).
- [85] D. I. Sober, H. Crannell, A. Longhi, S. K. Matthews, J. T. O’Brien, B. L. Berman, W. J. Briscoe, P. L. Cole, J. P. Connelly, and W. R. Dodge *et al.* Nucl. Instrum. Meth. A **440**, 263 (2000).
- [86] K. Livingston, arXiv:0809.1739v1 [nucl-ex] (2008).
- [87] S. Taylor, S. Ahmad, J. Distelbrink, G. S. Mutchler, E. Smith, and T. Smith, Nucl. Instrum. Meth. A **462**, 484 (2001).

- [88] M. D. Mestayer, D. S. Carman, B. Asavapibhop, F. J. Barbosa, P. Bonneau, S. B. Christo, G. E. Dodge, T. Dooling, W. S. Duncan, and S. A. Dytman *et al.* Nucl. Instrum. Meth. A **449**, 81 (2000).
- [89] E. S. Smith, T. Carstens, J. Distelbrink, M. Eckhause, H. Egiyan, L. Elouadrhiri, J. Ficenec, M. Guidal, A. D. Hancock, F. W. Hersman *et al.* Nucl. Instrum. Meth. A **432**, 265 (1999).
- [90] M. Amarian, G. Asrian, K. Beard, W. Brooks, V. Burkert, T. Carstens, A. Coleman, R. Demirchian, Y. Efremenko, H. Egiian *et al.* Nucl. Instrum. Meth. A **460**, 239 (2001).
- [91] M. Anghinolfi, H. Avakian, M. Battaglieri, N. Bianchi, P. Corvisiero, R. De Vita, E. Golovach, V. Gyuriyan, M. Mirazita, V. Mokeev *et al.* Nucl. Instrum. Meth. A **537**, 562 (2005).
- [92] G. P. Heath, Nucl. Instrum. Meth. A **278**, 431 (1989).
- [93] C. D. Keith, J. Brock, C. Carlin, S. A. Comer, D. Kashy, J. McAndrew, D. G. Meekins, E. Pasyuk, J. J. Pierce. and M. L. Seely, Nucl. Instrum. Meth. A **684**, 27 (2012).
- [94] <https://userweb.jlab.org/~ckeith/Frozen/Photos/Photos.html>
- [95] H. Olsen and L. C. Maximon, Phys. Rev. **114**, 887 (1959).
- [96] [https://clasweb.jlab.org/rungroups/g9/wiki/index.php/Beam_Polarization_\(Circ.\)](https://clasweb.jlab.org/rungroups/g9/wiki/index.php/Beam_Polarization_(Circ.))
- [97] N. Zachariou *et al.* [CLAS Collaboration], Phys. Lett. B **817**, 136304 (2021).
- [98] H. Jiang, “Polarization observables T and F in the $\gamma p \rightarrow \pi^0 p$ reaction,” CLAS-ANALYSIS 2014-04-01-v6 (2019)
- [99] E. Anciant *et al.*, “Tagger hit reconstruction software and tagger calibration overview,” CLAS-NOTE 1999-04 (1999).
- [100] J. Li, “The new Tagger calibration program,” CLAS-NOTE 2003-004 (2003).
- [101] D. Sokhan, “Beam asymmetry measurement from pion photoproduction on the neutron,” Ph.D. dissertation, University of Edinburgh (2009).
- [102] E. S. Smith *et al.*, “Calibration of the CLAS TOF system,” CLAS-NOTE 1999-011, (1999).
- [103] D. Lawrence and M. Mestayer, “CLAS Drift Chamber calibration: Software procedures,” CLAS-NOTE 1999-018 (1999).
- [104] M. Guillo *et al.*, “EC time calibration procedure for photon runs in CLAS,” CLAS-NOTE 2001-014 (2001).

- [105] C . K. Sinclair, “Electron Beam Polarimetry,” Thomas Jefferson National Accelerator Facility (U.S.) (1998).
- [106] H. Iwamoto, “Helicity asymmetry measurement for π^0 photoproduction with FROST,” Ph.D. dissertation, The George Washington University (2011).
- [107] S. Park, “Measurement of polarization observables in $\gamma p \rightarrow p\pi^+\pi^-$ using circular beam and longitudinal target polarization and the CLAS spectrometer at Jefferson laboratory,” Ph.D. dissertation, The Florida State University (2013).
- [108] S. Strauch *et al.* [CLAS Collaboration], Phys. Lett. B **750**, 53 (2015).
- [109] D. Schott *et al.* [CLAS Collaboration], AIP Conf. Proc. **1735**, 030016 (2016).
- [110] W. J. Briscoe *et al.* [A2 Collaboration at MAMI], Phys. Rev. C **100**, 065205 (2019).
- [111] D. Drechsel, S. S. Kamalov, and L. Tiator, Eur. Phys. J. A **34**, 69 (2007).
- [112] M. Gottschall *et al.* [CBELSA/TAPS Collaboration], Phys. Rev. Lett. **112**, 012003 (2014).
- [113] TMVA Website, <http://tmva.sourceforge.net/>
- [114] F. Klein, “TMVA Software Usage on g9a/FROST.” Private Communication (2017).
- [115] Rootbeer Website, <http://nuclear.gla.ac.uk/~kl/rootbeer/>
- [116] J. Pivarski, P. Elmer, and D. Lange, Eur. Phys. J. Web Conf. **245**, 05023 (2020).
- [117] W. McKinney *et al.*, *Data structures for statistical computing in Python*, Proc. of the 9th Python in science conf. (SCIPY 2010) **445**, 51 (2010).
- [118] C. R. Harris, K. J. Millman, S. J. van der Walt, R. Gommers, P. Virtanen, D. Cournapeau, E. Wieser, J. Taylor, S. Berg, N. J. Smith *et al.* Nature **585**, 357 (2020).
- [119] P. Virtanen, R. Gommers, T. E. Oliphant, M. Haberland, T. Reddy, D. Cournapeau, E. Burovski, P. Peterson, W. Weckesser, J. Bright *et al.* “SciPy 1.0—Fundamental Algorithms for Scientific Computing in Python,” Nature Meth. **17**, 261 (2020).
- [120] M. Abadi, A. Agarwal, P. Barham, E. Brevdo, Z. Chen, C. Citro, G. S. Corrado, A. Davis, J. Dean, M. Devin *et al.* “TensorFlow: Large-Scale Machine Learning on Heterogeneous Distributed Systems,” [arXiv:1603.04467 [cs.DC]].
- [121] E. Pasyuk, “Energy loss corrections for charged particles in CLAS,” CLAS Note 2007-016 (2007).

- [122] E. Pasyuk, *Brief User Guid to GPID*, CLAS NOTE 2007-008 (2007).
- [123] S. Strauch, “Polarization observable E in the $p(\gamma, \pi^+)n$ reaction,” CLAS-ANALYSIS 2014-101 (2014).
- [124] J. W. Fowler, J. Low Temp. Phys. **176**, 414 (2014).
- [125] W. Cash, Astrophys. J. **228**, 939 (1979).
- [126] D. P. Kingma and J. Ba, “Adam: A Method for Stochastic Optimization,” [arXiv:1412.6980 [cs.LG]].
- [127] I. Goodfellow, Y. Bengio, and A. Courville, “Deep Learning,” (MIT Press, 2016).
- [128] C. Bishop, “Pattern recognition and Machine Learning,” (New York, Springer, 2006).
- [129] O. Dürr and B. Sick, “Probabilistic Deep Learning,” (Manning, 2020).